The Influence of Section Thickness on the Ultrasonic Fatigue Response of 316L Stainless Steel Manufactured via Laser Powder Bed Fusion

by

Megan L. Trombley

A dissertation submitted in partial fulfillment
of the requirements for the degree of
Doctor of Philosophy
(Materials Science and Engineering)
in the University of Michigan
2024

Doctoral Committee:

Professor John E. Allison, Chair
Associate Professor Jerard V. Gordon
Professor Amit Misra
Professor Alan I. Taub

Megan L. Trombley

mltrombl@umich.edu

ORCID iD: 0000-0003-3971-015X

Dedication

To my family.

Acknowledgements

Throughout this journey of graduate education, I have received the support of many individuals. Without their guidance, words of encouragement, knowledge, and feedback this dissertation would not have been possible.

First, I would like to recognize my advisor Dr. John Allison for the support and patience shown to me over the past five years. He has provided countless hours of feedback, insight, and mentorship that has helped shape me into the researcher I am today. I am particularly thankful for his patience and understanding during times of a global pandemic and when I decided to embark on the adventure of becoming a mother while pursuing a graduate education. Despite an unconventional journey, he has given me the confidence and the resources to see this through. I would also like to thank each member of my committee: Dr. Amit Misra, Dr. Alan Taub, and Dr. Jerard Gordon. Their expertise, advise, and feedback was crucial in the completion of this dissertation.

The experiments conducted in this dissertation would not have been possible without the support of the U.S. Office of Naval Research (ONR). Project conceptualization, all materials, and thoughtful discussions were generously provided by the Naval Research Laboratory (NRL) and the Naval Surface Warfare Center – Carderock Division (NSWC). In particular, I would like to recognize Dr. Andrew Birnbaum (NRL), Dr. Charles Fisher (NSWC), Zach Heinkel (NSWC), and Bernie LaFrance (NSWC) for their direct contribution of providing materials and insight. Additionally, I am thankful for helpful discussions with many others, including: Dr. Athanasios

Iliopoulos (NRL), Dr. John Michopoulos (NRL), Dr. Aeriel Murphy-Leonard (Ohio State University), Dr. David Rowenhorst (NRL), and Dr. Herwig Mayer (BOKU). Lastly, I would like to recognize Dr. Carlos Engler-Pinto Jr. (Ford Motor Company) whose methods for estimating fatigue strength were instrumental in this work, and Dr. Chris Torbet (UCSB) who provided critical support in testing instrumentation.

I am incredibly grateful to the entire Allison/Jones research group. Dr. Qianying Shi laid the groundwork for this dissertation with her initial testing of fatigue specimens. She also graciously provided equipment training for ultrasonic fatigue testing, crack growth testing, SEM fractography, and tensile testing. Dr. Wayne Jones provided years of experience in operating ultrasonic fatigue testing equipment and many delightful conversations. To Dr. Tracy Berman I am thankful for training in sample preparation and EBSD techniques, as well as for showing me that being a mom while being a Ph.D. student is possible. Lastly, I am thankful to the countless other students and post-docs of the Allison/Jones research group who provided support and camaraderie during my time there, including Dr. Duncan Greely, Dr. Zhenjie Yao, Dr. Chaitali Patil, Alexis Parrish, and Ryan Gast.

I am thankful for the financial support provided by the University of Michigan Rackham Merit Fellowship Program. I also gratefully acknowledge the U.S. Office of Naval Research for providing and materials tested.

Finally, I would like to recognize my family, without whom this graduate work would not have been possible. To my husband, words cannot express how grateful I am for the endless support and encouragement. Not only for supporting me but for being such a lovely and caring father to our daughter while I finish this degree. Of all the things we’ve seen and done together, my favorite part was being there with you. To my parents, Charles and Kate, and my brother, Nolan, thank you for fostering my love of science and learning that has brought me here today. I am honored by your selflessness in encouraging me to pursue my passions even when it means moving a thousand miles away from home. To my in-laws, Cindi and Paul, Isabel and Derek, Joe, Ann, Tyler and Katie, thank you for welcoming me, making me feel at home in Michigan, and serving as surrogates of support that I know my family wishes they could give me in person. Lastly, to my daughter, Murphy, thank you for teaching me to slow down and savor every moment. You were a beacon of light in the hardest moments of this endeavor, and I am forever grateful.

Table of Contents

List of Tables

List of Figures

Abstract

Metal additive manufacturing (AM) is an important modern manufacturing method that offers many advantages over conventional manufacturing. Due to its complex thermal history, metal AM is still the focus of active research directed at fully understanding process-structure-property (PSP) relationships. In the age of integrated computational materials engineering (ICME), understanding the mechanisms that drive PSP relationships are critical in enabling robust modeling and optimization of AM processes. The AM processing parameters largely dictate the thermal history, which in turn influences the microstructure, macrostructure, and mechanical properties. In this dissertation, the fatigue behavior of 316L stainless steel made via laser-powder bed fusion (L-PBF) was investigated. There is a particular lack of research addressing the influence of part geometry on fatigue behavior. With the goal being to accelerate the design process, it is imperative to understand how mechanical behavior changes with section thickness to accurately predict when and where failure will occur in large, complex parts. The focus of this dissertation is on the effects of section thickness and AM machine on high cycle fatigue behavior in AM 316L stainless steel.

The high cycle fatigue (HCF) behavior was characterized using ultrasonic fatigue (UF) testing. Specimens with a gauge diameter of 5.0 mm, 2.5 mm, and 1.5 mm were fabricated on a GE Additive Concept Laser M2 machine. Specimens with a gauge diameter of 5.0 mm and 1.5 mm were fabricated on a 3D Systems ProX DMP 200 machine. Additionally, selected samples were subjected to a stress relieving heat treatment and others were tested with the as-built surface removed. A random fatigue limit (RFL) model informed by the maximum likelihood estimation

(MLE) was used to quantify statistical variability and estimate an S-N curve fit along with fatigue strength at 10^8 cycles.

It was observed that HCF behavior is improved as the gauge diameter is reduced for both AM machines. Thorough investigation revealed that the surface condition and residual stress state are the primary factors influencing the observed section thickness effects on HCF. The influence of AM machine on HCF was modest. Removal of the as-built surface led to a substantial improvement in HCF properties. Stress relieving heat treatment led to an improvement in the HCF properties compared to as-built samples. The residual stress state was determined to be tensile on the surface of the as-built samples with higher stresses in the 5.0 mm specimens compared to the 1.5 mm specimens. There was also a significant difference in residual stress magnitude between the CL M2 and ProX 200 specimens despite showing a similar fatigue response.

The small fatigue crack growth (FCG) behavior of 316L made on both the CL M2 and ProX 200 were compared. No significant difference in FCG behavior was observed when altering processing parameters, build orientation, or feedstock supplier. Despite different types of defects and residual stress states, small crack growth rates (CGR) are largely the same. When crack initiation in HCF specimens occurs sub-surface, crack growth begins in vacuum at multiple orders of magnitude slower CGRs, leading to longer fatigue lives. A model for the prediction of HCF behavior informed by CGRs and defect sizes was verified for each condition.

The results from this investigation can be used to design new AM processing routes and post-processing routines for improving the predictability of the HCF response of AM fabricated components.

Chapter 1 Introduction

Additive manufacturing (AM) is a rapidly evolving technology whose process-structure-property (PSP) relationships are the focus of active research. AM is a modern manufacturing method that has garnered particular interest for its ability to create intricate geometries in single-step manufacturing processes aiding to the complexity of parts that can be manufactured while reducing the amount of assembly required [1–5]. The automotive, aerospace, naval, and medical industries have all found applications where AM is better suited than conventional manufacturing methods [6,7].

Laser-powder bed fusion (L-PBF) is one of the most widely researched metal AM techniques, with over 130 process variables that dictate the final product [8,9]. Optimizing the process parameters is the focus of many studies, with a primary goal to reduce porosity, surface roughness, and manufacturing defects while improving the microstructure and mechanical properties [10–28]. The easiest to control process parameters – laser power, scan speed, hatch spacing, layer thickness, laser spot size, and scan strategy – are the ones most widely investigated. Of the over 65 L-PBF machines currently available, most come with recommended process parameters for each common material used, and as such this dissertation does not focus on altering the process parameters. Rather, a focus will be placed on the effects that may be observed across build platforms using the manufacturer’s recommended settings.

For structural components, fatigue is a critical design property that has been shown to depend largely on the surface finish, residual stresses, and processing defects. Both surface finish [2,29–32] and internal defects [33,34] have been found to significantly impact the fatigue behavior due to their role in serving as points of stress concentration [35,36]. As such, the residual stress state also plays a role in the fatigue behavior as it alters the mean stress experienced by the specimen, with tensile residual stresses reducing the fatigue strength [37].

Given L-PBF's ability to fabricate intricate components, an understanding of how the section thickness alters the fatigue behavior is imperative. So-called 'size effects' are a phenomenon seen in conventionally manufactured materials whereby a reduced thickness results in an improved fatigue performance [38–44]. As it stands, size effects in conventionally manufactured materials are thought to be governed by Weibull's weakest link theory [44]. This theory suggests that a larger volume will have a higher probability of shorter fatigue life due to the abundance of more crack initiating elements [35,44,45]. In all the efforts to characterize processing parameter effects on mechanical performance, size effects have not been explicitly shown in occur in AM. This dissertation serves to fill this gap while evaluating which aspects of the PSP relationships have the strongest influence on the fatigue behavior observed.

The overarching goal of this dissertation is to lay the groundwork for understanding the mechanistic PSP relationships in regards to fatigue behavior of AM as a means to inform ICME models [46]. This work focuses on 316L stainless steel manufactured by L-PBF. The fatigue response, crack growth behavior, microstructure, surface roughness, critical flaws, and residual stresses are investigated as a product of the processing parameters chosen. The specific objectives of this dissertation were to:

1. Investigate the influence of AM machine and gauge diameter on the microstructure, macrostructure, and residual stress state of the as-printed L-PBF specimens.
2. Determine the section thickness (gauge diameter) effects on the fatigue response in the high cycle fatigue (HCF) regime.

3. Characterize the source of fatigue crack initiation relative to the different AM machines and gauge diameters.
4. Establish the primary mechanisms responsible for the observed gauge diameter effects.
5. Characterize the short crack growth behavior and determine if influences of additive machine or heat treatment can influence short crack growth rates.
6. Confirm the validity of a short crack fracture mechanics approach for predicting HCF (S-N) behavior of AM materials.

Chapter 2 consists of a literature review of current research pertaining to metal AM and L-PBF, 316L stainless steel, ultrasonic fatigue testing and high cycle fatigue (HCF) behavior, crack growth behavior and stress concentrations, and factors that influence the fatigue of AM. Chapters 3, 4, and 5 each focus on a separate study that has been prepared for publication. As such, the introduction and discussion sections of each may contain repetitive information from Chapter 2. Chapters 3 and 4 investigate the gauge diameter effects on fatigue behavior of GE Additive Concept Laser M2 and 3D Systems ProX DMP 200 L-PBF machines, respectively. The crack growth behavior of samples produced on both machines is investigated in Chapter 5. The final chapter, Chapter 6, presents the conclusions and recommendations for future work.

This dissertation work is conducted as part of a collaborative study between the University of Michigan and the Office of Naval Research (ONR) on a multi-lab, multi-university program referred to as Agile Integrated Computational Materials Engineering (ICME). The Naval Research Laboratory (NRL) and the Carderock Division of the Naval Surface Warfare Center (NSWC) were key members of this collaborative effort and instrumental in providing test specimens for this dissertation. The University of Michigan's role in this program was split into two goals: HCF testing and critical flaw evaluation, and crystal plasticity modeling of L-PBF 316L stainless steel.

This dissertation represents the entirety of the work done on HCF testing and critical flaw evaluation.

References

[1] ISO/TC 261, ASTM Committee F42, ISO/ASTM 52900:2017 Additive manufacturing. General principles. Terminology, (2017).

[2] T. DebRoy, H.L. Wei, J.S. Zuback, T. Mukherjee, J.W. Elmer, J.O. Milewski, A.M. Beese, A. Wilson-Heid, A. De, W. Zhang, Additive manufacturing of metallic components – Process, structure and properties, Prog. Mater. Sci. 92 (2018) 112–224. https://doi.org/10.1016/j.pmatsci.2017.10.001.

[3] H. Fayazfar, M. Salarian, A. Rogalsky, D. Sarker, P. Russo, V. Paserin, E. Toyserkani, A critical review of powder-based additive manufacturing of ferrous alloys: Process parameters, microstructure and mechanical properties, Mater. Des. 144 (2018) 98–128. https://doi.org/10.1016/j.matdes.2018.02.018.

[4] I. Gibson, D.W. Rosen, B. Stucker, Additive Manufacturing Technologies, Springer US, Boston, MA, 2010. https://doi.org/10.1007/978-1-4419-1120-9.

[5] N. Sanaei, A. Fatemi, Defects in additive manufactured metals and their effect on fatigue performance: A state-of-the-art review, Prog. Mater. Sci. 117 (2021) 100724. https://doi.org/10.1016/j.pmatsci.2020.100724.

[6] E. Herderick, Additive manufacturing of metals: A review, in: Addit. Manuf. Met., Columbus, Ohio, 2011: p. 13.

[7] P. Bajaj, A. Hariharan, A. Kini, P. Kürnsteiner, D. Raabe, E.A. Jägle, Steels in additive manufacturing: A review of their microstructure and properties, Mater. Sci. Eng. A 772 (2020) 138633. https://doi.org/10.1016/j.msea.2019.138633.

[8] Y. Murakami, N.N. Yokoyama, J. Nagata, Mechanism of fatigue failure in ultralong life regime: Fatigue failure in ultralong life regime, Fatigue Fract. Eng. Mater. Struct. 25 (2002) 735–746. https://doi.org/10.1046/j.1460-2695.2002.00576.x.

[9] Y. Murakami, T. Nomoto, T. Ueda, Factors influencing the mechanism of superlong fatigue failure in steels: Superlong fatigue failure in steels, Fatigue Fract. Eng. Mater. Struct. 22 (1999) 581–590. https://doi.org/10.1046/j.1460-2695.1999.00187.x.

[10] D.R. Clymer, J. Cagan, J. Beuth, Power–velocity process design charts for powder bed additive manufacturing, J. Mech. Des. 139 (2017) 100907. https://doi.org/10.1115/1.4037302.

[11] K. Carpenter, A. Tabei, On residual stress development, prevention, and compensation in metal additive manufacturing, Materials 13 (2020) 255. https://doi.org/10.3390/ma13020255.

[12] T. Simson, A. Emmel, A. Dwars, J. Böhm, Residual stress measurements on AISI 316L samples manufactured by selective laser melting, Addit. Manuf. 17 (2017) 183–189. https://doi.org/10.1016/j.addma.2017.07.007.

[13] T. Mukherjee, V. Manvatkar, A. De, T. DebRoy, Mitigation of thermal distortion during additive manufacturing, Scr. Mater. 127 (2017) 79–83. https://doi.org/10.1016/j.scriptamat.2016.09.001.

[14] T. Larimian, M. Kannan, D. Grzesiak, B. AlMangour, T. Borkar, Effect of energy density and scanning strategy on densification, microstructure and mechanical properties of 316L stainless steel processed via selective laser melting, Mater. Sci. Eng. A 770 (2020) 138455. https://doi.org/10.1016/j.msea.2019.138455.

[15] G.R. Buican, G. Oancea, C. Lancea, M.A. Pop, Influence of layer thickness on internal structure of parts manufactured from 316-L steel using SLM technology, Appl. Mech. Mater. 809–810 (2015) 369–374. https://doi.org/10.4028/www.scientific.net/AMM.809-810.369.

[16] O.O. Salman, F. Brenne, T. Niendorf, J. Eckert, K.G. Prashanth, T. He, S. Scudino, Impact of the scanning strategy on the mechanical behavior of 316L steel synthesized by selective laser melting, J. Manuf. Process. 45 (2019) 255–261. https://doi.org/10.1016/j.jmapro.2019.07.010.

[17] T. Kurzynowski, K. Gruber, W. Stopyra, B. Kuźnicka, E. Chlebus, Correlation between process parameters, microstructure and properties of 316 L stainless steel processed by selective laser melting, Mater. Sci. Eng. A 718 (2018) 64–73. https://doi.org/10.1016/j.msea.2018.01.103.

[18] A.K. Agrawal, G. Meric de Bellefon, D. Thoma, High-throughput experimentation for microstructural design in additively manufactured 316L stainless steel, Mater. Sci. Eng. A 793 (2020) 139841. https://doi.org/10.1016/j.msea.2020.139841.

[19] Y. Deng, Z. Mao, N. Yang, X. Niu, X. Lu, Collaborative optimization of density and surface roughness of 316L stainless steel in selective laser melting, Materials 13 (2020) 1601. https://doi.org/10.3390/ma13071601.

[20] D. Gu, Y. Shen, Balling phenomena in direct laser sintering of stainless steel powder: Metallurgical mechanisms and control methods, Mater. Des. 30 (2009) 2903–2910. https://doi.org/10.1016/j.matdes.2009.01.013.

[21] G.B. Bang, W.R. Kim, H.K. Kim, H.-K. Park, G.H. Kim, S.-K. Hyun, O. Kwon, H.G. Kim, Effect of process parameters for selective laser melting with SUS316L on mechanical and microstructural properties with variation in chemical composition, Mater. Des. 197 (2021) 109221. https://doi.org/10.1016/j.matdes.2020.109221.

[22] A. Röttger, K. Geenen, M. Windmann, F. Binner, W. Theisen, Comparison of microstructure and mechanical properties of 316 L austenitic steel processed by selective laser melting with hot-isostatic pressed and cast material, Mater. Sci. Eng. A 678 (2016) 365–376. https://doi.org/10.1016/j.msea.2016.10.012.

[23] O. Andreau, E. Pessard, I. Koutiri, J.-D. Penot, C. Dupuy, N. Saintier, P. Peyre, A competition between the contour and hatching zones on the high cycle fatigue behaviour of a 316L stainless steel: Analyzed using X-ray computed tomography, Mater. Sci. Eng. A 757 (2019) 146–159. https://doi.org/10.1016/j.msea.2019.04.101.

[24] G. Wang, Q. Liu, H. Rao, H. Liu, C. Qiu, Influence of porosity and microstructure on mechanical and corrosion properties of a selectively laser melted stainless steel, J. Alloys Compd. 831 (2020) 154815. https://doi.org/10.1016/j.jallcom.2020.154815.

[25] W.M. Tucho, V.H. Lysne, H. Austbø, A. Sjolyst-Kverneland, V. Hansen, Investigation of effects of process parameters on microstructure and hardness of SLM manufactured SS316L, J. Alloys Compd. 740 (2018) 910–925. https://doi.org/10.1016/j.jallcom.2018.01.098.

[26] R. Cunningham, S.P. Narra, C. Montgomery, J. Beuth, A.D. Rollett, Synchrotron-based X-ray microtomography characterization of the effect of processing variables on porosity

formation in laser power-bed additive manufacturing of Ti-6Al-4V, JOM 69 (2017) 479–484. https://doi.org/10.1007/s11837-016-2234-1.

[27] R. Cunningham, C. Zhao, N. Parab, C. Kantzos, J. Pauza, K. Fezzaa, T. Sun, A.D. Rollett, Keyhole threshold and morphology in laser melting revealed by ultrahigh-speed x-ray imaging, Science 363 (2019) 849–852. https://doi.org/10.1126/science.aav4687.

[28] T. Niendorf, S. Leuders, A. Riemer, H.A. Richard, T. Tröster, D. Schwarze, Highly anisotropic steel processed by selective laser melting, Metall. Mater. Trans. B 44 (2013) 794–796. https://doi.org/10.1007/s11663-013-9875-z.

[29] A. Riemer, S. Leuders, M. Thöne, H.A. Richard, T. Tröster, T. Niendorf, On the fatigue crack growth behavior in 316L stainless steel manufactured by selective laser melting, Eng. Fract. Mech. 120 (2014) 15–25. https://doi.org/10.1016/j.engfracmech.2014.03.008.

[30] A.B. Spierings, T.L. Starr, K. Wegener, Fatigue performance of additive manufactured metallic parts, Rapid Prototyp. J. 19 (2013) 88–94. https://doi.org/10.1108/13552541311302932.

[31] H. Javadi, W. Jomaa, D. Texier, M. Brochu, P. Bocher, Surface roughness effects on the fatigue behavior of as-machined Inconel 718, Solid State Phenom. 258 (2016) 306–309. https://doi.org/10.4028/www.scientific.net/SSP.258.306.

[32] D. Wu, D. Zhang, C. Yao, Effect of turning and surface polishing treatments on surface integrity and fatigue performance of nickel-based alloy GH4169, Metals 8 (2018) 549. https://doi.org/10.3390/met8070549.

[33] A. Damiens, H. Bonnefoy, I. Titeux, Influence of processing parameters on mechanical and fatigue properties of 316 L steel manufactured by selective laser melting, Weld. World 64 (2020) 1321–1328. https://doi.org/10.1007/s40194-020-00885-4.

[34] M. Zhang, C.-N. Sun, X. Zhang, J. Wei, D. Hardacre, H. Li, High cycle fatigue and ratcheting interaction of laser powder bed fusion stainless steel 316L: Fracture behaviour and stress-based modelling, Int. J. Fatigue 121 (2019) 252–264. https://doi.org/10.1016/j.ijfatigue.2018.12.016.

[35] Y. Murakami, Metal Fatigue: Effects of Small Defects and Nonmetallic Inclusions, Second, Elsevier, 2019.

[36] Y. Murakami, M. Endo, Effects of defects, inclusions and inhomogeneities on fatigue strength, Int. J. Fatigue 16 (1994) 163–182. https://doi.org/10.1016/0142-1123(94)90001-9.

[37] E.J. Czyryca, ASM Committee on Fatigue Crack Propagation, R.P. Gangloff, eds., Fatigue Testing, in: Met. Handb. Mech. Test., 9th ed., American Society for Metals, Metals Park, Ohio 44073, 1985: pp. 361–436.

[38] A. Carpinteri, A. Spagnoli, S. Vantadori, An approach to size effect in fatigue of metals using fractal theories, Fatigue Fract. Eng. Mater. Struct. 25 (2002) 619–627. https://doi.org/10.1046/j.1460-2695.2002.00506.x.

[39] D.S. Paolino, A. Tridello, G. Chiandussi, M. Rossetto, On specimen design for size effect evaluation in ultrasonic gigacycle fatigue testing: SPECIMEN FOR SIZE EFFECT IN GIGAFATIGUE, Fatigue Fract. Eng. Mater. Struct. 37 (2014) 570–579. https://doi.org/10.1111/ffe.12149.

[40] G. Qian, W.-S. Lei, A statistical model of fatigue failure incorporating effects of specimen size and load amplitude on fatigue life, Philos. Mag. 99 (2019) 2089–2125. https://doi.org/10.1080/14786435.2019.1609707.

[41] A. Tridello, C.B. Niutta, F. Berto, D.S. Paolino, Size-effect in Very High Cycle Fatigue: A review, Int. J. Fatigue 153 (2021) 106462. https://doi.org/10.1016/j.ijfatigue.2021.106462.

[42] P. Wang, M.H. Goh, Q. Li, M.L.S. Nai, J. Wei, Effect of defects and specimen size with rectangular cross-section on the tensile properties of additively manufactured components, Virtual Phys. Prototyp. 15 (2020) 251–264. https://doi.org/10.1080/17452759.2020.1733430.
[43] M. Muniz-Calvente, A.M.P. de Jesus, J.A.F.O. Correia, A. Fernández-Canteli, A methodology for probabilistic prediction of fatigue crack initiation taking into account the scale effect, Eng. Fract. Mech. 185 (2017) 101–113. https://doi.org/10.1016/j.engfracmech.2017.04.014.
[44] W. Weibull, A statistical theory of the strength of materials, Swed. R. Inst. Eng. Res. (1939).
[45] E. Castillo, A. Fernandez-Canteli, A Unified Statistical Methodology for Modeling Fatigue Damage, Springer, 2009.
[46] J. Allison, D. Backman, L. Christodoulou, Integrated computational materials engineering: A new paradigm for the global materials profession, JOM 58 (2006) 25–27.

Chapter 2 Background and Literature Review

2.1 Metal Additive Manufacturing

ISO and ASTM define additive manufacturing (AM) as a "process of joining materials to make parts from 3D model data, usually layer upon layer, as opposed to subtractive manufacturing and formative manufacturing methodologies" [1]. With this, seven AM processing categories are defined: binder jetting, directed energy deposition, material extrusion, material jetting, powder bed fusion, sheet lamination, and vat photopolymerization. ASTM F3122-14 [2] defines these as

> *Binder Jetting* – additive manufacturing process in which a liquid bonding agent is selectively deposited to join powder materials.
>
> *Directed Energy Deposition* – additive manufacturing process in which focused thermal energy is used to fuse materials by melting as they are being deposited.
>
> *Material Extrusion* – additive manufacturing process in which material is selectively dispensed through a nozzle or orifice.
>
> *Material Jetting* – additive manufacturing process in which droplets of build material are selectively deposited.
>
> *Powder Bed Fusion* – additive manufacturing process in which thermal energy selectively fuses regions of a powder bed.
>
> *Sheet Lamination* – additive manufacturing process in which sheets of material are bonded to form a part.
>
> *Vat Photopolymerization* – additive manufacturing process in which liquid photopolymer in a vat is selectively cured by light-activated polymerization.

There are seven different AM processes because they all have advantages and disadvantages. Despite these differences, all AM processes follow the same generic process [3]:

1) 3D CAD model
2) Convert the model file to STL
3) Transfer file to machine
4) Machine setup
5) Build
6) Removal
7) Post-processing
8) Application

In general, all AM process are identified by the material used, the method of joining the material, and the state in which the feedstock is brought into the process [1]. For metal AM, the system is largely divided into three categories based on feedstock type: powder bed, powder feed, and wire feed. AM is then further broken down into the process, which largely describes the energy source. The manufacturing method can largely be separated into single-step and multi-step processes [1]. For metal AM, this is often referred to as direct-to-metal and indirect processes, respectively [4]. Direct-to-metal produces a net shape part directly from the computer model to the printer, while indirect processes require some sort of intermediate processing steps [4]. Intermediate processing steps do not include post-processing (e.g. support removal, surface finishing, heat treatment, etc.) because this is almost always required in a process. Instead, intermediate processing steps are defined by operations following the initial AM fabrication that consolidates the part to the desired shape, size, and properties [1]. Examples of this would be casting, sintering, and machining, with sintering being the most common processing step seen in a multi-step process as multiple AM processes produce green bodies/composites that need to be reduced to their desired shape and material. AM processes are also separated into the mechanism for fusion, for fusion-based (melting) methods. In powder-bed fusion (PBF), the fusion mechanics can be full melting, liquid phase sintering, chemically induced binding, or solid state sintering, where full melting and liquid phase sintering fall in the direct-to-metal category and chemically induced binding and solid state sintering are indirect processes [3]. The most commonly used PBF process involves full melting, and that is the focus of this review. Focusing on this direct-to-metal AM process, we can further categorize this process by defining the heat source responsible for the fusion. There are four main heat sources used: laser (L), electron beam (EB), plasma arc (PA), and gas metal arc (GMA) [4].

2.1.1 Powder Bed Fusion

Powder bed fusion (PBF) is an AM process whereby a thermal energy selectively melts and solidifies specified regions of a bed of powder feedstock [1]. When thermal energy is provided by a laser this process is called laser powder bed fusion (L-PBF) or selective laser melting (SLM). As is inherent in the name, the feedstock used in L-PBF is powder, and specifically a powder bed (as opposed to powder-feed or wire-feed systems). The L-PBF process works by focusing a laser onto a bed of metallic powder feedstock and moving the laser (or bed) such that the powder is melted in the desired shape [3–7]. The scan path, processing parameters, and build supports are determined and added into the part file code to achieve the product. There are a few main components to a L-PBF system, namely: the build chamber, powder bed, powder supply, recoater arm, laser, and mirrors (Figure 2.1). The feedstock powder is held in its own platform, raised slightly for each subsequent layer to allow the recoater arm/roller to spread a thin layer of the feedstock onto the build platform. The build platform hosts the end product, which is built on to a removable build plate (substrate) that acts as a mechanically and thermally robust base on which the first layers of the build adhere [7]. Layer by layer, feedstock material is spread onto the powder bed where the laser melts the powder into the desired shape. The laser works to not only melt the new layer of powder but also fuse this layer with the previous layers. L-PBF is a precise AM technique that can produce parts with a high dimensional accuracy at a fine resolution through the use of mirrors that direct the focus of the beam. Often one or more scanning mirror or galvanometer driven mirror is used to achieve this [4,7]. After the laser is finished scanning a build layer, the build plate is lowered to allow for more feedstock and the recoater distributes a new layer. During this time, the melted powder has solidified, thus requiring this layer to be re-melted to allow for proper fusion of the new layer of powder on top. The scanning strategy has a significant impact on the quality of the end product, as it affects the thermal history, porosity, and microstructure. In L-PBF there are over 130 process variables that contribute to the manufacture of the final product. Of those variables, the most influential ones to consider are the laser power, layer thickness, scan velocity, scan pattern, and hatch distance, illustrated in Figure 2.2 [8]. The influence these parameters have will be discussed further in Section 2.3.3.

2.2 **Metallurgy of Stainless Steel**

2.2.1 Physical metallurgy of stainless steel

Stainless steel is a classification of iron-based alloys which contain 10.5% or more chromium. Within this classification are five subgroups: austenitic, ferritic, martensitic, precipitation hardening, and duplex. The focus of this work is on AISI 316L (UNS S31603) stainless steel, an austenitic stainless steel [9,10]. Austenitic stainless steels are typically used for their corrosion resistance and good formability. 316L is altered from the base austenitic stainless steel AISI 302 by increasing the molybdenum content for improved corrosion resistance, and reduced carbon content for welding capabilities [10]. The chemical composition to be considered AISI 316L is shown in Table 2.1. L-PBF 316L has the same composition requirements as AISI 316L [11]. The subsequent nominal mechanical properties of an annealed sheet of conventional wrought 316L are shown in Table 2.2.

Table 2.1. Chemical composition (in wt. %) of AISI 316L stainless steel [9,10]. Maximum allowable values unless otherwise specified.

Fe	Cr	Ni	Mo	C	Mn	P	S	Si
Balance	16.00-18.00	10.00-14.00	2.00-3.00	0.030	2.00	0.045	0.030	1.00

Table 2.2. Nominal mechanical properties [9,10] of conventional wrought 316L SS as annealed sheet.

Elastic Modulus [GPa]	Tensile Strength [MPa]	Yield Strength (0.2% offset) [MPa]	Elongation in 50mm [%]	Rockwell Hardness	Endurance limit [MPa]
193	558	290	50	B79	269

2.2.2 316L powder particles for use in Laser-Powder Bed Fusion

Feedstock in the case of L-PBF is the metallic powder particles placed in the bed to be melted together to form the desired workpiece. The powder particles supplied for this have to be manufactured, and there are four main methods to achieving this: gas atomization (GA), rotary atomization (RA), plasma rotating electrode process (PREP), and water atomization (WA) [4,7]. GA produces particles by using highly pressurized gases to atomize molten material. RA takes that same molten material and instead is poured onto a rotating disk. The centrifugal force causes molten droplets to be flung from the disk and cooled into solid particles while flying through the air. PREP is similar to RA in that it involves rotation to create particles, but in this case the end of a solid metal bar is melted using an electric arc or plasma while at the same time the bar is rotated releasing molten droplets to solidify into particles. WA is similar to GA but instead of highly pressurized gas, highly pressurized water is used [12]. Figure 2.3 shows the results of these methods found in the literature. PREP produces the most uniform particles out of all the methods, in both individual particle geometry and batch particle size distribution. The downside of PREP being that it is costly and has a low production yield. GA also produces spherical particles, but these particles typically are not smooth like PREP particles. They exhibit a dimpled surface texture with random satellite particles across the surface. Additionally, due to the gas used for atomization, these particles often contain entrapped gas, which is released during the AM process causing porosity in the workpiece. RA produces smooth particles much like PREP but the centrifugal forces in this process cause the particles to be elongated rather than spherical. WA is the least desirable method for producing feedstock as it results in irregular and coarse particles. A spherical, uniform size distribution feedstock powder is most desirable as it has the best packing structure, resulting in less porosity. Spherical powders are also advantageous in that they flow better, so during the recoating process in AM the new layer of feedstock will be more uniformly distributed as opposed to a feedstock with coarse and irregular powder particles.

There are no standards dictating the sphericity or symmetry of powder particles but there are standards for the chemical composition. ASTM standard F3184-16 [11] outlines the material requirements of 316L stainless steel powder particles for use in powder bed fusion AM. The chemical composition requirements match that of wrought 316L, as shown in Table 2.3. F3184-16 also specifies minimum requirements for tensile properties at room temperature, shown in Table 2.4.

Table 2.3. Chemical composition (in wt. %) of AISI 316L stainless steel powder particles for the use of powder bed fusion [11]. Maximum allowable values unless otherwise specified.

Fe	Cr	Ni	Mo	C	Mn	P	S	Si
Balance	16.00-18.00	10.00-14.00	2.00-3.00	0.030	2.00	0.045	0.030	1.00

Table 2.4. Minimum tensile requirements in the stress relieved, solution annealed, and hot isostatic pressing (HIP) conditions for X, Y, and Z directions [11].

Tensile Strength [MPa]	Yield Strength (0.2% offset) [MPa]	Elongation in 50mm [%]
515	205	30

2.3 **Fatigue of 316L Stainless Steel Laser-Powder Bed Fusion**

2.3.1 Fatigue and crack growth in metals

Fatigue is broadly described as permanent structural change that results from cyclic stress or strain [4,13–16]. In order for fracture to occur from fatigue, cyclic stress, tensile stress, and either macroscopic plastic strain (for low cycle fatigue) or microscopic plastic strain (for high cycle fatigue) all need to occur simultaneously – the absence of one will prevent fatigue cracks from initiating and propagating [14,16]. The fatigue process can be separated into three stages based on the work with aluminum alloys reported by P. J. E. Forsyth in 1963 [17]. Stage I is when the initial fatigue damage can produce cyclic slip bands and other microscopic damage eventually leading to a physical separation of surfaces to become an initiated crack which is parallel to the local shear stress. Stage II is crack propagation, where the direction of crack propagation is dominated by the direction of maximum tensile stress. Stage III is fracture, which occurs once the crack has propagated sufficiently that the specimen is unable to sustain the imposed loads [14] – in other words, catastrophic fracture occurs. These three stages are demonstrated in Figure 2.4.

In stage I fatigue, the microstructure and grain morphology play an important role in crack nucleation and this stage is often referred to as the microstructure-sensitive stage [18]. During Stage I, a crack is often referred to as a microcrack or short crack [19]. These cracks can be microstructurally short (i.e., the size of grains), locally short (i.e., the size of the crack tip plastic zone), or physically short (i.e., less than a mm in length). Stage I can be broken further into three stages: initial cyclic damage, formation of initial microscopic flaw (microcrack initiation), and coalescence of microcracks to form an initial fatal (detectable) flaw [19]. The mechanisms by which cracks nucleate in pure metals is through cyclic slip bands, extrusion-intrusion pairs, twin boundaries, or grain boundaries [16]. In alloys, nucleation can occur via these mechanisms but can also occur due to inclusions, second-phase particles, and other discontinuities [16]. Fatigue cracks can also initiate at geometric notches or other stress concentration sites. Once a microcrack is formed it will grow at an accelerated rate compared to long crack; the study of which is referred to as "short" crack growth [19]. A short crack can propagate into a long crack from either a defect, stress concentrator, or slip band; or a fatigue crack can result from a pre-existing crack that occurred during manufacturing [20].

In AM, many fatigue cracks initiate at stress concentrators. Murakami defines stress concentrators as a discontinuity in the material structure, exhibiting a higher stress than the bulk material [20]. The two most basic stress concentrators occur at holes and notches. These stress concentrators are quantified by the stress concentration factor, k_t. This factor varies by the loading imparted on the specimen and the type of stress concentrator, so k_t is found with the appropriate use of standard equations found in reference books [20]. The notch root radius, ρ, (graphically defined in Figure 2.5) is an important parameter used in determining k_t, as the smaller the radius, the larger the stress concentration factor will be.

The stress concentration factor, k_t, is defined for holes and notches however it is inappropriate for cracks. A crack has a root radius ρ approaching zero because the crack end is so sharp [20]. For a crack, we could estimate the stress concentration using the concept of equivalent ellipse since the crack tip can be thought of as an extremely sharp ellipse, however, the root radius equal to zero results in an unbounded stress concentration [20]. G.R. Irwin described a singularity at which the stress from the crack tip occurs at $r^{-1/2}$, with r being the distance from the crack tip [20]. For characterizing crack propagation, the stress intensity factor, K_I, (for mode I cracking) is used to quantify the intensity of the stress singularity distribution [21]. For a crack of length $2a$ under uniaxial tensile stress, σ_0, the stress intensity in the vicinity of the crack tip is given by Eq.

2.1. It is important to understand which regime we are measuring crack growth in as long crack growth behaves differently than short crack growth. For short crack growth the fracture mechanics approach may have limitations because the crack extension mechanisms may differ from those observed in long cracks [19].

$$K_I = \sigma_0\sqrt{\pi a} \tag{2.1}$$

At low stresses, cracks have been observed to initiate, propagate a short distance and then stop. When a crack stops propagating even under continued cycling and does not contribute to failure or fracture it is deemed a non-propagating crack [13]. This non-propagating crack phenomenon has been associated with the fatigue limit seen in certain metal alloys. In fatigue testing, each specimen has a specific fatigue life, N_f, which is the number of stress (strain) cycles a specimen has experienced prior to failure [16]. The fatigue strength, S_N, is defined as the stress needed to cause failure at a specific number of cycles [15] or similarly the stress that a specimen can endure for a specific number of cycles [14]. The median fatigue strength is defined as the "[stress] at which 50% of the specimens of a given sample could survive N stress cycles" [15]. In contrast to the fatigue strength, the fatigue limit (also known as the endurance limit) is "the maximum stress that the metal can withstand for an infinitely large number of cycles with 50% probability of failure" [14]. Murakami confirms this definition for unnotched, defect free specimens, but goes further to specify that the fatigue limit is the threshold for crack propagation. A specimen at the fatigue limit that has not failed may not be devoid of cracks but have cracks that are non-propagating cracks [20]. To think of this graphically, as the number of cycles grows infinitely large, the stress will reach a horizontal asymptote, as shown in Figure 2.6. Murakami identifies the clear bend in the curve as the "knee point," and attributes this effect to non-propagating cracks [13]. This then explains why Murakami believes a fatigue limit is the threshold for crack propagation. Fatigue life, fatigue strength, and fatigue limit are all metrics used to describe the fatigue behavior of a material.

2.3.2 Fatigue of additive manufacturing

Fatigue of 316L stainless steel in L-PBF has been widely researched [22–34] with three main attributes being known to affect the fatigue behavior: as-built surface finish, residual stresses, and processing defects. In multiple studies on fatigue of AM samples, both surface roughness [4,28,30,35,36] and internal defects [22,34] were found to be significantly influential on fatigue behavior because they served as points of stress concentration [20,37]. The site for crack initiation is dictated by the stress-concentration factor, K_t, whose value depends on the geometry of the defect [14]. Local cyclic stresses are also affected by the local residual stresses. In general, surface residual stresses increase the fatigue strength when they are compressive and decrease when tensile, particularly in hard steels [14]. Investigations into the residual stress states of L-PBF printed parts have shown axial tensile residual stresses reaching or exceeding the bulk room temperature yield stress of the wrought material [38]. Residual stresses arise from melting, solidification, and re-melting during the laser processing which leads to large thermal stress gradients [8,39–42]. Irrespective of processing parameters and orientation, in nearly every instance, axial residual stresses in L-PBF application of 316L are generally compressive at the center of a sample and tensile at the surface [38,41–44]. This distribution of residual stresses can lead to part distortion and degradation of fatigue performance [39,45–47].

2.3.3 Factors that influence fatigue behavior in additive manufacturing

Substantial progress has been made in understanding how the AM process parameters interact with one another to produce a desired product and a user can design a process map to meet multiple specifications simultaneously [48]. Since AM is a relatively slow manufacturing process, it is important to recognize the importance of manufacturing specific parameters such as build time. Not every parameter can be fully optimized, so it is important to identify the parameters that are most influential to the desired outcome. In terms of fatigue response, important characteristics have been determined to be residual stresses, defects, surface roughness, and microstructure. Important to the current investigation, we must understand not only how changing these parameters influences the final products but also how the influence of these parameters changes with sample geometry.

2.3.3.1 Residual stress

Residual stresses are defined as stresses that exist within a body without any externally applied loads [45,49]. Residual stresses can have a detrimental influence in AM parts, with high residual stresses leading to part distortion and fatigue performance degradation [39,45–47]. Residual stresses in L-PBF applications have been reported to reach as high as the bulk room temperature yield stress of the wrought material and sometimes even higher [38]. Residual stresses in AM arise from melting, solidification, and re-melting of the specimen during laser processing [8,39–41]. The laser powder bed fusion process is such that a layer of metallic powder particles is distributed across the build plate, the high-intensity point-source of heat, typically a laser, is focused on the material and moves in a way to build up the desired three-dimensional (3D) geometry layer-by-layer. The laser used to melt the powder particles creates large thermal gradients in its path leading to thermal stress. In general, this process can be thought of in three stages [42]. Stage 1: the laser is focused onto the material, which is heated and melted. Stage 2: the laser moves away from this location and the material begins to cool. Stage 3: the material fully cools to the ambient temperature. When a new powder layer is added, this process is repeated.

Previous layers will be re-heated with the new layer and depending on the energy input may re-melt. Eventually, the layers are built up enough that the first layers no longer experience any re-heating by the new layers. The build can be divided into three regions based on thermal experience: the melted zone (region I), the heat-affected zone (region II), and the non-heat affected zone (region III), shown in Figure 2.7.

The formation of residual stress is from the large thermal gradients that occur in the L-BPF process. These thermal gradients are often described by the temperature gradient mechanism (TGM) model (Figure 2.8) [43,40]. This model depicts the formation of residual stresses through the three stages of the LBPF process. During stage 1, the rise in temperature causes the heated material in region I and region II to expand. The cooler temperature of region III restricts the expansion of material and causes compressive stresses in regions I and II and tensile stresses in region III. During stage 2, as the laser moves away from this location and the material begins to cool, regions I and II begin contracting. Region III being cooler, again restricts this motion, creating tensile stresses in region I. Tensile residual stresses become locked in in region I, with compressive residual stresses in region II. Region II becomes more compressive and reduces the magnitude of tensile stresses in region III. As this process is repeated, the region that was region I moves into region II and eventually region II moves into region III. The next layer of powder is added and melted then becomes Region I. The thermal gradients can vary significantly depending on part size, build time, built plate and/or powder bed temp, atmosphere used in the build chamber, thermal characteristics of the powder used, and the melt pool size [38]. With their wide variation, residual stressed are often described by the size of their influence in the material [49,50]. Type I residual stresses, also referred to as macro-residual stress, act over a larger area with respect to the dimension of the part. Type II, or micro-residual stresses, act over areas equivalent to the grain-size. Type III residual stresses act over areas on the atomic scale [49,50]. The type of residual stress effects different scales of parameters like part geometry and mechanical properties, phase transformations, and dislocation stress field and crystal lattice defects, respectively [40,49,50].

Irrespective of processing parameters and orientation, in nearly every instance, axial residual stresses in L-PBF applications of 316L are spherical (Figure 2.9b) with compressive stresses at the core and tensile stresses at the surface [38,41–44]. The largest tensile stresses exist at the surface nearest the build plate [38,41,43] with the largest compressive stresses at the center of the specimen along the build direction [38,42,43]. Wu et al. [38] depicts this behavior using neutron diffraction and DIC measurements shown in Figure 2.9. DIC measures the axial residual stress on the surface of a specimen, while neutron diffraction measures the internal residual stresses. These measurements were taken at a depth of 15 mm from the top surface, so the depiction of residual stress here is two-dimensional. Neutron diffraction measurements were taken at multiple points along the build direction two show the residual stress behavior in a third direction (Figure 2.10) [38]. The magnitude of these stresses can be altered by adjusting the processing parameters, but the distribution of residual stresses largely stays the same.

Though the distribution of residual stresses is inherent in the process itself, the prevention, reduction, and mitigation of these stresses can significantly improve part performance. Since residual stresses are formed due to thermal gradients, any processing parameter that can alter the thermal history can influence their formation and magnitude. The most influential parameters are energy input, scanning strategy, layer thickness, orientation, pre-heating, and dwell time.

Many L-PBF equipment manufacturers provide a set of optimized printing parameters for a given material to aid in producing quality builds [51]. Often these parameters are optimized for part density as it is generally thought that defects and porosity are the leading cause of part failure and poor mechanical behavior. With this, many researchers have studied the effects of different processing parameters on the final product, often creating what is called an optimized process window. An optimized process window generally focuses on laser power as a function of scan speed (also known as energy input) and will highlight the energy inputs that lead to various types of defects. This is discussed further in Section 2.3.3.2 but the idea of a process window can also be thought of in terms of thermal impact.

While energy input looks at the laser power versus scan speed and is given units J/mm^2, energy density factors in the volume of the part and is in units of J/mm^3. Often energy density is described by Eq. 2.2

$$E = \frac{P}{v \cdot h \cdot d} \tag{2.2}$$

where P is the laser power, v is the scan speed, h is the hatch distance, and d is the layer thickness. It should be noted that this is an approximation as it does not accurately represent the actual volume of the material that is affected, but it can be used approximate energy per unit volume [45]. Researchers have investigated both energy input and energy density effects on residual stress. Liu et al. determined that increasing the energy input by decreasing the scan velocity will increase the magnitude of residual stresses in 316L [42]. Simson et al. also determined that when the energy density is increased sufficiently that the porosity is reduced to below 1%, the residual stress increases. [52]. They attribute this, however, to the porosity itself. Residual stresses can be relaxed by porosity and defects when the porosity is greater than 1%. At structural densities greater than 99%, the residual stress values are nominally the same (Figure 2.11) [52]. Similarly, by calculating the strain, Mukherjee et al. concluded that the residual stress would increase with increasing power and decrease with decreasing scan speed (Figure 2.12) [53]. Aside from residual stress, higher energy density has been shown to improve the mechanical properties of 316L [54], so energy density will need to be low enough to reduce the residual stress but high enough to improve the mechanical properties [45].

Some other rules-of-thumb for residual stresses in L-PBF 316L have been established in the literature. A shorter dwell time can result in lower magnitude residual stresses [41] because a longer dwell time allows the material to cool further. When a new layer of material is added and melted the thermal gradient between the new layer and the previous layers is much higher. A high thermal gradient can be more restrictive to the expansion and reduction occurring in the new layer during thermal cycling, causing higher residual stresses to form [8,46,49]. With the same logic, pre-heating the build plate can also result in lower magnitude residual stresses [43]. Increasing the layer thickness without changing the power or velocity will result in larger grains [55], higher magnitude tensile near surface residual stresses, and more porosity. In one study this combination led to a modest reduction in fatigue strength, however, the author notes the sample size may not be statistically robust [23].

The L-PBF scanning strategy has been the focus of much research as it has a great impact on the thermal history. Scanning strategy can be broken down into pattern, sequence, track length, layer rotation, and orientation. The majority of scan patterns are directional [44,56–60], crosshatch [54,60,61], sector (island) [44,58,62–64], helix [44,56], fractal [65–67], or point (spot) [68]. Altering the scan pattern seeks to change the thermal history by reducing the track length, increasing the energy density, increasing the amount of remelting, and decreasing thermal gradients. In general, a shorter track length reduces the magnitude of residual stresses [42,44,56,58,62,63,65–67]. Remelting refines the microstructure [57,61,69], increases part density [61], improves the surface finish [61], and increases the yield strength [57]. Changing the orientation of the scan direction either through layer rotation or bidirectional scanning has been shown to reduce the magnitude of residual stresses [40,44,70,71]. Changing the orientation of the build is also used for residual stress mitigation since residual stress changes depending on the direction in which they are measured. In a typical L-PBF build, on the top surface, the highest residual stress will be in the scan direction, while in a side surface the highest residual stress will be in the build direction [52]. The magnitude of these residual stresses, however, can be greatly reduced with altered build orientations [72].

To modify residual stresses, in addition to adjusting the processing parameters, post-processing treatments like heat treating, hot isostatic pressing (HIP), and surface machining can also be effective. Heat treating (HT) 316L is generally performed as an annealing process at temperatures between 400ºC and 1100ºC in an argon atmosphere. An annealing HT can be divided into two main types: stress-relief and recrystallization. These two differ in the temperature of the heat treatment and the effect they have on the microstructure. 316L stainless steel made by L-PBF has a recrystallization temperature around 1050ºC to 1100ºC, above which full recrystallization can occur [39]. A summary of heat treatments done on L-PBF 316L can be found in Table 2.5. The higher the HT temperature the more residual stress relaxation is observed but one must be cognizant of microstructural changes. Changes in the microstructure can begin around 650ºC with minor dislocation annihilation and the formation of fine precipitates, though this is not universally observed [73,74]. At 800ºC the cellular substructure may begin to decompose, and some have noted the formation of a σ phase [73,74]. Significant microstructural changes and recrystallization have been noted to occur at 1050-1100ºC, with equiaxed grains and δ ferrite phases being formed at 1400ºC.

Table 2.5. Summary of heat treatments performed on LPBF 316L.

Condition	Duration	Observation	References
388ºC on build plate	4 hr	Increased yield strength, decreased fatigue behavior	Mower and Long [26]
400ºC argon + air cool	4 hr	24% relaxation of residual stresses No change in mechanical properties or microstructure	Chao et al. [73] Cruz et al. [74]
450ºC on build plate + argon	4 hr	No residual stress relaxation	Sprengel et al. [39]
650ºC argon	2 hr	25 to 46% relaxation of residual stresses Reduced yield strength, poorer fatigue behavior	Riemer et al. [28] Leuders et al. [25]
650ºC argon + air cool	2 hr	63.5% relaxation of residual stresses Reduced yield strength Minor dislocation annihilation, fine precipitates found at grain boundaries and dislocation walls (enrichment of Mn and O)	Chao et al. [73] Cruz et al. [74]
650ºC furnace cool	1 hr	No change in crack growth behavior No microstructural changes	Fergani et al. [75]
650ºC on build plate	2 hr	Improved fatigue behavior in horizontal samples but no noticeable change in vertical samples	Blinn et al. [76]
700ºC furnace cool	2 hr	3 to 66% relaxation of residual stresses measured by XRD	Williams et al. [77]
700ºC furnace cool	2 hr	10 to 50% relaxation of residual stresses measured by ND	Williams et al. [77]
700ºC air cool	2 hr	Increased fatigue life	Polishetty and Littlefair [27]
700ºC vacuum	1 hr	Reduced hardness	Carlton et al. [78]
800ºC argon + air cool	2 hr	Cellular substructure decomposition, new intergranular particles appear with increased Mo, Si, and O concentrations. Could be a precursor to σ phase.	Chao et al. [73]
800ºC gas quench	1 hr	75% relaxation of residual stresses	Sprengel et al. [39]
900ºC gas quench	1 hr	86% relaxation of residual stresses Minor grain growth	Sprengel et al. [39]
900ºC furnace cool	2 hr	~90% relaxation of residual stresses Increased fatigue strength	Lai et al. [79]
1050ºC furnace cool	1 hr	Recrystallization has occurred Improved crack growth resistance	Fergani et al. [75]
1050ºC water quench	1 hr	Recrystallization has occurred Highest crack growth resistance	Fergani et al. [75]
1095ºC vacuum + argon quench	1 hr	Reduced hardness, reduced yield strength	Carlton et al. [78]
1100ºC argon + air cool	5 min	92.4% relaxation of residual stresses Reduced yield strength Complete cellular dendrite annihilation, fully austenitic structure maintained	Chao et al. [73] Cruz et al. [74]
1100ºC argon + air cool	8 hr	Inclusion particle coarsening, recrystallization occurs, and microstructure becomes equiaxed	Chao et al. [73]
1100ºC ArH2 mix + furnace cool	30 min	Reduced residual stresses Recrystallization has occurred	Shin et al. [64]
1400ºC argon + air cool	10 min	Inclusion particle coarsening, δ ferrite formation	Chao et al. [73]

Hot isostatic pressing (HIP) is another post-processing treatment that aims to improve the mechanical behavior. HIP works by raising the temperature of the material while simultaneously placing it under a high hydrostatic stress state. HIP alters the microstructure in the same way that HT does, often resulting in indistinguishable microstructure changes. [80]. HIP is used when it is desirable to both densify the material and produce a recrystallized microstructure. The high pressure of HIP works to reduce porosity. However, the literature is inconclusive with regards to HIP of 316L, likely due to variability in porosity. It appears that HIP generally reduces porosity and therefore may improve metrics such as the fatigue behavior, but only for the specific types of porosity that control fatigue crack initiation. HIP works best on porosity that is closed (i.e., keyholing and gas entrapment) and is ineffective with open porosity (i.e., lack of fusion, LOF) [80]. Leuders et al. and Riemer et al. demonstrated that HIP resulted in increased high cycle fatigue limits and longer fatigue lives [25,28]. Shin et al. also showed how HIP can reduce the residual stress but found no difference in fatigue response comparing HT and HIP conditions. Both HT and HIP produced nominally the same porosity reduction and residual stress relaxation, likely due to the fact that densification was high in the as-built condition and the porosity that did exist had a low aspect ratio [64].

2.3.3.2 Manufacturing defects

In laser powder bed fusion, there are over 130 process variables that can contribute to the manufacture of a part [81,82], meaning that each of these variables could have some significant impact on the microstructure, mechanical behavior, and quality of the part. With so many variables at play, the most commonly explored are the variables that are the easiest to control. Variables such as laser power and scan speed have been the most widely researched and as such these variables are the basis for what is known as a power-velocity (P-V) map (or process window). The energy density (J/mm^3), described by Eq. 2.2, is the basic metric shown in a P-V map. These maps are then overlayed with various aspects of the end part, such as microstructure, defects, or mechanical behavior. In this section we consider process maps with respect to defects. In Section 2.3.3.4 we consider process maps with respect to the microstructure.

A general representation of a process window for L-PBF application with respect to defect formation is shown in Figure 2.13. Across most metals, we notice trends of high power and low velocity resulting in keyholing, low power and high velocity resulting in lack-of-fusion (LOF), and high power and high velocity resulting in "balling". Balling occurs via two different mechanisms: a) when the laser power is such that incomplete melting occurs causing a discontinuity in the scan track or b) excessive scan speed creates spattering of liquid metal droplets [83]. The first type of balling is often thought of in terms of wettability with an insufficiently melted powder particle attaching to the bulk but not becoming uniform with it. Spattering balling occurs from the liquid metal droplets partially solidifying before re-attaching to the bulk. Keyholing is a phenomenon that occurs under high energy densities by which a capillary metal vapor is formed and trapped into the material by collapsed molten material that begins to solidify before the vapor can escape or be backfilled [8]. LOF occurs when the energy density is low or the scanning pattern is such that complete melting is not achieved resulting in previous melt pools not being completely filled by a new melted layer. In recent years it has been standard for the manufacturers of L-PBF systems to provide the customer with a set of nominal parameters that should result in a satisfactory build, but there has been continued research done to further optimize this process window for a variety of metals.

There are many aspects to defect quantification but in L-PBF defects are generally associated with porosity, melt pools, or inclusions. Clymer et al. created a tool to generate P-V process maps based on variables of interest [48]. The work of Clymer et al. was done to create process maps of multiple variables (relative density, surface finish, precision, deposition rate, and yield strength) so that they could be overlayed to determine the optimum parameters to meet certain build requirements (Figure 2.14). On the experimental side, Bang et al. were able to visually represent the changes in porosity with energy density by associating micrographs in a process map (Figure 2.15) [84]. This is only part of a defect process map, however, since it only considers energy densities that would result in predominantly LOF pores, rather than keyholing. Röttger et al. conducted a similar study but instead of analyzing the laser power and velocity, evaluated point distance and exposure time as variables (Figure 2.16) [85]. In this case, point distance was set equal to the hatch spacing and exposure time was a measure of time exposed to a given energy density. Taking it one step further, Deng et al. looked at not just the laser power (P) and scan speed (V), but also the hatch spacing (S) [82]. They investigated all three parameters to create process maps for both relative density (RD) and surface roughness (SR). They produced the process maps in Figure 2.17 for 316L to show the optimized values of power, speed, and hatch spacing to achieve a part with the highest relative density and smoother surface finish. In general, we notice certain trends like increasing scan speed resulting in higher porosity [86], reduced energy density resulting in higher porosity levels and larger pores [87,88], too little remelting resulting in more porosity while too much remelting resulting in keyhole porosity [89,90], and that in general higher levels of porosity result in poorer fatigue properties [22]. These processing maps can also be overlayed with other results, such as the fatigue response, shown by Zhang et al. in Figure 2.18, or yield strength shown by Clymer et al. in Figure 2.19.

Even with these process maps available, it is important to know the mechanisms behind defects impacting fatigue behavior. As discussed in Section 2.3.2 defects are critical in fatigue as they are often the source of stress concentrators which lead to crack initiation. There are various types of defects: binding defects [91,92], lack of fusion (LOF) porosity [22,92–95], gas entrapment porosity [92,93], keyhole porosity [92,96–99], residual stress cavities [91], spattering [100–102], and powder defects [92,103,104]. Their shape and size largely determine the amount of influence they have. The shape of a defect determines its stress concentration factor. A perfectly round defect, such as gas entrapment and keyholing, has a lower stress concentration factor compared with a sharp narrow crack-like defect. Murakami argues that the size of a defect is more influential than the shape [37]. If a defect exists that is larger than the non-propagating crack size at the fatigue limit, this defect will decrease the fatigue strength. Defects smaller than the non-propagating crack size will not cause crack propagation and therefore will not change the fatigue strength. Defects of similar geometry influence the fatigue strength greater depending on their size than on the stress concentration factor, since K_t for defects of similar geometries would be the same. Even if the stress concentration factor is high, if the defect is smaller than the non-propagating crack size, it will not be detrimental to the fatigue strength [20]. The extent to which each type of defect influences the fatigue behavior of AM materials is an active area of research.

2.3.3.3 Surface roughness

When considering fatigue behavior, surface roughness can be considered a surface defect. Similar to internal defects, surface defects can be stress concentrators and lead to cracking. There are many parameters that quantify surface texture according to ISO 25178-2 [105], with the primary parameters for quantifying surface roughness being S_v, S_z, and S_a. These parameters characterize the surface roughness of irregular profiles seen on L-PBF surface finishes by quantifying the maximum pit depth, the maximum height of the profile, and the deviation of the surface profile from the mean, respectively [105]. The surface roughness is quantified over an evaluation area, A, defined as a portion of the scale-limited surface specified as the area under evaluation. The key topographical features within an evaluation area are the peak/hill and pit/dale. These parameters are visually explained in Figure 2.20.

In multiple studies on fatigue of AM, surface roughness was deemed to be either significantly influential on fatigue behavior or at the very least a smoother surface performs better compared to the as-built surface [4,28,30,35,36]. Surface roughness occurs in AM, and specifically in L-PBF, for two main reasons: the ‘stair step effect’ and improper melting and balling [4]. The stair step effect is a result of the layer-by-layer process inherent in AM and is dramatically affected by the slicing process in AM preparation. The slicing process approximates the geometry of a specimen with built-up layers, causing curved surfaces across multiple build layers to have a ‘step’ effect rather than being a perfectly smooth curve. Even in straight cylindrical samples, however, an inherent surface roughness still exists. In powder bed processes this roughness is due to improper melting and balling [58,83,106]. True balling occurs with increased scanning speed and laser power and causes the scan track to break apart instead of stay as one continuous track [106]. This interruption of the scan path occurs because of the wettability of the material. Rather than the spherical powder particles wetting into the material surface to form a half cylinder, the surface tension of the molten material causes balling to occur [58]. Other, less severe types of “balling” occur either as result of vaporization of the particles during melting, or improper melting of the particles. Vaporization causes high recoil pressure in the melt pool resulting in melt expulsion or splashes [58]. Improper melting occurs when the laser power is too low and the particles do not receive sufficient energy to fully melt into the material surface [83]. Increasing the layer thickness has been shown to increase the surface roughness for this reason [23]. Surface roughness has such a great impact on fatigue life due to the geometry of the roughness in the same way that internal defects impact fatigue. As previously mentioned, fatigue failure is more likely to occur from stress initiators. A stress initiator can be found at any location where the surface is neither perfectly flat nor perfectly round, so a rough surface can be the host of many stress initiators. In a specimen free from all internal defects, the location for crack initiation is at a surface imperfection [14]. In fact, Murakami asserts that fatigue crack initiation most readily occurs at the free surface [107]. Similarly, a specimen free from all surface imperfections with have crack initiation occurring below the surface at internal defects. There has yet to be a definitive answer on whether surface roughness or surface connected defects are more critical in fatigue applications.

2.3.3.4 Microstructure

Microstructure is largely dependent on the thermal history and solidification behavior during the manufacturing process. L-PBF processes are characterized by large thermal gradients and multiple re-heating thermal cycles. This process often results in crystal growth direction aligned with build direction, higher texture degree, and higher aspect ratio of grains [69]. Generally, columnar grains form along the build direction, owing to the melt pools formed during manufacturing. The microstructure perpendicular to the build direction is a result of the scanning strategy and can therefore vary greatly, but typically has lower grain aspect ratios. This anisotropy in microstructure results in an anisotropy of mechanical properties. The processing parameters can affect different aspects of the microstructure, such as the grain size, the aspect ratio of the grains, the average misorientation angle, and the primary dendritic arm spacing. Optimizing the microstructure can be done with P-V process maps (Figure 2.21) as was done with defects discussed previously.

For L-PBF applications with 316L, the microstructure formed is typically single phase austenite regardless of scanning strategy [57]. Additionally, 316L has a preferential <001> texture in the build direction [108]. Heat treatment can further change this microstructure, often resulting in more equiaxed grains, inclusion particle coarsening, and the formation of σ and δ ferrite phases [73]. In general, a microstructure with larger, more equiaxed grains will result in improved fatigue behavior.

Figures

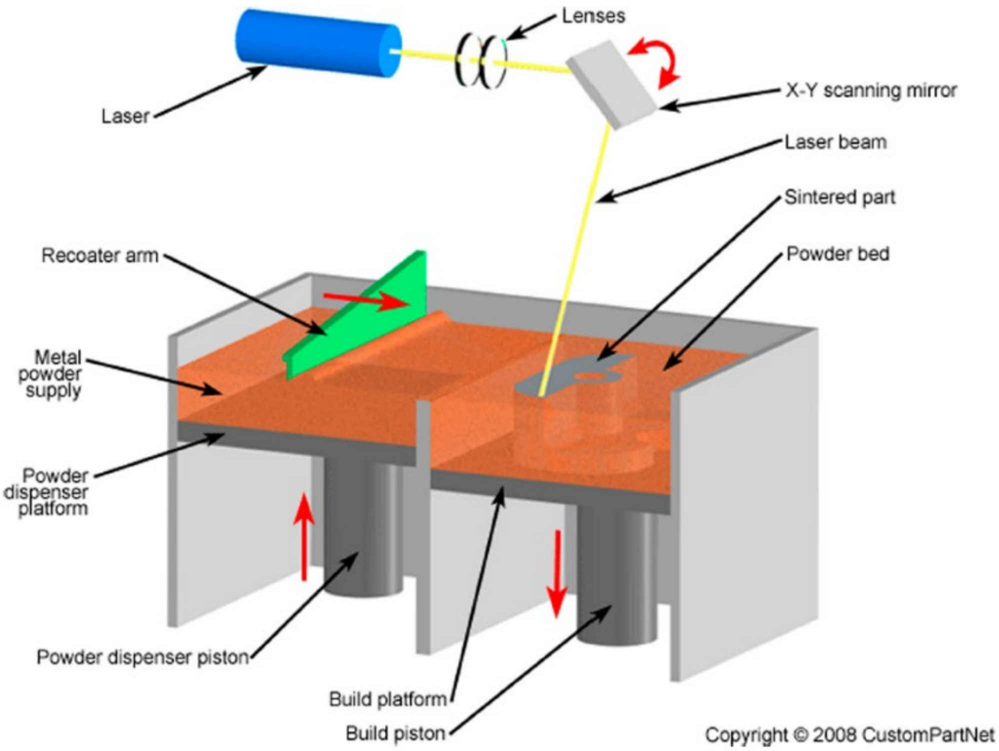

Figure 2.1. Laser powder bed fusion system schematic. Image downloaded from CustomPartNet Inc. website.

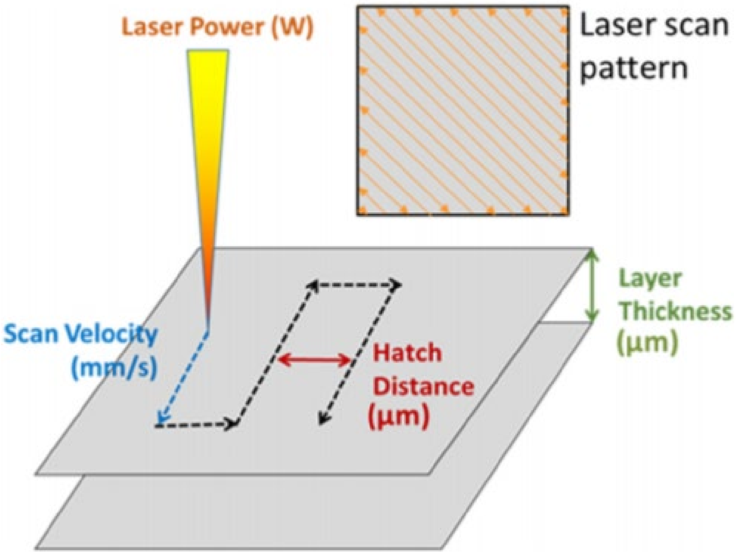

Figure 2.2. Common process parameters regarding the scanning of the laser that takes place in laser powder bed fusion systems [7].

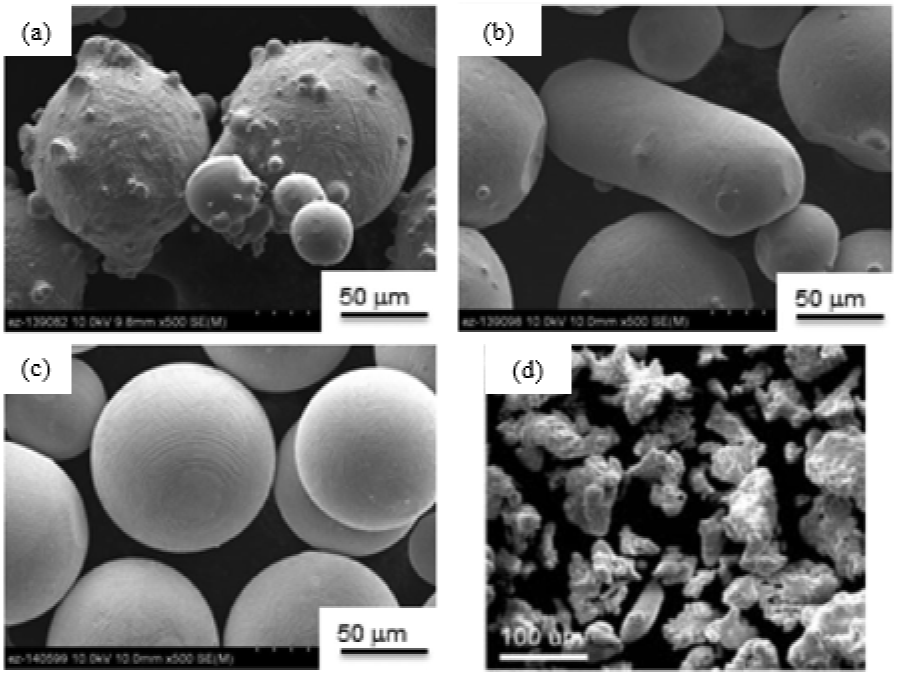

Figure 2.3. SEM images of (a) gas atomization (GA) of Inconel 718 [109], (b) rotary atomization (RA) of Inconel 718 [109], (c) plasma rotating electrode process (PREP) of Inconel 718 [109], and (d) water atomization (WA) of H13 tool steel [12].

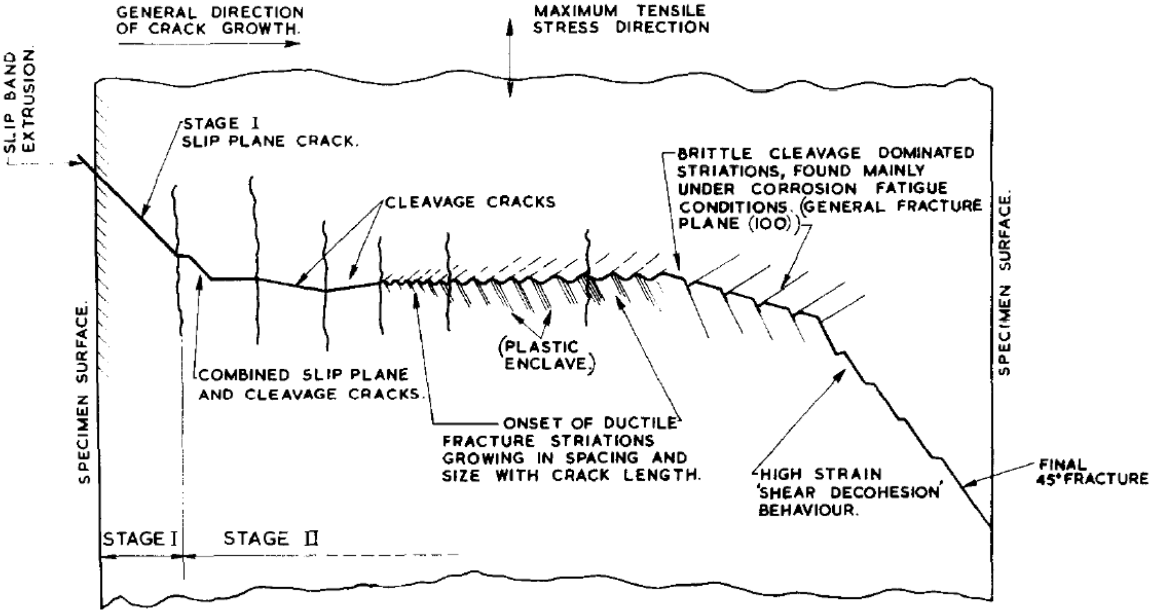

Figure 2.4. The three stages of fatigue crack growth and various modes associated with each as described by Forsyth. This schematic was created specifically for strong aluminum alloys but is generally applicable to many metals. Forsyth adds that the modes depicted here are a composite arrangement of possible modes and does not necessarily represent a general sequence [17].

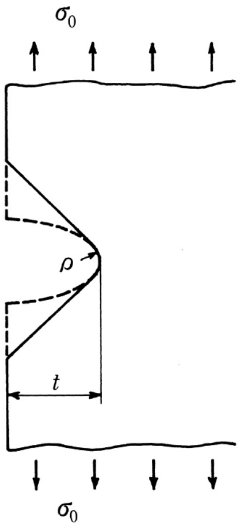

Figure 2.5. Variables used in calculating the stress concentration factor of a surface notch under remote uniform tension [21].

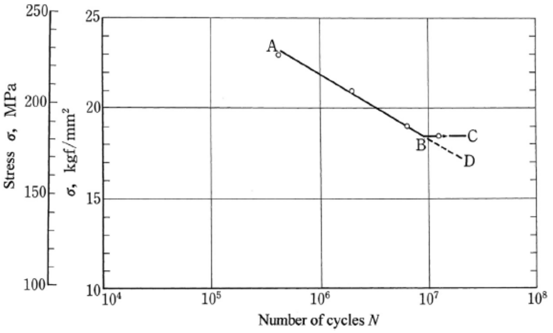

Figure 2.6. Graphical representation of the fatigue limit. Curve ABC demonstrates the S-N curve of a material with a fatigue limit. Curve ABD demonstrates the S-N curve of a material without a fatigue limit [13].

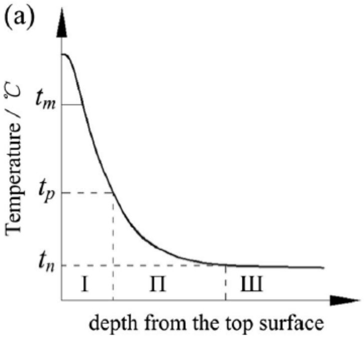

Figure 2.7. Temperature distribution as a function of depth from the top surface. The material depth is segmented into the melted zone (region I), heat-affected zone (region II), and non-affected zone (region III) [42].

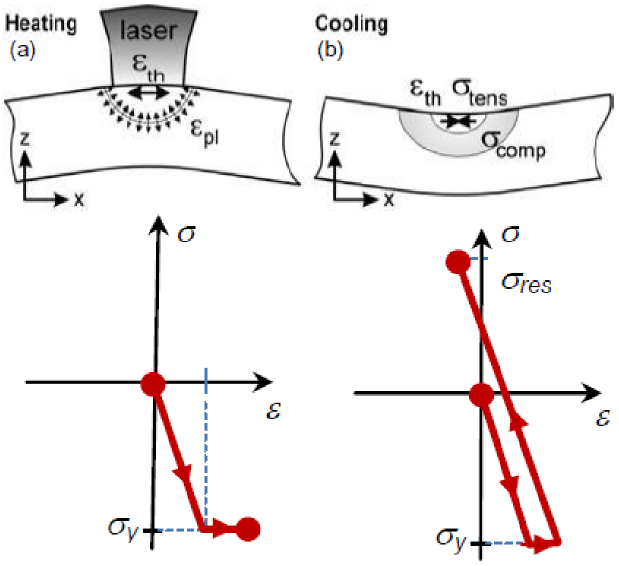

Figure 2.8. Thermal gradient mechanism (TGM) model first proposed by Mercelis and Kruth [43] with diagram modified by Li et al. [40] to graphically depict the residual stress formation.

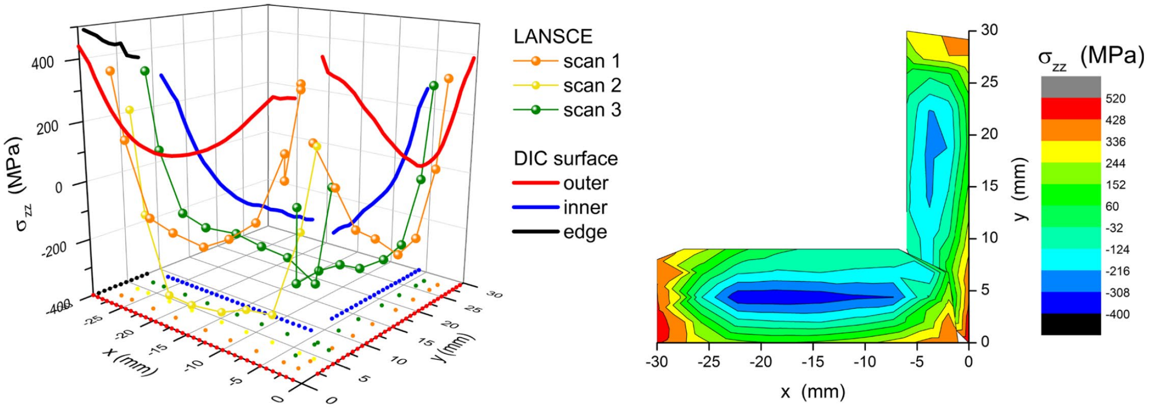

(a) **(b)**

Figure 2.9. Axial residual stresses in AM L-shaped structure. Measurements are from both neutron diffraction (LANSCE) and DIC measurements. Measurements were taken at 15 mm down from the top surface with the bottom surface being at z=0 and the top at z=30. The L-shaped rectangular prism was built at 400 W laser power, 1800 mm/s scan speed, and 45° rotated 5 x 5 mm^2 island scanning. (a) shows the values of the data and the location of measurements in the x and y direction while (b) shows a representative contour plot made from this data [38].

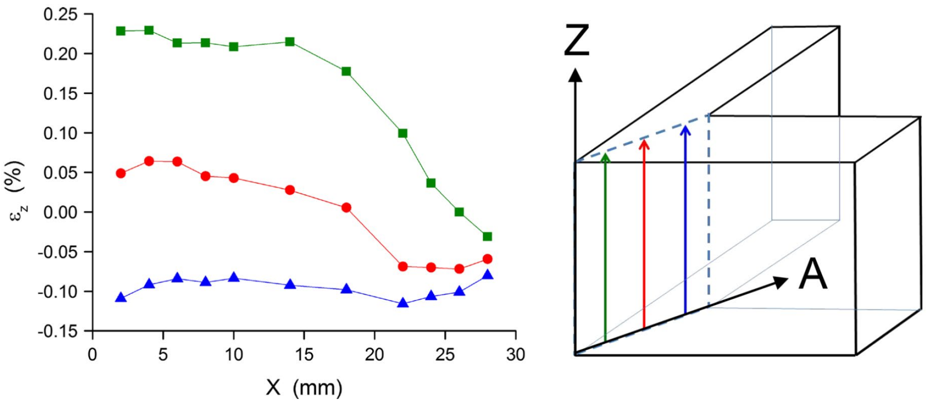

Figure 2.10. Residual axial strains measured via neutron diffraction along the bend of an L-shape specimen. X here represents a measure of distance from the build plate in the z-direction and is not a measure of distance along the x-direction. A scan was done near the outer corner (green), inner corner (blue), and between the two (red). Measurements were taken on a L-shape specimen built at 400 W laser power, 1800 mm/s scan speed, and 45^{o} rotated 5 x 5 mm^2 island scanning [38].

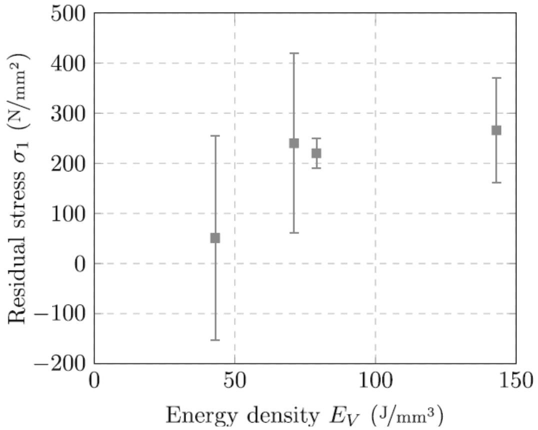

Figure 2.11. Residual stresses in L-PBF 316L at energy densities 43 J/mm^3, 71 J/mm^3, 79 J/mm^3, and 143 J/mm^3 [52].

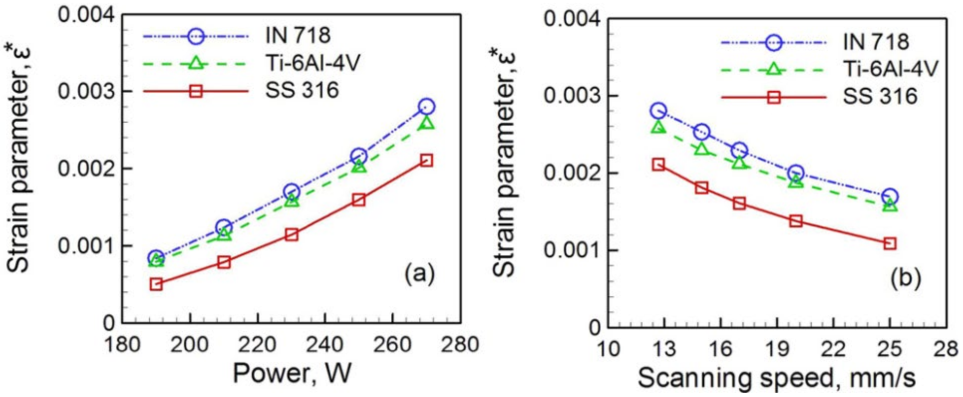

Figure 2.12. Response of residual strain with increasing power (left) and scanning speed (right) [53].

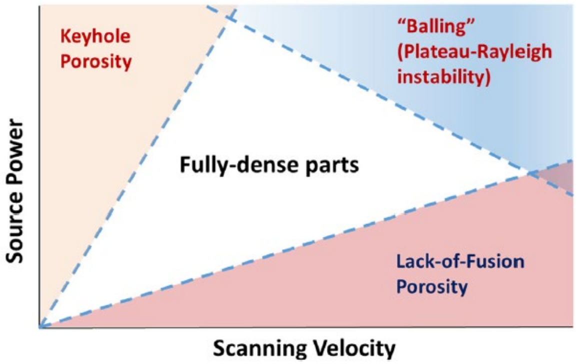

Figure 2.13. Defect process map for laser powder bed fusion applications [8].

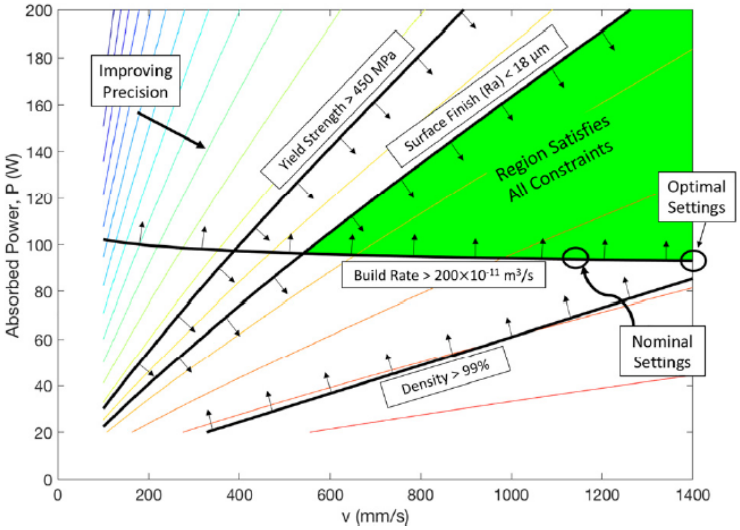

Figure 2.14. Example of a P-V map that seeks to optimize or meet certain requirements for multiple variables [48].

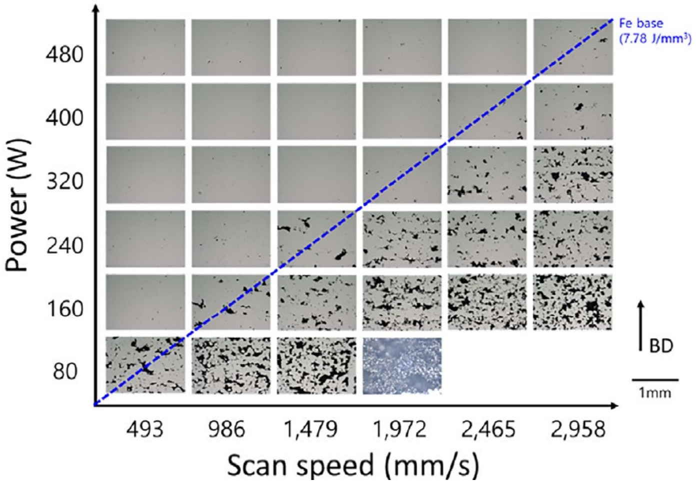

Figure 2.15. Porosity defect process window for 316L on a Farsoon FS271M L-PBF system [84].

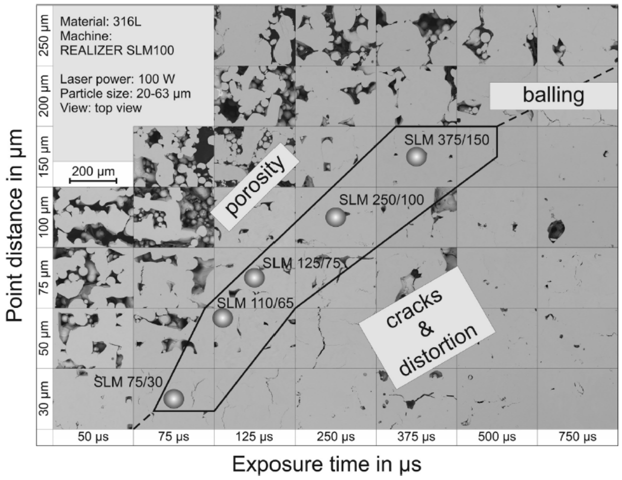

Figure 2.16. Micrographs of 316L built at varying point distances and exposure times [85].

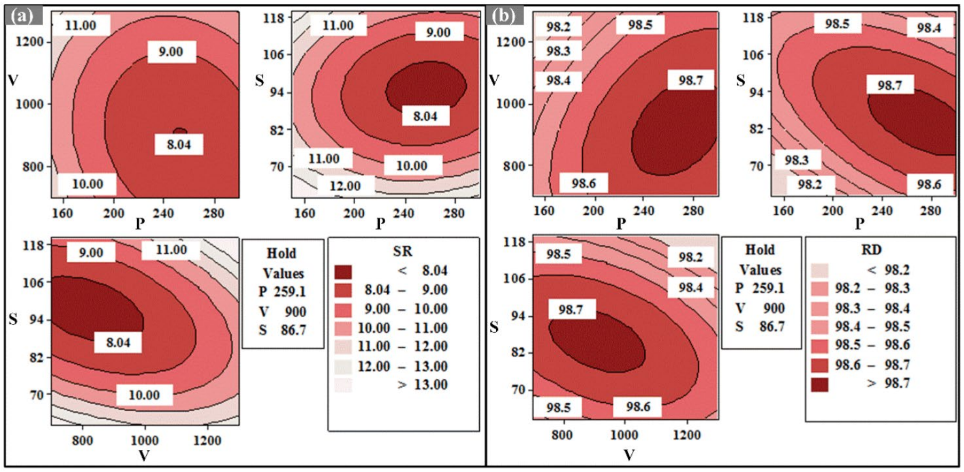

Figure 2.17. Process contour maps of (a) surface roughness and (b) relative density of 316L given laser power (P), scan speed (V), and hatch spacing (S) [82].

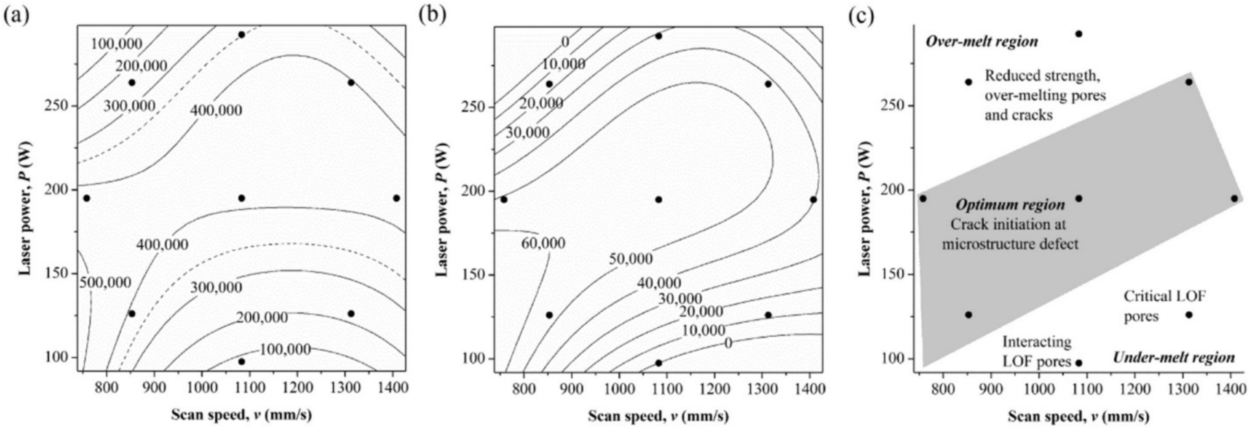

Figure 2.18. Process contour map of laser powder bed fusion 316L showing the response at (a) low stress fatigue life and (b) high stress fatigue life. (c) relates these results back to defects in a defect process map [34].

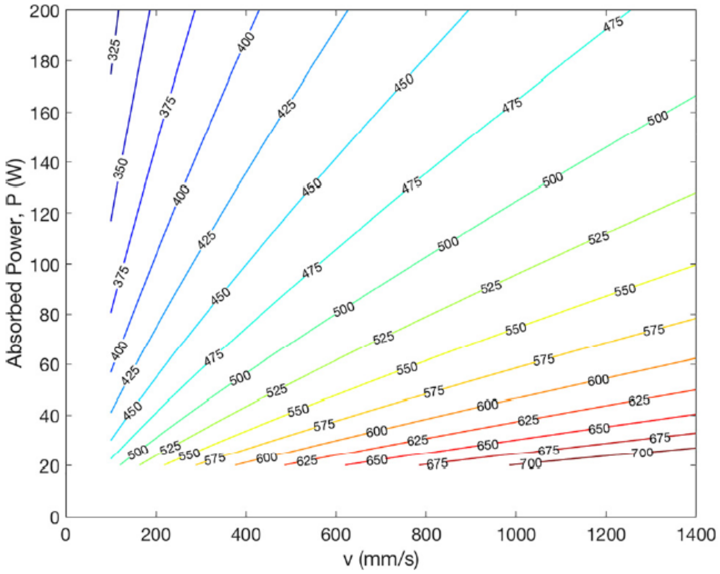

Figure 2.19. P-V process map of 316L laser powder bed fusion showing the response in yield strength [48].

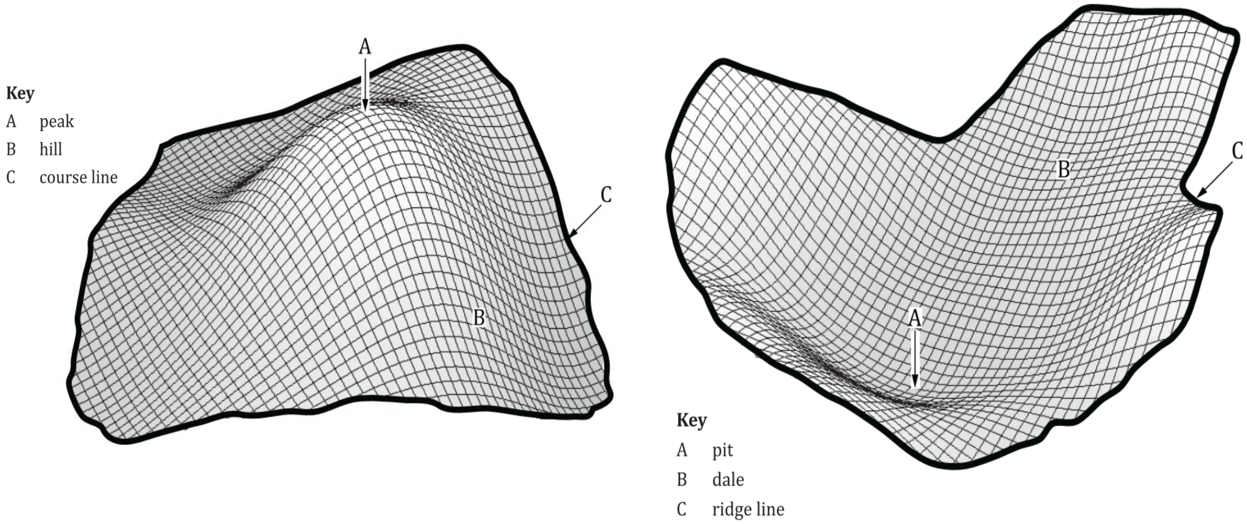

Figure 2.20. Visual representation of hill and dale profile elements with their respective peaks and pits [110].

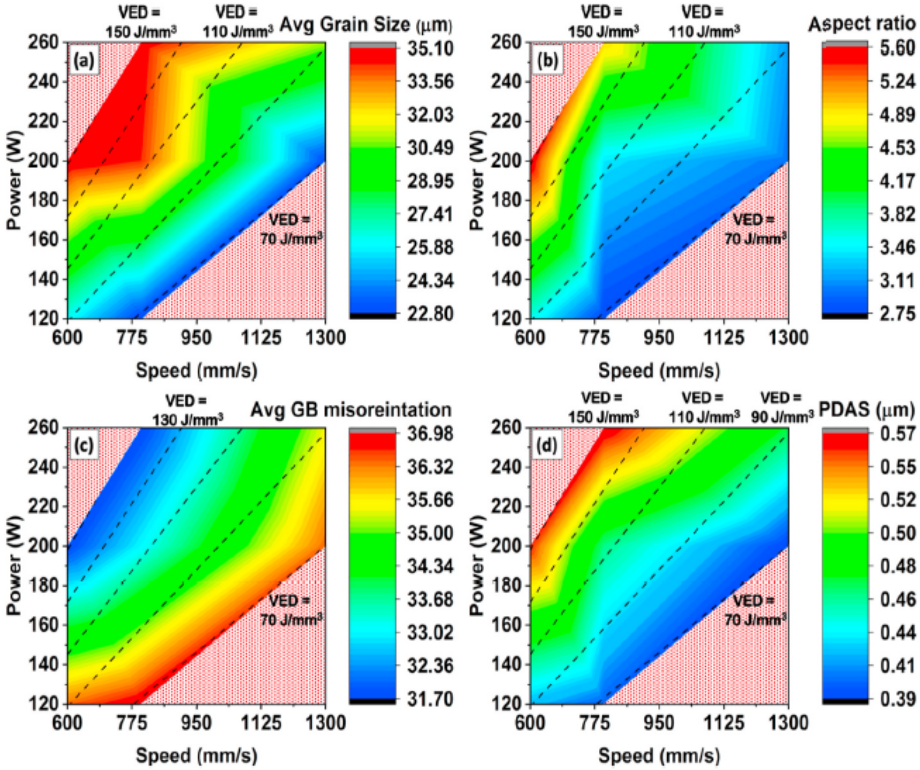

Figure 2.21. P-V process maps for 316L focusing on the resulting (a) average grain size, (b) grain aspect ratio, (c) average grain boundary misorientation, and (d) primary dendritic arms spacing [81].

References

[1] ISO/TC 261, ASTM Committee F42, ISO/ASTM 52900:2017 Additive manufacturing. General principles. Terminology, (2017).

[2] ASTM International, F3122-14 Standard guide for evaluating mechanical properties of metal materials made via additive manufacturing processes, (2014).

[3] I. Gibson, D.W. Rosen, B. Stucker, Additive Manufacturing Technologies, Springer US, Boston, MA, 2010. https://doi.org/10.1007/978-1-4419-1120-9.

[4] T. DebRoy, H.L. Wei, J.S. Zuback, T. Mukherjee, J.W. Elmer, J.O. Milewski, A.M. Beese, A. Wilson-Heid, A. De, W. Zhang, Additive manufacturing of metallic components – Process, structure and properties, Prog. Mater. Sci. 92 (2018) 112–224. https://doi.org/10.1016/j.pmatsci.2017.10.001.

[5] W.E. Frazier, Metal additive manufacturing: A review, J. Mater. Eng. Perform. 23 (2014) 1917–1928. https://doi.org/10.1007/s11665-014-0958-z.

[6] E. Herderick, Additive manufacturing of metals: A review, in: Addit. Manuf. Met., Columbus, Ohio, 2011: p. 13.

[7] W.J. Sames, F.A. List, S. Pannala, R.R. Dehoff, S.S. Babu, The metallurgy and processing science of metal additive manufacturing, Int. Mater. Rev. 61 (2016) 315–360. https://doi.org/10.1080/09506608.2015.1116649.

[8] J.P. Oliveira, A.D. LaLonde, J. Ma, Processing parameters in laser powder bed fusion metal additive manufacturing, Mater. Des. 193 (2020) 108762. https://doi.org/10.1016/j.matdes.2020.108762.

[9] P.D. Harvey, ed., Stainless and Heat-Resisting Steels, in: Eng. Prop. Steel, American Society for Metals, Metals Park, Ohio 44073, 1999.

[10] American Iron and Steel Institute, Specialty Steel Institute of North America, Specialty Steel Industry of the United States, Nickel Development Institute (Canada), Design guidelines for the selection and use of stainless steel, Specialty Steel Industry of the United States, Pennsylvania State University, 1993.

[11] ASTM International, Standard Specification for Additive Manufacturing Stainless Steel Alloy (UNS S31603) with Powder Bed Fusion, (2023).

[12] A.J. Pinkerton, L. Li, Direct additive laser manufacturing using gas- and water-atomised H13 tool steel powders, Int. J. Adv. Manuf. Technol. 25 (2005) 471–479. https://doi.org/10.1007/s00170-003-1844-2.

[13] Y. Murakami, Mechanism of fatigue in the absence of defects and inclusions, in: Met. Fatigue Eff. Small Defects Nonmet. Incl., Second, Elsevier, 2019.

[14] E.J. Czyryca, ASM Committee on Fatigue Crack Propagation, R.P. Gangloff, eds., Fatigue Testing, in: Met. Handb. Mech. Test., 9th ed., American Society for Metals, Metals Park, Ohio 44073, 1985: pp. 361–436.

[15] ASTM Committee E08, E1823-20b Standard terminology relating to fatigue and fracture testing, (2020).

[16] S.D. Antolovich, A. Saxena, eds., Failure Mechanisms and Related Environmental Factors - Fatigue Failures, in: Met. Handb. Fail. Anal. Prev., 9th ed., American Society for Metals, Metals Park, Ohio 44073, n.d.: pp. 102–135.

[17] P.J.E. Forsyth, Fatigue damage and crack growth in aluminum alloys, Acta Metall. 11 (1963) 703. https://doi.org/10.1016/0001-6160(63)90008-7.

[18] P. Chowdhury, H. Sehitoglu, Mechanisms of fatigue crack growth - a critical digest of theoretical developments, Fatigue Fract. Eng. Mater. Struct. 39 (2016) 652–674. https://doi.org/10.1111/ffe.12392.
[19] S. Suresh, R.O. Ritchie, Propagation of short fatigue cracks, Int. Met. Rev. 29 (1984) 31.
[20] Y. Murakami, Metal Fatigue: Effects of Small Defects and Nonmetallic Inclusions, Second, Elsevier, 2019.
[21] Y. Murakami, Stress concentration, in: Met. Fatigue Eff. Small Defects Nonmet. Incl., Second, Elsevier, 2019.
[22] A. Damiens, H. Bonnefoy, I. Titeux, Influence of processing parameters on mechanical and fatigue properties of 316 L steel manufactured by selective laser melting, Weld. World 64 (2020) 1321–1328. https://doi.org/10.1007/s40194-020-00885-4.
[23] S. Hatami, T. Ma, T. Vuoristo, J. Bertilsson, O. Lyckfeldt, Fatigue strength of 316 L stainless steel manufactured by selective laser melting, J. Mater. Eng. Perform. 29 (2020) 3183–3194. https://doi.org/10.1007/s11665-020-04859-x.
[24] P. Kumar, R. Jayaraj, J. Suryawanshi, U.R. Satwik, J. McKinnell, U. Ramamurty, Fatigue strength of additively manufactured 316L austenitic stainless steel, Acta Mater. 199 (2020) 225–239. https://doi.org/10.1016/j.actamat.2020.08.033.
[25] S. Leuders, T. Lieneke, S. Lammers, T. Tröster, T. Niendorf, On the fatigue properties of metals manufactured by selective laser melting – The role of ductility, J. Mater. Res. 29 (2014) 1911–1919. https://doi.org/10.1557/jmr.2014.157.
[26] T.M. Mower, M.J. Long, Mechanical behavior of additive manufactured, powder-bed laser-fused materials, Mater. Sci. Eng. A 651 (2016) 198–213. https://doi.org/10.1016/j.msea.2015.10.068.
[27] A. Polishetty, G. Littlefair, Heat treatment effect on the fatigue characteristics of additive manufactured stainless steel 316L, Int. J. Mater. Mech. Manuf. 7 (2019) 114–118. https://doi.org/10.18178/ijmmm.2019.7.2.442.
[28] A. Riemer, S. Leuders, M. Thöne, H.A. Richard, T. Tröster, T. Niendorf, On the fatigue crack growth behavior in 316L stainless steel manufactured by selective laser melting, Eng. Fract. Mech. 120 (2014) 15–25. https://doi.org/10.1016/j.engfracmech.2014.03.008.
[29] R. Shrestha, J. Simsiriwong, N. Shamsaei, Fatigue behavior of additive manufactured 316L stainless steel parts: Effects of layer orientation and surface roughness, Addit. Manuf. 28 (2019) 23–38. https://doi.org/10.1016/j.addma.2019.04.011.
[30] A.B. Spierings, T.L. Starr, K. Wegener, Fatigue performance of additive manufactured metallic parts, Rapid Prototyp. J. 19 (2013) 88–94. https://doi.org/10.1108/13552541311302932.
[31] F. Stern, J. Kleinhorst, J. Tenkamp, F. Walther, Investigation of the anisotropic cyclic damage behavior of selective laser melted AISI 316L stainless steel, Fatigue Fract. Eng. Mater. Struct. 42 (2019) 2422–2430. https://doi.org/10.1111/ffe.13029.
[32] M. Zhang, C.-N. Sun, X. Zhang, P.C. Goh, J. Wei, D. Hardacre, H. Li, Fatigue and fracture behaviour of laser powder bed fusion stainless steel 316L: Influence of processing parameters, Mater. Sci. Eng. A 703 (2017) 251–261. https://doi.org/10.1016/j.msea.2017.07.071.
[33] M. Zhang, C.-N. Sun, X. Zhang, J. Wei, D. Hardacre, H. Li, Predictive models for fatigue property of laser powder bed fusion stainless steel 316L, Mater. Des. 145 (2018) 42–54. https://doi.org/10.1016/j.matdes.2018.02.054.

[34] M. Zhang, C.-N. Sun, X. Zhang, J. Wei, D. Hardacre, H. Li, High cycle fatigue and ratcheting interaction of laser powder bed fusion stainless steel 316L: Fracture behaviour and stress-based modelling, Int. J. Fatigue 121 (2019) 252–264. https://doi.org/10.1016/j.ijfatigue.2018.12.016.

[35] H. Javadi, W. Jomaa, D. Texier, M. Brochu, P. Bocher, Surface roughness effects on the fatigue behavior of as-machined Inconel 718, Solid State Phenom. 258 (2016) 306–309. https://doi.org/10.4028/www.scientific.net/SSP.258.306.

[36] D. Wu, D. Zhang, C. Yao, Effect of turning and surface polishing treatments on surface integrity and fatigue performance of nickel-based alloy GH4169, Metals 8 (2018) 549. https://doi.org/10.3390/met8070549.

[37] Y. Murakami, M. Endo, Effects of defects, inclusions and inhomogeneities on fatigue strength, Int. J. Fatigue 16 (1994) 163–182. https://doi.org/10.1016/0142-1123(94)90001-9.

[38] A.S. Wu, D.W. Brown, M. Kumar, G.F. Gallegos, W.E. King, An experimental investigation into additive manufacturing-induced residual stresses in 316L stainless steel, Metall. Mater. Trans. A 45 (2014) 6260–6270. https://doi.org/10.1007/s11661-014-2549-x.

[39] M. Sprengel, A. Ulbricht, A. Evans, A. Kromm, K. Sommer, T. Werner, J. Kelleher, G. Bruno, T. Kannengiesser, Towards the optimization of post-laser powder bed fusion stress-relieve treatments of stainless steel 316L, Metall. Mater. Trans. A 52 (2021) 5342–5356. https://doi.org/10.1007/s11661-021-06472-6.

[40] C. Li, Z.Y. Liu, X.Y. Fang, Y.B. Guo, Residual stress in metal additive manufacturing, Procedia CIRP 71 (2018) 348–353. https://doi.org/10.1016/j.procir.2018.05.039.

[41] L. van Belle, G. Vansteenkiste, J.C. Boyer, Investigation of residual stresses induced during the selective laser melting process, Key Eng. Mater. 554–557 (2013) 1828–1834. https://doi.org/10.4028/www.scientific.net/KEM.554-557.1828.

[42] Y. Liu, Y. Yang, D. Wang, A study on the residual stress during selective laser melting (SLM) of metallic powder, Int. J. Adv. Manuf. Technol. 87 (2016) 647–656. https://doi.org/10.1007/s00170-016-8466-y.

[43] P. Mercelis, J. Kruth, Residual stresses in selective laser sintering and selective laser melting, Rapid Prototyp. J. 12 (2006) 254–265. https://doi.org/10.1108/13552540610707013.

[44] B. Cheng, S. Shrestha, K. Chou, Stress and deformation evaluations of scanning strategy effect in selective laser melting, Addit. Manuf. 12 (2016) 240–251. https://doi.org/10.1016/j.addma.2016.05.007.

[45] J.L. Bartlett, X. Li, An overview of residual stresses in metal powder bed fusion, Addit. Manuf. 27 (2019) 131–149. https://doi.org/10.1016/j.addma.2019.02.020.

[46] Z.-C. Fang, Z.-L. Wu, C.-G. Huang, C.-W. Wu, Review on residual stress in selective laser melting additive manufacturing of alloy parts, Opt. Laser Technol. 129 (2020) 106283. https://doi.org/10.1016/j.optlastec.2020.106283.

[47] W. Chen, T. Voisin, Y. Zhang, J.-B. Florien, C.M. Spadaccini, D.L. McDowell, T. Zhu, Y.M. Wang, Microscale residual stresses in additively manufactured stainless steel, Nat. Commun. 10 (2019) 4338. https://doi.org/10.1038/s41467-019-12265-8.

[48] D.R. Clymer, J. Cagan, J. Beuth, Power–velocity process design charts for powder bed additive manufacturing, J. Mech. Des. 139 (2017) 100907. https://doi.org/10.1115/1.4037302.

[49] K. Carpenter, A. Tabei, On residual stress development, prevention, and compensation in metal additive manufacturing, Materials 13 (2020) 255. https://doi.org/10.3390/ma13020255.

[50] P.J. Withers, H.K.D.H. Bhadeshia, Residual stress. Part 2 – Nature and origins, Mater. Sci. Technol. 17 (2001) 366–375. https://doi.org/10.1179/026708301101510087.

[51] A. Röttger, J. Boes, W. Theisen, M. Thiele, C. Esen, A. Edelmann, R. Hellmann, Microstructure and mechanical properties of 316L austenitic stainless steel processed by different SLM devices, Int. J. Adv. Manuf. Technol. 108 (2020) 769–783. https://doi.org/10.1007/s00170-020-05371-1.

[52] T. Simson, A. Emmel, A. Dwars, J. Böhm, Residual stress measurements on AISI 316L samples manufactured by selective laser melting, Addit. Manuf. 17 (2017) 183–189. https://doi.org/10.1016/j.addma.2017.07.007.

[53] T. Mukherjee, V. Manvatkar, A. De, T. DebRoy, Mitigation of thermal distortion during additive manufacturing, Scr. Mater. 127 (2017) 79–83. https://doi.org/10.1016/j.scriptamat.2016.09.001.

[54] T. Larimian, M. Kannan, D. Grzesiak, B. AlMangour, T. Borkar, Effect of energy density and scanning strategy on densification, microstructure and mechanical properties of 316L stainless steel processed via selective laser melting, Mater. Sci. Eng. A 770 (2020) 138455. https://doi.org/10.1016/j.msea.2019.138455.

[55] G.R. Buican, G. Oancea, C. Lancea, M.A. Pop, Influence of layer thickness on internal structure of parts manufactured from 316-L steel using SLM technology, Appl. Mech. Mater. 809–810 (2015) 369–374. https://doi.org/10.4028/www.scientific.net/AMM.809-810.369.

[56] B. Qian, Y. Shi, Q. Wei, H.-B. Wang, The helix scan strategy applied to the selective laser melting, Int. J. Adv. Manuf. Technol. 63 (2012) 631–640. https://doi.org/10.1007/s00170-012-3922-9.

[57] O.O. Salman, F. Brenne, T. Niendorf, J. Eckert, K.G. Prashanth, T. He, S. Scudino, Impact of the scanning strategy on the mechanical behavior of 316L steel synthesized by selective laser melting, J. Manuf. Process. 45 (2019) 255–261. https://doi.org/10.1016/j.jmapro.2019.07.010.

[58] J.P. Kruth, L. Froyen, J. Van Vaerenbergh, P. Mercelis, M. Rombouts, B. Lauwers, Selective laser melting of iron-based powder, J. Mater. Process. Technol. 149 (2004) 616–622. https://doi.org/10.1016/j.jmatprotec.2003.11.051.

[59] J. Li, D. Deng, X. Hou, X. Wang, G. Ma, D. Wu, G. Zhang, Microstructure and performance optimization of stainless steel formed by laser additive manufacturing, Mater. Sci. Technol. 32 (2016) 1223–1230. https://doi.org/10.1080/02670836.2015.1114774.

[60] R.H. Morgan, A.J. Papworth, C. Sutcliffe, P. Fox, W. O'Neill, High density net shape components by direct laser re-melting of single-phase powders, J. Mater. Sci. 37 (2002) 3093–3100.

[61] E. Yasa, J.-P. Kruth, Microstructural investigation of selective laser melting 316L stainless steel parts exposed to laser re-melting, Procedia Eng. 19 (2011) 389–395. https://doi.org/10.1016/j.proeng.2011.11.130.

[62] X. Yan, J. Pang, Y. Jing, Ultrasonic measurement of stress in SLM 316L stainless steel forming parts manufactured using different scanning strategies, Materials 12 (2019) 2719. https://doi.org/10.3390/ma12172719.

[63] Y. Lu, S. Wu, Y. Gan, T. Huang, C. Yang, L. Junjie, J. Lin, Study on the microstructure, mechanical property and residual stress of SLM Inconel-718 alloy manufactured by differing island scanning strategy, Opt. Laser Technol. 75 (2015) 197–206. https://doi.org/10.1016/j.optlastec.2015.07.009.
[64] W.-S. Shin, B. Son, W. Song, H. Sohn, H. Jang, Y.-J. Kim, C. Park, Heat treatment effect on the microstructure, mechanical properties, and wear behaviors of stainless steel 316L prepared via selective laser melting, Mater. Sci. Eng. A 806 (2021) 140805. https://doi.org/10.1016/j.msea.2021.140805.
[65] J. Yu, X. Lin, L. Ma, J. Wang, X. Fu, J. Chen, W. Huang, Influence of laser deposition patterns on part distortion, interior quality and mechanical properties by laser solid forming (LSF), Mater. Sci. Eng. A 528 (2011) 1094–1104. https://doi.org/10.1016/j.msea.2010.09.078.
[66] L. Ma, H. Bin, Temperature and stress analysis and simulation in fractal scanning-based laser sintering, Int. J. Adv. Manuf. Technol. 34 (2007) 898–903. https://doi.org/10.1007/s00170-006-0665-5.
[67] S. Catchpole-Smith, N. Aboulkhair, L. Parry, C. Tuck, I.A. Ashcroft, A. Clare, Fractal scan strategies for selective laser melting of ‘unweldable’ nickel superalloys, Addit. Manuf. 15 (2017) 113–122. https://doi.org/10.1016/j.addma.2017.02.002.
[68] E. Onal, A.E. Medvedev, M.A. Leeflang, A. Molotnikov, A.A. Zadpoor, Novel microstructural features of selective laser melted lattice struts fabricated with single point exposure scanning, Addit. Manuf. 29 (2019) 100785. https://doi.org/10.1016/j.addma.2019.100785.
[69] T. Kurzynowski, K. Gruber, W. Stopyra, B. Kuźnicka, E. Chlebus, Correlation between process parameters, microstructure and properties of 316 L stainless steel processed by selective laser melting, Mater. Sci. Eng. A 718 (2018) 64–73. https://doi.org/10.1016/j.msea.2018.01.103.
[70] H. Jia, H. Sun, H. Wang, Y. Wu, H. Wang, Scanning strategy in selective laser melting (SLM): a review, Int. J. Adv. Manuf. Technol. 113 (2021) 2413–2435. https://doi.org/10.1007/s00170-021-06810-3.
[71] W. Zhang, M. Tong, N.M. Harrison, Scanning strategies effect on temperature, residual stress and deformation by multi-laser beam powder bed fusion manufacturing, Addit. Manuf. 36 (2020) 101507. https://doi.org/10.1016/j.addma.2020.101507.
[72] M. Güden, H. Yavaş, A.A. Tanrıkulu, A. Taşdemirci, B. Akın, S. Enser, A. Karakuş, B.A. Hamat, Orientation dependent tensile properties of a selective-laser-melt 316L stainless steel, Mater. Sci. Eng. A 824 (2021) 141808. https://doi.org/10.1016/j.msea.2021.141808.
[73] Q. Chao, S. Thomas, N. Birbilis, P. Cizek, P.D. Hodgson, D. Fabijanic, The effect of post-processing heat treatment on the microstructure, residual stress and mechanical properties of selective laser melted 316L stainless steel, Mater. Sci. Eng. A 821 (2021) 141611. https://doi.org/10.1016/j.msea.2021.141611.
[74] V. Cruz, Q. Chao, N. Birbilis, D. Fabijanic, P.D. Hodgson, S. Thomas, Electrochemical studies on the effect of residual stress on the corrosion of 316L manufactured by selective laser melting, Corros. Sci. 164 (2020) 108314. https://doi.org/10.1016/j.corsci.2019.108314.
[75] O. Fergani, A. Bratli Wold, F. Berto, V. Brotan, M. Bambach, Study of the effect of heat treatment on fatigue crack growth behaviour of 316L stainless steel produced by selective

laser melting, Fatigue Fract. Eng. Mater. Struct. 41 (2018) 1102–1119. https://doi.org/10.1111/ffe.12755.

[76] B. Blinn, F. Krebs, M. Ley, R. Teutsch, T. Beck, Determination of the influence of a stress-relief heat treatment and additively manufactured surface on the fatigue behavior of selectively laser melted AISI 316L by using efficient short-time procedures, Int. J. Fatigue 131 (2020) 105301. https://doi.org/10.1016/j.ijfatigue.2019.105301.

[77] R.J. Williams, F. Vecchiato, J. Kelleher, M.R. Wenman, P.A. Hooper, C.M. Davies, Effects of heat treatment on residual stresses in the laser powder bed fusion of 316L stainless steel: Finite element predictions and neutron diffraction measurements, J. Manuf. Process. 57 (2020) 641–653. https://doi.org/10.1016/j.jmapro.2020.07.023.

[78] H.D. Carlton, A. Haboub, G.F. Gallegos, D.Y. Parkinson, A.A. MacDowell, Damage evolution and failure mechanisms in additively manufactured stainless steel, Mater. Sci. Eng. A 651 (2016) 406–414. https://doi.org/10.1016/j.msea.2015.10.073.

[79] W.-J. Lai, A. Ojha, Z. Li, C. Engler-Pinto, X. Su, Effect of residual stress on fatigue strength of 316L stainless steel produced by laser powder bed fusion process, Prog. Addit. Manuf. 6 (2021) 375–383. https://doi.org/10.1007/s40964-021-00164-8.

[80] T. Cegan, M. Pagac, J. Jurica, K. Skotnicova, J. Hajnys, L. Horsak, K. Soucek, P. Krpec, Effect of hot isostatic pressing on porosity and mechanical properties of 316 L stainless steel prepared by the selective laser melting method, Materials 13 (2020) 4377. https://doi.org/10.3390/ma13194377.

[81] A.K. Agrawal, G. Meric de Bellefon, D. Thoma, High-throughput experimentation for microstructural design in additively manufactured 316L stainless steel, Mater. Sci. Eng. A 793 (2020) 139841. https://doi.org/10.1016/j.msea.2020.139841.

[82] Y. Deng, Z. Mao, N. Yang, X. Niu, X. Lu, Collaborative optimization of density and surface roughness of 316L stainless steel in selective laser melting, Materials 13 (2020) 1601. https://doi.org/10.3390/ma13071601.

[83] D. Gu, Y. Shen, Balling phenomena in direct laser sintering of stainless steel powder: Metallurgical mechanisms and control methods, Mater. Des. 30 (2009) 2903–2910. https://doi.org/10.1016/j.matdes.2009.01.013.

[84] G.B. Bang, W.R. Kim, H.K. Kim, H.-K. Park, G.H. Kim, S.-K. Hyun, O. Kwon, H.G. Kim, Effect of process parameters for selective laser melting with SUS316L on mechanical and microstructural properties with variation in chemical composition, Mater. Des. 197 (2021) 109221. https://doi.org/10.1016/j.matdes.2020.109221.

[85] A. Röttger, K. Geenen, M. Windmann, F. Binner, W. Theisen, Comparison of microstructure and mechanical properties of 316 L austenitic steel processed by selective laser melting with hot-isostatic pressed and cast material, Mater. Sci. Eng. A 678 (2016) 365–376. https://doi.org/10.1016/j.msea.2016.10.012.

[86] O. Andreau, E. Pessard, I. Koutiri, J.-D. Penot, C. Dupuy, N. Saintier, P. Peyre, A competition between the contour and hatching zones on the high cycle fatigue behaviour of a 316L stainless steel: Analyzed using X-ray computed tomography, Mater. Sci. Eng. A 757 (2019) 146–159. https://doi.org/10.1016/j.msea.2019.04.101.

[87] G. Wang, Q. Liu, H. Rao, H. Liu, C. Qiu, Influence of porosity and microstructure on mechanical and corrosion properties of a selectively laser melted stainless steel, J. Alloys Compd. 831 (2020) 154815. https://doi.org/10.1016/j.jallcom.2020.154815.

[88] W.M. Tucho, V.H. Lysne, H. Austbø, A. Sjolyst-Kverneland, V. Hansen, Investigation of effects of process parameters on microstructure and hardness of SLM manufactured

SS316L, J. Alloys Compd. 740 (2018) 910–925. https://doi.org/10.1016/j.jallcom.2018.01.098.

[89] R. Cunningham, S.P. Narra, C. Montgomery, J. Beuth, A.D. Rollett, Synchrotron-based X-ray microtomography characterization of the effect of processing variables on porosity formation in laser power-bed additive manufacturing of Ti-6Al-4V, JOM 69 (2017) 479–484. https://doi.org/10.1007/s11837-016-2234-1.

[90] R. Cunningham, C. Zhao, N. Parab, C. Kantzos, J. Pauza, K. Fezzaa, T. Sun, A.D. Rollett, Keyhole threshold and morphology in laser melting revealed by ultrahigh-speed x-ray imaging, Science 363 (2019) 849–852. https://doi.org/10.1126/science.aav4687.

[91] E. Liverani, S. Toschi, L. Ceschini, A. Fortunato, Effect of selective laser melting (SLM) process parameters on microstructure and mechanical properties of 316L austenitic stainless steel, J. Mater. Process. Technol. 249 (2017) 255–263. https://doi.org/10.1016/j.jmatprotec.2017.05.042.

[92] N. Sanaei, A. Fatemi, Defects in additive manufactured metals and their effect on fatigue performance: A state-of-the-art review, Prog. Mater. Sci. 117 (2021) 100724. https://doi.org/10.1016/j.pmatsci.2020.100724.

[93] N. Sanaei, A. Fatemi, Phan, Defect characteristics and analysis of their variability in metal L-PBF additive manufacturing, Mater. Des. (2019). https://doi.org/10.1016/j.matdes.2019.108091.

[94] A.E. Wilson-Heid, T.C. Novak, A.M. Beese, Characterization of the effects of internal pores on tensile properties of additively manufactured austenitic stainless steel 316L, Exp. Mech. 59 (2019) 793–804. https://doi.org/10.1007/s11340-018-00465-0.

[95] H. Yao, R. Katona, J. Zhou, M.I. Islam, J. Raush, F. Lu, S. Guo, Defects evaluation of selective laser melting stainless steel 316 parts using positron annihilation lifetime measurement, in: Vol. 8B Heat Transf. Therm. Eng., American Society of Mechanical Engineers, Pittsburgh, Pennsylvania, USA, 2018: p. V08BT10A057. https://doi.org/10.1115/IMECE2018-86729.

[96] J.V. Gordon, S.P. Narra, R.W. Cunningham, H. Liu, H. Chen, R.M. Suter, J.L. Beuth, A.D. Rollett, Defect structure process maps for laser powder bed fusion additive manufacturing, Addit. Manuf. 36 (2020) 101552. https://doi.org/10.1016/j.addma.2020.101552.

[97] N. Kouraytem, X. Li, R. Cunningham, C. Zhao, N. Parab, T. Sun, A.D. Rollett, A.D. Spear, W. Tan, Effect of laser-matter interaction on molten pool flow and keyhole dynamics, Phys. Rev. Appl. 11 (2019) 064054. https://doi.org/10.1103/PhysRevApplied.11.064054.

[98] J. Ning, D.E. Sievers, H. Garmestani, S.Y. Liang, Analytical modeling of part porosity in metal additive manufacturing, Int. J. Mech. Sci. 172 (2020) 105428. https://doi.org/10.1016/j.ijmecsci.2020.105428.

[99] C. Zhao, N.D. Parab, X. Li, K. Fezzaa, W. Tan, A.D. Rollett, T. Sun, Critical instability at moving keyhole tip generates porosity in laser melting, Science 370 (2020) 1080–1086. https://doi.org/10.1126/science.abd1587.

[100] D. Wang, S. Wu, F. Fu, S. Mai, Y. Yang, Y. Liu, C. Song, Mechanisms and characteristics of spatter generation in SLM processing and its effect on the properties, Mater. Des. 117 (2017) 121–130. https://doi.org/10.1016/j.matdes.2016.12.060.

[101] S.A. Khairallah, A.T. Anderson, A. Rubenchik, W.E. King, Laser powder-bed fusion additive manufacturing: Physics of complex melt flow and formation mechanisms of pores, spatter, and denudation zones, Acta Mater. 108 (2016) 36–45. https://doi.org/10.1016/j.actamat.2016.02.014.

[102] A.A. Martin, N.P. Calta, S.A. Khairallah, J. Wang, P.J. Depond, A.Y. Fong, V. Thampy, G.M. Guss, A.M. Kiss, K.H. Stone, C.J. Tassone, J. Nelson Weker, M.F. Toney, T. van Buuren, M.J. Matthews, Dynamics of pore formation during laser powder bed fusion additive manufacturing, Nat. Commun. 10 (2019) 1987. https://doi.org/10.1038/s41467-019-10009-2.

[103] F.C. Pinto, I.R. Souza Filho, M.J.R. Sandim, H.R.Z. Sandim, Defects in parts manufactured by selective laser melting caused by δ-ferrite in reused 316L steel powder feedstock, Addit. Manuf. 31 (2020) 100979. https://doi.org/10.1016/j.addma.2019.100979.

[104] Z. Wu, D. Basu, J.L.L. Meyer, E. Larson, R. Kuo, J. Beuth, A. Rollett, Study of powder gas entrapment and its effects on porosity in 17-4 PH stainless steel parts fabricated in laser powder bed fusion, JOM 73 (2021) 177–188. https://doi.org/10.1007/s11837-020-04491-z.

[105] ISO/TC 213, Geometrical product specifications (GPS) - Surface texture: Areal - Part 2: Terms, definitions and surface texture parameters (ISO 25178-2:2021), (2021).

[106] H.J. Niu, I.T.H. Chang, Instability of scan tracks of selective laser sintering of high speed steel powder, Scr. Mater. 41 (1999) 1229–1234. https://doi.org/10.1016/S1359-6462(99)00276-6.

[107] Y. Murakami, Effect of surface roughness on fatigue strength, in: Met. Fatigue, Elsevier, 2019: pp. 407–430. https://doi.org/10.1016/B978-0-12-813876-2.00016-9.

[108] T. Niendorf, S. Leuders, A. Riemer, H.A. Richard, T. Tröster, D. Schwarze, Highly anisotropic steel processed by selective laser melting, Metall. Mater. Trans. B 44 (2013) 794–796. https://doi.org/10.1007/s11663-013-9875-z.

[109] W.J. Sames, F. Medina, W.H. Peter, S.S. Babu, R.R. Dehoff, Effect of process control and powder quality on Inconel 718 produced using electron beam melting, in: 8th Int. Symp. Superalloy 718 Deriv., John Wiley & Sons, Inc., Hoboken, NJ, USA, 2014: pp. 409–423. https://doi.org/10.1002/9781119016854.ch32.

[110] ISO/TC 213, CEN/TC 290, ISO 4287:1998+A1:2009 Geometrical product specifications (GPS) - Surface texture: Profile method - Terms, definitions and surface texture parameters, (2009).

Chapter 3 The Influence of Section Diameter on the Ultrasonic Fatigue Response of 316L Stainless Steel Manufactured via GE Additive's Concept Laser M2 Laser Powder Bed Fusion Systems

3.1 Introduction

Additive manufacturing (AM) is a rapidly evolving technology which allows for complex geometry, single-step manufacturing processes, and reduced assembly that offers many advantages over conventional manufacturing methods [1,2]. Laser-powder bed fusion (L-PBF) is one of the best-known metal AM methods, having been one of the first most widely used methods. In L-PBF, there are over 130 process variables that can contribute to the manufacture of a part [3,4] each impacting the microstructure, mechanical behavior, and quality of the part. The establishment of quantitative understanding of these effects is important for development of integrated computational materials engineering (ICME) methods [5] which have the potential to accelerate the design of robust AM processes and components [6,7]. In order to inform ICME models, the process-structure-property relationships for AM materials must be well understood. The most investigated process parameters are those which are easiest to control (e.g., laser power, scan speed, hatch spacing, layer thickness, laser spot size, scan strategy, etc.). Currently, most L-PBF equipment manufacturers designate ideal process parameters for a wide range of materials to reduce porosity, surface roughness, and manufacturing defects. These optimized parameters are based on research investigating the ways in which process parameters influence microstructures and properties [8–35]. For many structural components, fatigue is a critical design property and thus establishing quantitative understanding of the fatigue behavior of AM components is essential.

Fatigue of 316L stainless steel in L-PBF has been widely researched [36–48] with three main attributes being known to affect the fatigue behavior: as-built surface finish, residual stresses, and processing defects. In multiple studies on fatigue of AM samples, both surface roughness [2,42,44,49,50] and internal defects [36,48] were found to be significantly influential on fatigue behavior because they served as points of stress concentration [51,52]. The site for crack initiation is dictated by the stress-concentration factor, K_t, whose value depends on the geometry of the defect [53]. Local cyclic stresses are also affected by the local residual stresses. In general, surface residual stresses increase the fatigue strength when they are compressive and decrease when tensile, particularly in hard steels [53]. Investigations into the residual stress states of L-PBF printed parts have shown axial tensile residual stresses reaching or exceeding the bulk room temperature yield stress of the wrought material [54]. Residual stresses arise from melting, solidification, and re-melting during the laser processing which leads to large thermal stress gradients [55–59]. Irrespective of processing parameters and orientation, in nearly every instance, axial residual stresses in L-PBF application of 316L are generally compressive at the center of a sample and tensile at the surface [54,58–61]. This distribution of residual stresses can lead to part distortion and degradation of fatigue performance [56,62–64].

One of the advantages of L-PBF AM is the ability to fabricate components with complex geometries which may have substantial variations in section thicknesses throughout the component. The influence of AM section thickness on fatigue behavior has not been the subject of significant study. In conventionally manufactured components, it has been shown that the fatigue strength of metallic materials can decrease with increasing specimen size [65–71]. The prevailing theory behind this phenomenon comes from Weibull's weakest link theory, which postulates a larger volume will have a higher probability of shorter life due to the abundance of more crack initiating elements [70,72,51]. This phenomenon has not been explicitly shown to occur in L-PBF components, although some aspects of this have been investigated. Studies have shown the effect of powder layer thickness [13,20,37,58] and overall part height (number of layers) [58,60] on structural and mechanical results in AM materials, but only limited investigation has been conducted on geometric scaling. In this instance, geometric scaling can be thought of as scaling in three dimensions such that similar geometries are maintained. The current investigation aims to characterize gauge section diameter effects occurring in 316L L-PBF, as well as evaluate various aspects of processing-structure-property relationships to determine the degree of influence each has on these scaling effects.

Ultrasonic fatigue (UF) testing is used in this research for its ability to rapidly obtain high cycle fatigue (HCF, 10^4 to 10^7 cycles) [38,73–75] and very high cycle fatigue (VHCF, $>10^7$ cycles) [3,4,75–77] data. UF testing is conducted by stimulating specimens at resonant frequencies close to 20 kHz [78,79], compared to the conventional servo-hydraulic HCF testing apparatus which is typically conducted at 20-60 Hz. This reduces testing time in the HCF and VHCF regime to hours or days rather than months or, in the case of VHCF, years. This enables testing of a significantly larger number of samples which, in turn, substantially improves the statistical significance of inferences which can be made on the factors influencing fatigue responses. Prior research suggests that there are no frequency effects on the fatigue behavior in austenitic stainless steels [80].

In this study, the effects of sample gauge section diameter on the ultrasonic fatigue behavior of 316L SS produced via L-PBF are investigated. In particular, the HCF fatigue behavior was evaluated for three different gauge diameters (1.5 mm, 2.5 mm, and 5.0 mm) in L-PBF samples manufactured using identical processing parameters. These samples were also evaluated for changes in surface roughness, defect morphology, and microstructure that may arise due to changes in gauge diameter. The influence of surface roughness was examined by comparing as-built samples to samples with the surface removed by low stress grinding. As-built residual stress distributions were also characterized for two different gauge diameters (1.5 mm and 5.0 mm). In the 5.0 mm gauge diameter sample the influence of stress relieving heat treatment on HCF and residual stress was quantified.

3.2 Materials and Methods

3.2.1 Material properties

A single batch of AISI 316L stainless steel powder particles produced by GE Additive Concept Laser GmbH (CL 20ES) was used to fabricate all specimens. The powder was reported by GE Additive to have a chemical composition shown in Table 3.1 which is generally consistent with standard AISI 316L stainless steel used for L-PBF [81]. A combination of virgin and sieved particles were used in the fabrication of all specimens. Particle size analysis revealed the median particle size to be approximately 30 μm with 90% of particles being less than 45 μm (Table 3.2). Additionally, 73.6% of particles measured were found to have a sphericity of 0.9 or less, with the average sphericity being 0.791. A portion of the powder batch was used to fabricate L-PBF tensile samples to measure bulk mechanical properties. The results indicated that the elastic modulus for this condition was 165 GPa with a yield strength of 466 MPa, showing a significantly lower elastic modulus and higher yield strength compared to wrought 316L stainless steel [82,83] (Table 3.3).

Table 3.1. Chemical composition (in wt. %) of CL 20ES 316L stainless steel powder particles according to GE Additive compared to the ASTM standard composition for 316L laser-powder bed fusion powder particles. Single values represent maximum allowable contents for that given element.

Type	Fe	Cr	Ni	Mo	C	Mn	P	S	Si
GE Additive	Balance	16.5-18.5	10.0-13.0	2.0-2.5	0.030	2.0	0.045	0.030	1.0

Table 3.2. Powder particle size (in µm) cumulative distribution function of GE Additive CL 20ES stainless steel powder.

	10%	50%	90%
Virgin	21.5	30.4	43.5
Virgin + Sieved	20.2	30.1	44.8

Table 3.3. Mechanical properties of 316L austenitic stainless steel at room temperature.

Type	Elastic Modulus [GPa]	Tensile Strength [MPa]	Yield Strength 0.2% Offset [MPa]
Wrought	193	558-560	290
Experimental	165	565	466

3.2.2 Specimen fabrication

All fatigue specimens were fabricated using a GE Additive Concept Laser M2 (CL M2) at the US Naval Research Laboratory. The processing parameters, listed in Table 3.4, are the recommended parameters for 316L by GE Additive.

Table 3.4. Laser powder bed fusion (L-PBF) process parameters for every build.

Machine	Laser Power	Scan Speed	Layer Thickness	Laser Spot Size
CL M2	370 W	900 mm/s	25 µm	160 µm

The specimens were fabricated in a cylindrical dog-bone geometry (Figure 3.1) in the vertical orientation for ultrasonic fatigue testing. To test size effects, the gauge diameter was built to be 5.0 mm, 2.5 mm, or 1.5 mm, with the length of the specimen adjusted to maintain a 20 kHz resonant frequency for each gauge diameter. L-PBF samples were fabricated in 4 different builds, with 32 to 40 samples per build. For each layer, individual fatigue samples were fabricated first by building the sample interior (infill region) with multiple line scans, followed by a number of final contour scans to fabricate the sample as-built surface. Individual samples were removed from the base using electro-discharge machining (EDM) prior to thread machining.

3.2.3 Ultrasonic fatigue testing

Ultrasonic fatigue (UF) testing is conducted at room temperature on equipment developed by University of Natural Resources and Life Sciences, Vienna (BOKU) [79] and operated at 20 kHz. Experimentation was conducted under fully reversed ($R = -1$) loading. Failure was defined as the point in life at which the UF instrumentation detects a change in frequency greater than 200 Hz from the starting resonant frequency of approximately 20 kHz. A value of 200 Hz was chosen to allow the crack to propagate sufficiently to be observed by the unaided eye but not fully fracture the specimen. If a specimen does not meet this failure criteria prior to 10^8 cycles, it was deemed a runout.

The HCF testing protocol consists of four steps: (1) statistical sample of intermediate-stress level fatigue (~20 samples); (2) statistical sample of high-stress level fatigue (~10 samples); (3) quantification of fatigue strength at 10^8 cycles using staircase testing at low-stress fatigue (~10 samples); and (4) application of a Random Fatigue Limit (RFL) model using a Maximum Likelihood Estimation (MLE) to quantify statistical variability and estimate the S-N curve and fatigue strength, S_N.

3.2.4 Fatigue strength calculations

A life-regression model (S-N curve) is used to quantitatively describe the fatigue properties of a given sample group from experimental fatigue tests. There are multiple models that can be used to generate an S-N curve from fatigue data, including the Random Fatigue Limit (RFL) model [84] which is used herein. The RFL curve fit also acts as a metric to more readily determine the fatigue strength, S_N, of a material condition by using the entire S-N curve population including runout data points. The RFL model can be used for a range of different distributions and constraints, making it important to implement a Maximum Likelihood Estimation (MLE) to the calculation of the RFL model. In the current investigation, this was done following the methods outlined by Engler-Pinto Jr. et al. [75]. MLE analysis has shown that a Weibull distribution is the best fit in most cases, so, in the current investigation this is the distribution used in each RFL analysis. Once the appropriate RFL model is selected, the fatigue limit and fatigue strength can be calculated for the dataset. The RFL model was selected in place of other models such as the Modified Basquin model [74,85] as it has been shown to generally provide a better fit to HCF data as determined by MLE [74].

Another common method for estimating the fatigue strength, S_N, is the staircase method. This is a fatigue testing method which sequentially tests samples at varying stress levels. The first sample is tested at a pre-determined stress and observed to be either a failure or a runout. The following sample is tested at a higher stress if the previous sample was a runout and a lower stress if it was a failure. This continues for any number of samples, resulting in a roughly even split of runouts and failures. The median stress of these tests is used as an estimate of the median fatigue strength of the material, with the assumption that the fatigue strength is normally distributed. For its simplicity, this method was used to test a portion of the sample group, however, an RFL model is still applied to the entire dataset as it is more accurate in predicting the fatigue strength of data that is not normally distributed [74].

3.2.5 Surface roughness

Surface roughness was measured on all samples using a Keyence optical microscope. Both line roughness and surface roughness were measured from the included Keyence software on as-built dog-bone samples. A shape correction is applied to account for the cylindrical surface. Nine images of the surface were taken at 600x magnification and stitched together to form an area of interest approximately 900 x 1200 μm. Surface characteristics measured include the arithmetic mean height of the surface profile (S_a), root mean square height of the surface profile (S_q), and the maximum height of the surface profile (S_z), as defined by ISO 25178-2.

3.2.6 As-built surface removal

Removal of the as-built sample surface was conducted to characterize both the impact of reducing the as-built surface roughness and also removing the L-PBF contour passes from the printed part. In both cases, material removal is done using a RTS Leeds low-stress sample polishing machine at Element Materials Technology in Wixom, MI. The CL M2 samples show a clear distinction between the infill and contour regions, with differing microstructures and defect concentrations, as shown in Figure 3.2. Removing the as-built surface was characterized into two groups: surface removal (Figure 3.2 b) and contour removal (Figure 3.2 c). The surface removal machines approximately 75 μm from the surface while the contour removal removes the entire contour passes (approximately 150 μm) from the surface.

3.2.7 Residual stress

The axial residual stress was measured on three samples: one as-built 5.0 mm CL M2, one as-built 1.5 mm CL M2, and one stress relief heat treated 5.0 mm CL M2. Residual stress measurements are done using x-ray diffraction (XRD) with material removal via electropolishing to get a profile of residual stress versus depth from the surface. Samples were measured using an LXRD 13115 with a Mn target, x-ray elastic constant of 20,199 ksi (139,000 MPa), {311} crystallographic plane, and 152.8° Bragg angle. Residual stress measurements were conducted by Proto Manufacturing Inc. in Taylor, MI.

In addition to measuring the residual stress, a partial relief of the residual stress was conducted by heat treating eight 5.0 mm CL M2 samples. A stress relief heat treatment was completed in a Lindberg 1700°C tube furnace in a sealed Argon environment. The heat treatment consisted of a forty-five minute heat-up, four hour soak at 650°C, and a three hour furnace cool to room temperature. These conditions were chosen to provide stress relief while limiting microstructural changes [39,42,86–89].

3.2.8 Microstructure and fractography

Microstructural characterization was conducted to evaluate the influence of gauge diameter. The samples were cut using a low speed saw, ground using increasingly fine grit SiC grinding paper, and polished using 1 μm diamond suspension followed by 0.04 μm colloidal silica, using the procedure outlined by Rowenhorst et al. [90]. Sections were taken from the gauge area both parallel and normal to the build direction. Electron backscatter diffraction (EBSD) was used to evaluate the microstructure in multiple orientations. EBSD scans were taken in both the interior and at the edge of each sample to obtain an understanding of how the microstructure changes throughout the samples, most notably from the contour to the infill. EBSD characterization was accomplished using an EDAX Hikari EBSD camera on a Tescan MIRA-3 GMH electron microscope at 30 kV and a beam intensity of 18, with a scan area 600 X 600 μm and a step size of 0.5 μm. Analysis was completed using EDAX OIM Analysis^{TM} in the austenite phase with a minimum grain boundary misorientation angle of 1°.

Analysis of the fracture surface was conducted utilizing SEM on a Tescan Mira-3 GMH electron microscope. Analysis of defects on the fracture surface was completed with the use of SEM images and ImageJ.

3.3 Results

3.3.1 Microstructure

The microstructure was characterized for each unique build and a representative sample of images are shown in Figure 3.3. The microstructure was evaluated both normal and parallel to the build direction to observe the anisotropic morphology. Each orientation was evaluated in the specimen interior and the near surface region (edge). This allowed for understanding of microstructural changes that may occur between the infill and contour regions. Figure 3.3 (a-d) depicts the microstructure observed for the 1.5 mm CL M2 specimens for direct comparison to the 5.0 mm CL M2 specimens below (Figure 3.3 e-h). All samples show a distinct change in microstructure from the contour to the infill regions. In general, a uniform crosshatch patterning normal to the build direction and columnar grains parallel to the build direction in the infill region are seen. The contour region consists of generally smaller and more equiaxed grains. Additionally, an increase in the density of pore-like defects at the intersection of the contour and infill regions is observed as indicated by the arrows in Figure 3.2 a, c, e, and g.

3.3.2 Surface roughness

Surface roughness measurements indicated that there was no significant change in surface roughness as the diameter of the as-built sample is changed (Table 3.5). The as-built surface was also evaluated by examining cross-sectioned samples perpendicular to the build direction (Figure 3.4) using SEM. The Keyence, with its limited resolution, measures surface roughness predominantly from the evidence of build layers and partially melted particles adhered to the sample surface. Using the SEM, evidence of individual particles and build layers, as well as deeper crevices (denoted in Figure 4 with red circles) that are generally not picked up by the Keyence are seen. For this reason, future discussion will distinguish between the surface roughness (Keyence) and surface crevices (SEM).

Table 3.5. Surface roughness characteristics for each gauge diameter sample group. Characteristics include the arithmetic mean deviation of the surface profile, root mean squared deviation of the surface profile, and maximum height of the surface profile as defined by ISO 25178-2. At least 3 samples were characterized for each gauge diameter.

Type	S_a [μm]	S_q [μm]	S_z [μm]
1.5 mm CL M2	3.38 ± *0.87*	4.28 ± *1.05*	32.83 ± *5.73*
2.5 mm CL M2	3.11 ± *0.97*	3.92 ± *1.19*	29.35 ± *5.83*
5.0 mm CL M2	3.93 ± *0.49*	5.00 ± *0.67*	37.05 ± *5.78*

3.3.3 Residual stress

Axial residual stress measurements were taken on both a 1.5 mm and 5.0 mm sample. Measurements were made through the depth of the as-built samples, showing the residual stress profile throughout the thickness of the samples (Figure 3.5). This shows that both samples have tensile residual stresses on the surface and compressive residual stresses in the sample interior. The magnitude of tensile residual stresses (at the sample edge) was significantly higher in the 5.0 mm sample and the magnitude of the compressive residual stresses (in the sample interior) was higher in the 1.5 mm sample. It should be noted that the residual stress profile in the 5.0 mm sample was measured prior to fatigue testing while the residual stress profile in the 1.5 mm sample was measured after the sample had been tested in fatigue and the sample fractured. This was required due to lack of additional unfatigued samples for the 1.5mm sample diameter. In the 1.5 mm sample, residual stress measurements were taken well below the fracture surface while still being within the gauge length in order to avoid large deviations in residual stress due to stress relaxation that occurs during fatigue fracture. Axial tensile residual stress peaks just below the surface, exceeding the measured values of yield strength and ultimate tensile strength in the 5.0 mm sample. Despite this, no evidence of deformation or fracture was seen in these samples prior to testing. As suggested by Wu et. al. [54], comparisons between residual stress and the uniaxial yield strength may not be appropriate in AM materials due to the multiaxial nature of the residual stress states.

Axial residual stress measurements are also taken on the surface of two 5.0 mm samples and one 1.5 mm sample. These measurements were made in either three or six different regions around the sample circumference. The surface axial residual stress measurements are non-destructive which allows for one of the samples to be measured before and after stress relief heat treatment. Figure 3.6a shows a comparison of the 5.0 mm samples measured in the as-built condition and stress relieved condition. Figure 3.6b shows how the surface axial residual stress of the 5.0 mm stress-relieved samples compares to the as-built 1.5 mm sample. Table 3.6 shows the stress-relieved 5.0 mm had lower magnitude tensile residual stress compared to the as-built 5.0 mm, but still a higher magnitude tensile residual stress compared to the as-built 1.5 mm. Due to lack of sample availability, residual stress measurements in the 2.5 mm CL M2 samples were not conducted.

Table 3.6. Averaged values of the measured surface axial residual stress for each sample type.

Type	Average Measured Stress [MPa]	Number of measurements
5.0 mm As-built	292 ± *13*	12
5.0 mm Stress-relieved	143 ± *11*	3
1.5 mm As-built	69 ± *17*	3

3.3.4 Ultrasonic fatigue behavior

A total of 130 as-built CL M2 specimens were tested for the three different gauge diameters (1.5 mm, 2.5 mm, and 5.0 mm). An additional eight stress-relief heat treated, eight surface-removed, and eight contour-removed specimens were fatigue tested to show the influence of residual stress, surface roughness, and contour/infill defect density on fatigue behavior, respectively. Each group was UF tested across a range of maximum stress levels to capture behavioral changes at different stresses and to obtain a more complete view of the RFL estimated S-N curve. The UF results for each as-built CL M2 sample group are graphically represented in Figure 3.7. Fitting each sample group to an RFL model assuming a Weibull distribution informed by MLE indicates that reasonable curve fits were obtained for all of the fatigue data groups. As shown in Figure 3.7, significant improvements in fatigue behavior are observed with decreasing gauge diameter. From the RFL model curve fit, a value for the fatigue strength can be calculated along with a standard deviation of the data. The fatigue strength can also be calculated from the staircase testing procedure. Comparing the two methods of calculating the fatigue strength (Table 3.7) shows they are in good agreement. The fatigue results of Figure 3.7 show that with decreasing gauge diameter, a general increase in fatigue life, N_f, and fatigue strength, S_N, at 10^8 cycles, was observed. The variability for the 1.5 mm as-built samples is rather substantial, with a standard deviation for the calculated fatigue strength of 26.1 MPa (Table 3.7). The standard deviation in the RFL calculation is high in this case due to the two samples that were runouts at 160 MPa. Despite this variability, there is a statistically significant gauge diameter effect on fatigue behavior occurring between 5.0 mm and 2.5 mm samples ($p<0.0001$) and between 2.5mm and 1.5mm samples ($p=0.0467$).

Table 3.7. Fatigue strength for each sample group as determined by random fatigue limit (RFL) model and the staircase testing procedure. The fatigue strength is defined as the stress needed to cause failure at 10^8 cycles.

	Fatigue Strength [MPa] via RFL	Fatigue Strength [MPa] via Staircase
1.5 mm As-built	123.0 ± *26.1*	122.5 ± *6.6*
2.5 mm As-built	98.7 ± *7.0*	97.0 ± *6.4*
5.0 mm As-built	89.5 ± *5.7*	91.0 ± *7.0*

The UF results for samples which had the as-built surface removed and the contour removed are shown in Figure 3.8. Both the surface-removed and contour-removed results show a marked improvement in fatigue strength, S_N, at 10^8 cycles and fatigue life, N_f in all cycle regimes. The improvement is such that these 5.0 mm samples perform even better than the 2.5 mm and 1.5 mm as-built samples, demonstrating that the surface region has a substantial influence on the HCF behavior. This improvement is attributed to the removal of the surface crevices, as well as a general reduction in surface roughness. This surface removal reduces both the number of potential crack initiation sites and the severity of the stress concentration at these sites. A further slight improvement in fatigue strength was observed when the entire contour (including the contour/infill zone) is removed. In general, the fatigue strength estimates from the RFL analysis (Table 3.8) show no statistically significant difference between the surface-removed and contour-removed samples. It should be noted that the sample populations for both these groups is limited which makes estimating statistical significance of these small differences difficult.

Table 3.8. Fatigue strength for contour-removed and surface-removed sample groups compared to the as-built 5.0 mm diameter condition. Fatigue strength is determined by random fatigue limit (RFL) model and staircase testing procedure. The fatigue strength is defined as the stress needed to cause failure at 10^8 cycles.

	Fatigue Strength [MPa] via RFL	Fatigue Strength [MPa] via Staircase
5.0 mm Contour-Removed	179.0 ± *3.8*	181.4 ± *6.4*
5.0 mm Surface-Removed	170.0 ± *12.9*	175.0 ± *5.0*
5.0 mm As-built	89.5 ± *5.7*	91.0 ± *7.0*

The UF results for the stress-relief heat treated samples are shown in Figure 3.9. The implementation of a stress relief heat treatment on as-built samples results in a moderate improvement in fatigue strength at 10^8 cycles and a slight improvement in fatigue life. The stress relief heat treatment reduced the surface residual stress from 292 MPa to 143 MPa and improved the fatigue strength from 89.5 MPa to 116 MPa as shown in Table 3.9. For comparison, the surface residual stress in the as-built 1.5 mm samples is 69 MPa and the fatigue strength is 123 MPa.

Table 3.9. Fatigue strength for the stress-relief heat treated 5.0 mm sample group compared to the as-built 5.0 mm diameter and 1.5 mm diameter conditions. Fatigue strength is determined by random fatigue limit (RFL) model. The fatigue strength is defined as the stress needed to cause failure at 10^8 cycles.

	Fatigue Strength [MPa] via RFL	Fatigue Strength [MPa] via Staircase
1.5 mm As-built	123.0 ± *26.1*	122.5 ± *6.6*
5.0 mm Stress-Relief Heat Treat	116.0 ± *4.9*	115.0 ± *8.7*
5.0 mm As-built	89.5 ± *5.7*	91.0 ± *7.0*

3.3.5 Fracture surface analysis of as-built samples

Fatigue fracture surfaces were characterized using SEM fractography. Figure 3.10 shows a representative view of the fracture surfaces for each as-built sample group. The fracture surface has two distinct regions: fatigue crack growth in the bottom region of the images and ductile overload in the top region of the images. The bottom regions show the path of crack growth caused by ultrasonic fatigue. The top region experiences ductile failure from manual overload by sample bending. This manual overload is done to reveal the entire fracture surface as the criteria for failure in the UF testing does not result in complete fracture of the specimen. As can be seen, the macroscopic fracture surface morphology is similar for all three gauge diameters.

While the images in Figure 3.10 are the typical fatigue fracture surface seen in most samples, some of the 5.0 mm as-built samples showed multiple fatigue crack initiation sites as shown in Figure 3.11. Evidence of multiple initiation sites were also seen in 2.5 mm and 1.5 mm samples, however much less common. In all cases, multiple fatigue fracture surfaces were most often seen in higher maximum stress, σ_{max}, conditions.

The fatigue fracture surface of each as-built sample reveals many different types of sub-surface defects, as highlighted in Figure 3.12. The primary defects were lack of fusion (LOF) porosity [36,55,91–94], gas entrapment porosity [91,92,95,96], keyhole porosity [25,28,97–100], improperly melted particles [92,95,101–103], and discontinuities in the composition [104]. For these samples, an increase in defect concentration was observed at the contour/infill region (Figure 3.12 a & b), consistent with what was observed in EBSD (Figure 3.3). The defects in this region were a variety of improper melting causing both porosity (Figure 3.12 c & d) and solid defects such as melt pool boundaries or unmelted particles (Figure 3.12 g-i). Additionally, some of these samples have shown evidence of composition variation either due to a change in concentration of certain elements (typically increased carbon and decreased iron) or the inclusion of foreign elements (Figure 3.12 e & f). Despite the abundance of these subsurface defects, the crack initiation in as-built samples were generally due to surface crevices or surface-connected defects (Figure 3.12 k & l), not internal defects.

The size of the defects observed on the fracture surface were analyzed using ImageJ. Both the area and the longest distance across the defect (diameter) were measured. All defects were quantified in the same manner, regardless of whether they are a pore, inclusion, or irregular melting. In this part of the study, all defects in the as-built samples were measured regardless of whether or not they could be the initiating defect. Only obvious three-dimensional defects were characterized. Discontinuities associated with local composition differences (e.g., oxides, carbides, etc.) such as in Figure 3.12 f and near surface LOF such as in Figure 3.12 j have not been included in this population. This defect study also does not include or account for crack initiation at the surface due to surface defects, such as surface crevices or surface-connected defects (Figure 3.12 k & l), as the morphology of these defects cannot be seen from the fracture surface. The results for defect size (diameter), shown in Figure 3.13, indicate that the size of defects is not affected by the gauge diameter. This effectively rules out processing defect size or defect morphology as being the leading cause of the gauge diameter effects on HCF observed on the as-built samples.

As stated previously, crack initiation in nearly every as-built sample occurs at or near the surface. Our investigation into surface roughness showed that there is no significant difference between gauge diameters, but that the presence of surface crevices must also be considered. The crevices are not detectable by the normal surface roughness measurements. The frequency of surface crevices in each sample set is difficult to determine as they are most readily observed in cross-sectioned samples which only isolates two locations around the circumference of the gauge section. The cross-section observations were inadequate to determine if the size or distribution of these crevices is affected by gauge diameter. However, it could be determined that in all as-built samples these crevices are the likely the source of crack initiation. Figure 3.14 shows examples of secondary cracks that had formed within the gauge section but away from the primary fatigue fracture surface in both 5.0 mm and 2.5 mm as-built samples. In both cases the cracks appear to have formed at a surface crevice.

Crack initiation also occurs at the surface region in the 5.0 mm stress relief heat treated samples. Despite showing improvements in fatigue behavior due to the reduction of tensile stresses on the surface, the as-built surface finish remains the source of fatigue cracking just as in the as-built samples. For this reason, the fracture surfaces of both sample groups are largely indistinguishable, as shown in Figure 3.15.

3.3.6 Fracture surface analysis of samples with as-built surface regions removed

To summarize what is known so far: gauge diameter effects on fatigue behavior have been shown to occur in 316L L-PBF. It is also shown that the microstructure, surface roughness, defect morphology, and defect size distribution do not change with changing gauge diameter. In addition to this, it is shown that a concentration of defects as well as a change in microstructure occurs at the contour/infill zone but that crack initiation generally occurs at or near the surface. For this reason, an investigation was conducted to analyze the influence the as-built surface morphology and the contour/infill zone morphology has on the fatigue behavior. Figure 3.16 shows a representative fracture surface of 5.0 mm surface-removed and contour-removed samples, compared to the as-built fracture surface. The general shape of the fracture surface is nominally the same as the as-built samples, but the source of crack initiation is starkly different.

While the as-built samples typically showed crack initiation occurring at or near the surface, the surface- and contour-removed samples show sub-surface, internal defects as the source of crack initiation. Figure 3.17 shows the general initiation site morphology of both surface- and contour-removed samples. The initiation sites in the surface-removed samples were generally from AM processing defects that can be characterized as a complex conglomerate of lack of fusion (LOF) and melt pool defects. Evidence of these types of defects were also seen on the fracture surface of as-built samples, however they were rarely the source of crack initiation. The initiation site in the contour-removed samples has a defect morphology not reported by previous researchers. There is a distinct "fish-eye" surrounding each defect, showing that initial crack growth occurred sub-surface and in vacuum [4,105]. Once the crack reaches the surface, the fracture surface morphology changes to that of a typical "in-air" crack path. These defects tend to be larger and further from the surface than the defects found in the surface-removed samples. They also all tend to have a roughly square shape and a relatively flat surface. The morphology of the defect surfaces suggest that these are LOF voids between melt pool boundaries, however the reason for this shape is unknown.

The initiating defects for the surface-removed and contour-removed samples can be further compared by looking at the 3D morphology of the LOF defects. Fracture surface topology and profilometry were conducted on all failed samples using the Keyence optical microscope to assess the defect height in the build direction. Matching halves of a given fractured sample are shown in Figure 3.18 to help visualize the 3D morphology of the initiating defect. The average height (along the build direction) for an initiating defect is 46 μm for a surface-removed sample and 19 μm for a contour-removed sample. The cross-sectional area of the initiating defect is on average 3,803 μm^2 and 11,335 μm^2 for surface- and contour-removed samples, respectively. While the initiating defect in both sample groups were determined to be LOF defects, the initiating defects in the contour-removed samples were more expansive across a given build layer but rarely permeates through multiple build layers – a build layer being 25 μm thick. The defects found in the surface-removed samples almost always extended through multiple build layers, suggesting a different formation mechanism.

Since the LOF defects in surface-removed and contour-removed samples differed morphologically, composition analysis was conducted to provide insight into the defect formation mechanisms. Composition analysis via EDS for the surface-removed initiating defects shows an essentially uniform composition across the initiating defect and fracture surface. The contour-removed samples, on the other hand, show compositional variation specifically at the LOF defects (Figure 3.19). EDS shows increased concentrations of Si and Mn, indicative of Si-oxides (SiO_2), Mn-oxides (MnO), and silicates ($MnSiO_3$, Mn_2SiO_4) [106,107]. This suggests that these silicate-oxides form due to Si and Mn reacting with O trapped in the powder particles and/or O trapped in the voids of LOF defects.

To further investigate the differences between the surface-removed and contour-removed samples, the microstructures beneath the fracture surfaces are compared via EBSD. Figure 3.20 depicts a cross-sectional view of a surface-removed sample (Figure 3.20 a) and contour-removed sample (Figure 3.20 b). These images show both the external ground surface and the path of crack growth from the initiating defect. Figure 3.20 a shows that part of the contour and the contour/infill zone remain intact in the surface-removed sample, while Figure 3.20 b shows that in the contour-removed sample this region has been removed. The surface-removed sample shows a crack growth path that is relatively tortuous, as opposed to the contour-removed sample which has a smooth crack growth path. This suggests different crack growth mechanisms and behavior between the two sample types, which would help explain why the contour-removed specimens have longer fatigue lives despite having larger initiating defects.

3.4 Discussion

In this study we have characterized the influence of AM section thickness on HCF, using fatigue sample gauge diameter as a measure of section thickness. A pronounced gauge diameter effect on HCF in AM 316L stainless steel has been observed. In particular, 1.5 mm diameter samples show a substantial increase in fatigue life and fatigue strength at 10^8 cycles compared to 5.0 mm samples. The HCF response of 2.5 mm diameter samples was intermediate to these results. We have also attempted to identify the underlying factors that produce this gauge diameter effect as discussed below.

Previous studies [e.g., 14,16] have shown that adjusting the processing parameters can alter the microstructure, however, in the current investigation, the processing parameters were not altered for the different gauge diameter fabrication, therefore changes in microstructure with gauge diameter were not expected and were not observed. Additionally, gauge diameter did not have an observable effect on the microstructure as shown in Figure 3.3. Normal to the build direction, all groups have a crosshatch pattern (Figure 3.3 e-f, i-j), characteristic of directional scanning strategies in L-PBF. Parallel to the build direction, columnar grains that extend across multiple build layers were observed. This cross-hatched cell microstructure is common in many L-PBF systems as grains will preferentially grow in the direction of heat flow (along the build direction) and correlate with melt pools which span multiple layers. A cell represents a given grain or grain cluster that matches with a single square in the crosshatch pattern, as demonstrated in Figure 3.21. Comparing cell sizes for each gauge diameter (Figure 3.3 b & f), it can be observed that the cells are roughly the same size at approximately 125 μm in width in the infill regions. Additionally, the melt pool depth (Figure 3.3 d & h) and width of the contour zone (Figure 3.3 a, c, e, g) appears unchanged between the 1.5 mm and 5.0 mm as-built samples. If only microstructure was taken into consideration, one may not expect any change in fatigue with changing gauge diameter. Since we do see changes in fatigue behavior with gauge diameter, this indicates that factors other than the mesoscale microstructure dominate the HCF response of these samples.

Processing-related AM defects found on the entire fracture surface were characterized by SEM and determined to be consistent with lack-of-fusion porosity and solid defects such as melt pool boundaries or unmelted particles. These defects were not associated with fatigue crack initiation but were taken to be indicative of the general porosity from AM. Quantification of these images indicated that the size of these defects follows a log normal distribution and both the size and distribution are statistically indistinguishable for all three gauge diameters. The mean size of these defects was approximately 34 μm in diameter. In addition, an increased concentration of defects was observed at the infill/contour zone for all sample diameters. This suggests that defect sizes, distribution, and morphology do not significantly impact the gauge diameter effect on fatigue behavior of these as-built samples.

For samples tested in the as-built condition, crack initiation is observed to occur at the as-built surface in the majority of cases. These cracks generally were related to surface connected crevices that are assumed to have formed during individual AM processing passes and can be considered AM processing-related defects. There did not appear to be a correlation between crevice depth and sample gauge diameter, so this did not appear to explain the gauge diameter influence on fatigue lives. The measured value of the as-built surface roughness showed no significant difference between gauge diameters, indicating that surface roughness does not significantly impact the gauge diameter effect on fatigue behavior.

While the processing parameters themselves were unchanged for the different builds, the complexity of the thermal history required to produce different gauge diameters can affect the residual stresses produced in each build set. All as-built samples, regardless of gauge diameter, demonstrate a peak tensile axial residual stress near the surface and transition into a peak compressive axial residual stress at the sample interior. This type of residual stress distribution has been observed previously for L-PBF processes [54,58–61]. The difference between gauge sizes lies in the magnitude of residual stresses, which shows a higher magnitude near-surface tensile stress in the 5.0 mm as-built samples and a higher magnitude sub-surface compressive stress in the 1.5 mm as-built samples. Our results are consistent with at least one previous study [54]. Wu et al. reported that a reduction in part thickness can result in a lower magnitude tensile axial residual stress on the surface [54]. It should be noted that they also reported a lower magnitude compressive stress in the thinner region of the sample interior. Our observation is the opposite of this with a somewhat lower magnitude of compressive residual stresses in the sample interior for the 1.5 mm sample compared with the 5.0 mm sample. To ensure resonance of the ultrasonic fatigue samples, changes in sample diameter also require changes in the length of the sample scaled with the gauge diameter. Mercelis and Kruth found that the more layers added (more layers results in a taller height) the higher the residual stress is in the final part [60]. Our results are consistent with this observation, in that the longer gauge length in 5.0 mm samples correlated with a higher tensile residual stress on the surface.

The residual stress analysis in this current work showed that the axial residual stress is of greater magnitude and is tensile on and near the surface for 5.0 mm samples compared to 1.5 mm samples which exhibited a lower tensile residual stress on the surface. This could contribute to the observed gauge diameter effect but it is important to note the degree to which the tensile residual stress negatively affects the fatigue behavior. Fatigue testing shows a moderate improvement in fatigue strength at 10^8 cycles and slight improvement in fatigue life with a stress relief heat treatment of the 5.0 mm as-built samples (Figure 3.9 b). Additionally, fatigue crack initiation occurs at or near the surface, in the same manner as the as-built samples. Since the crack initiation sites and general fracture surface appear to be unaffected by gauge diameter, the improvement in fatigue behavior is attributed to the reduction in tensile residual stresses at the sample surface in the 1.5mm samples. The higher magnitude tensile residual stress observed in the 5.0 mm sample would in general increase the local mean stress and/or crack opening stress during fatigue testing resulting in shorter fatigue life. The strong correlation between residual stress distribution and fatigue behavior is consistent with previous work. Lueders et al. [39,42] has shown that the tensile residual stresses present in L-PBF parts negatively impact the fatigue behavior in the high cycle regime as it affects crack growth.

In the current study, experiments conducted in samples subjected to a stress relief heat treatment showed a pronounced reduction in the residual stresses and also improvements in the HCF behavior. This further demonstrates the importance of residual stresses on fatigue behavior. This observation is consistent with previous studies [41,86,87,89].

For fatigue critical AM components, the results of this study show the importance of controlling residual stresses that are produced during AM fabrication. Without mitigating residual stress formation, AM components of varying section thickness can be expected to have significant variations in HCF lives, with thick sections exhibiting an increase in the probability of fatigue failure. The effect of section thickness can be somewhat moderated by subjecting AM components to stress relief heat treatment.

3.5 Conclusions

In this study, the fatigue behavior of L-PBF 316L SS under fully reversed ($R = -1$) ultrasonic fatigue loading in the high to very high cycle fatigue regime was investigated. Cylindrical dogbones of three gauge diameters (1.5 mm, 2.5 mm, 5.0 mm) were fabricated in the vertical direction with no post-processing to study the effects of sample diameter on fatigue behavior in the as-built condition. An additional set of samples were fabricated for post-processing for the purpose of studying the effects of the surface removal, contour removal, and stress-relief heat treatment on HCF in the 5.0 mm diameter samples. The following conclusions can be drawn:

1) The high to very high cycle ultrasonic fatigue behavior of these AM samples is strongly influenced by the diameter of the specimen. A reduction in gauge diameter results in an increased fatigue strength at 10^8 cycles and increased fatigue lives in the high cycle fatigue regime.
2) For samples built on the same AM machine (Concept Laser M2) and using the same processing variables, the fabrication of samples with varying diameter does not result in differences in microstructure (grain size, morphology and texture), defect size and distributions, or surface roughness. This indicates that the mesoscale microstructure and defect structure are not responsible for the observed changes in fatigue behavior.

3) Fractography suggests that crack initiation occurs at or near the surface in as-built samples. Cross-section analysis revealed that the surface initiation is likely due to deep surface crevices.
4) Axial residual stress magnitudes are affected by the gauge diameter, and likely contribute to sample diameter effect. Large diameter samples have a higher magnitude tensile residual stress near the surface, while smaller diameter samples have a higher magnitude compressive residual stress at the center of the samples. Partial relaxation of residual stress via stress relief heat treatment demonstrates that the high magnitude tensile stresses on the surface negatively affect the high cycle fatigue behavior.
5) Removing the as-built surface significantly improves the fatigue life and fatigue strength at 10^8 cycles. The fatigue behavior is further improved when the contour/infill zone is removed. In samples which have had the surface removed, fatigue crack initiation occurs at relatively large lack-of-fusion defects that are typical of AM processing.

Figures

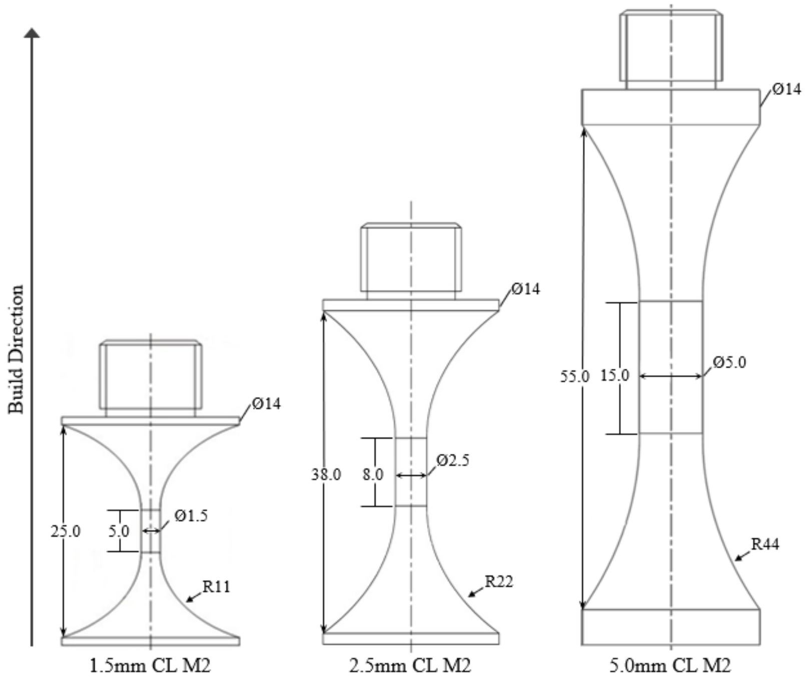

Figure 3.1 Concept laser M2 specimen geometry for ultrasonic fatigue tests.

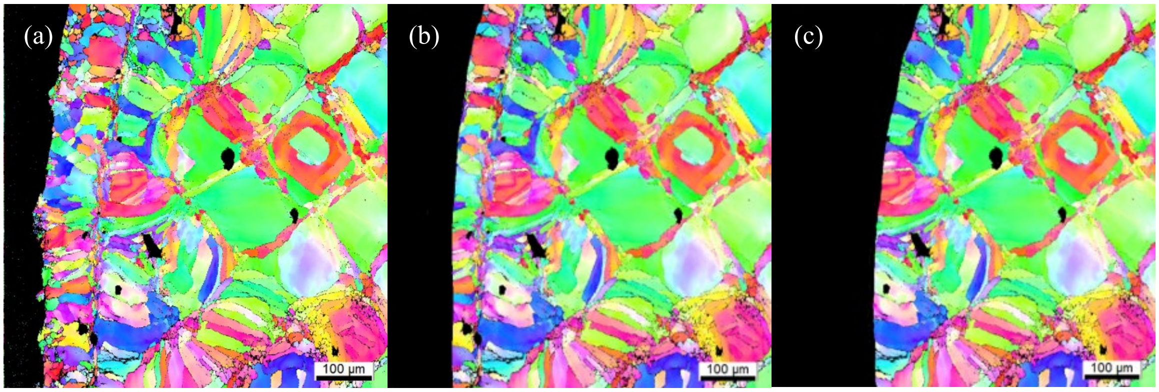

Figure 3.2. EBSD images showing cross sections of the as-built sample microstructure (a) and depictions of sample cross sections with surface removal (b), and with contour removal (c). In (a) the entire contour zone is intact, (b) depicts the removal of approximately 75 µm with the contour zone partially intact, and (c) the entire contour zone is depicted as removed.

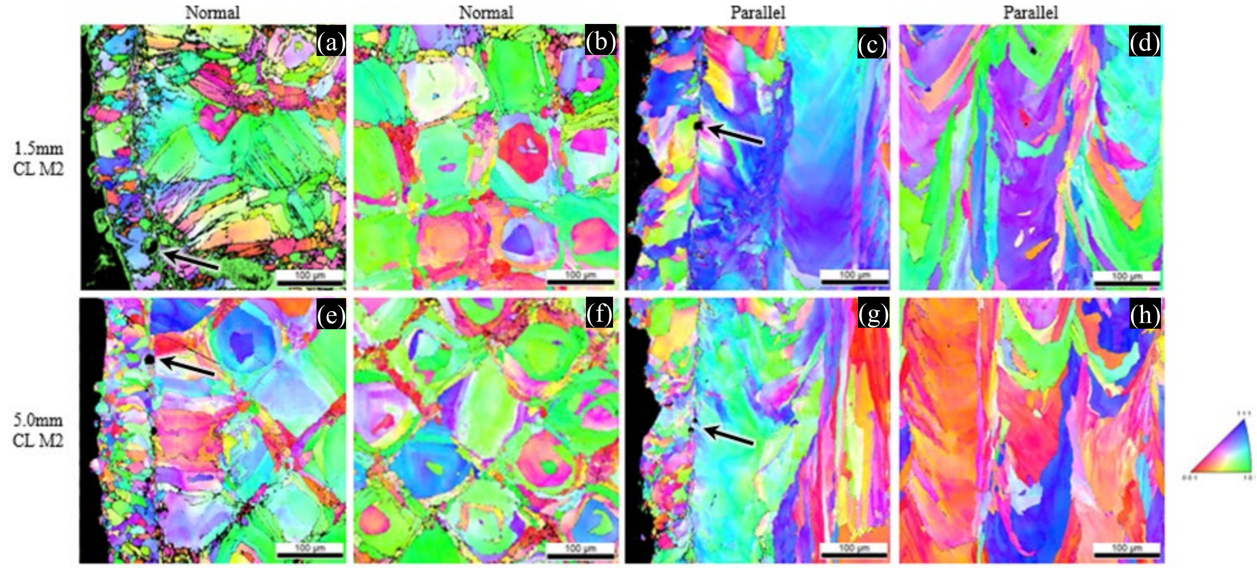

Figure 3.3. Inverse pole figure (IPF) maps generated via EBSD indicating the microstructure present in the (a-d) 1.5mm CL M2 and (e-h) 5.0mm CL M2 sample groups. Arrows indicate pore-like defects at the intersection of the infill and contour regions.

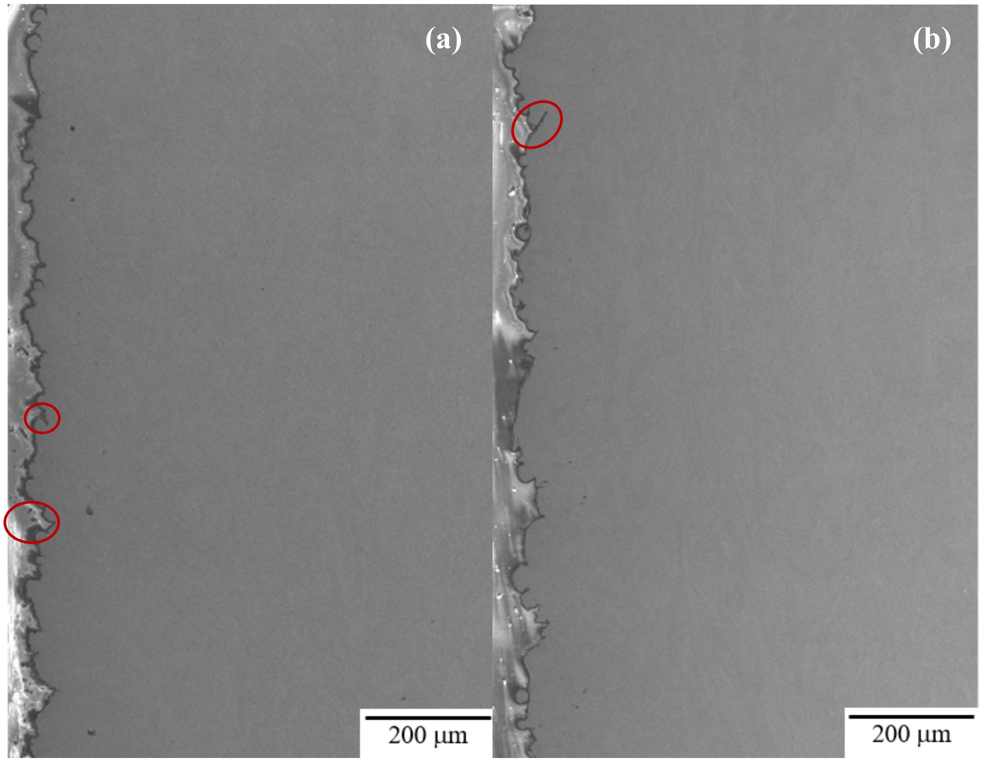

Figure 3.4. SEM profile view, perpendicular to the build direction for the as-built surface roughness in (a) 2.5 mm CL M2 and (b) 5.0 mm CL M2 samples. The red circles indicate the presence of surface crevices that are deeper than the surface roughness measurements shown in Table 5.

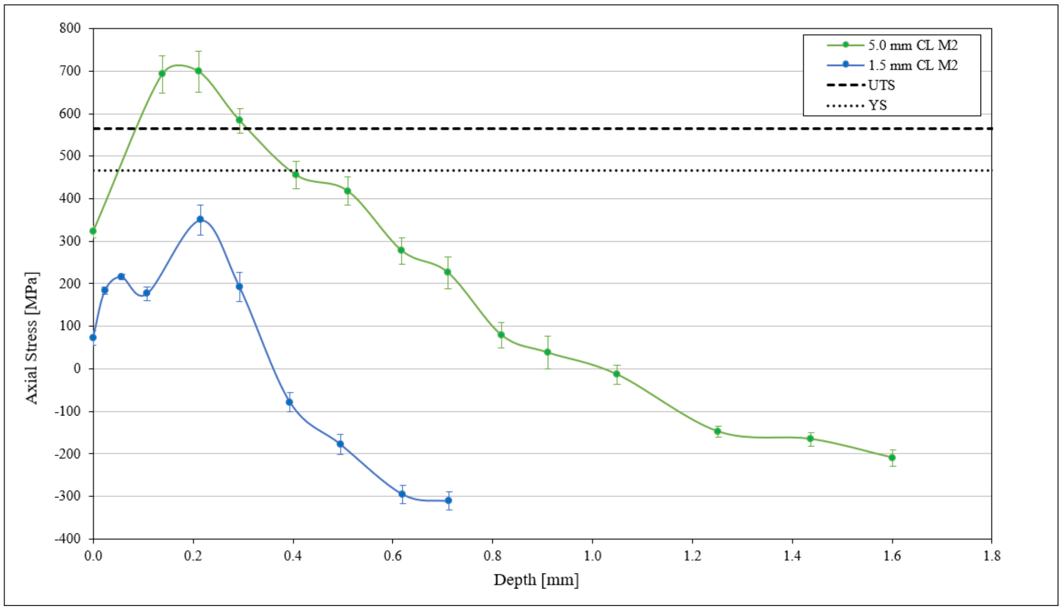

Figure 3.5. Comparison of the axial residual stress depth profile of a 1.5 mm and 5.0 mm as-built CL M2 sample.

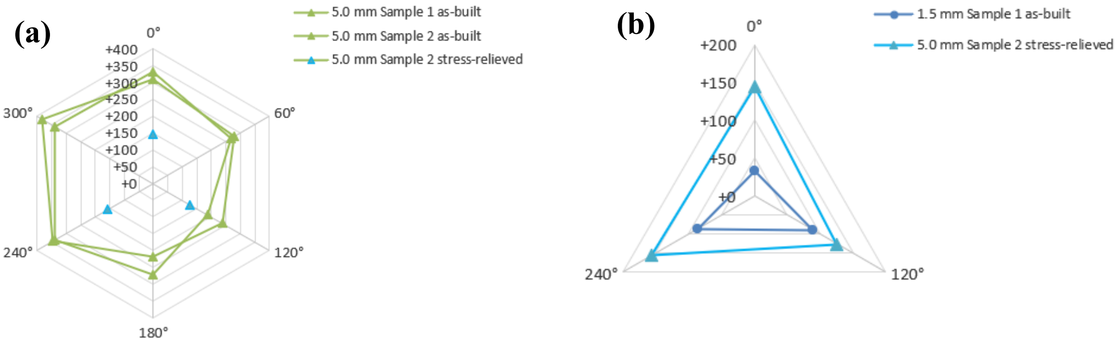

Figure 3.6. (a) Comparison of surface axial residual stress of 5.0 mm as-built and stress-relieved samples. (b) Comparison of 1.5 mm as-built and 5.0 mm stress-relieved samples.

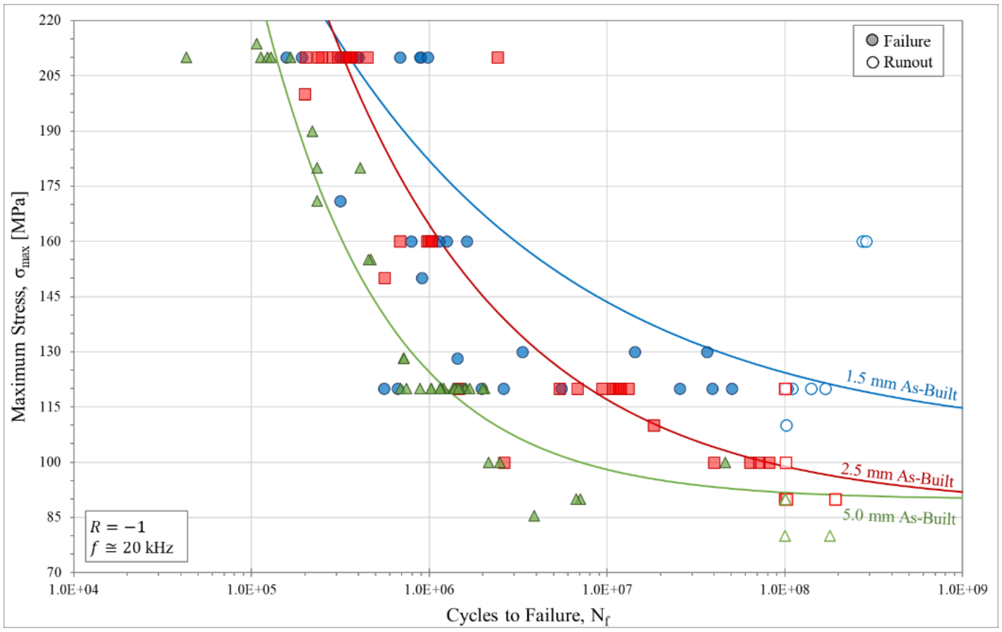

Figure 3.7. Stress-life (S-N) ultrasonic high cycle fatigue curves for all as-built CL M2 samples. Runout samples are indicated by unfilled data icons and are classified as cycling longer than 10^8 cycles without failure. Each set of data is accompanied by a Weibull distribution curve fit determined via random fatigue limit (RFL) analysis.

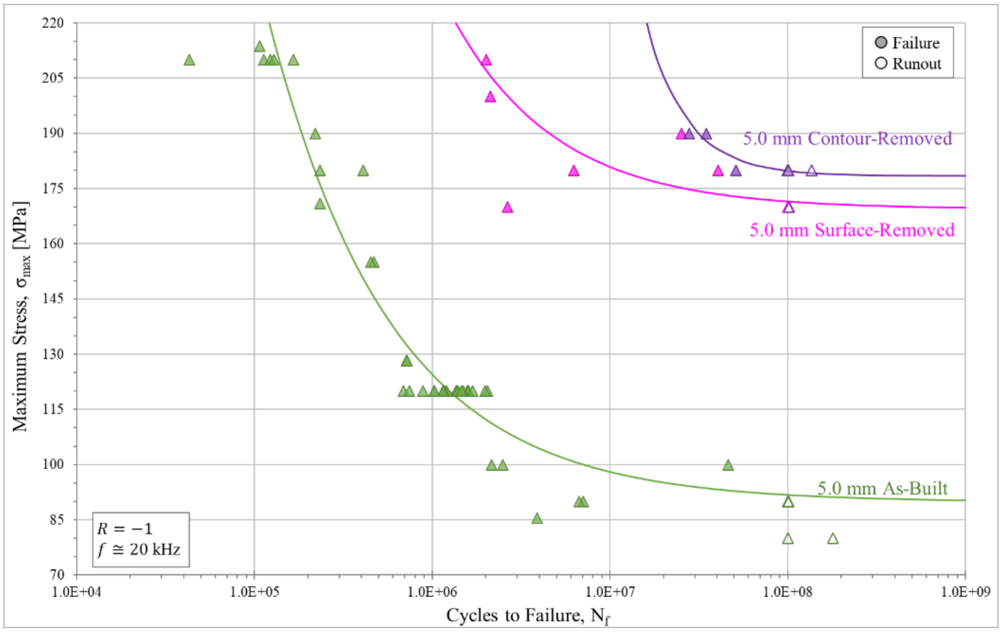

Figure 3.8. Stress-life (S-N) ultrasonic high cycle fatigue curves for surface-removed and contour-removed samples. Samples are shown compared to their 5.0 mm CL M2 as-built counterpart. Runout samples are indicated by unfilled data icons and are classified as cycling longer than 10^8 cycles without failure. Each set of data is accompanied by a curve fit determined via random fatigue limit (RFL) analysis assuming a Weibull distribution.

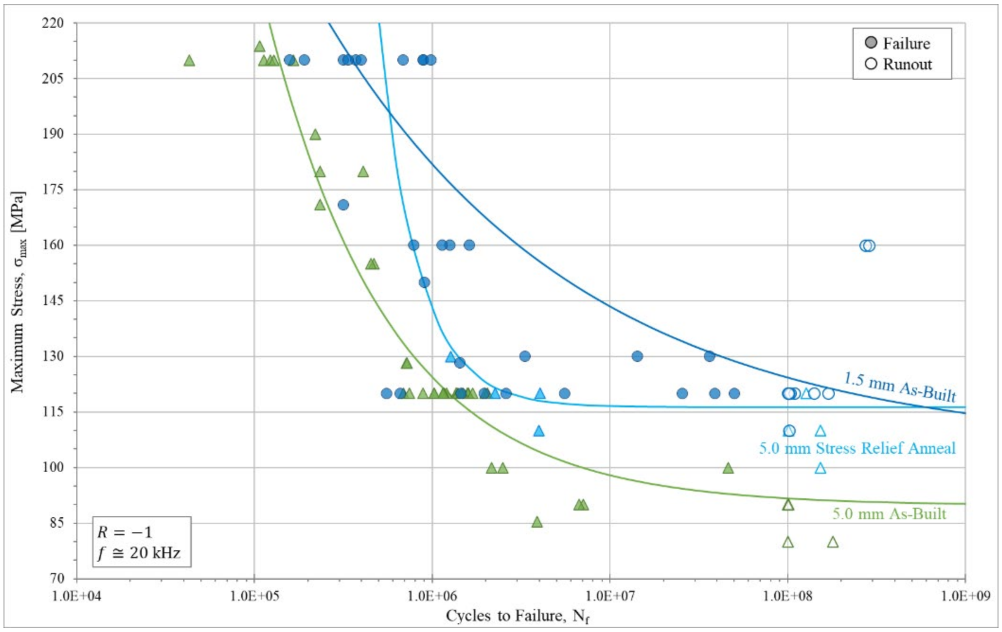

Figure 3.9. Stress-life (S-N) ultrasonic high cycle fatigue curves for as-built samples having undergone a stress-relief heat treatment. All samples are shown compared to their 5.0mm CL M2 as-built counterpart. Runout samples are indicated by unfilled data icons and are classified as cycling longer than 10^8 cycles without failure. Each set of data is accompanied by a curve fit determined via random fatigue limit (RFL) analysis assuming a Weibull distribution.

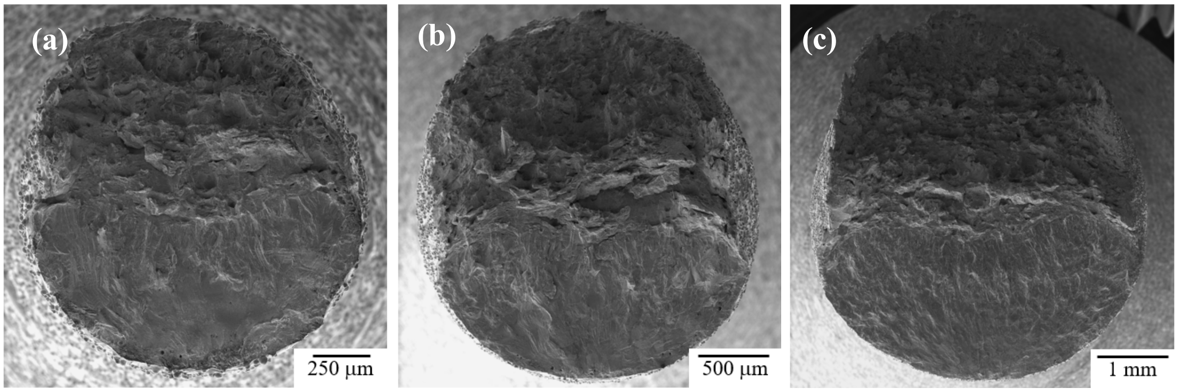

Figure 3.10. Representative ultrasonic fatigue fracture surface fractography for as-built (a) 1.5 mm CL M2, (b) 2.5 mm CL M2, and (c) 5.0 mm CL M2.

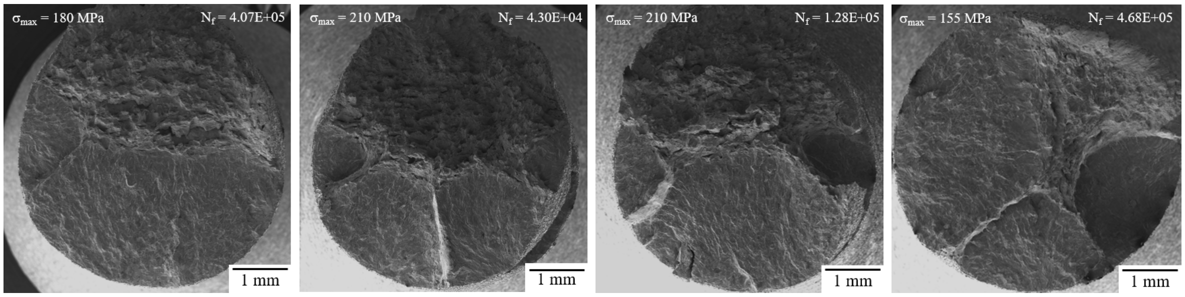

Figure 3.11. Multiple fatigue fracture surfaces found on 5.0 mm as-built high-stress, low-cycle samples.

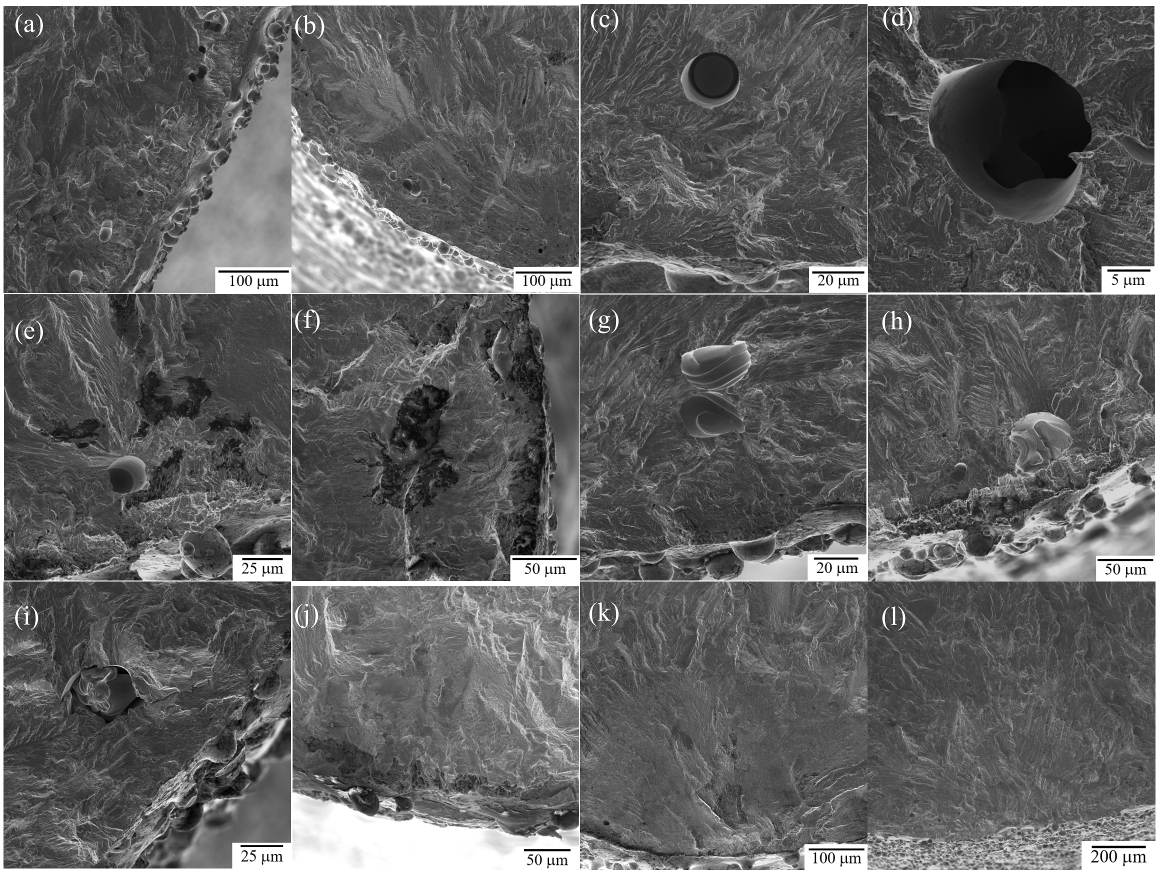

Figure 3.12. Examples of common defects seen on the fracture surface in each sample group. (a-b) increase in defect concentration at contour/infill region of CL M2 samples. (c) – (d) porosity via gas entrapment or keyholing found in CL M2 samples. (e) – (f) discontinuity in composition. (g) – (h) melt pool boundaries. (i) – (j) lack of fusion and irregular melting found in CL M2 samples. (k) – (l) surface initiation from surface crevice.

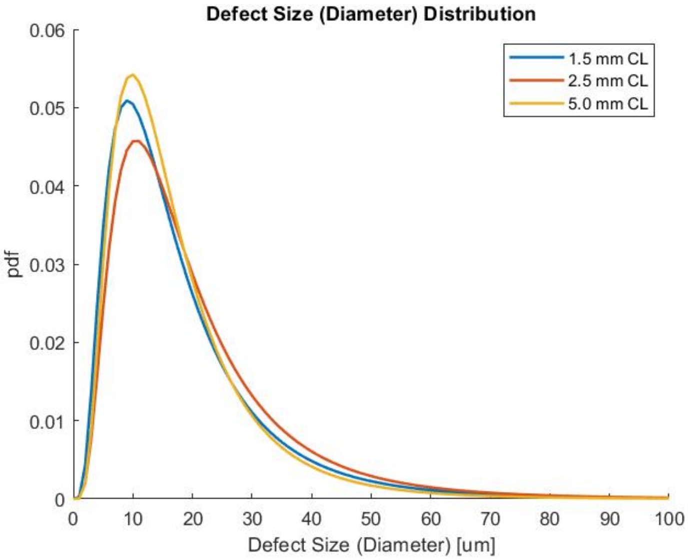

Figure 3.13. Defect size distribution is shown to compare the 1.5 mm, 2.5 mm, and 5.0 mm as-built samples. All defects on the fracture surface are measured. Defect size is quantified as the longest distance across the surface of a defect (diameter).

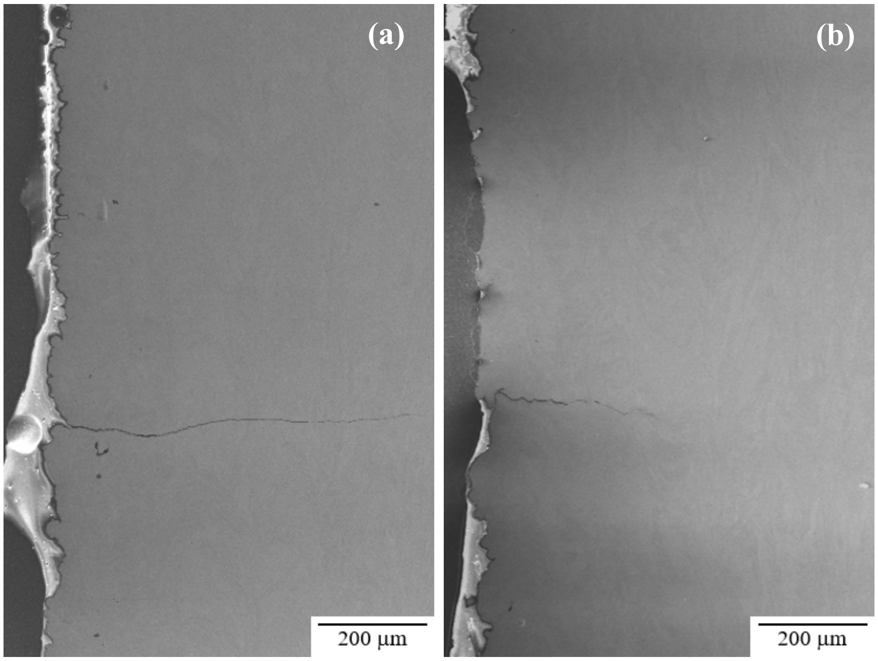

Figure 3.14. Example of crack initiating at surface crevice and propagating during UF testing in (a) 2.5 mm CL M2 and (b) 5.0 mm CL M2.

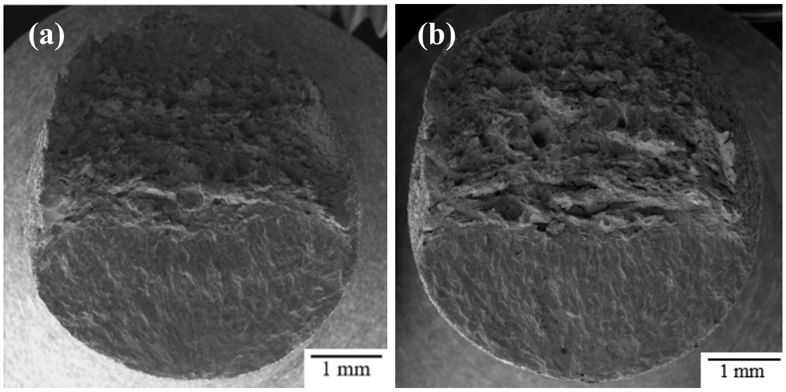

Figure 3.15. Representative ultrasonic fatigue fracture surface fractography for 5.0 mm CL M2 samples (a) as-built and (b) stress-relief heat treated.

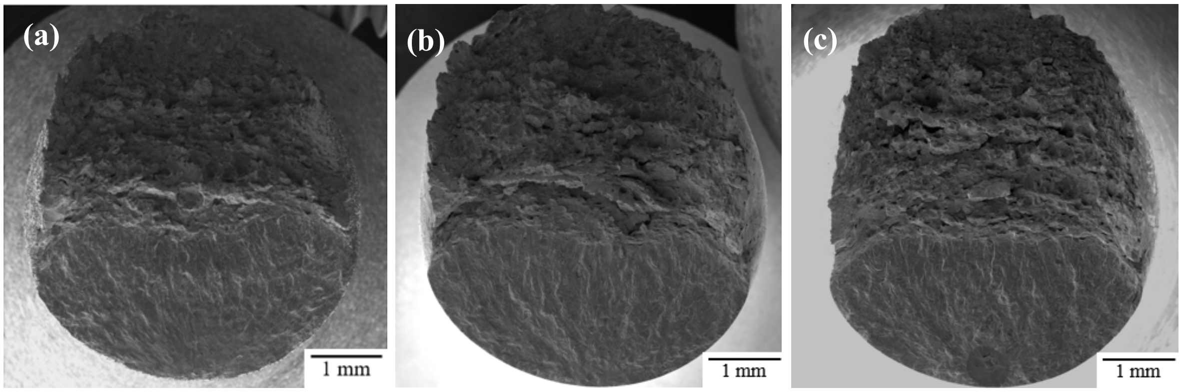

Figure 3.16. Representative ultrasonic fatigue fracture surface fractography for 5.0 mm CL M2 samples (a) as-built, (b) surface removal, and (c) contour removal samples.

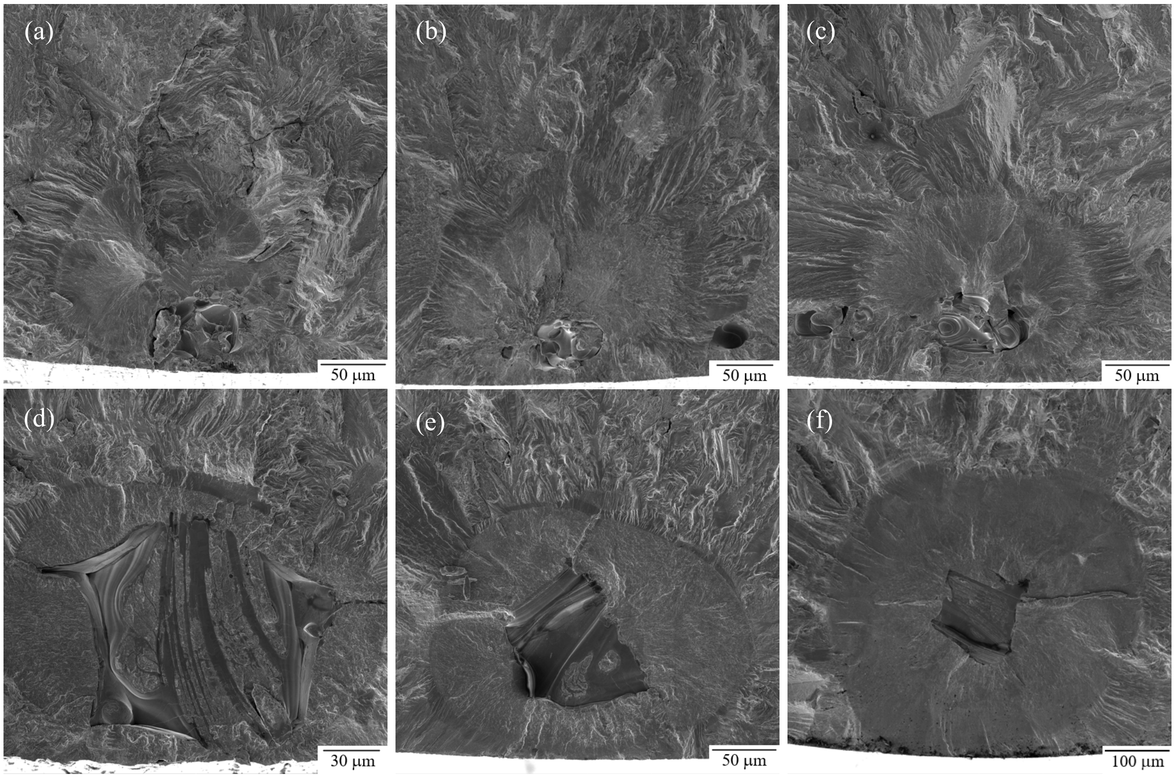

Figure 3.17. Examples of common initiating defects seen in (a-c) surface removal and (d-f) contour removal samples.

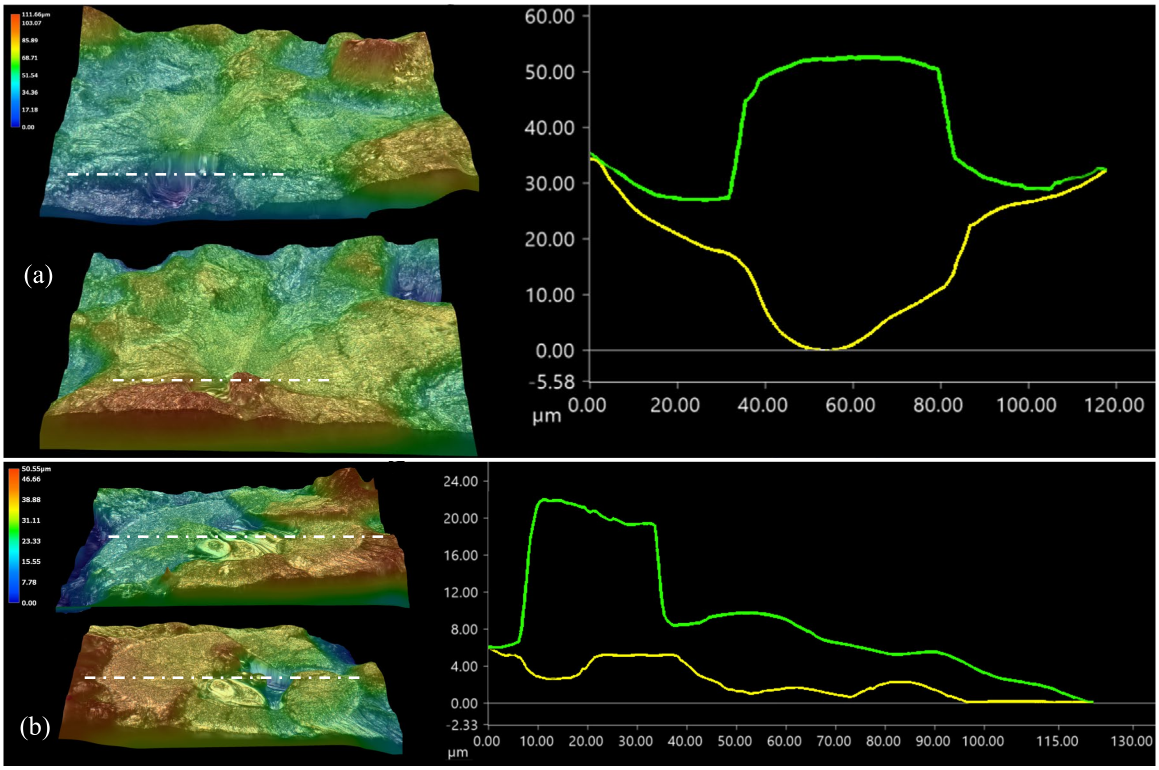

Figure 3.18. 3D topological maps of both matching halves for a fractured (a) surface removal sample and (b) contour removal sample. A cross-sectional profile is taken for each sample at the location indicated by the white dashed line and is plotted to depict the total height of a LOF defect.

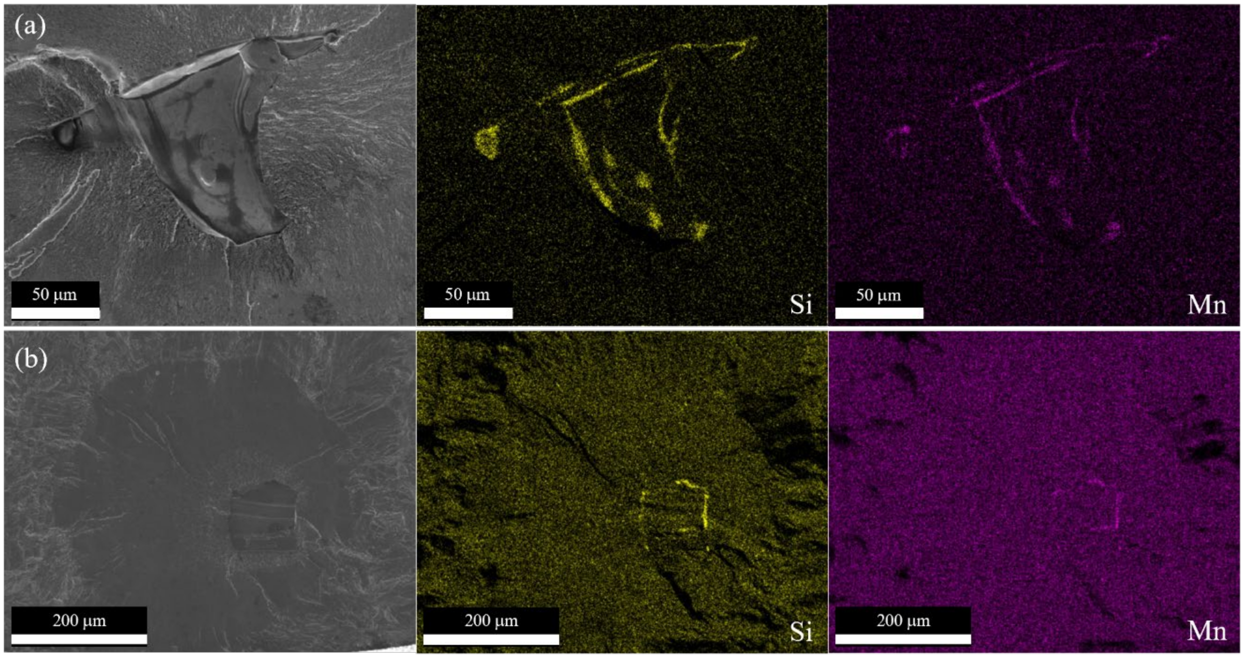

Figure 3.19. LOF structure of initiating defects in contour removal samples. (a) and (b) SEM micrographs of initiating defects with their corresponding Si and Mn EDS elemental maps.

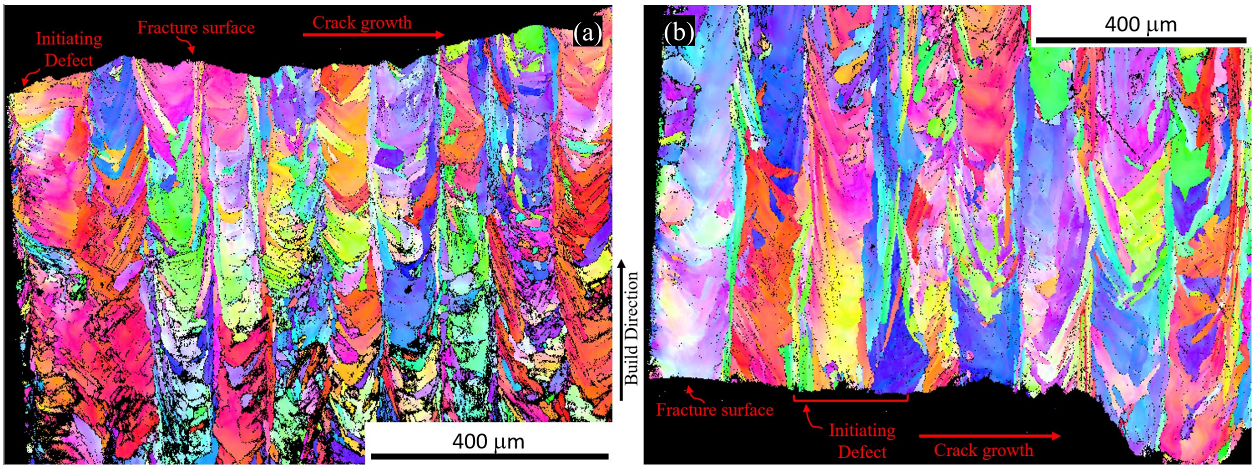

Figure 3.20. EBSD inverse pole figure (IPF) showing the microstructure beneath the initiating defect and fracture surface for (a) surface removal sample, and (b) contour removal sample. The left side of each image shows the sample surface. The surface removal sample shows the contour/infill zone still intact while the contour removal sample shows no evidence of the contour.

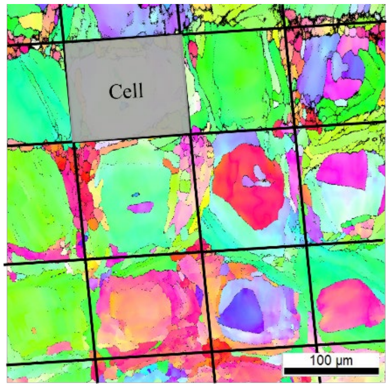

Figure 3.21. Depiction of what constitutes a cell in the microstructural analysis. The size of the cell (width) is used to qualitatively represent microstructural changes in each build.

References

[1] ISO/TC 261, ASTM Committee F42, ISO/ASTM 52900:2017 Additive manufacturing. General principles. Terminology, (2017).

[2] T. DebRoy, H.L. Wei, J.S. Zuback, T. Mukherjee, J.W. Elmer, J.O. Milewski, A.M. Beese, A. Wilson-Heid, A. De, W. Zhang, Additive manufacturing of metallic components – Process, structure and properties, Prog. Mater. Sci. 92 (2018) 112–224. https://doi.org/10.1016/j.pmatsci.2017.10.001.

[3] Y. Murakami, N.N. Yokoyama, J. Nagata, Mechanism of fatigue failure in ultralong life regime: Fatigue failure in ultralong life regime, Fatigue Fract. Eng. Mater. Struct. 25 (2002) 735–746. https://doi.org/10.1046/j.1460-2695.2002.00576.x.

[4] Y. Murakami, T. Nomoto, T. Ueda, Factors influencing the mechanism of superlong fatigue failure in steels: Superlong fatigue failure in steels, Fatigue Fract. Eng. Mater. Struct. 22 (1999) 581–590. https://doi.org/10.1046/j.1460-2695.1999.00187.x.

[5] J. Allison, D. Backman, L. Christodoulou, Integrated computational materials engineering: A new paradigm for the global materials profession, JOM 58 (2006) 25–27.

[6] S.A.H. Motaman, F. Kies, P. Köhnen, M. Létang, M. Lin, A. Molotnikov, C. Haase, Optimal design for metal additive manufacturing: An integrated computational materials engineering (ICME) approach, JOM 72 (2020) 1092–1104. https://doi.org/10.1007/s11837-020-04028-4.

[7] P.-A. Pires, O. Desmaison, M. Megahed, ICME manufacturability assessment in powder bed fusion additive manufacturing, JOM 70 (2018) 1677–1685. https://doi.org/10.1007/s11837-018-3024-8.

[8] D.R. Clymer, J. Cagan, J. Beuth, Power–velocity process design charts for powder bed additive manufacturing, J. Mech. Des. 139 (2017) 100907. https://doi.org/10.1115/1.4037302.

[9] K. Carpenter, A. Tabei, On residual stress development, prevention, and compensation in metal additive manufacturing, Materials 13 (2020) 255. https://doi.org/10.3390/ma13020255.

[10] T. Simson, A. Emmel, A. Dwars, J. Böhm, Residual stress measurements on AISI 316L samples manufactured by selective laser melting, Addit. Manuf. 17 (2017) 183–189. https://doi.org/10.1016/j.addma.2017.07.007.

[11] T. Mukherjee, V. Manvatkar, A. De, T. DebRoy, Mitigation of thermal distortion during additive manufacturing, Scr. Mater. 127 (2017) 79–83. https://doi.org/10.1016/j.scriptamat.2016.09.001.

[12] T. Larimian, M. Kannan, D. Grzesiak, B. AlMangour, T. Borkar, Effect of energy density and scanning strategy on densification, microstructure and mechanical properties of 316L stainless steel processed via selective laser melting, Mater. Sci. Eng. A 770 (2020) 138455. https://doi.org/10.1016/j.msea.2019.138455.

[13] G.R. Buican, G. Oancea, C. Lancea, M.A. Pop, Influence of layer thickness on internal structure of parts manufactured from 316-L steel using SLM technology, Appl. Mech. Mater. 809–810 (2015) 369–374. https://doi.org/10.4028/www.scientific.net/AMM.809-810.369.

[14] O.O. Salman, F. Brenne, T. Niendorf, J. Eckert, K.G. Prashanth, T. He, S. Scudino, Impact of the scanning strategy on the mechanical behavior of 316L steel synthesized by selective

laser melting, J. Manuf. Process. 45 (2019) 255–261. https://doi.org/10.1016/j.jmapro.2019.07.010.

[15] T. Kurzynowski, K. Gruber, W. Stopyra, B. Kuźnicka, E. Chlebus, Correlation between process parameters, microstructure and properties of 316 L stainless steel processed by selective laser melting, Mater. Sci. Eng. A 718 (2018) 64–73. https://doi.org/10.1016/j.msea.2018.01.103.

[16] A.K. Agrawal, G. Meric de Bellefon, D. Thoma, High-throughput experimentation for microstructural design in additively manufactured 316L stainless steel, Mater. Sci. Eng. A 793 (2020) 139841. https://doi.org/10.1016/j.msea.2020.139841.

[17] Y. Deng, Z. Mao, N. Yang, X. Niu, X. Lu, Collaborative optimization of density and surface roughness of 316L stainless steel in selective laser melting, Materials 13 (2020) 1601. https://doi.org/10.3390/ma13071601.

[18] D. Gu, Y. Shen, Balling phenomena in direct laser sintering of stainless steel powder: Metallurgical mechanisms and control methods, Mater. Des. 30 (2009) 2903–2910. https://doi.org/10.1016/j.matdes.2009.01.013.

[19] G.B. Bang, W.R. Kim, H.K. Kim, H.-K. Park, G.H. Kim, S.-K. Hyun, O. Kwon, H.G. Kim, Effect of process parameters for selective laser melting with SUS316L on mechanical and microstructural properties with variation in chemical composition, Mater. Des. 197 (2021) 109221. https://doi.org/10.1016/j.matdes.2020.109221.

[20] A. Röttger, K. Geenen, M. Windmann, F. Binner, W. Theisen, Comparison of microstructure and mechanical properties of 316 L austenitic steel processed by selective laser melting with hot-isostatic pressed and cast material, Mater. Sci. Eng. A 678 (2016) 365–376. https://doi.org/10.1016/j.msea.2016.10.012.

[21] O. Andreau, E. Pessard, I. Koutiri, J.-D. Penot, C. Dupuy, N. Saintier, P. Peyre, A competition between the contour and hatching zones on the high cycle fatigue behaviour of a 316L stainless steel: Analyzed using X-ray computed tomography, Mater. Sci. Eng. A 757 (2019) 146–159. https://doi.org/10.1016/j.msea.2019.04.101.

[22] G. Wang, Q. Liu, H. Rao, H. Liu, C. Qiu, Influence of porosity and microstructure on mechanical and corrosion properties of a selectively laser melted stainless steel, J. Alloys Compd. 831 (2020) 154815. https://doi.org/10.1016/j.jallcom.2020.154815.

[23] W.M. Tucho, V.H. Lysne, H. Austbø, A. Sjolyst-Kverneland, V. Hansen, Investigation of effects of process parameters on microstructure and hardness of SLM manufactured SS316L, J. Alloys Compd. 740 (2018) 910–925. https://doi.org/10.1016/j.jallcom.2018.01.098.

[24] R. Cunningham, S.P. Narra, C. Montgomery, J. Beuth, A.D. Rollett, Synchrotron-based X-ray microtomography characterization of the effect of processing variables on porosity formation in laser power-bed additive manufacturing of Ti-6Al-4V, JOM 69 (2017) 479–484. https://doi.org/10.1007/s11837-016-2234-1.

[25] R. Cunningham, C. Zhao, N. Parab, C. Kantzos, J. Pauza, K. Fezzaa, T. Sun, A.D. Rollett, Keyhole threshold and morphology in laser melting revealed by ultrahigh-speed x-ray imaging, Science 363 (2019) 849–852. https://doi.org/10.1126/science.aav4687.

[26] T. Niendorf, S. Leuders, A. Riemer, H.A. Richard, T. Tröster, D. Schwarze, Highly anisotropic steel processed by selective laser melting, Metall. Mater. Trans. B 44 (2013) 794–796. https://doi.org/10.1007/s11663-013-9875-z.

[27] J. Gockel, L. Sheridan, B. Koerper, B. Whip, The influence of additive manufacturing processing parameters on surface roughness and fatigue life, Int. J. Fatigue 124 (2019) 380–388. https://doi.org/10.1016/j.ijfatigue.2019.03.025.

[28] J.V. Gordon, S.P. Narra, R.W. Cunningham, H. Liu, H. Chen, R.M. Suter, J.L. Beuth, A.D. Rollett, Defect structure process maps for laser powder bed fusion additive manufacturing, Addit. Manuf. 36 (2020) 101552. https://doi.org/10.1016/j.addma.2020.101552.

[29] G.T. Gray, V. Livescu, P.A. Rigg, C.P. Trujillo, C.M. Cady, S.R. Chen, J.S. Carpenter, T.J. Lienert, S.J. Fensin, Structure/property (constitutive and spallation response) of additively manufactured 316L stainless steel, Acta Mater. 138 (2017) 140–149. https://doi.org/10.1016/j.actamat.2017.07.045.

[30] P. Hanzl, M. Zetek, T. Bakša, T. Kroupa, The influence of processing parameters on the mechanical properties of SLM parts, Procedia Eng. 100 (2015) 1405–1413. https://doi.org/10.1016/j.proeng.2015.01.510.

[31] C. Herriott, X. Li, N. Kouraytem, V. Tari, W. Tan, B. Anglin, A.D. Rollett, A.D. Spear, A multi-scale, multi-physics modeling framework to predict spatial variation of properties in additive-manufactured metals, Model. Simul. Mater. Sci. Eng. 27 (2019) 025009. https://doi.org/10.1088/1361-651X/aaf753.

[32] J.M. Jeon, J.M. Park, J.-H. Yu, J.G. Kim, Y. Seong, S.H. Park, H.S. Kim, Effects of microstructure and internal defects on mechanical anisotropy and asymmetry of selective laser-melted 316L austenitic stainless steel, Mater. Sci. Eng. A 763 (2019) 138152. https://doi.org/10.1016/j.msea.2019.138152.

[33] J. Liu, Y. Song, C. Chen, X. Wang, H. Li, C. Zhou, J. Wang, K. Guo, J. Sun, Effect of scanning speed on the microstructure and mechanical behavior of 316L stainless steel fabricated by selective laser melting, Mater. Des. 186 (2020) 108355. https://doi.org/10.1016/j.matdes.2019.108355.

[34] K. Lin, D. Gu, L. Xi, L. Yuan, S. Niu, P. Lv, Q. Ge, Selective laser melting processing of 316L stainless steel: effect of microstructural differences along building direction on corrosion behavior, Int. J. Adv. Manuf. Technol. 104 (2019) 2669–2679. https://doi.org/10.1007/s00170-019-04136-9.

[35] E. Liverani, S. Toschi, L. Ceschini, A. Fortunato, Effect of selective laser melting (SLM) process parameters on microstructure and mechanical properties of 316L austenitic stainless steel, J. Mater. Process. Technol. 249 (2017) 255–263. https://doi.org/10.1016/j.jmatprotec.2017.05.042.

[36] A. Damiens, H. Bonnefoy, I. Titeux, Influence of processing parameters on mechanical and fatigue properties of 316 L steel manufactured by selective laser melting, Weld. World 64 (2020) 1321–1328. https://doi.org/10.1007/s40194-020-00885-4.

[37] S. Hatami, T. Ma, T. Vuoristo, J. Bertilsson, O. Lyckfeldt, Fatigue strength of 316 L stainless steel manufactured by selective laser melting, J. Mater. Eng. Perform. 29 (2020) 3183–3194. https://doi.org/10.1007/s11665-020-04859-x.

[38] P. Kumar, R. Jayaraj, J. Suryawanshi, U.R. Satwik, J. McKinnell, U. Ramamurty, Fatigue strength of additively manufactured 316L austenitic stainless steel, Acta Mater. 199 (2020) 225–239. https://doi.org/10.1016/j.actamat.2020.08.033.

[39] S. Leuders, T. Lieneke, S. Lammers, T. Tröster, T. Niendorf, On the fatigue properties of metals manufactured by selective laser melting – The role of ductility, J. Mater. Res. 29 (2014) 1911–1919. https://doi.org/10.1557/jmr.2014.157.

[40] T.M. Mower, M.J. Long, Mechanical behavior of additive manufactured, powder-bed laser-fused materials, Mater. Sci. Eng. A 651 (2016) 198–213. https://doi.org/10.1016/j.msea.2015.10.068.
[41] A. Polishetty, G. Littlefair, Heat treatment effect on the fatigue characteristics of additive manufactured stainless steel 316L, Int. J. Mater. Mech. Manuf. 7 (2019) 114–118. https://doi.org/10.18178/ijmmm.2019.7.2.442.
[42] A. Riemer, S. Leuders, M. Thöne, H.A. Richard, T. Tröster, T. Niendorf, On the fatigue crack growth behavior in 316L stainless steel manufactured by selective laser melting, Eng. Fract. Mech. 120 (2014) 15–25. https://doi.org/10.1016/j.engfracmech.2014.03.008.
[43] R. Shrestha, J. Simsiriwong, N. Shamsaei, Fatigue behavior of additive manufactured 316L stainless steel parts: Effects of layer orientation and surface roughness, Addit. Manuf. 28 (2019) 23–38. https://doi.org/10.1016/j.addma.2019.04.011.
[44] A.B. Spierings, T.L. Starr, K. Wegener, Fatigue performance of additive manufactured metallic parts, Rapid Prototyp. J. 19 (2013) 88–94. https://doi.org/10.1108/13552541311302932.
[45] F. Stern, J. Kleinhorst, J. Tenkamp, F. Walther, Investigation of the anisotropic cyclic damage behavior of selective laser melted AISI 316L stainless steel, Fatigue Fract. Eng. Mater. Struct. 42 (2019) 2422–2430. https://doi.org/10.1111/ffe.13029.
[46] M. Zhang, C.-N. Sun, X. Zhang, P.C. Goh, J. Wei, D. Hardacre, H. Li, Fatigue and fracture behaviour of laser powder bed fusion stainless steel 316L: Influence of processing parameters, Mater. Sci. Eng. A 703 (2017) 251–261. https://doi.org/10.1016/j.msea.2017.07.071.
[47] M. Zhang, C.-N. Sun, X. Zhang, J. Wei, D. Hardacre, H. Li, Predictive models for fatigue property of laser powder bed fusion stainless steel 316L, Mater. Des. 145 (2018) 42–54. https://doi.org/10.1016/j.matdes.2018.02.054.
[48] M. Zhang, C.-N. Sun, X. Zhang, J. Wei, D. Hardacre, H. Li, High cycle fatigue and ratcheting interaction of laser powder bed fusion stainless steel 316L: Fracture behaviour and stress-based modelling, Int. J. Fatigue 121 (2019) 252–264. https://doi.org/10.1016/j.ijfatigue.2018.12.016.
[49] H. Javadi, W. Jomaa, D. Texier, M. Brochu, P. Bocher, Surface roughness effects on the fatigue behavior of as-machined Inconel 718, Solid State Phenom. 258 (2016) 306–309. https://doi.org/10.4028/www.scientific.net/SSP.258.306.
[50] D. Wu, D. Zhang, C. Yao, Effect of turning and surface polishing treatments on surface integrity and fatigue performance of nickel-based alloy GH4169, Metals 8 (2018) 549. https://doi.org/10.3390/met8070549.
[51] Y. Murakami, Metal Fatigue: Effects of Small Defects and Nonmetallic Inclusions, Second, Elsevier, 2019.
[52] Y. Murakami, M. Endo, Effects of defects, inclusions and inhomogeneities on fatigue strength, Int. J. Fatigue 16 (1994) 163–182. https://doi.org/10.1016/0142-1123(94)90001-9.
[53] E.J. Czyryca, ASM Committee on Fatigue Crack Propagation, R.P. Gangloff, eds., Fatigue Testing, in: Met. Handb. Mech. Test., 9th ed., American Society for Metals, Metals Park, Ohio 44073, 1985: pp. 361–436.
[54] A.S. Wu, D.W. Brown, M. Kumar, G.F. Gallegos, W.E. King, An experimental investigation into additive manufacturing-induced residual stresses in 316L stainless steel, Metall. Mater. Trans. A 45 (2014) 6260–6270. https://doi.org/10.1007/s11661-014-2549-x.

[55] J.P. Oliveira, A.D. LaLonde, J. Ma, Processing parameters in laser powder bed fusion metal additive manufacturing, Mater. Des. 193 (2020) 108762. https://doi.org/10.1016/j.matdes.2020.108762.

[56] M. Sprengel, A. Ulbricht, A. Evans, A. Kromm, K. Sommer, T. Werner, J. Kelleher, G. Bruno, T. Kannengiesser, Towards the optimization of post-laser powder bed fusion stress-relieve treatments of stainless steel 316L, Metall. Mater. Trans. A 52 (2021) 5342–5356. https://doi.org/10.1007/s11661-021-06472-6.

[57] C. Li, Z.Y. Liu, X.Y. Fang, Y.B. Guo, Residual stress in metal additive manufacturing, Procedia CIRP 71 (2018) 348–353. https://doi.org/10.1016/j.procir.2018.05.039.

[58] L. van Belle, G. Vansteenkiste, J.C. Boyer, Investigation of residual stresses induced during the selective laser melting process, Key Eng. Mater. 554–557 (2013) 1828–1834. https://doi.org/10.4028/www.scientific.net/KEM.554-557.1828.

[59] Y. Liu, Y. Yang, D. Wang, A study on the residual stress during selective laser melting (SLM) of metallic powder, Int. J. Adv. Manuf. Technol. 87 (2016) 647–656. https://doi.org/10.1007/s00170-016-8466-y.

[60] P. Mercelis, J. Kruth, Residual stresses in selective laser sintering and selective laser melting, Rapid Prototyp. J. 12 (2006) 254–265. https://doi.org/10.1108/13552540610707013.

[61] B. Cheng, S. Shrestha, K. Chou, Stress and deformation evaluations of scanning strategy effect in selective laser melting, Addit. Manuf. 12 (2016) 240–251. https://doi.org/10.1016/j.addma.2016.05.007.

[62] J.L. Bartlett, X. Li, An overview of residual stresses in metal powder bed fusion, Addit. Manuf. 27 (2019) 131–149. https://doi.org/10.1016/j.addma.2019.02.020.

[63] Z.-C. Fang, Z.-L. Wu, C.-G. Huang, C.-W. Wu, Review on residual stress in selective laser melting additive manufacturing of alloy parts, Opt. Laser Technol. 129 (2020) 106283. https://doi.org/10.1016/j.optlastec.2020.106283.

[64] W. Chen, T. Voisin, Y. Zhang, J.-B. Florien, C.M. Spadaccini, D.L. McDowell, T. Zhu, Y.M. Wang, Microscale residual stresses in additively manufactured stainless steel, Nat. Commun. 10 (2019) 4338. https://doi.org/10.1038/s41467-019-12265-8.

[65] A. Carpinteri, A. Spagnoli, S. Vantadori, An approach to size effect in fatigue of metals using fractal theories, Fatigue Fract. Eng. Mater. Struct. 25 (2002) 619–627. https://doi.org/10.1046/j.1460-2695.2002.00506.x.

[66] D.S. Paolino, A. Tridello, G. Chiandussi, M. Rossetto, On specimen design for size effect evaluation in ultrasonic gigacycle fatigue testing: Specimen for size effect in gigafatigue, Fatigue Fract. Eng. Mater. Struct. 37 (2014) 570–579. https://doi.org/10.1111/ffe.12149.

[67] G. Qian, W.-S. Lei, A statistical model of fatigue failure incorporating effects of specimen size and load amplitude on fatigue life, Philos. Mag. 99 (2019) 2089–2125. https://doi.org/10.1080/14786435.2019.1609707.

[68] A. Tridello, C.B. Niutta, F. Berto, D.S. Paolino, Size-effect in very high cycle fatigue: A review, Int. J. Fatigue 153 (2021) 106462. https://doi.org/10.1016/j.ijfatigue.2021.106462.

[69] P. Wang, M.H. Goh, Q. Li, M.L.S. Nai, J. Wei, Effect of defects and specimen size with rectangular cross-section on the tensile properties of additively manufactured components, Virtual Phys. Prototyp. 15 (2020) 251–264. https://doi.org/10.1080/17452759.2020.1733430.

[70] W. Weibull, A statistical theory of the strength of materials, Swed. R. Inst. Eng. Res. (1939).

[71] M. Muniz-Calvente, A.M.P. de Jesus, J.A.F.O. Correia, A. Fernández-Canteli, A methodology for probabilistic prediction of fatigue crack initiation taking into account the scale effect, Eng. Fract. Mech. 185 (2017) 101–113. https://doi.org/10.1016/j.engfracmech.2017.04.014.

[72] E. Castillo, A. Fernandez-Canteli, A Unified Statistical Methodology for Modeling Fatigue Damage, Springer, 2009.

[73] W.D. Callister Jr, D.G. Rethwisch, Failure, in: Mater. Sci. Eng. Introd., 9th ed., Wiley, 2014: pp. 251–296.

[74] C.C. Engler-Pinto Jr, J.V. Lasecki, R.J. Frisch Sr, M.A. Dejack, J.E. Allison, Statistical approaches applied to fatigue test data analysis, in: SAE 2005 World Congr. Exhib., SAE, 2005: pp. 2005-01–0802. https://doi.org/10.4271/2005-01-0802.

[75] C.C. Engler-Pinto Jr, J.V. Lasecki, R.J. Frisch Sr, J.E. Allison, Statistical approaches applied to very high cycle fatigue, in: VHCF4, TMS, 2007: pp. 369–376.

[76] Y. Murakami, T. Nomoto, T. Ueda, Y. Murakami, On the mechanism of fatigue failure in the superlong life regime (N>10^7 cycles). Part 1: influence of hydrogen trapped by inclusions, Fatigue Fract. Eng. Mater. Struct. 23 (2000) 893–902. https://doi.org/10.1046/j.1460-2695.2000.00328.x.

[77] Y. Murakami, T. Nomoto, T. Ueda, Y. Murakami, On the mechanism of fatigue failure in the superlong life regime (N>10^7 cycles). Part II: influence of hydrogen trapped by inclusions, Fatigue Fract. Eng. Mater. Struct. 23 (2000) 903–910. https://doi.org/10.1046/j.1460-2695.2000.00343.x.

[78] L.D. Roth, ed., High Strain Rate Testing - Ultrasonic Fatigue Testing, in: Met. Handb. Mech. Test., 9th ed., American Society for Metals, Metals Park, Ohio 44073, 1985: pp. 240–258.

[79] Institute of Physics and Materials Science, BOKU, Vienna, Ultrasonic Fatigue Testing Equipment, (2009).

[80] M. Fitzka, B.M. Schönbauer, R.K. Rhein, N. Sanaei, S. Zekriardehani, S.A. Tekalur, J.W. Carroll, H. Mayer, Usability of ultrasonic frequency testing for rapid generation of high and very high cycle fatigue data, Materials 14 (2021) 2245. https://doi.org/10.3390/ma14092245.

[81] ASTM International, F3184-16 Standard specification for additive manufacturing stainless steel alloy (UNS S31603) with powder bed fusion, (2023).

[82] American Iron and Steel Institute, Specialty Steel Institute of North America, Specialty Steel Industry of the United States, Nickel Development Institute (Canada), Design guidelines for the selection and use of stainless steel, Specialty Steel Industry of the United States, Pennsylvania State University, 1993.

[83] P.D. Harvey, ed., Stainless and Heat-Resisting Steels, in: Eng. Prop. Steel, American Society for Metals, Metals Park, Ohio 44073, 1999.

[84] F.G. Pascual, W.Q. Meeker, Estimating fatigue curves with the random fatigue-limit model, Technometrics 41 (1999) 277–289. https://doi.org/10.1080/00401706.1999.10485925.

[85] O.H. Basquin, The exponential law of endurance tests, in: ASTM Proc., 1910: pp. 625–630.

[86] Q. Chao, S. Thomas, N. Birbilis, P. Cizek, P.D. Hodgson, D. Fabijanic, The effect of post-processing heat treatment on the microstructure, residual stress and mechanical properties of selective laser melted 316L stainless steel, Mater. Sci. Eng. A 821 (2021) 141611. https://doi.org/10.1016/j.msea.2021.141611.

[87] V. Cruz, Q. Chao, N. Birbilis, D. Fabijanic, P.D. Hodgson, S. Thomas, Electrochemical studies on the effect of residual stress on the corrosion of 316L manufactured by selective laser melting, Corros. Sci. 164 (2020) 108314. https://doi.org/10.1016/j.corsci.2019.108314.

[88] O. Fergani, A. Bratli Wold, F. Berto, V. Brotan, M. Bambach, Study of the effect of heat treatment on fatigue crack growth behaviour of 316L stainless steel produced by selective laser melting, Fatigue Fract. Eng. Mater. Struct. 41 (2018) 1102–1119. https://doi.org/10.1111/ffe.12755.

[89] B. Blinn, F. Krebs, M. Ley, R. Teutsch, T. Beck, Determination of the influence of a stress-relief heat treatment and additively manufactured surface on the fatigue behavior of selectively laser melted AISI 316L by using efficient short-time procedures, Int. J. Fatigue 131 (2020) 105301. https://doi.org/10.1016/j.ijfatigue.2019.105301.

[90] D.J. Rowenhorst, L. Nguyen, A.D. Murphy-Leonard, R.W. Fonda, Characterization of microstructure in additively manufactured 316L using automated serial sectioning, Curr. Opin. Solid State Mater. Sci. 24 (2020) 100819. https://doi.org/10.1016/j.cossms.2020.100819.

[91] N. Sanaei, A. Fatemi, Phan, Defect characteristics and analysis of their variability in metal L-PBF additive manufacturing, Mater. Des. (2019). https://doi.org/10.1016/j.matdes.2019.108091.

[92] N. Sanaei, A. Fatemi, Defects in additive manufactured metals and their effect on fatigue performance: A state-of-the-art review, Prog. Mater. Sci. 117 (2021) 100724. https://doi.org/10.1016/j.pmatsci.2020.100724.

[93] A.E. Wilson-Heid, T.C. Novak, A.M. Beese, Characterization of the effects of internal pores on tensile properties of additively manufactured austenitic stainless steel 316L, Exp. Mech. 59 (2019) 793–804. https://doi.org/10.1007/s11340-018-00465-0.

[94] H. Yao, R. Katona, J. Zhou, M.I. Islam, J. Raush, F. Lu, S. Guo, Defects evaluation of selective laser melting stainless steel 316 parts using positron annihilation lifetime measurement, in: Vol. 8B Heat Transf. Therm. Eng., American Society of Mechanical Engineers, Pittsburgh, Pennsylvania, USA, 2018: p. V08BT10A057. https://doi.org/10.1115/IMECE2018-86729.

[95] A.A. Martin, N.P. Calta, S.A. Khairallah, J. Wang, P.J. Depond, A.Y. Fong, V. Thampy, G.M. Guss, A.M. Kiss, K.H. Stone, C.J. Tassone, J. Nelson Weker, M.F. Toney, T. van Buuren, M.J. Matthews, Dynamics of pore formation during laser powder bed fusion additive manufacturing, Nat. Commun. 10 (2019) 1987. https://doi.org/10.1038/s41467-019-10009-2.

[96] Z. Wu, D. Basu, J.L.L. Meyer, E. Larson, R. Kuo, J. Beuth, A. Rollett, Study of powder gas entrapment and its effects on porosity in 17-4 PH stainless steel parts fabricated in laser powder bed fusion, JOM 73 (2021) 177–188. https://doi.org/10.1007/s11837-020-04491-z.

[97] A. du Plessis, I. Yadroitsava, I. Yadroitsev, Effects of defects on mechanical properties in metal additive manufacturing: A review focusing on X-ray tomography insights, Mater. Des. (2019). https://doi.org/10.1016/j.matdes.2019.108385.

[98] N. Kouraytem, X. Li, R. Cunningham, C. Zhao, N. Parab, T. Sun, A.D. Rollett, A.D. Spear, W. Tan, Effect of laser-matter interaction on molten pool flow and keyhole dynamics, Phys. Rev. Appl. 11 (2019) 064054. https://doi.org/10.1103/PhysRevApplied.11.064054.

[99] C. Zhao, N.D. Parab, X. Li, K. Fezzaa, W. Tan, A.D. Rollett, T. Sun, Critical instability at moving keyhole tip generates porosity in laser melting, Science 370 (2020) 1080–1086. https://doi.org/10.1126/science.abd1587.

[100] J. Ning, D.E. Sievers, H. Garmestani, S.Y. Liang, Analytical modeling of part porosity in metal additive manufacturing, Int. J. Mech. Sci. 172 (2020) 105428. https://doi.org/10.1016/j.ijmecsci.2020.105428.

[101] C. Gu, W. Liu, J. Lian, Y. Bao, In-depth analysis of the fatigue mechanism induced by inclusions for high-strength bearing steels, Int. J. Miner. Metall. Mater. (2021). https://doi.org/10.1007/s12613-020-2223-9.

[102] D. Wang, S. Wu, F. Fu, S. Mai, Y. Yang, Y. Liu, C. Song, Mechanisms and characteristics of spatter generation in SLM processing and its effect on the properties, Mater. Des. 117 (2017) 121–130. https://doi.org/10.1016/j.matdes.2016.12.060.

[103] S.A. Khairallah, A.T. Anderson, A. Rubenchik, W.E. King, Laser powder-bed fusion additive manufacturing: Physics of complex melt flow and formation mechanisms of pores, spatter, and denudation zones, Acta Mater. 108 (2016) 36–45. https://doi.org/10.1016/j.actamat.2016.02.014.

[104] F.C. Pinto, I.R. Souza Filho, M.J.R. Sandim, H.R.Z. Sandim, Defects in parts manufactured by selective laser melting caused by δ-ferrite in reused 316L steel powder feedstock, Addit. Manuf. 31 (2020) 100979. https://doi.org/10.1016/j.addma.2019.100979.

[105] S. Stanzl-Tschegg, B. Schönbauer, Near-threshold fatigue crack propagation and internal cracks in steel, Procedia Eng. 2 (2010) 1547–1555. https://doi.org/10.1016/j.proeng.2010.03.167.

[106] M. Laleh, A.E. Hughes, S. Yang, J. Wang, J. Li, A.M. Glenn, W. Xu, M.Y. Tan, A critical insight into lack-of-fusion pore structures in additively manufactured stainless steel, Addit. Manuf. 38 (2021) 101762. https://doi.org/10.1016/j.addma.2020.101762.

[107] C. Lu, R. Zhang, X. Wei, M. Xiao, Y. Yin, Y. Qu, H. Li, P. Liu, X. Qiu, T. Guo, An investigation on the oxidation behavior of spatters generated during the laser powder bed fusion of 316L stainless steel, Appl. Surf. Sci. 586 (2022) 152796. https://doi.org/10.1016/j.apsusc.2022.152796.

Chapter 4 The Influence of Section Diameter on the Ultrasonic Fatigue Response of 316L Stainless Steel Manufactured via 3D Systems' ProX DMP 200 Laser Powder Bed Fusion System

4.1 Introduction

Additive manufacturing (AM) is a modern technology subject to continued research and innovation. Metal AM offers many advantages over conventional manufacturing methods [1,2] but still requires further investigation to fully understand AM process-structure-property (PSP) relationships. The PSP relationships are of particular importance for development of integrated computational materials engineering (ICME) models [3]. A key outcome of ICME is to model and predict complex production part performance without the need for laboratory testing [4,5]. Understanding complex part performance is important for factors such as fatigue behavior which is not only material dependent but geometry dependent. The phenomenon of seeing an improved fatigue response when reducing section thickness has been well known in conventionally manufactured metallic materials for quite some time now [6–12]. Until recent work by Trombley et. al. (Chapter 3), this had not been explicitly shown to occur in AM materials as well. Due to the complex thermal history AM parts experience during fabrication, it is worthwhile not only to show that this newer manufacturing method also exhibits size effects, but to investigate the aspects of AM processing that influence the fatigue response seen. Once a fundamental understanding of how the part geometry influences the fatigue response in AM materials, this can then be implemented into ICME models.

The focus of the work herein is on 316L stainless steel manufactured via laser-powder bed fusion (L-PBF). L-PBF is well-established in metal AM with at least 65 L-PBF systems commercially available. Most L-PBF systems manufacturers designate ideal process parameters for a range of materials that result in reduced porosity, surface roughness, and manufacturing defects. There are over 130 process variables, all of which have some influence on the part's microstructure, mechanical behavior, or overall quality [13,14]. Extensive research has been done on how these processing parameters interact to create the desired outcome, the most investigated of which are the ones easiest to control (e.g., laser power, scan speed, hatch spacing, layer thickness, laser spot size, scan strategy, etc.) [15–33]. Given the extensive amount of variability possible in L-PBF systems, it is important to show that the effects observed, namely that of gauge diameter effects observed on the GE Additive Concept Laser M2 (CL M2) in Chapter 3, are not unique to that system. This current work investigates whether the gauge diameter effects seen on the CL M2 also exist on the 3D Systems ProX DMP 200 (ProX 200).

Typically, fatigue behavior of L-PBF materials is governed by surface finish [2,34–37], processing defects [38,39], and residual stresses. Surface finish and defects act as stress concentrators [40,41] and are most readily the site of fatigue crack initiation. How quickly an external applied stress results in a fatigue crack is aided by the stress-concentration factor, K_t, at the source of crack initiation. This value varies based on the geometry of the notch, hole, or crack [42]. Fatigue cracking is also aided by tensile residual stresses [43–46]. Prior research has shown that L-PBF parts typically exhibit tensile residual stresses at the surface and compressive residual stresses at the core of the part [47–51]. This pattern of residual stresses arises from the melting, solidification, and re-melting inherent in L-PBF which creates large thermal stress gradients that follow the path of heat flow [43,48,49,52,53].

In this study, the effects of gauge section diameter on the ultrasonic fatigue behavior of 316L stainless steel is investigated. The specimens are fabricated in two diameters (1.5 mm and 5.0 mm) using L-PBF. With processing parameters kept the same between both builds, the overarching goal of this work is to investigate how the geometry of a specimen influences the melting, solidification, and re-melting process that occurs in L-PBF. A look at how the microstructure, surface roughness, defect morphology and distribution, and residual stresses are influenced by part geometry is shown in the Results section. This is paired with an investigation on how the high cycle fatigue (HCF) behavior changes with gauge section diameter, surface condition, and residual stress state. Finally, a comparison is made between the work utilizing the CL M2 (Chapter 3) and the current work utilizing the ProX 200.

4.2 Materials and Methods

4.2.1 Material properties

Each specimen was manufactured using GE Additive Concept Laser CL 20ES Stainless steel powder meeting composition standards of 316L for L-PBF [54]. The powder was manufactured by GE Additive, who provided the composition of the material as given in Table 4.1. A combination of virgin and sieved powder was used for the manufacture of test specimens. Particle size analysis revealed the median particle in both virgin and virgin + sieved to be approximately 30 μm with 90% of particles being less than 45 μm (Table 4.2). Additionally, 73.6% of particles measured were found to have a sphericity of 0.9 or less, with the average sphericity being 0.791. A portion of the powder batch was used to manufacture L-PBF tensile samples to measure bulk mechanical properties. The results indicated that the elastic modulus for this condition was 165 GPa with a yield strength of 466 MPa, showing a significantly lower elastic modulus and higher yield strength compared to wrought 316L stainless steel [55,56] (Table 4.3).

Table 4.1. Chemical composition (in wt. %) of GE Additive CL 20ES powder particles as provided by GE Additive.

Type	Fe	Cr	Ni	Mo	C	Mn	P	S	Si
GE Additive	Balance	16.5-18.5	10.0-13.0	2.0-2.5	0-0.03	0-2.0	0-0.045	0-0.03	0-1.0

Table 4.2. Powder particle size (in μm) cumulative distribution function of GE Additive CL 20ES stainless steel powder.

	10%	50%	90%
Virgin	21.5	30.4	43.5
Virgin + Sieved	20.2	30.1	44.8

Table 4.3. Mechanical properties of L-PBF 316L austenitic stainless steel at room temperature.

Type	Elastic Modulus [GPa]	Tensile Strength [MPa]	Yield Strength 0.2% Offset [MPa]
Measured	165	565	466

4.2.2 Specimen fabrication

All fatigue specimens were manufactured using a 3D Systems ProX DMP 200 (ProX 200) at the Naval Surface Warfare Center – Carderock Division (NSWC). The 3D Systems recommended processing parameters for 316L were used for the manufacture of all specimens (Table 4.4).

Table 4.4. Laser powder bed fusion (L-PBF) process parameters for every build, as recommended by 3D Systems for 316L stainless steel.

Laser Power	Scan Speed	Layer Thickness	Jump Speed	Hatch Spacing	Spot Size
129 W	1400 mm/s	30 μm	5000 mm/s	50 μm	50 μm

The specimens were fabricated in a cylindrical dog-bone geometry (Figure 4.1) in the vertical orientation for ultrasonic fatigue testing in the as-built condition. To assess the influence of part thickness on fatigue behavior, specimens with a gauge diameter of 5.0 mm and 1.5 mm were built. The geometry of the specimens was designed to resonate at 20 kHz despite different gauge diameters. Thirty-six 5.0 mm and eighty-eight 1.5 mm specimens were built across four separate build plates. In every build, the infill of all specimens was completed prior to the contour pass on each specimen. All specimens were removed from the build plates using electro-discharge machining (EDM), followed by machining an M8x1.0mm thread on one end for insertion into the ultrasonic fatigue testing equipment.

4.2.3 Ultrasonic fatigue testing

Ultrasonic fatigue (UF) testing is used in this study for its ability to rapidly obtain high cycle fatigue (HCF, 10^4 to 10^7 cycles) and very high cycle fatigue (VHCF, >10^7 cycles) data. UF testing is conducted at room temperature on equipment developed by University of Natural Resources and Life Sciences, Vienna (BOKU) [57] and operated at 20 kHz. Operating at 20 kHz allows for HCF and VHCF data to be obtained in hours or days compared to months or years it would take operating at 20-60 Hz as is typical in servo-hydraulic fatigue testing. UF testing can be used and compared to conventional fatigue data in this work as it has been shown that the frequency of testing has no effect on the fatigue behavior in austenitic stainless steels [58]. Experimentation was conducted under fully reversed ($R = -1$) loading. Failure was defined as the point in life at which the UF instrumentation detects a change in frequency greater than 200 Hz from the starting resonant frequency of approximately 20 kHz. A value of 200 Hz was chosen to allow the crack to propagate sufficiently to be observed by the naked eye but not fully fracture the specimen. If a specimen does not meet this failure criteria prior to 10^8 cycles, it was deemed a runout.

The HCF testing protocol consists of four steps: (1) statistical sample of intermediate-stress level fatigue (~20 samples); (2) statistical sample of high-stress level fatigue (~10 samples); (3) quantification of fatigue strength at 10^8 cycles using staircase testing at low-stress fatigue (10 samples); and (4) application of a Random Fatigue Limit (RFL) model using a Maximum Likelihood Estimation (MLE) to quantify statistical variability and estimate the S-N curve and fatigue strength.

4.2.4 Fatigue strength calculations

A life-regression model (S-N curve) is used to quantitatively describe the fatigue properties of a given sample group from experimental fatigue tests. There are multiple models that can be used to generate an S-N curve from fatigue data, including the Random Fatigue Limit (RFL) model [59] which is used herein. The RFL curve fit acts as a metric to more readily compare the fatigue life and strength of each sample group at varying stresses. The RFL model can be used for a range of different distributions and constraints, making it important to implement a Maximum Likelihood Estimation (MLE) to the calculation of the RFL model. In the current investigation, this was done following the methods outlined by Engler-Pinto Jr. et al. [60]. MLE analysis has shown that a Weibull distribution is the best fit in most cases, so, in the current investigation this is the distribution used in each RFL analysis. Once the appropriate RFL model is selected, the fatigue limit and fatigue strength can be calculated for the entire dataset, including runout values. The RFL model was selected in place of other models such as the Modified Basquin model [61,62] as it has been shown to generally provide a better fit to HCF data as determined by MLE [62].

An experimental method for estimating the fatigue strength is the staircase method. This is a fatigue testing method which sequentially tests samples at varying stress levels. The first sample is tested at a pre-determined stress and observed to be either a failure or a runout. The following sample is tested at a higher stress if the previous sample was a runout and a lower stress if it was a failure. This continues for any number of samples, resulting in a roughly even split of runouts and failures. The median stress of these tests is used as an estimate of the median fatigue strength of the material, with the assumption that the fatigue strength is normally distributed. For its simplicity, this method was used to test a portion of the sample group, however, an RFL model is still applied to the entire dataset as it is more accurate in predicting the fatigue strength of data that is not normally distributed [62].

4.2.5 Surface roughness

Surface roughness was measured on all samples using a Keyence optical microscope. Both line roughness and surface roughness were measured from the included Keyence software on as-built dog-bone specimens. Values of S_a, S_v, and S_z as defined by ISO 25178-2 [63] are reported to assess differences in surface roughness. A shape correction is applied to account for the cylindrical surface. Nine images of the surface were taken at 600x optical magnification and stitched together to form an area of interest approximately 900 x 1200 μm.

4.2.6 As-built surface removal

The as-built surface was removed from twenty 1.5 mm ProX 200 specimens to characterize the impact removing the as-built surface roughness has on the fatigue behavior. Material removal was done using a RTS Leeds low-stress sample polishing machine at Element Materials Technology in Wixom, MI. The surface removal process removes approximately 75 μm from the surface, reducing the diameter by 0.15 mm. This process both improves the surface finish by reducing the surface roughness and completely removes the contour pass on each specimen. The contour pass shows a differing grain morphology than that of the infill, as seen in Figure 4.2, so removing this may influence the fatigue behavior.

4.2.7 Residual stress

The axial residual stress was measured on four specimens: one as-built 5.0 mm ProX 200, two as-built 1.5 mm ProX 200, and one stress relief heat treated 1.5 mm ProX 200. Residual stress measurements are done using x-ray diffraction with material removal via electropolishing to get a profile of residual stress versus depth from the surface. Specimens were measured using an LXRD 13115 with a Mn target, x-ray elastic constant of 20,199 ksi (139,000 MPa), {311} crystallographic plane, and 152.8° Bragg angle. Residual stress measurements were conducted by Proto Manufacturing Inc in Taylor, MI.

In addition to measuring the residual stress, a partial relief of the residual stress was conducted by heat treating thirty-three 1.5 mm ProX 200 specimens. A stress relief heat treatment was completed in a Lindberg 1700°C tube furnace in a sealed Argon environment. The heat treatment consisted of a forty-five minute heat-up, four hour soak at 650°C, and a three hour furnace cool to room temperature. These conditions were chosen to provide stress relief while limiting microstructural changes [34,64–68].

4.2.8 Microstructure and fractography

Microstructural characterization was conducted to determine if the gauge diameter of the as-printed part influenced the grain morphology in any way. The samples were cut using a low speed saw, ground using increasingly fine grit SiC grinding paper, and polished using 1 μm diamond suspension followed by 0.04 μm colloidal silica, using the procedure outlined by Rowenhorst et al. [69]. Sections were taken from the gauge area both parallel and normal to the build direction. Electron backscatter diffraction (EBSD) was used to evaluate the microstructure in multiple orientations. EBSD scans were taken in both the interior and at the edge of each sample to obtain an understanding of how the microstructure changes throughout the samples, most notably from the contour to the infill. EBSD characterization was accomplished using an EDAX Hikari EBSD camera on a Tescan MIRA-3 GMH electron microscope at 30 kV and a beam intensity of 18, with a scan area 600 X 600 μm and a step size of 0.5 μm. Analysis was completed using EDAX OIM Analysis^{TM} in the austenite phase with a minimum grain boundary misorientation angle of 1°.

Analysis of the fracture surface was conducted utilizing SEM on a Tescan Mira-3 GMH electron microscope. Analysis of defects on the fracture surface was completed with the use of SEM images and ImageJ.

4.3 Results

4.3.1 Microstructure

The microstructure was characterized for the 5.0 mm and 1.5 mm specimens with a representative sample of images shown in Figure 4.3. Images were taken normal and parallel to the build direction to observe the anisotropic microstructure morphology. Both the sample interior and surface region were captured to observe microstructural changes caused by the use of contour passes. Figure 4.3 highlights the differences in microstructure between the two specimen sizes (1.5 mm and 5.0 mm) using the ProX 200. Processing parameters were kept the same between the two builds so any difference in microstructure would be attributed to thermal gradient differences during fabrication. All samples show the characteristic cross-hatch grain morphology normal to the build direction and columnar grains parallel to the build direction commonly observed in L-PBF. Evidence of a contour pass is seen in Figure 4.3, which shows a differing microstructure characteristic of smaller grains, no cross-hatch pattering, and no columnar grains. The contour zone shows a different grain morphology which results from a different scan pattern used for the infill raster scan.

4.3.2 Surface roughness

Surface roughness measurements indicated that there was no significant change in surface roughness as the diameter of the as-built sample changed (Table 4.5). The surface roughness values reported are from Keyence optical measurements, which measures surface roughness by means of evidence of build layers and partially melted particles adhered to the sample surface. Cross-sectional analysis on the SEM revealed that the specimens have features of surface roughness that would be obstructed in the Keyence optical measurements. Previous research has referred to the obstructed surface roughness of the specimens as surface crevices (Chapter 3). Evidence of obstructed surface crevices is also observed in the ProX 200 specimens, as shown in Figure 4.4. Subsequent discussion will distinguish between the surface roughness (Keyence) and surface crevices (SEM).

Table 4.5. Surface roughness characteristics for each gauge diameter sample group. Characteristics include the arithmetic mean deviation of the surface profile, maximum height of the surface profile, and maximum pit depth as defined by ISO 25178-2:2021. At least 3 samples were characterized for each gauge diameter.

Type	Sa [μm]	Sz [μm]	Sv [μm]
5.0 mm ProX 200	8.88 ± *2.77*	78.84 ± *30.12*	33.52 ± *10.64*
1.5 mm ProX 200	5.30 ± *1.45*	52.83 ± *19.25*	25.25 ± *7.22*

4.3.3 Residual stress

Axial surface residual stress measurements were taken at three radial locations within the gauge section of five as-built specimens: three 5.0 mm and two 1.5 mm specimens, as shown in Figure 4.5 a. Of the five specimens, one 5.0 mm and both 1.5 mm specimens, were also incrementally electropolished to get an axial residual stress depth profile (Figure 4.5 b). The 5.0

mm specimens from Build 6 and 1.5 mm specimens from Build 3 were measured in the as-built un-tested condition, while the 5.0 mm specimen from Build 1 was measured post-mortem.

An axial residual stress surface and depth profile were measured on one stress-relieved 1.5 mm specimen for comparison to the as-built state, as shown in Figure 4.6. Due to testing availability the stress-relieved 1.5 mm specimen did not have a surface or depth profile measured prior to heat treatment.

4.3.4 Ultrasonic fatigue behavior

The ultrasonic fatigue behavior of 36 as-built 5.0 mm specimens were compared to 30 as-built 1.5 mm specimens. An additional 48 1.5 mm specimens were subjected to post-processing, with 31 specimens being stress-relieved and 17 were surface-removed. Trombley et al. previously reported the effects of stress-relief heat treatment and surface removal on the fatigue behavior of CL M2 samples (Chapter 3), whose testing procedure and analysis was replicated for the ProX 200 specimens in this study.

The UF results for each as-built ProX 200 group are graphically represented in Figure 4.7. Each sample group is separately fitted using an RFL model assuming a Weibull distribution informed by MLE. The ProX 200 specimens show a significant increase in fatigue life, N_f, and fatigue strength, S_N, at 10^8 cycles with decreasing gauge diameter. The fatigue strength as determined by RFL and staircase testing is shown in Table 4.6 indicating that both methods are in good agreement.

Table 4.6. Fatigue strength for each sample group as determined by random fatigue limit (RFL) model and the staircase testing procedure. The fatigue strength is defined as the stress needed to cause failure at 10^8 cycles.

	Fatigue Strength [MPa] via RFL	Fatigue Strength [MPa] via Staircase
1.5 mm ProX 200	117.0 ± *19.7*	107.0 ± *9.0*
5.0 mm ProX 200	88.9 ± *9.9*	93.0 ± *9.0*

The UF results for the surface-removed 1.5 mm ProX 200 specimens are shown in Figure 4.8. Removing the as-built surface significantly improves the fatigue strength, S_N, at 10^8 cycles and fatigue life, N_f in all cycle regimes. The fatigue strength estimations are summarized in Table 4.7. Due to material availability, 5.0 mm ProX 200 specimens were not subjected to surface-removal.

Table 4.7. Fatigue strength for surface-removed 1.5 mm specimens compared to the as-built 1.5 mm ProX 200 specimens. Fatigue strength is determined by random fatigue limit (RFL) model and the staircase testing procedure. The fatigue strength is defined as the stress needed to cause failure at 10^8 cycles.

	Fatigue Strength [MPa] via RFL	Fatigue Strength [MPa] via Staircase
1.5 mm Surface-Removed	143.0 ± *29.6*	146.7 ± *9.4*
1.5 mm As-Built	117.0 ± *19.7*	107.0 ± *9.0*

The UF results for the stress-relief heat treated 1.5 mm ProX 200 specimens are shown in Figure 4.9. The stress-relief heat treatment imparts a mild improvement in fatigue strength at 10^8 cycles with no significant difference in fatigue life at higher stresses. The fatigue strength estimations are summarized in Table 4.8. Due to material availability, 5.0 mm ProX 200 specimens were not subjected to stress-relief heat treatment.

Table 4.8. Fatigue strength for stress-relieved 1.5 mm specimens compared to the as-built 1.5 mm ProX 200 specimens. Fatigue strength is determined by random fatigue limit (RFL) model and the staircase testing procedure. The fatigue strength is defined as the stress needed to cause failure at 10^8 cycles.

	Fatigue Strength [MPa] via RFL	Fatigue Strength [MPa] via Staircase
1.5 mm Stress-Relief	126.0 ± *9.7*	124.4 ± *8.3*
1.5 mm As-Built	117.0 ± *19.7*	107.0 ± *9.0*

4.3.5 Fracture surface analysis and defect characterization

Fatigue fracture surface analysis is done to compare the crack growth path in each sample group. Figure 4.10 shows a representative view of the fracture surface for both 5.0 mm and 1.5 mm ProX 200 specimens. Every fracture surface shows two distinct regions, with fatigue crack growth in the lower half and ductile overload in the top half of each image. The bottom half shows the amount of crack growth that occurred during fatigue testing. The top half shows the ductile failure that occurred due to manual overload by bending after the test had been completed. The testing criteria is such that “failure” is detected after a resonant frequency change of 200 Hz and therefore does not correlate to complete fracture of the sample. Manual overload is required to reveal the entire fracture surface for the purpose of fractography. Figure 4.10 shows that macroscopic fracture surface morphology is similar between the two diameters.

Upon closer inspection of each fatigue fracture surface, the researchers noticed lack-of-fusion (LOF) pores spread across the entire area. It was apparent that the source of fatigue crack initiation in all samples was due to LOF pores connected to the specimen surface. A selection of representative higher magnification SEM images are shown in Figure 4.11 highlighting these initiating defects in both the 5.0 mm and 1.5 mm specimens. These defects appear to be LOF pores due to their irregular shape (as seen in Figure 4.4 and Figure 4.11) and presence of unmelted powder particles within the defect, as shown in Figure 4.12 [38,70–73].

When the specimens are stress-relieved, the source of crack initiation does not change. Figure 4.13 shows the representative fractography of the as-built 1.5 mm ProX 200 specimens compared to the stress-relieved 1.5 mm specimens. The fracture surface morphology and source of crack initiation are nominally the same. LOF pores connected to the sample surface are also the only source of fatigue crack initiation when the as-built surface is removed. Figure 4.13 also compares the as-built 1.5 mm ProX 200 specimens to the surface-removed ProX 200 specimens. Analysis of the defect size and morphology for stress-relieved and surface-removed specimens indicates that these LOF pores are indistinguishable from those in the as-built specimens (Figure 4.14).

The size of the initiating defects on the fracture surface were analyzed using ImageJ. The area of each defect was measured by tracing the perimeter of the LOF pore as seen by the fracture surface. The area of the defects were also approximated using the $area$ and $\sqrt{area}$ parameter defined by Murakami for irregularly shaped cracks [42]. The size of initiating defect is compared between the 5.0 mm and 1.5 mm ProX 200 specimen groups, as shown in Figure 4.14, and shows that defect size does not appear to have any correlation with specimen diameter. The initiating defects in both groups are essentially indistinguishable.

4.4 Discussion

For AM 316L stainless steel fabricated on the ProX 200 system, as the gauge diameter of a specimen is reduced, a marked improvement in the HCF response is shown. The ProX 200 1.5 mm specimens show a substantial improvement in fatigue strength at 10^8 cycles and fatigue life in all stress regimes compared to the 5.0 mm specimens. Literature suggestions there are five main factors that can influence the HCF response in AM specimens: microstructure, defect morphology, surface roughness, section thickness effects, and residual stress state.

4.4.1 Influence of microstructure, defects, and surface roughness

The microstructure in both the 1.5 mm and 5.0 mm ProX 200 specimens is nominally the same. As seen in Figure 4.3, both specimen groups show a cross-hatch pattern normal to the build direction and short columnar grains parallel to the build direction. Both groups have similar grain size and morphology, contour pass grain morphology, and porosity.

The source of crack initiation in both the 1.5 mm and 5.0 mm specimen groups is LOF pores at the specimen surface. In most specimens, there is one primary LOF pore acting as the source of crack initiation, though at higher stresses multiple LOF pores are often seen to initiate cracks and lead to multiple cracks on the fracture surface. Despite differences in gauge thickness (diameter), the 1.5 mm and 5.0 mm specimens show an average initiating defect size of 174 μm and 134 μm, respectively. The size of the initiating defect is not significantly different between the two different as-built specimen groups. The overall size distribution of defects seen on the fracture surface is largely the same between the two groups.

In all ProX 200 specimens, the measured surface roughness was determined to be influenced by a combination of build layers, adhered and partially melted powder particles, and LOF defects at the surface. The specimens also showed evidence of surface crevices that were otherwise obstructed during optical measurements of surface roughness but would likely also contribute to surface roughness effects. Due to consistent processing parameters, the measured surface roughness was nominally the same between the 1.5 mm and 5.0 mm specimen groups.

It can be concluded from the above that the significant differences in HCF behavior observed between the 1.5mm and 5.0 mm gauge diameter samples are not due to any differences in microstructure, initiating defect size or surface roughness.

4.4.2 Influence of residual stress

The tensile residual stress magnitude is substantially lower in the 1.5 mm specimens compared to the 5.0 mm specimens. Literature has shown that high tensile residual stresses in the loading direction are detrimental to HCF behavior [43–46,74]. This is commonly thought of as an increase in tensile mean stress which is known to lead to lower resistance to cyclic stresses in the high cycle fatigue regime. Due to the higher tensile residual stresses on the surfaces, it is concluded that the 5.0 mm specimens experience a higher mean stress under cyclic loading than the 1.5 mm specimens leading to the reduced fatigue strength.

4.4.3 Influence of L-PBF machine

Both the ProX 200 and CL M2 exhibit gauge diameter effects on HCF behavior in 316L stainless steel. In both cases, decreasing gauge diameter for samples built of identical geometries led to improved HCF resistance. Processing parameters for the CL M2 machine are provided in Table 4.9. Despite differences in processing parameters each AM system produces specimens with remarkably similar fatigue behavior. Figure 4.15 shows that the fatigue strength at 10^8 cycles for the 1.5 mm specimens are within 10% of each other, while the 5.0 mm specimens are within 1% of each other – far below one standard deviation for each group. This suggests that despite these differences in processing parameters, specimens of identical geometries exhibit nominally similar HCF response.

Table 4.9. Laser powder bed fusion (L-PBF) process parameters for every build done on the GE Additive Concept Laser M2. All processing parameters used come recommended from GE Additive for use with 316L stainless steel.

System	Laser Power	Scan Speed	Layer Thickness	Jump Speed	Hatch Spacing	Spot Size
CL M2	370 W	900 mm/s	25 μm	*unknown*	*unknown*	160 μm

4.4.3.1 Processing parameter influence on microstructure

When comparing the microstructure of the ProX 200 to the CL M2, both systems show cross-hatch patterning normal to the build direction and columnar grains parallel to the build direction, as seen in Figure 4.16. The cross-hatch patterning is typical for L-PBF systems that use a raster scanning strategy, as both of these do. Columnar grains are seen in most L-PBF systems due to the remelting of previous layers and preferential heat flow along the build direction. The microstructure in the ProX 200 specimens shows generally smaller grains both normal and parallel to the build direction. This is to be expected given the 50 μm laser spot size of the ProX 200 compared to the 160 μm spot size of the CL M2. The shorter columnar grains are due to a reduced energy density, E (in J/mm^3), given by Eq. 4.1.

$$E = \frac{P}{v \cdot h \cdot d} \tag{4.1}$$

where P is the laser power (in W), v is the scan speed (in mm/s), h is the hatch distance (in mm), and d is the layer thickness (in mm). The ProX 200 system has an energy density of 61 J/mm^3 while the CL M2 has an energy density of 103 J/mm^3, meaning the specimen experiences a higher average energy per material volume in each build layer when manufactured on the CL M2. When looking at the contour zones, both systems show evidence of at least one contour pass, with the CL M2 showing a more distinct contour zone than ProX 200. In both cases, the contour passes contain smaller, less columnar grains. The CL M2 is prone to a higher porosity concentration at the contour-infill zone, while the ProX 200 has greater porosity throughout. The differences between these two systems suggest that the HCF response is not greatly dependent on grain morphology, given their similar fatigue responses.

4.4.3.2 Processing parameter influence on surface roughness

The as-built surface in any L-PBF system is largely dependent on the processing parameters, namely scan pattern, energy density, and layer thickness. In recent years, the implementation of one or more contour passes following fabrication of the bulk of the specimen geometry in each layer has become common practice. The contour passes serve to reduce the as-built surface roughness by smoothing the area between scan paths in raster scanning strategies. Additionally, the contour passes tend to have different built parameters than the infill scan, optimized to improve surface finish. Even with this improvement, an inherent as-built surface roughness is still left due to unmelted and partially melted powder particles adhered to the specimen surface and the stair-step effect that exists between build layers. The fact that the surface roughness is different between the ProX 200 and CL M2 is therefore unsurprising. The exact parameters of the contour passes are unknown in both systems as these are programmed by the manufacturer and cannot be modified by the user. The only known quantitative difference is the layer thickness of 30 μm for the ProX 200 and 25 μm for the CL M2. Qualitatively, the differences seen are thicker, more distinct contour zones in the CL M2, and more adhered, less melted powder particles in the ProX 200. Since it has been determined that fatigue crack initiation does not occur at the measured surface roughness but rather obstructed surface crevices (CL M2) and LOF pores (ProX 200), the optically measured value of surface roughness should have little effect on the similarities in HCF response seen in both systems.

4.4.3.3 Processing parameter influence on fatigue crack initiation

The only source of crack initiation in all ProX 200 specimens was LOF at the surface. In the CL M2 as-built specimens, crack initiation most often occurred at surface crevices. These surface crevices are a combined result of minor layer delamination caused by tensile axial residual stresses and printing discrepancies resulting in higher stress concentrations between build layers. The surface crevices act as shallow surface cracks [42] in terms of stress concentration factor, where the maximum stress intensity factor is given by Eq. 4.2,

$$K_{Imax} \cong 0.65\sigma_0\sqrt{\pi c\sqrt{10}} \qquad 4.2$$

where c is the depth of the crack from the surface and σ_0 is the maximum stress applied during fatigue testing. In specimens with insufficiently long surface crevices ($l \leq 10c$), the shallow surface crack overestimates the size of the defect, and as such should be quantified by the $\sqrt{area}$ parameter instead of $c\sqrt{10}$. The surface LOF pores in the ProX 200 specimens would be treated as an irregular surface crack [42], as given by Eq. 4.3.

$$K_{Imax} \cong 0.65\sigma_0\sqrt{\pi\sqrt{area}} \qquad 4.3$$

For 5.0 mm specimens tested at 120 MPa, the average crevice depth, c, in CL M2 specimens is 24 μm, resulting in a K_{Imax} of approximately 1.2, while the average crack size, $\sqrt{area}$, is 53 μm, resulting in a K_{Imax} of approximately 1.0. The average crack size, $\sqrt{area}$, in ProX 200 specimens is 124 μm, resulting in a K_{Imax} of 1.54. Thus the average LOF pore in the 5.0 mm ProX 200 specimen produces a slightly higher stress intensity than the average 5.0 mm CL M2 specimen. These results are summarized in Table 4.10.

Table 4.10. Comparison of the average defect size of specimens tested at 120 MPa. Defect size is quantified either by the crevice depth, c, or the $\sqrt{area}$ parameter. Resulting maximum stress intensity factors, K_{Imax}, are given with respect to the average defect size, as calculated by Eq. 4.2 and 4.3.

Specimens	Defect size metric	Average defect size [μm]	K_{Imax}
5.0 mm CL M2	Crevice depth, c	24	1.20
5.0 mm CL M2	$\sqrt{area}$	53	1.01
5.0 mm ProX 200	$\sqrt{area}$	124	1.54

4.4.3.4 Processing parameter influence on residual stress states

The state of residual stress along the loading direction has an additive effect on the total stress felt at the start of fatigue crack initiation. Tensile stress adds to the external stress applied while compressive stress acts to reduce the applied stress. Since the source of crack initiation for all specimens regardless of L-PBF system is at or near the surface, the axial residual stress at the surface has the greatest impact on crack initiation and effectively increases the cyclic mean stress. The surface axial residual stress is measured for each system (ProX 200 and CL M2) and each geometry (5.0 mm and 1.5 mm) and shown in Figure 4.17. For the 5.0 mm geometry, the CL M2 produces specimens with higher tensile residual stress. For the 1.5 mm geometry, the tensile residual stress is nominally the same between the two systems. Table 4.11 shows the average measured stress for each build group for easier comparison.

Table 4.11. Average measured surface axial residual stress for each build group.

Type	Average Measured Stress [MPa]	Number of measurements
5.0 mm CL M2	292 ± *13*	12
5.0 mm ProX Build 6	152 ± *15*	6
5.0 mm ProX Build 1	111 ± *12*	3
1.5 mm CL M2	69 ± *17*	3
1.5 mm ProX	58 ± *16*	6

Residual stresses arise due to the melting, solidification, and re-melting of the specimen during fabrication, making the processing parameters highly influential on the resulting residual stress state. In general, a larger thermal gradient will result in larger magnitude residual stresses as described by the temperature gradient mechanisms (TGM) model [50,53]. While nearly every processing parameter has a hand in altering the residual stress, the processing parameter with the greatest influence is the energy density from Eq. 4.1. The CL M2 system has the higher energy density of 103 J/mm^3 compared to 61 J/mm^3 in the ProX 200. While a complete understanding of how each processing parameter influences the residual stress formation in each system is beyond the scope of this work, suffice to say it makes logical sense that the CL M2 specimens will have a higher residual stress magnitude than the ProX 200 specimens. This is in agreement with literature which has shown that higher energy densities tend to increase the magnitude of residual stresses in L-PBF 316L applications [17,18,49]. The nearly double tensile residual stress of the 5.0 mm CL M2 specimens compared to the 5.0 mm ProX 200 would suggest a significantly poorer fatigue behavior, however Figure 4.15 shows they are nearly identical. One possible explanation for this lies in the maximum stress intensity produced by the initiating defect, as discussed in the previous section. The LOF pores in the ProX 200 specimens produce a higher magnitude stress intensity compared to the CL M2 specimens. The higher stress intensity combined with the lower residual stress present in the specimen could result in a similar overall HCF response during testing to the CL M2 specimens, resulting in nearly identical fatigue behavior.

4.5 Conclusions

The influence of gauge diameter (1.5 mm vs 5.0 mm diameter) on the fatigue behavior of L-PBF 316L SS was investigated on specimens produced using a ProX DMP 200. The following conclusions can be drawn for the ProX DMP 200 specimens:

1) The fatigue behavior in the high to very high cycle fatigue regime was strongly influenced by gauge diameter. A reduction in gauge diameter results in an increased fatigue strength at 10^8 cycles and increased fatigue lives in the high cycle fatigue regime.
2) The microstructure, initiating defect size, and surface roughness did not change with varying gauge diameter. This indicates that the mesoscale microstructure, defect size, and surface roughness are not the primary factors producing the observed differences in fatigue behavior.
3) The source of fatigue crack initiation in ProX DMP 200 specimens was lack-of-fusion (LOF) pores at the specimen surface. The LOF defects were not affected by gauge diameter so these defects were also not the source of the differences in fatigue behavior.
4) Axial residual stress magnitudes were strongly influenced by the gauge diameter, with a larger diameter corresponding to higher magnitude tensile residual stress near the sample surface.
5) Removal of the as-built surface finish significantly improves the fatigue behavior. Crack initiation still occurs at lack-of-fusion pores connected the specimen surface, though the defects are made effectively smaller due to the surface removal.

A comparison is made between identical specimens fabricated on the ProX DMP 200 and the Concept Laser M2. The following conclusions can be drawn from this comparison:

6) The high cycle fatigue (S-N) responses of specimens produced on different L-PBF systems were very similar, including the influence of gauge diameter.
7) The source of fatigue crack initiation is different for the two systems. Fractography indicates that crack initiation in the Concept Laser M2 occurs at the surface due to deep surface crevices. Crack initiation in the ProX DMP 200 occurs at the surface due to lack-of-fusion defects.
8) There is no significant difference in residual stress magnitudes between the two systems. The residual stresses dominate the high cycle fatigue resistance in both systems.

Figures

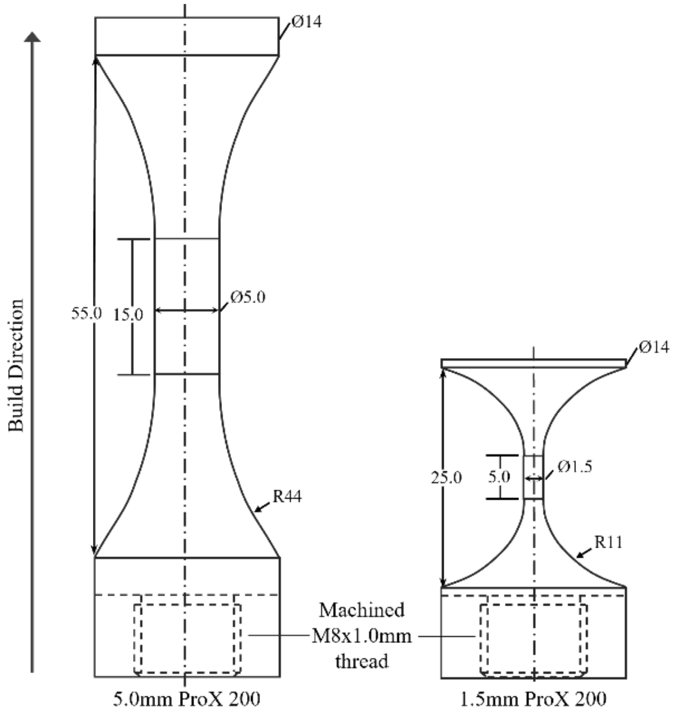

Figure 4.1 As-printed specimen geometry for 5.0 mm and 1.5 mm diameter dog-bone ultrasonic fatigue tests. Dashed lines represent final specimen geometry after machine threading.

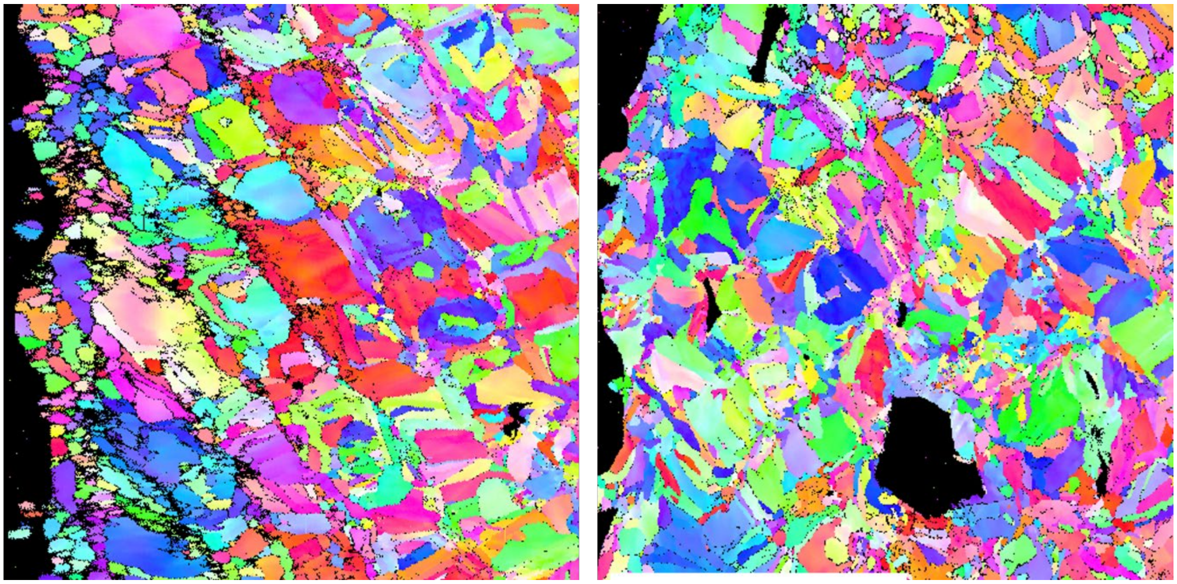

Figure 4.2. Evidence of contour pass seen normal to the build direction in both 5.0 mm (left) and 1.5 mm (right) specimens as depicted by electron backscatter diffraction (EBSD) inverse pole figures (IPF).

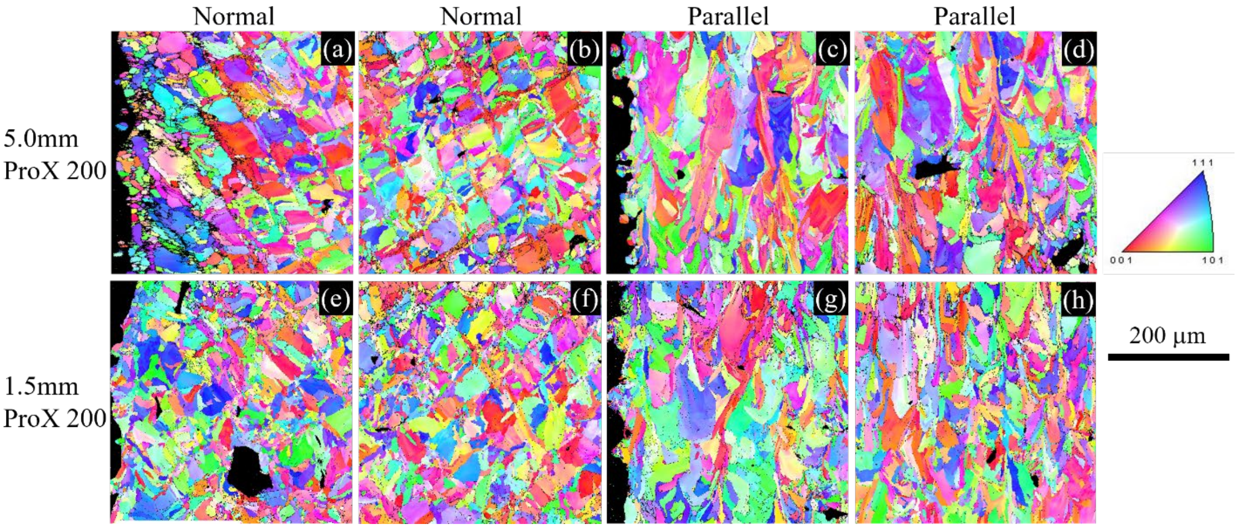

Figure 4.3. Inverse pole figure (IPF) maps generated via EBSD indicating the microstructure present in the (a-d) 5.0mm ProX 200, and (e-h) 1.5mm ProX 200 specimen groups.

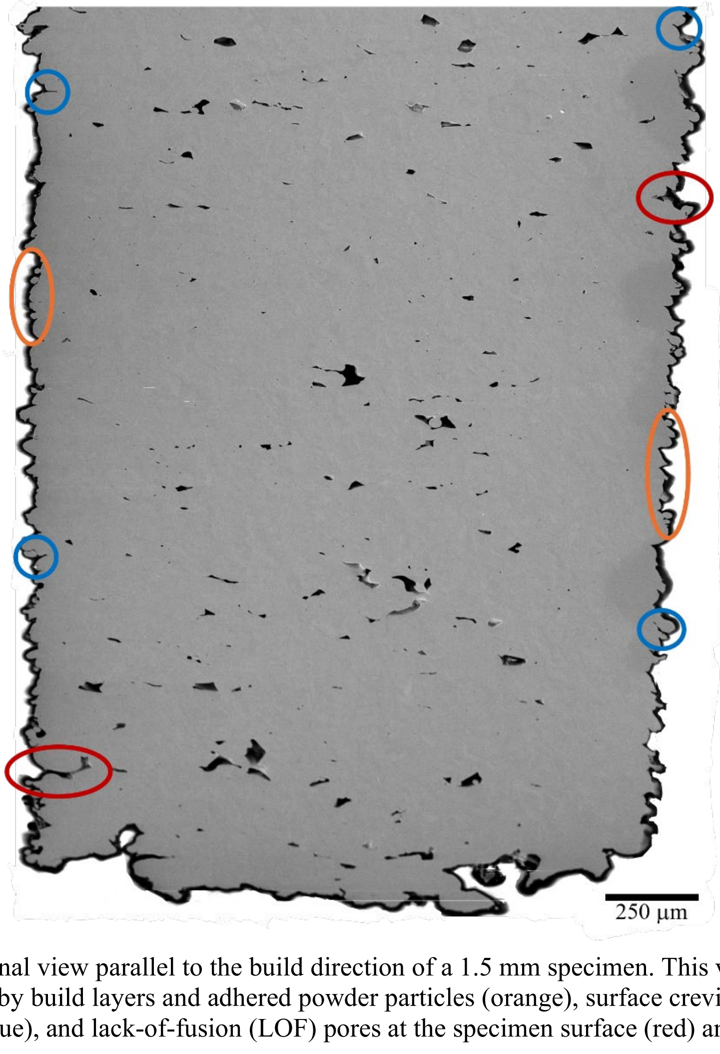

Figure 4.4. Cross-sectional view parallel to the build direction of a 1.5 mm specimen. This view shows the surface roughness as generated by build layers and adhered powder particles (orange), surface crevices due to printing defects and cracking (blue), and lack-of-fusion (LOF) pores at the specimen surface (red) and interior.

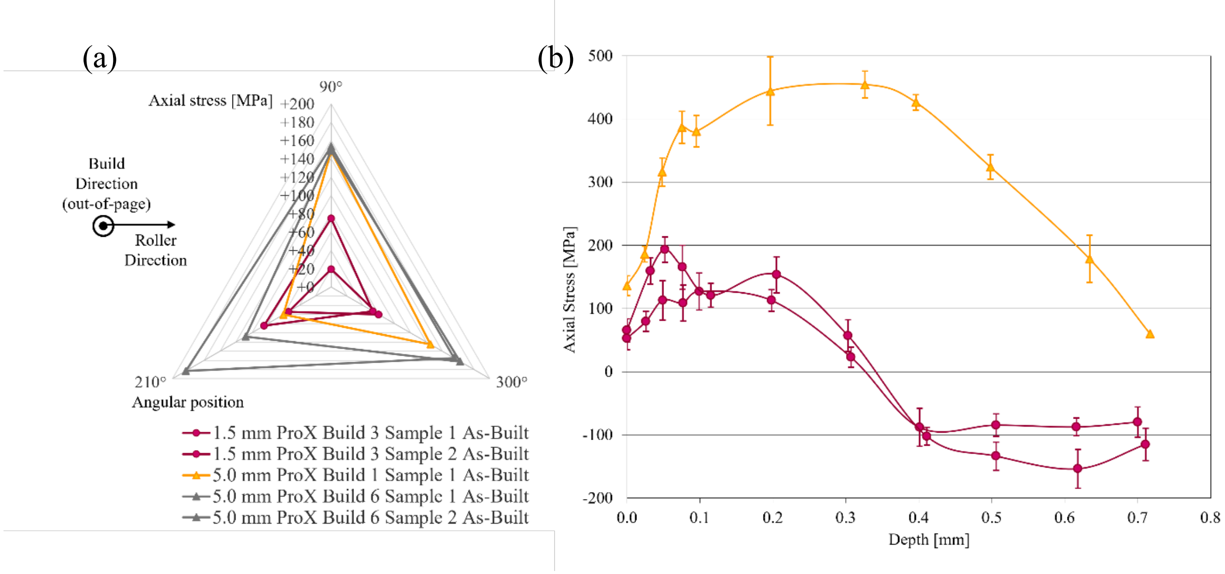

Figure 4.5. Axial residual stress as measured by XRD for as-built 5.0 mm and 1.5 mm specimens. (a) Axial residual stress surface profile, measured at three angular positions (90°, 210°, and 300° relative to roller direction) on each specimen. (b) Axial residual stress depth profile, measured at one angular position per specimen.

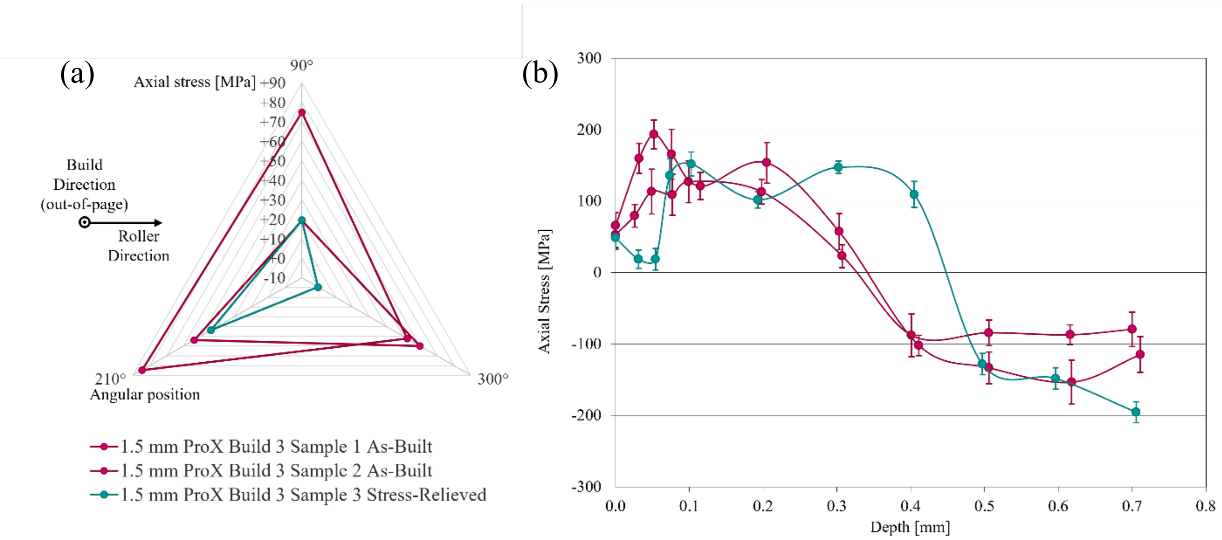

Figure 4.6. Axial residual stress as measured by XRD for stress-relieved compared to as-built 1.5 mm specimens. (a) Axial residual stress surface profile, measured at three angular positions (90°, 210°, and 300° relative to roller direction) on each specimen. (b) Axial residual stress depth profile, measured at one angular position per specimen.

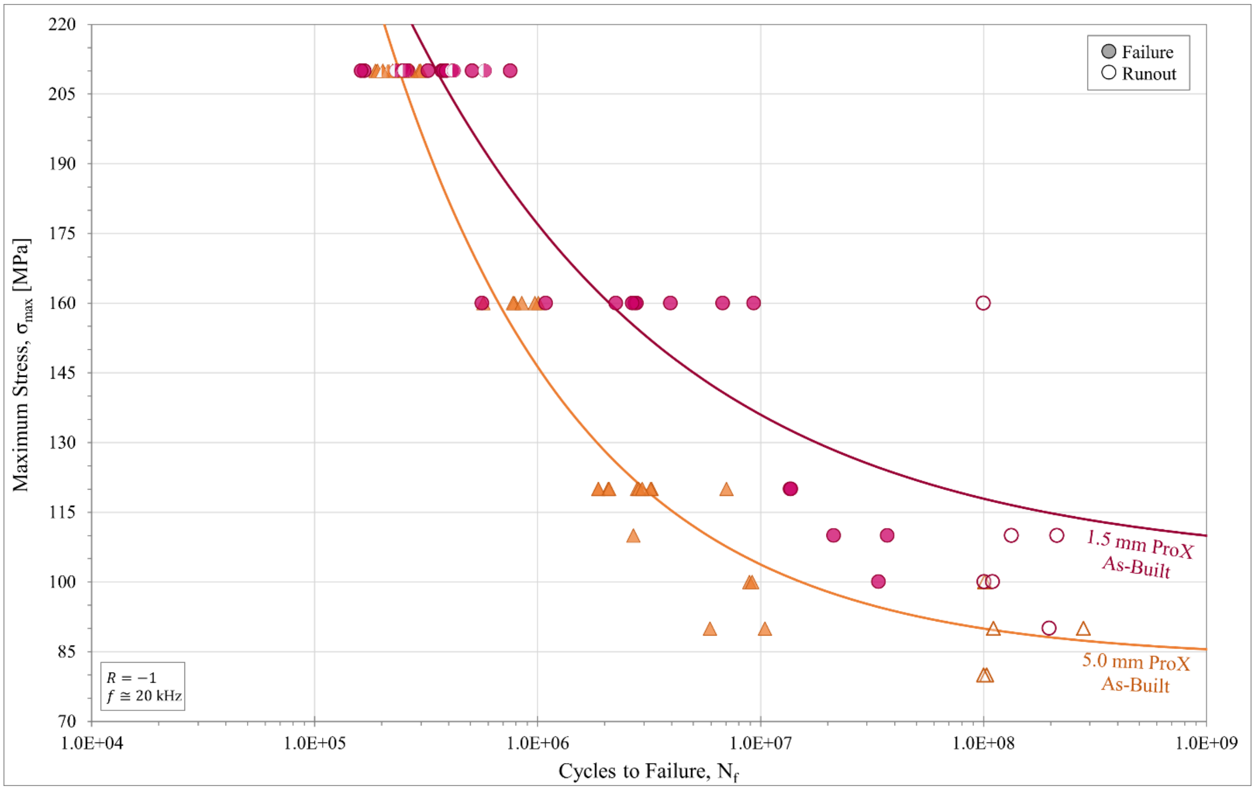

Figure 4.7. Stress-life (S-N) ultrasonic high cycle fatigue curves for all as-built ProX 200 specimens. Runout samples are indicated by unfilled data icons and are classified as cycling longer than 10^8 cycles without failure. Runout samples were re-tested at 210 MPa and are indicated by the half-filled icons. Each set of data is accompanied by a Weibull distribution curve fit determined via random fatigue limit (RFL) analysis.

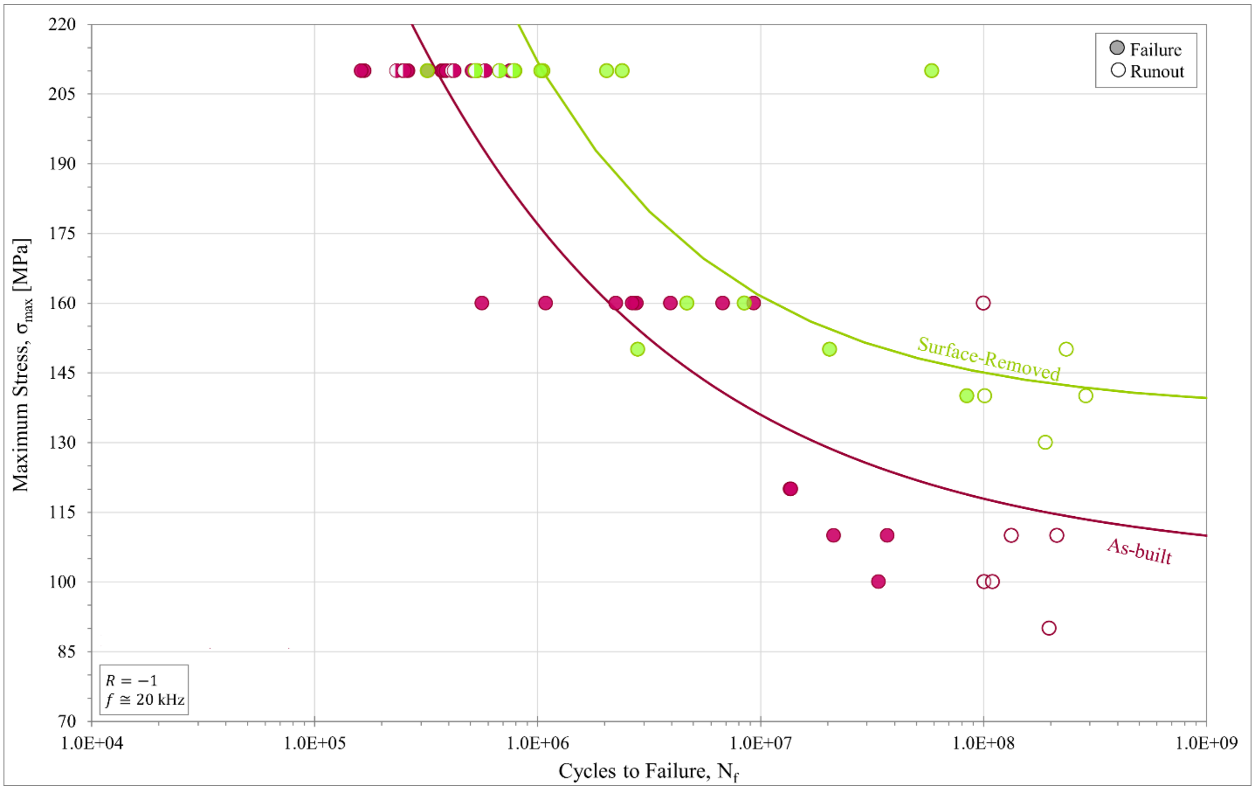

Figure 4.8. Stress-life (S-N) ultrasonic high cycle fatigue curves for 1.5 mm ProX 200 specimens in the as-built and surface-removed conditions. Runout samples are indicated by unfilled data icons and are classified as cycling longer than 10^8 cycles without failure. Runout samples were re-tested at 210 MPa and are indicated by the half-filled icons. Each set of data is accompanied by a Weibull distribution curve fit determined via random fatigue limit (RFL) analysis.

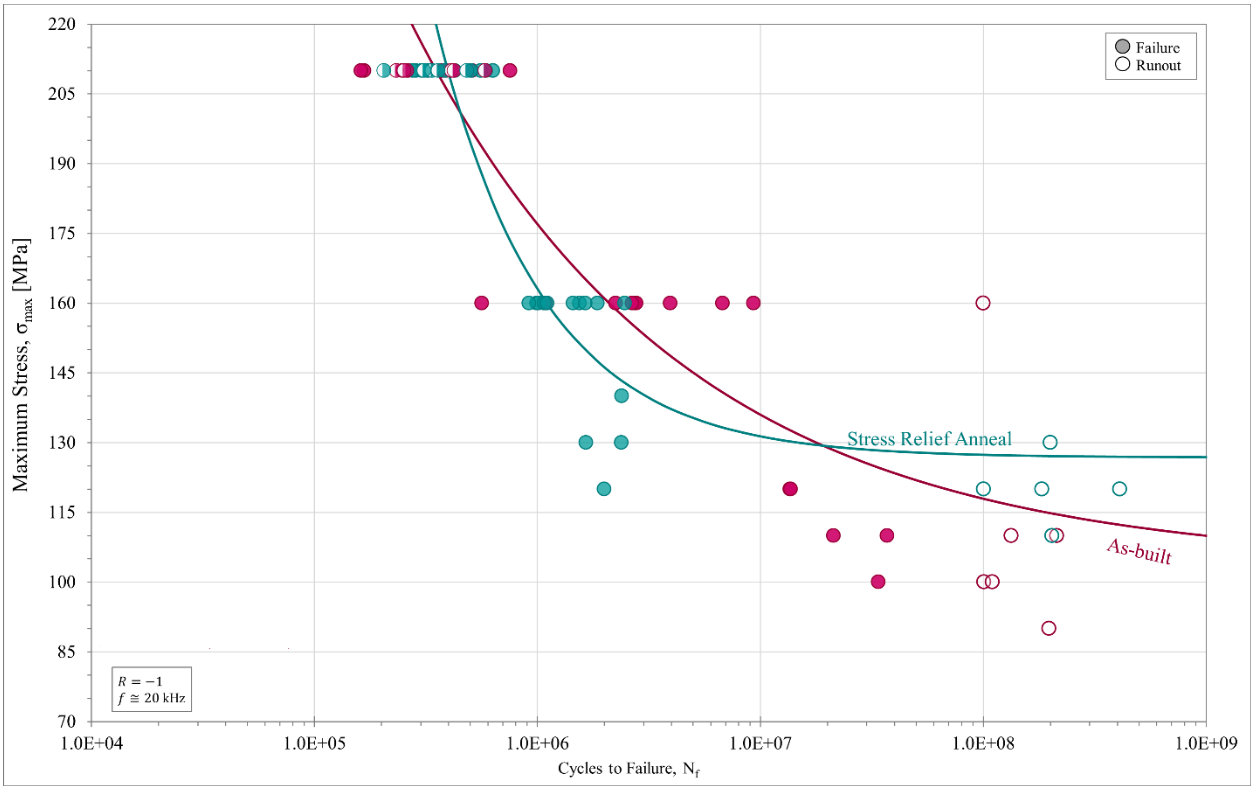

Figure 4.9. Stress-life (S-N) ultrasonic high cycle fatigue curves for 1.5 mm ProX 200 specimens in the as-built and stress-relieved conditions. Runout samples are indicated by unfilled data icons and are classified as cycling longer than 10^8 cycles without failure. Runout samples were re-tested at 210 MPa and are indicated by the half-filled icons. Each set of data is accompanied by a Weibull distribution curve fit determined via random fatigue limit (RFL) analysis.

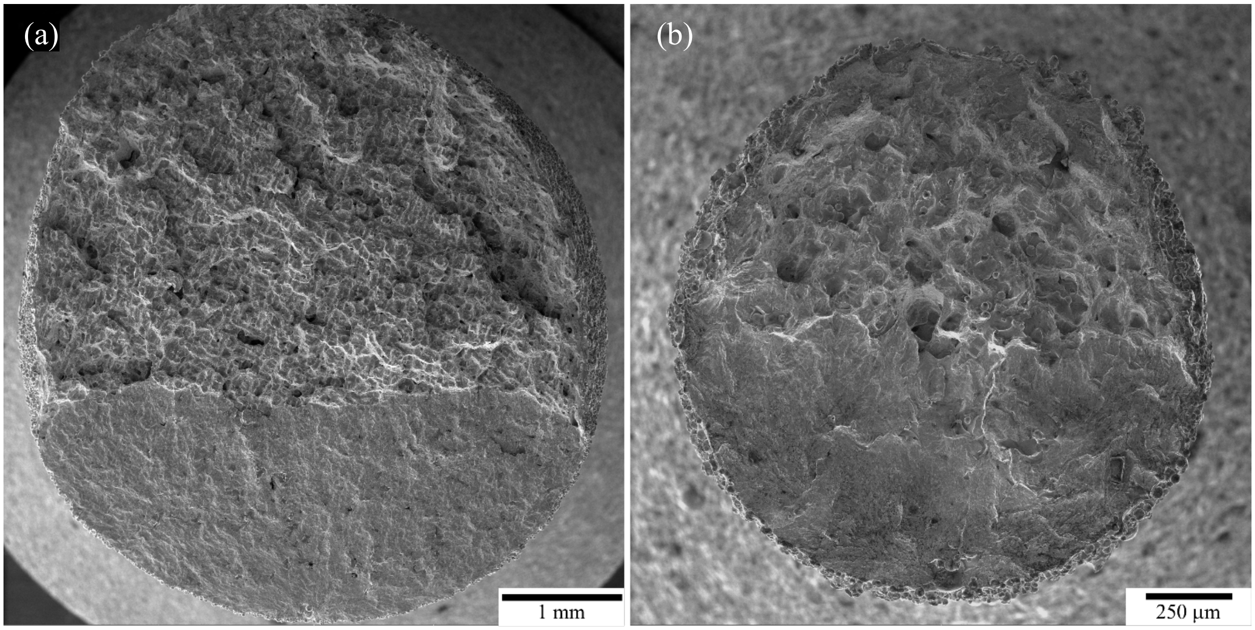

Figure 4.10. Representative ultrasonic fatigue fracture surface for as-built (a) 5.0 mm and (b) 1.5 mm ProX 200 specimens.

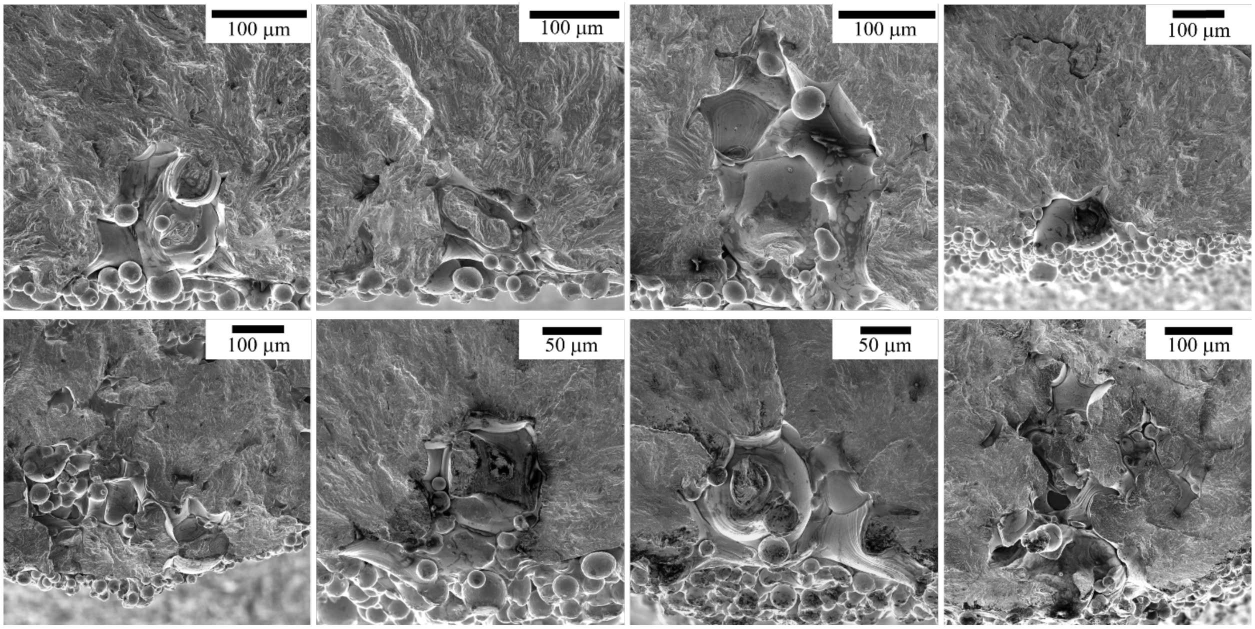

Figure 4.11. Selection of initiating defects seen on the fracture surface in both (top) 5.0 mm and (bottom) 1.5 mm ProX 200 specimens.

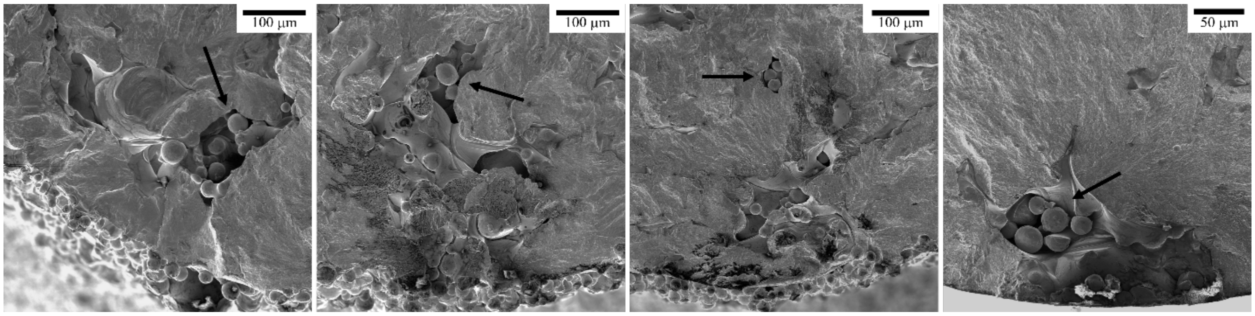

Figure 4.12. Evidence of lack-of-fusion (LOF) porosity in 5.0 mm and 1.5 mm ProX 200 specimens. Arrows show evidence of unmelted powder particles trapped with the LOF pore.

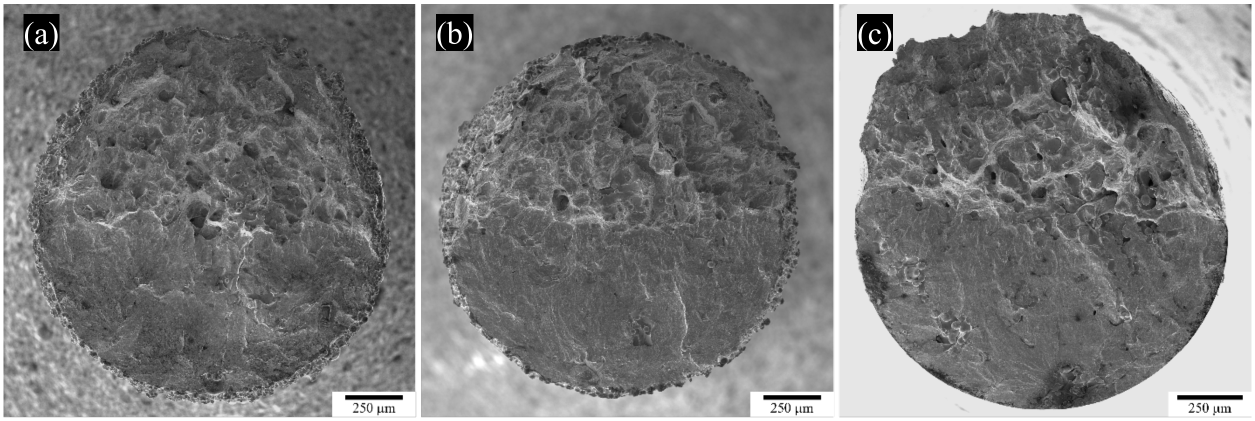

Figure 4.13. Representative fatigue fracture surface for 1.5 mm ProX 200 specimens in the (a) as-built, (b) stress-relieved, and (c) surface-removed conditions.

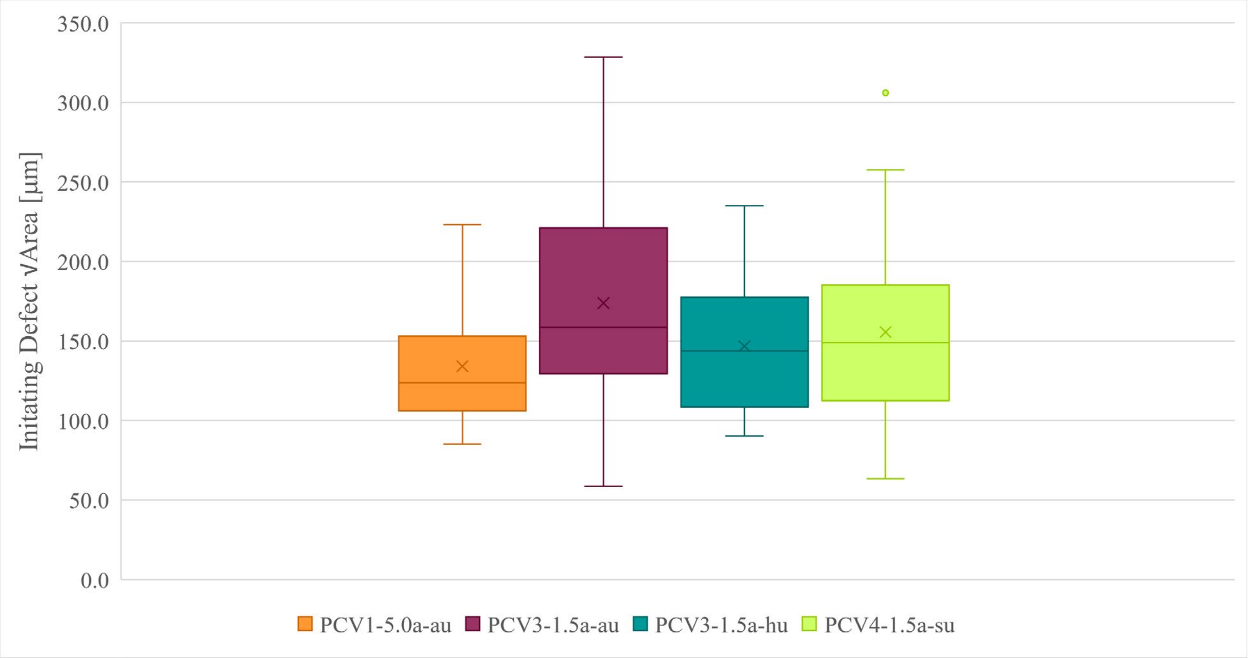

Figure 4.14. Initiating defect size distribution comparing the 5.0 mm as-built, 1.5 mm as-built, 1.5 mm stress-relieved, and 1.5 mm surface-removed ProX 200 specimens. Defect size is quantified as the traced √area of the LOF defect as defined by Murakami [42]. 'X' icons represent the average defect size.

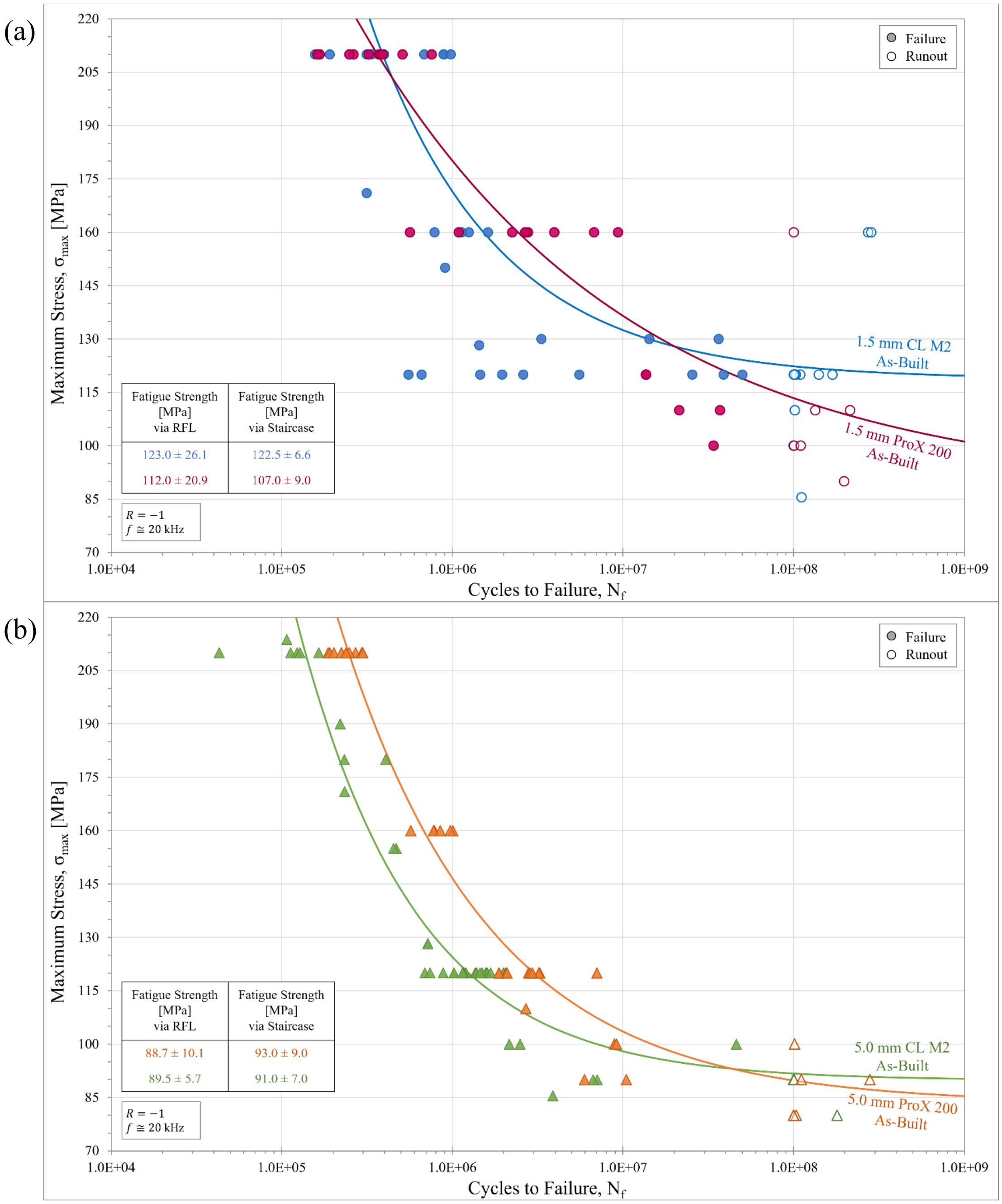

Figure 4.15. Ultrasonic fatigue response in as-built specimens fabricated using the 3D Systems ProX DMP 200 compared to the GE Additive Concept Laser M2 in (a) 1.5 mm diameter dog-bone specimens and (b) 5.0 mm diameter dog-bone specimens.

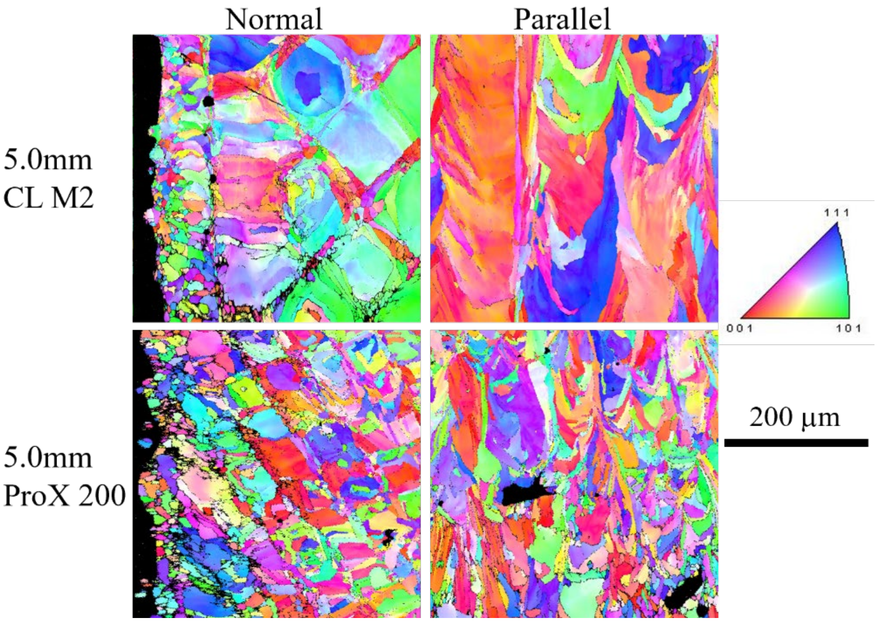

Figure 4.16. Inverse pole figure (IPF) maps generated via EBSD indicating the microstructure present in the 5.0mm CL M2 compared to the 5.0mm ProX 200 specimens both normal and parallel to the build direction.

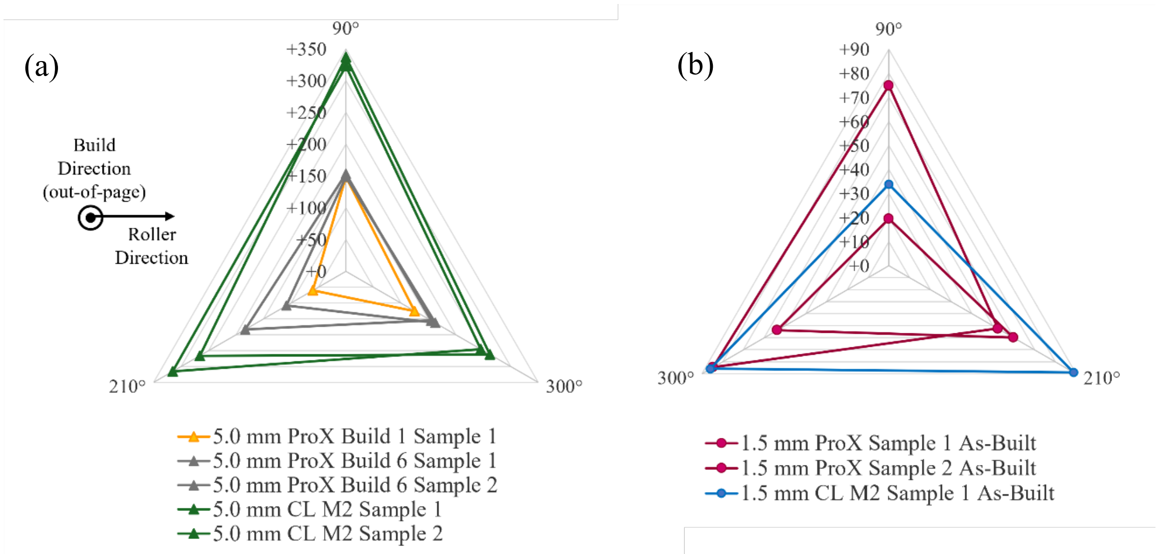

Figure 4.17. Comparison of surface axial residual stress states between specimens built on the ProX 200 and CL M2 in the (a) 5.0 mm geometry and (b) 1.5 mm geometry.

References

[1] ISO/TC 261, ASTM Committee F42, ISO/ASTM 52900:2017 Additive manufacturing. General principles. Terminology, (2017).

[2] T. DebRoy, H.L. Wei, J.S. Zuback, T. Mukherjee, J.W. Elmer, J.O. Milewski, A.M. Beese, A. Wilson-Heid, A. De, W. Zhang, Additive manufacturing of metallic components – Process, structure and properties, Prog. Mater. Sci. 92 (2018) 112–224. https://doi.org/10.1016/j.pmatsci.2017.10.001.

[3] J. Allison, D. Backman, L. Christodoulou, Integrated computational materials engineering: A new paradigm for the global materials profession, JOM 58 (2006) 25–27.

[4] S.A.H. Motaman, F. Kies, P. Köhnen, M. Létang, M. Lin, A. Molotnikov, C. Haase, Optimal design for metal additive manufacturing: An integrated computational materials engineering (ICME) approach, JOM 72 (2020) 1092–1104. https://doi.org/10.1007/s11837-020-04028-4.

[5] P.-A. Pires, O. Desmaison, M. Megahed, ICME manufacturability assessment in powder bed fusion additive manufacturing, JOM 70 (2018) 1677–1685. https://doi.org/10.1007/s11837-018-3024-8.

[6] W. Weibull, A statistical theory of the strength of materials, Swed. R. Inst. Eng. Res. (1939).

[7] A. Carpinteri, A. Spagnoli, S. Vantadori, An approach to size effect in fatigue of metals using fractal theories, Fatigue Fract. Eng. Mater. Struct. 25 (2002) 619–627. https://doi.org/10.1046/j.1460-2695.2002.00506.x.

[8] D.S. Paolino, A. Tridello, G. Chiandussi, M. Rossetto, On specimen design for size effect evaluation in ultrasonic gigacycle fatigue testing: Specimen for size effect in gigafatigue, Fatigue Fract. Eng. Mater. Struct. 37 (2014) 570–579. https://doi.org/10.1111/ffe.12149.

[9] G. Qian, W.-S. Lei, A statistical model of fatigue failure incorporating effects of specimen size and load amplitude on fatigue life, Philos. Mag. 99 (2019) 2089–2125. https://doi.org/10.1080/14786435.2019.1609707.

[10] A. Tridello, C.B. Niutta, F. Berto, D.S. Paolino, Size-effect in very high cycle fatigue: A review, Int. J. Fatigue 153 (2021) 106462. https://doi.org/10.1016/j.ijfatigue.2021.106462.

[11] P. Wang, M.H. Goh, Q. Li, M.L.S. Nai, J. Wei, Effect of defects and specimen size with rectangular cross-section on the tensile properties of additively manufactured components, Virtual Phys. Prototyp. 15 (2020) 251–264. https://doi.org/10.1080/17452759.2020.1733430.

[12] M. Muniz-Calvente, A.M.P. de Jesus, J.A.F.O. Correia, A. Fernández-Canteli, A methodology for probabilistic prediction of fatigue crack initiation taking into account the scale effect, Eng. Fract. Mech. 185 (2017) 101–113. https://doi.org/10.1016/j.engfracmech.2017.04.014.

[13] Y. Murakami, N.N. Yokoyama, J. Nagata, Mechanism of fatigue failure in ultralong life regime: Fatigue failure in ultralong life regime, Fatigue Fract. Eng. Mater. Struct. 25 (2002) 735–746. https://doi.org/10.1046/j.1460-2695.2002.00576.x.

[14] Y. Murakami, T. Nomoto, T. Ueda, Factors influencing the mechanism of superlong fatigue failure in steels: Superlong fatigue failure in steels, Fatigue Fract. Eng. Mater. Struct. 22 (1999) 581–590. https://doi.org/10.1046/j.1460-2695.1999.00187.x.

[15] D.R. Clymer, J. Cagan, J. Beuth, Power–velocity process design charts for powder bed additive manufacturing, J. Mech. Des. 139 (2017) 100907. https://doi.org/10.1115/1.4037302.
[16] K. Carpenter, A. Tabei, On residual stress development, prevention, and compensation in metal additive manufacturing, Materials 13 (2020) 255. https://doi.org/10.3390/ma13020255.
[17] T. Simson, A. Emmel, A. Dwars, J. Böhm, Residual stress measurements on AISI 316L samples manufactured by selective laser melting, Addit. Manuf. 17 (2017) 183–189. https://doi.org/10.1016/j.addma.2017.07.007.
[18] T. Mukherjee, V. Manvatkar, A. De, T. DebRoy, Mitigation of thermal distortion during additive manufacturing, Scr. Mater. 127 (2017) 79–83. https://doi.org/10.1016/j.scriptamat.2016.09.001.
[19] T. Larimian, M. Kannan, D. Grzesiak, B. AlMangour, T. Borkar, Effect of energy density and scanning strategy on densification, microstructure and mechanical properties of 316L stainless steel processed via selective laser melting, Mater. Sci. Eng. A 770 (2020) 138455. https://doi.org/10.1016/j.msea.2019.138455.
[20] G.R. Buican, G. Oancea, C. Lancea, M.A. Pop, Influence of layer thickness on internal structure of parts manufactured from 316-L steel using SLM technology, Appl. Mech. Mater. 809–810 (2015) 369–374. https://doi.org/10.4028/www.scientific.net/AMM.809-810.369.
[21] O.O. Salman, F. Brenne, T. Niendorf, J. Eckert, K.G. Prashanth, T. He, S. Scudino, Impact of the scanning strategy on the mechanical behavior of 316L steel synthesized by selective laser melting, J. Manuf. Process. 45 (2019) 255–261. https://doi.org/10.1016/j.jmapro.2019.07.010.
[22] T. Kurzynowski, K. Gruber, W. Stopyra, B. Kuźnicka, E. Chlebus, Correlation between process parameters, microstructure and properties of 316 L stainless steel processed by selective laser melting, Mater. Sci. Eng. A 718 (2018) 64–73. https://doi.org/10.1016/j.msea.2018.01.103.
[23] A.K. Agrawal, G. Meric de Bellefon, D. Thoma, High-throughput experimentation for microstructural design in additively manufactured 316L stainless steel, Mater. Sci. Eng. A 793 (2020) 139841. https://doi.org/10.1016/j.msea.2020.139841.
[24] Y. Deng, Z. Mao, N. Yang, X. Niu, X. Lu, Collaborative optimization of density and surface roughness of 316L stainless steel in selective laser melting, Materials 13 (2020) 1601. https://doi.org/10.3390/ma13071601.
[25] D. Gu, Y. Shen, Balling phenomena in direct laser sintering of stainless steel powder: Metallurgical mechanisms and control methods, Mater. Des. 30 (2009) 2903–2910. https://doi.org/10.1016/j.matdes.2009.01.013.
[26] G.B. Bang, W.R. Kim, H.K. Kim, H.-K. Park, G.H. Kim, S.-K. Hyun, O. Kwon, H.G. Kim, Effect of process parameters for selective laser melting with SUS316L on mechanical and microstructural properties with variation in chemical composition, Mater. Des. 197 (2021) 109221. https://doi.org/10.1016/j.matdes.2020.109221.
[27] A. Röttger, K. Geenen, M. Windmann, F. Binner, W. Theisen, Comparison of microstructure and mechanical properties of 316 L austenitic steel processed by selective laser melting with hot-isostatic pressed and cast material, Mater. Sci. Eng. A 678 (2016) 365–376. https://doi.org/10.1016/j.msea.2016.10.012.

[28] O. Andreau, E. Pessard, I. Koutiri, J.-D. Penot, C. Dupuy, N. Saintier, P. Peyre, A competition between the contour and hatching zones on the high cycle fatigue behaviour of a 316L stainless steel: Analyzed using X-ray computed tomography, Mater. Sci. Eng. A 757 (2019) 146–159. https://doi.org/10.1016/j.msea.2019.04.101.

[29] G. Wang, Q. Liu, H. Rao, H. Liu, C. Qiu, Influence of porosity and microstructure on mechanical and corrosion properties of a selectively laser melted stainless steel, J. Alloys Compd. 831 (2020) 154815. https://doi.org/10.1016/j.jallcom.2020.154815.

[30] W.M. Tucho, V.H. Lysne, H. Austbø, A. Sjolyst-Kverneland, V. Hansen, Investigation of effects of process parameters on microstructure and hardness of SLM manufactured SS316L, J. Alloys Compd. 740 (2018) 910–925. https://doi.org/10.1016/j.jallcom.2018.01.098.

[31] R. Cunningham, S.P. Narra, C. Montgomery, J. Beuth, A.D. Rollett, Synchrotron-based X-ray microtomography characterization of the effect of processing variables on porosity formation in laser power-bed additive manufacturing of Ti-6Al-4V, JOM 69 (2017) 479–484. https://doi.org/10.1007/s11837-016-2234-1.

[32] R. Cunningham, C. Zhao, N. Parab, C. Kantzos, J. Pauza, K. Fezzaa, T. Sun, A.D. Rollett, Keyhole threshold and morphology in laser melting revealed by ultrahigh-speed x-ray imaging, Science 363 (2019) 849–852. https://doi.org/10.1126/science.aav4687.

[33] T. Niendorf, S. Leuders, A. Riemer, H.A. Richard, T. Tröster, D. Schwarze, Highly anisotropic steel processed by selective laser melting, Metall. Mater. Trans. B 44 (2013) 794–796. https://doi.org/10.1007/s11663-013-9875-z.

[34] A. Riemer, S. Leuders, M. Thöne, H.A. Richard, T. Tröster, T. Niendorf, On the fatigue crack growth behavior in 316L stainless steel manufactured by selective laser melting, Eng. Fract. Mech. 120 (2014) 15–25. https://doi.org/10.1016/j.engfracmech.2014.03.008.

[35] A.B. Spierings, T.L. Starr, K. Wegener, Fatigue performance of additive manufactured metallic parts, Rapid Prototyp. J. 19 (2013) 88–94. https://doi.org/10.1108/13552541311302932.

[36] H. Javadi, W. Jomaa, D. Texier, M. Brochu, P. Bocher, Surface roughness effects on the fatigue behavior of as-machined Inconel 718, Solid State Phenom. 258 (2016) 306–309. https://doi.org/10.4028/www.scientific.net/SSP.258.306.

[37] D. Wu, D. Zhang, C. Yao, Effect of turning and surface polishing treatments on surface integrity and fatigue performance of nickel-based alloy GH4169, Metals 8 (2018) 549. https://doi.org/10.3390/met8070549.

[38] A. Damiens, H. Bonnefoy, I. Titeux, Influence of processing parameters on mechanical and fatigue properties of 316 L steel manufactured by selective laser melting, Weld. World 64 (2020) 1321–1328. https://doi.org/10.1007/s40194-020-00885-4.

[39] M. Zhang, C.-N. Sun, X. Zhang, J. Wei, D. Hardacre, H. Li, High cycle fatigue and ratcheting interaction of laser powder bed fusion stainless steel 316L: Fracture behaviour and stress-based modelling, Int. J. Fatigue 121 (2019) 252–264. https://doi.org/10.1016/j.ijfatigue.2018.12.016.

[40] Y. Murakami, Metal Fatigue: Effects of Small Defects and Nonmetallic Inclusions, Second, Elsevier, 2019.

[41] Y. Murakami, M. Endo, Effects of defects, inclusions and inhomogeneities on fatigue strength, Int. J. Fatigue 16 (1994) 163–182. https://doi.org/10.1016/0142-1123(94)90001-9.

[42] Y. Murakami, Stress concentration, in: Met. Fatigue Eff. Small Defects Nonmet. Incl., Second, Elsevier, 2019.

[43] M. Sprengel, A. Ulbricht, A. Evans, A. Kromm, K. Sommer, T. Werner, J. Kelleher, G. Bruno, T. Kannengiesser, Towards the optimization of post-laser powder bed fusion stress-relieve treatments of stainless steel 316L, Metall. Mater. Trans. A 52 (2021) 5342–5356. https://doi.org/10.1007/s11661-021-06472-6.
[44] J.L. Bartlett, X. Li, An overview of residual stresses in metal powder bed fusion, Addit. Manuf. 27 (2019) 131–149. https://doi.org/10.1016/j.addma.2019.02.020.
[45] Z.-C. Fang, Z.-L. Wu, C.-G. Huang, C.-W. Wu, Review on residual stress in selective laser melting additive manufacturing of alloy parts, Opt. Laser Technol. 129 (2020) 106283. https://doi.org/10.1016/j.optlastec.2020.106283.
[46] W. Chen, T. Voisin, Y. Zhang, J.-B. Florien, C.M. Spadaccini, D.L. McDowell, T. Zhu, Y.M. Wang, Microscale residual stresses in additively manufactured stainless steel, Nat. Commun. 10 (2019) 4338. https://doi.org/10.1038/s41467-019-12265-8.
[47] A.S. Wu, D.W. Brown, M. Kumar, G.F. Gallegos, W.E. King, An experimental investigation into additive manufacturing-induced residual stresses in 316L stainless steel, Metall. Mater. Trans. A 45 (2014) 6260–6270. https://doi.org/10.1007/s11661-014-2549-x.
[48] L. van Belle, G. Vansteenkiste, J.C. Boyer, Investigation of residual stresses induced during the selective laser melting process, Key Eng. Mater. 554–557 (2013) 1828–1834. https://doi.org/10.4028/www.scientific.net/KEM.554-557.1828.
[49] Y. Liu, Y. Yang, D. Wang, A study on the residual stress during selective laser melting (SLM) of metallic powder, Int. J. Adv. Manuf. Technol. 87 (2016) 647–656. https://doi.org/10.1007/s00170-016-8466-y.
[50] P. Mercelis, J. Kruth, Residual stresses in selective laser sintering and selective laser melting, Rapid Prototyp. J. 12 (2006) 254–265. https://doi.org/10.1108/13552540610707013.
[51] B. Cheng, S. Shrestha, K. Chou, Stress and deformation evaluations of scanning strategy effect in selective laser melting, Addit. Manuf. 12 (2016) 240–251. https://doi.org/10.1016/j.addma.2016.05.007.
[52] J.P. Oliveira, A.D. LaLonde, J. Ma, Processing parameters in laser powder bed fusion metal additive manufacturing, Mater. Des. 193 (2020) 108762. https://doi.org/10.1016/j.matdes.2020.108762.
[53] C. Li, Z.Y. Liu, X.Y. Fang, Y.B. Guo, Residual stress in metal additive manufacturing, Procedia CIRP 71 (2018) 348–353. https://doi.org/10.1016/j.procir.2018.05.039.
[54] ASTM International, F3184-16 Standard specification for additive manufacturing stainless steel alloy (UNS S31603) with powder bed fusion, (2023).
[55] American Iron and Steel Institute, Specialty Steel Institute of North America, Specialty Steel Industry of the United States, Nickel Development Institute (Canada), Design guidelines for the selection and use of stainless steel, Specialty Steel Industry of the United States, Pennsylvania State University, 1993.
[56] P.D. Harvey, ed., Stainless and Heat-Resisting Steels, in: Eng. Prop. Steel, American Society for Metals, Metals Park, Ohio 44073, 1999.
[57] Institute of Physics and Materials Science, BOKU, Vienna, Ultrasonic Fatigue Testing Equipment, (2009).
[58] M. Fitzka, B.M. Schönbauer, R.K. Rhein, N. Sanaei, S. Zekriardehani, S.A. Tekalur, J.W. Carroll, H. Mayer, Usability of ultrasonic frequency testing for rapid generation of high and very high cycle fatigue data, Materials 14 (2021) 2245. https://doi.org/10.3390/ma14092245.

[59] F.G. Pascual, W.Q. Meeker, Estimating fatigue curves with the random fatigue-limit model, Technometrics 41 (1999) 277–289. https://doi.org/10.1080/00401706.1999.10485925.

[60] C.C. Engler-Pinto Jr, J.V. Lasecki, R.J. Frisch Sr, J.E. Allison, Statistical approaches applied to very high cycle fatigue, in: VHCF4, TMS, 2007: pp. 369–376.

[61] O.H. Basquin, The exponential law of endurance tests, in: ASTM Proc., 1910: pp. 625–630.

[62] C.C. Engler-Pinto Jr, J.V. Lasecki, R.J. Frisch Sr, M.A. Dejack, J.E. Allison, Statistical approaches applied to fatigue test data analysis, in: SAE 2005 World Congr. Exhib., SAE, 2005: pp. 2005-01–0802. https://doi.org/10.4271/2005-01-0802.

[63] ISO/TC 213, Geometrical product specifications (GPS) - Surface texture: Areal - Part 2: Terms, definitions and surface texture parameters (ISO 25178-2:2021), (2021).

[64] S. Leuders, T. Lieneke, S. Lammers, T. Tröster, T. Niendorf, On the fatigue properties of metals manufactured by selective laser melting – The role of ductility, J. Mater. Res. 29 (2014) 1911–1919. https://doi.org/10.1557/jmr.2014.157.

[65] Q. Chao, S. Thomas, N. Birbilis, P. Cizek, P.D. Hodgson, D. Fabijanic, The effect of post-processing heat treatment on the microstructure, residual stress and mechanical properties of selective laser melted 316L stainless steel, Mater. Sci. Eng. A 821 (2021) 141611. https://doi.org/10.1016/j.msea.2021.141611.

[66] V. Cruz, Q. Chao, N. Birbilis, D. Fabijanic, P.D. Hodgson, S. Thomas, Electrochemical studies on the effect of residual stress on the corrosion of 316L manufactured by selective laser melting, Corros. Sci. 164 (2020) 108314. https://doi.org/10.1016/j.corsci.2019.108314.

[67] O. Fergani, A. Bratli Wold, F. Berto, V. Brotan, M. Bambach, Study of the effect of heat treatment on fatigue crack growth behaviour of 316L stainless steel produced by selective laser melting, Fatigue Fract. Eng. Mater. Struct. 41 (2018) 1102–1119. https://doi.org/10.1111/ffe.12755.

[68] B. Blinn, F. Krebs, M. Ley, R. Teutsch, T. Beck, Determination of the influence of a stress-relief heat treatment and additively manufactured surface on the fatigue behavior of selectively laser melted AISI 316L by using efficient short-time procedures, Int. J. Fatigue 131 (2020) 105301. https://doi.org/10.1016/j.ijfatigue.2019.105301.

[69] D.J. Rowenhorst, L. Nguyen, A.D. Murphy-Leonard, R.W. Fonda, Characterization of microstructure in additively manufactured 316L using automated serial sectioning, Curr. Opin. Solid State Mater. Sci. 24 (2020) 100819. https://doi.org/10.1016/j.cossms.2020.100819.

[70] N. Sanaei, A. Fatemi, Defects in additive manufactured metals and their effect on fatigue performance: A state-of-the-art review, Prog. Mater. Sci. 117 (2021) 100724. https://doi.org/10.1016/j.pmatsci.2020.100724.

[71] N. Sanaei, A. Fatemi, Phan, Defect characteristics and analysis of their variability in metal L-PBF additive manufacturing, Mater. Des. (2019). https://doi.org/10.1016/j.matdes.2019.108091.

[72] A.E. Wilson-Heid, T.C. Novak, A.M. Beese, Characterization of the effects of internal pores on tensile properties of additively manufactured austenitic stainless steel 316L, Exp. Mech. 59 (2019) 793–804. https://doi.org/10.1007/s11340-018-00465-0.

[73] H. Yao, R. Katona, J. Zhou, M.I. Islam, J. Raush, F. Lu, S. Guo, Defects evaluation of selective laser melting stainless steel 316 parts using positron annihilation lifetime measurement, in: Vol. 8B Heat Transf. Therm. Eng., American Society of Mechanical

Engineers, Pittsburgh, Pennsylvania, USA, 2018: p. V08BT10A057. https://doi.org/10.1115/IMECE2018-86729.

[74] E.J. Czyryca, ASM Committee on Fatigue Crack Propagation, R.P. Gangloff, eds., Fatigue Testing, in: Met. Handb. Mech. Test., 9th ed., American Society for Metals, Metals Park, Ohio 44073, 1985: pp. 361–436.

Chapter 5 Short Fatigue Crack Growth and S-N Prediction in 316L Stainless Steel Manufactured via Laser Powder Bed Fusion

5.1 Introduction

Metal additive manufacturing (AM) is a manufacturing technique which is increasingly becoming of interest for its many advantages over conventional manufacturing methods [1,2]. Due to the complex thermal history produced in AM components, metal AM is the subject of significant investigation to establish process-structure-property (PSP) relationships. In the age of integrated computational materials engineering (ICME) [3-5], it is often the goal to understand the mechanisms behind the PSP relationships in order to accurately model and predict material behavior) [3–5]. One topic that has been the subject of numerous studies is the fatigue behavior of AM parts. Fatigue behavior has been shown to strongly depend on the AM processing parameters as these dictate the thermal history of the part. While there is a fair understanding of how the thermal history influences the fatigue response [2], there is still much to learn about the mechanisms that drive this behavior. It is important to understand how changes to the AM process influence both fatigue crack initiation and growth.

Crack initiation and crack growth are influenced by microstructure, defects, and residual stresses. In laser-powder bed fusion (L-PBF), there are over 130 process variables that collectively dictate the final microstructure, defect morphology, and residual stress of the component [6,7]. Extensive research has been done on how these processing parameters interact to create the desired outcome, the most investigated of which are the ones easiest to control (e.g., laser power, scan speed, hatch spacing, layer thickness, laser spot size, scan strategy, etc.) [8–26]. For 316L stainless steel, in particular, several studies have been conducted to determine the influence of build orientation and heat treatment on the crack growth behavior [27–31]. Of these studies, none have evaluated the crack growth behavior in ultrasonic fatigue test specimens, nor have they made a prediction of the fatigue life (S-N) behavior or made direct comparisons to S-N data. To the authors best knowledge, there have been no reports that involve direct comparisons of specimens fabricated using different L-PBF machines on fatigue crack growth behavior. This study aims to fill those gaps while discussing mechanisms behind crack initiation and growth under various conditions.

In this study, fatigue samples of 316L stainless steel were manufactured via L-PBF on either a Concept Laser M2 or a ProX DMP 200 AM machine for characterization of the high cycle fatigue (HCF) and fatigue crack growth (FCG) behavior. For fatigue lifetime analysis, specimens were built in the vertical orientation and were left in the as-built state, stress-relieved, or had the as-built surface removed via low stress grinding. For crack growth analysis, specimens were built in both the vertical and horizontal orientations and were left in the as-built state or were stress-relieved. Scanning electron microscopy (SEM) analysis of the fracture surfaces of failed specimens were used to identify and quantify fatigue crack initiation sites. Using the measured FCG characteristics and defect data, predictions were made of the S-N response and compared to the true S-N response of tested specimens. Conclusions are drawn regarding the mechanisms influencing HCF and FCG behavior in L-PBF applications.

5.2 Materials and Methods

5.2.1 Material properties

The focus of this work is on 316L stainless steel powder particles manufactured using L-PBF systems. All specimens were manufactured using either GE Additive Concept Laser GmbH CL 20ES or 3D Systems Phenix LaserForm 316L powder particles. The chemical composition of each powder is shown in Table 5.1, compared to the ASTM standard for AISI 316L used for additive manufacturing [32]. Both powders used were a combination of virgin and sieved particles, with particle size distribution and average sphericity shown in Table 5.2. A portion of the CL 20ES powder batch was used to manufacture L-PBF tensile samples for bulk mechanical property measurements (Table 5.3). Measurements were taken in both the vertical and horizontal build.

Table 5.1. Chemical composition (in wt. %) of AISI 316L stainless steel bulk and GE Additive CL 20ES powder particles as listed by GE Additive and measured vie EDS.

Type	Fe	Cr	Ni	Mo	C	Mn	P	S	Si
Standard [32]	Balance	16.0-18.0	10.0-14.0	2.0-3.0	0.030	2.00	0.045	0.030	1.00
Concept Laser	Balance	16.5-18.5	10.0-13.0	2.0-2.5	0.030	2.00	0.045	0.030	1.00
Phenix	Balance	16.0-18.0	10.0-14.0	2.0-3.0	0.030	2.00	0.045	0.030	1.00

Table 5.2. Powder particle size (in μm) cumulative distribution function of GE Additive CL 20ES and 3DSystems Phenix LaserForm 316L stainless steel powder.

	10%	50%	90%	Avg Sphericity
CL 20ES Virgin	21.5	30.4	43.5	0.790
CL 20ES Virgin + Sieved	20.2	30.1	44.8	0.791
LaserForm Virgin	14.6	24.6	40.3	0.793
LaserForm Virgin + Sieved	12.6	24.2	40.7	0.786

Table 5.3. Mechanical properties of CL 20ES virgin + sieved 316L austenitic stainless steel at room temperature.

Type	Elastic Modulus [GPa]	Tensile Strength [MPa]	Yield Strength 0.2% Offset [MPa]
Vertical	165 ± 4	565 ± 7	467 ± 4
Horizontal	202 ± 5	691 ± 13	579 ± 3

5.2.2 Specimen fabrication and processing

5.2.2.1 Processing parameters

All specimens were manufactured using either a GE Additive Concept Laser M2 (CL M2) at the US Naval Research Laboratory (NRL) or a 3D Systems ProX DMP 200 (ProX 200) at the Naval Surface Warfare Center – Carderock Division (NSWC). The processing parameters used, listed in Table 5.4, are the recommended parameters from each respective system manufacturer.

Table 5.4. Laser powder bed fusion (L-PBF) process parameters for every build, as recommended by 3D Systems for 316L stainless steel.

	Laser Power	Scan Speed	Layer Thickness	Jump Speed	Hatch Spacing	Spot Size
CL M2	370 W	900 mm/s	25 μm	unknown	unknown	160 μm
ProX 200	129 W	1400 mm/s	30 μm	5000 mm/s	50 μm	50 μm

All specimens were fabricated in a cylindrical dog-bone geometry to accommodate ultrasonic fatigue testing specimen requirements. Specimens built on the CL M2 were manufactured in the vertical orientation, while specimens manufactured on the ProX 200 were built in the vertical and horizontal orientations. The as-built gauge diameter was 5.0 mm for all specimens. The geometry for the specimens is identical across platforms (Figure 5.1) with the only change being orientation and support structures. This geometry was designed to resonate at 20 kHz, a necessity for ultrasonic fatigue testing. Each build layer starts with the infill and ends with multiple contour passes around the perimeter. The infill scan pattern for the CL M2 and ProX 200 are known to be different, however the specifics are proprietary and unknown to the authors. All specimens were removed from the build plates using electro-discharge machining (EDM), followed by machining an M8x1.0mm thread on one end for insertion into the ultrasonic fatigue (UF) testing equipment.

5.2.2.2 Test matrix

In this work, the specimens depicted in Figure 5.1 can be separated into seven operating groups, as described in Table 5.5. Each of the seven groups is designated for one or both uses: ultrasonic fatigue (UF) testing or fatigue crack growth (FCG) testing. Under the umbrella use of UF testing, specimens are investigated for the purposes of generating a high cycle fatigue-life (S-N) curve, calculating the fatigue strength, and quantifying crack initiating elements. These specimens are separated into five groups for UF testing: CCV-au, CCV-hu, CCV-su, CCV-cu, and PCV-au. Under the umbrella use of FCG testing, specimens are investigated for the purposes of generating FCG data, plotting the da/dN vs. ΔK behavior, and computing S-N predictions. Three groups were FCG tested: CCV-ad, CCV-hd, and PPH-ad. A fourth and fifth group (PCV-ad and PPV-ad) were planned, however due to AM miss-prints, the specimens exhibited excessive large lack-of-fusion (LOF) pores that precluded FCG characterization for these conditions.

Table 5.5. Specimen group designation by build system, powder, and orientation.

Designation	Machine	Powder	Orientation	Condition	Use
CCV-au/d	CL M2	CL 20ES	Vertical	As-built	UF, FCG
CCV-hu/d	CL M2	CL 20ES	Vertical	Stress-relieved	UF, FCG
CCV-su	CL M2	CL 20ES	Vertical	Surface-removed	UF
CCV-cu	CL M2	CL 20ES	Vertical	Contour-removed	UF
PCV-au	ProX 200	CL 20ES	Vertical	As-built	UF
PPH-au/d	ProX 200	LaserForm 316L	Horizontal	As-built	FCG
PPV-ad	ProX 200	LaserForm 316L	Vertical	As-built	-

5.2.2.3 Fatigue crack growth specimens

Specimens subjected to FCG testing underwent additional machining, polishing, and focused ion beam (FIB) notching. A 1.96 mm wide flat was machined out of the gauge section by removing 200 μm from the diameter via machining at Westmoreland Mechanical Testing & Research in Youngstown, PA. The flat was subsequently smoothed by hand using increasingly fine grit SiC grinding paper and polished using 1 μm diamond suspension followed by 0.04 μm colloidal silica. A PFIB notch was placed perpendicular to the loading axis to induce fatigue cracking at a specific location that can be observed by the researchers (Figure 5.2). This notch was made to be 100 μm deep, 200x20 μm and was cut out of the surface using a Thermo Scientific^{TM} Helios^{TM} G4 Plasma FIB UXe.

5.2.2.4 Surface removal

The as-built sample surface was removed from sixteen CL M2 specimens to characterize both the impact of reducing the as-built surface roughness and removing the L-PBF contour passes from the printed part. Material removal was done under low-stress using a RTS (Leeds) Ltd Sample Polishing Machine at Element Materials Technology in Wixom, MI. The CL M2 samples show a clear distinction between the infill and contour regions, with differing microstructures and defect concentrations, as shown in Figure 5.3. Removing the as-built surface was characterized into two groups: surface-removed (Figure 5.3 b) and contour-removed (Figure 5.3 c). The surface-removed specimens have approximately 75 μm removed from the surface while the contour-removed specimens have the entire contour passes (approximately 150 μm) removed from the surface.

5.2.2.5 Residual stress and stress relief

The axial residual stress was measured on three specimens: one as-built CL M2 specimen (CCV-au), one stress-relieved CL M2 specimen (CCV-hu), and one as built ProX 200 specimen (PCV-au). Residual stress measurements are done using x-ray diffraction with material removal via electropolishing to obtain a profile of residual stress versus depth from the surface. Specimens were measured using an LXRD 13115 with a Mn target, x-ray elastic constant of 20,199 ksi (139,000 MPa), {311} crystallographic plane, and 152.8° Bragg angle. Residual stress measurements were conducted by Proto Manufacturing Inc in Taylor, MI

In addition to measuring the residual stress, a partial relief of the residual stress was conducted by heat treating eight CL M2 specimens. A stress relief anneal was completed in a Lindberg 1700°C tube furnace in a sealed Argon environment. The anneal consisted of a forty-five minute heat-up, four hour soak at 650°C, and a three hour furnace cool to room temperature. These conditions were chosen to provide stress relief while limiting microstructural changes [27,28,33–36].

5.2.3 Ultrasonic fatigue testing

Ultrasonic fatigue (UF) testing is used in this study for its ability to rapidly obtain high cycle fatigue (HCF, 10^4 to 10^7 cycles) and very high cycle fatigue (VHCF, $>10^7$ cycles) data. UF testing is conducted at room temperature on equipment developed by University of Natural Resources and Life Sciences, Vienna (BOKU) [37] and operated at 20 kHz. Operating at 20 kHz allows for HCF and VHCF data to be obtained in hours or days compared to months or years it would take operating at 20-60 Hz as is typical in servo-hydraulic fatigue testing. UF testing can be used and compared to conventional fatigue data in this work as it has been shown that the frequency of testing has no effect on the fatigue behavior in austenitic stainless steels [38]. Experimentation was conducted under fully reversed ($R = -1$) loading. Failure was defined as the point in life at which the UF instrumentation detects a change in frequency greater than 200 Hz from the starting resonant frequency of approximately 20 kHz. A value of 200 Hz was chosen to allow the crack to propagate sufficiently to be observed by the naked eye but not fully fracture the specimen. If a specimen does not meet this failure criteria prior to 10^8 cycles, it was deemed a runout.

The HCF testing protocol consists of four steps: (1) statistical sample of intermediate-stress level fatigue (~20 samples); (2) statistical sample of high-stress level fatigue (~10 samples); (3)

quantification of fatigue strength at 10^8 cycles using staircase testing at low-stress fatigue (~10 samples); and (4) application of a Random Fatigue Limit (RFL) model using a Maximum Likelihood Estimation (MLE) to quantify statistical variability and estimate the S-N curve and fatigue strength.

5.2.4 Fatigue strength estimations

A life-regression model was used to quantitatively describe the fatigue properties of a given sample group from the experimental fatigue-life (S-N) tests described above. There are multiple models that can be used to generate an S-N curve from fatigue data, including the Random Fatigue Limit (RFL) model [39] which is used herein. The RFL curve fit acts as a metric to more readily compare the fatigue life and strength of each sample group at varying stresses. The RFL model can be used for a range of different distributions and constraints, making it important to implement a Maximum Likelihood Estimation (MLE) to the calculation of the RFL model. In the current investigation, this was done following the methods outlined by Engler-Pinto Jr. et al. [40]. MLE analysis has shown that a Weibull distribution is the best fit in most cases, so, in the current investigation this is the distribution used in each RFL analysis. Once the appropriate RFL model is selected, the fatigue limit and fatigue strength can be calculated for the entire dataset, including runout values. The RFL model was selected in place of other models such as the Modified Basquin model [41,42] as it has been shown to generally provide a better fit to HCF data as determined by MLE [42].

An experimental method for estimating the fatigue strength is the staircase method. This is a fatigue testing method which sequentially tests samples at varying stress levels. The first sample is tested at a pre-determined stress and observed to be either a failure or a runout. The following sample is tested at a higher stress if the previous sample was a runout and a lower stress if it was a failure. This continues for any number of samples, resulting in a roughly even split of runouts and failures. The median stress of these tests is used as an estimate of the median fatigue strength of the material, with the assumption that the fatigue strength is normally distributed. For its simplicity, this method was used to test a portion of the sample group, however, an RFL model is still applied to the entire dataset as it is more accurate in predicting the fatigue strength of data that is not normally distributed [42].

5.2.5 Fatigue crack growth testing

Fatigue crack growth (FCG) testing is done using the same UF set-up described above. A Keyence optical microscope was focused on the PFIB notch and images of the surface were taken every ~3,000 cycles. The resolution of the optical microscope was such that crack length measurements could be reliably taken as small as 2 μm. The total length of the crack emanating from both sides of the PFIB notch, including the length of the notch, defines the surface crack length, $2c$. The stress intensity factor, K_I, at each measure of the surface crack length is calculated following Eq. 5.1 defined by Newman-Raju [43]. S_t is the remote uniform-tension stress, a is the depth of the surface crack, c is the half-length of the surface crack, b is the half-width of the cracked surface (half the diameter of the gauge section, 2.5 mm), t is the plate thickness (diameter of the gauge section, 5.0 mm), Q is the shape factor for an elliptical crack ($Q = 2.464$), ϕ is the parametric angle of the ellipse, and F is the stress-intensity boundary-correction factor. In this work, a is assumed to be equal to c at all instances, subsequently making $\phi = 45°$. The fatigue crack growth rate, da/dN, is calculated using the seven-point sliding polynomial method and measured values of cycles, N, and crack length, a from the FCG tests.

$$K_I = S_t \sqrt{\pi \frac{a}{Q}} F\left(\frac{a}{t}, \frac{a}{c}, \frac{c}{b}, \phi\right) \qquad 5.1$$

5.2.6 Small crack fracture mechanics prediction

The fatigue lifetime (S-N curve) of a given sample group can be predicted using a small crack fracture mechanics approach [44,45]. Assuming the crack growth rate follows a power law function, the Paris law [46], shown in Eq. 5.2, is fit to the da/dN vs. ΔK data in order to find the constants C and m. A least square fit was used to determine the Paris Law constants C and m. An integration of Eq. 5.2 yields an equation for the propagation lifetime, N_p, as a function of crack length, shown in Eq. 5.3. The initiation life is assumed to be negligible and N_p is equated to the fatigue lifetime in the small diameter fatigue sample. As a means of predicting the fatigue behavior of a sample group, Eq. 5.3 utilizes the initiating defect size data obtained from the fracture surface analysis of UF test specimens. The initial crack length, a_i, is considered to be the effective initiating defect size, $\sqrt{area}$, as defined by Murakami [47]. The final crack length, a_f, is the size of the fracture surface, approximately half the gauge diameter, 2.5 mm. Minimum, maximum, and average defect size values were used as a_i to show the variation in fatigue lifetime prediction for different sized defects.

$$\frac{da}{dN} = C\Delta K^m \qquad 5.2$$

$$N_p = \int_{a_i}^{a_f} \frac{\Delta K^{-m}}{C} da \qquad 5.3$$

5.3 Results and Discussion

5.3.1 Ultrasonic fatigue behavior

5.3.1.1 As-built specimens

The ultrasonic fatigue behavior of 45 as-built CL M2 (CCV-au) and 36 as-built ProX 200 (PCV-au) specimens are compared. The UF results of the two groups, CCV-au and PCV-au, are shown in Figure 5.4. Each set of S-N results were fit using the RFL model assuming a Weibull distribution informed by MLE. The fatigue strength as determined by RFL and staircase testing is also shown in Figure 5.4. Both groups (CCV-au and PCV-au) use the same powder, sample geometry, and build orientation, but different L-PBF machines and different print parameters. The fatigue response indicates a slightly longer fatigue life at higher stress for the PCV-au samples. The fatigue strength at 10^8 cycles is nearly indistinguishable between the CCV-au and PCV-au specimen groups, at 89.5 ± 5.59 MPa and 89.0 ± 9.90 MPa, respectively. The fatigue strength as determined by staircase testing is in good agreement with that of the RFL analysis.

5.3.1.2 Stress-relief and residual stress

Eight as-built CL M2 specimens were stress-relieved and UF tested to characterize the effects of stress-relief on fatigue behavior. The eight stress-relieved specimens, designated CCV-hu, are compared to the 46 as-built CCV-au specimens and shown in Figure 5.5. Due to a limited number of test specimens and the stress they were tested at, the RFL analysis for the CCV-hu specimens is accurate only for lower stress fatigue behavior. Despite the few number of specimens, it can be concluded that the stress-relief results in a higher fatigue strength at 10^8 cycles. The fatigue strength for the stress-relieved specimens (CCV-hu) and as-built specimens (CCV-au) are 115.0 ± 7.36 MPa and 89.5 ± 5.59 MPa, respectively.

Axial residual stress measurements in the gauge section were conducted both before and after stress-relief on two CL M2 (CCV-hu) specimens. In one specimen, surface residual stresses were measured followed by measurement of a residual stress depth profile. The other specimen had surface residual stress measurements taken in the as-built condition followed by stress-relieving and subsequent residual stress measurement. The depth profile shown in Figure 5.6 shows that the residual stress distribution is in a tensile state at the surface and transitions to a compressive state at the specimen core region. Tensile residual stresses are highest just below the surface, where the contour and infill meet. The amount of stress reduction achieved by stress-relieving is shown in Figure 5.7 and is found to be an almost 50% reduction. Tensile residual stresses have been shown to negatively affect the fatigue behavior in L-PBF samples, so the fatigue response seen in Figure 5.5 is consistent with the stress reduction observed.

5.3.1.3 Surface removal

Removing the as-built surface finish by means of surface-removal (CCV-su) and contour-removal (CCV-cu) results in significant improvement in fatigue behavior. Figure 5.8 shows substantially longer fatigue lives at higher stress for the surface-removed and contour-removed CL M2 specimens as compared to the as-built (CCV-au) specimens. The fatigue strength at 10^8 cycles is found to be 168.0 ± 12.6 MPa and 182.0 ± 8.91 MPa for the CCV-su and CCV-cu groups, respectively. There is a mild improvement in the fatigue behavior of the CCV-cu specimens over the CCV-su specimens, though it should be noted that the small population sizes (8 specimens) of each group make estimating statistical significance of these small differences difficult. These results demonstrate that the surface region has a substantial influence on the fatigue behavior. This improvement is attributed to both the reduction in surface roughness and removal of surface crevices, which have been shown to be the source of crack initiation in these specimens [Chapter 3].

5.3.2 Fatigue crack growth behavior

Figure 5.9 shows the crack growth behavior of the three specimen groups that were tested, vertical CL M2 as-built (CCV-ad), vertical CL M2 stress-relieved (CCV-hd), and horizontal ProX 200 (PPH-au). Figure 5.9 indicates that the crack growth behavior is similar for L-PBF 316L despite build platform, source powder, build orientation, or stress-relieving. Despite the apparent lack of significant differences between groups, the crack length vs cycles curves shown in Figure 5.10, suggest that time to crack initiation differs significantly. This shows that the start of crack growth is slowest in the PPH-ad specimens, fastest in the CCV-ad and CCV-hd specimens. While crack growth rates are similar, it takes more time for the stress-relieved and horizontal specimens to reach the failure criteria, compared to the as-built, vertical specimens.

5.3.3 Fracture surface analysis

5.3.3.1 As-built ProX 200

The sole source of fatigue crack initiation in UF tested PCV-au specimens are surface-connected LOF pores (Figure 5.11). The stress concentration factor, K_{Imax}, near the crack tip emanating from these surface-connected LOF pores is defined by Murakami's equation for an arbitrarily shaped surface crack [47,48] in Eq. 5.4.

$$K_{Imax} \cong 0.65\sigma_0\sqrt{\pi\sqrt{area}} \qquad 5.4$$

Here, σ_0 is the maximum loading stress during UF testing, in MPa, and $\sqrt{area}$ is the square-root equivalent traced area of the initiating defect normal to the loading direction, in m [47,48]. The LOF pores likely arise due to the low energy density, indicated by the processing parameters in

Table 3.4. The largest, smallest, and average defect sizes in this specimen group are 223 μm, 85 μm, and 134 μm, respectively (Table 5.6).

5.3.3.2 As-built and stress-relieved CL M2

The primary source of fatigue crack initiation in UF tested CCV-au specimens is surface crevices. Surface crevices act as surface cracks whose stress intensity factor is also given by Eq. 5.4. The surface crevice arises from a combination of surface notches dictated by melt pool size between build layers on the outer surface of L-PBF parts [49] and tensile residual stress assisted crack opening causing mild delamination between build layers [Chapter 3]. The largest, smallest, and average defect sizes in this specimen group are 260 μm, 47 μm, and 121 μm, respectively (Table 5.6).

As with the as-built CL M2 specimens (CCV-au), the source of crack initiating in the CCV-hu specimens is predominantly surface crevices. The largest, smallest, and average defect sizes in this specimen group are 247 μm, 62 μm, and 149 μm, respectively (Table 5.6).

5.3.3.3 Surface-removed and contour-removed CL M2

Removing the as-built surface finish in CL M2 specimens removes the surface crevices that act as fatigue crack initiation sites in the CCV-au and CCV-hu specimens, leaving behind a smooth, relatively defect-free surface. The source of crack initiation in the surface-removed (CCV-su) and contour-removed (CCV-cu) specimens then comes from sub-surface defects. With no connection to the surface, the initial crack growth occurs in vacuum, leaving behind distinct fisheye fracture surfaces [7,38,50–52] seen in Figure 5.13. The CCV-su and CCV-cu specimens have differing fracture surface from each other, in that the CCV-su defects tend to be smaller and closer to the surface. The CCV-cu fracture surfaces also contain an additional feature within the fisheye: the fine granular area (FGA) [52,53]. The distinction between the FGA and the rest of the fisheye is demonstrated in Figure 5.14. The largest, smallest, and average defect sizes in the CCV-su specimen group are 80 μm, 47 μm, and 61 μm, respectively. The largest, smallest, and average defect sizes in the CCV-cu specimen group are 147 μm, 82 μm, and 105 μm, respectively (Table 5.6).

Table 5.6. Maximum, minimum, and average defect size as defined by Murakami's √area parameter for each group subjected to ultrasonic fatigue testing.

Specimens	Max defect size [μm]	Min defect size [μm]	Average defect size [μm]
PCV-au	223	85	134
CCV-au	260	47	121
CCV-hu	247	49	162
CCV-su	80	47	61
CCV-cu	147	82	105

5.3.4 Fatigue life prediction modeling

In every specimen group, crack initiation occurred at a pre-existing defect whose size can be quantified by Murakami's $\sqrt{area}$ parameter [54]. Pre-existing defects act as pre-existing cracks, therefore the crack initiation time can be neglected and sole focus can be placed on modeling crack growth behavior. In all specimens with the as-built surface maintained, crack initiation occurred at surface-connected defects whose K_{Imax} is described by Eq. 5.4, allowing for S-N prediction informed only by defect size and crack growth behavior.

5.3.4.1 Determining ΔK_{th}

316L stainless steel is known to exhibit an endurance limit (Figure 5.4, Figure 5.5, Figure 5.8) at which the test specimen can withstand an infinite number of cycles without failure [55]. This effect is attributed to non-propagating cracks [56], suggesting that the existence of cracks in the material does not necessitate fatigue failure if the crack is sufficiently small relative to the applied stress. This threshold for crack growth is denoted ΔK_{th} and its value can be determined in a number of ways. If crack growth testing in the threshold regime (typically 10^{-10} to 10^{-13} m/cycle [52]), ΔK_{th} can be taken as the lowest measured value of ΔK. The lowest average crack growth rates measured in this work were between 10^{-9} and 10^{-10} m/cycle for the CL M2 specimens and 10^{-10} m/cycle for the ProX 200 specimens. For values such as these it is possible to define the ΔK_{th} as the ΔK value at 10^{-10} m/cycle as determined by a fit of the FCG data by the Paris Law (Eq. 5.2). The ΔK_{th} can be seen in Figure 5.15 with their respective Paris Law fit. Figure 5.15 shows that the stress-relieved CL M2 (CCV-hd) specimens have the lowest ΔK_{th} value at 1 MPa√m, followed by as-built CL M2 (CCV-ad) at 1.15 MPa√m and as-built ProX 200 condition (PPH-ad) at 1.36 MPa√m. Another method for predicting ΔK_{th} comes from Murakami's $\sqrt{area}$ parameter model, which allows for the prediction of threshold values without the need of fatigue data [57]. For this current work, it was found that this method significantly overestimates ΔK_{th}, with the lowest value predicted being 3.49 MPa√m and the highest being 6.17 MPa√m. One final method of estimating an apparent ΔK_{th} comes directly from the UF data and the Paris Law. This method sets the apparent threshold stress value equal to the fatigue strength as determined by RFL analysis. Using the C and m constants determined by the Paris Law fit of the FCG data and the initial crack length determined in Section 5.3.3, the apparent ΔK_{th} values are determined to be 1.16 MPa√m, 1.21 MPa√m, and 1.66 MPa√m for the CCV-ad, PPH-ad, and CCV-hd specimen groups, respectively. It is important to note here that for the ProX 200 specimens, the UF S-N data were from samples that were built in the vertical orientation using Concept Laser powders (PCV-au) while the FCG data were from samples that were built in the horizontal orientation using LaserForm powders (PPH-ad). This complication arose due to miss-prints and lack of available powders however we believe that this analysis is useful. Since there is no UF test data for the PPH-ad group, the fatigue data from PCV-au is used to estimate the apparent ΔK_{th} value. Additionally, the values for initial crack length comes from PCV-au specimens. Since the difference seen between the fatigue crack growth rates of CCV-ad and PPH-ad specimen groups is negligible, we speculate that in the small crack regime, orientation effects on small crack growth rates is minimal and propose that this analysis is useful.

5.3.4.2 Using small crack growth data to predict S-N response

Using the Paris Law constants, the initial crack sizes determined in Section 5.3.3, and Eq. 5.3, the predicted fatigue lifetime (S-N response) is shown in Figure 5.17. This analysis assumes that the initiation life is negligible and the total life of an S-N fatigue sample can be estimated by the propagation life as is frequently done [44,45]. The UF data acquired for CCV-au is shown in Figure 5.17 (a1) and (a2) with an S-N prediction informed by as built CL M2 (CCV-au) defect data and crack growth data (CCV-ad). The UF data acquired for CCV-hu is shown in Figure 5.17 (b1) and (b2) with the S-N prediction informed by stress-relieved CL M2 (CCV-hu) defect data and stress-relieved CL M2 (CCV-hd) crack growth data. The UF data acquired for PCV-au is shown in Figure 5.17 (c1) and (c2) with the S-N prediction informed by vertical ProX 200 (PCV-au) defect data and horizontal ProX 200 (PPH-ad) crack growth data. Figure 5.17 (a1), (b1), and (c1) shows the S-N prediction with ΔK_{th} set as the ΔK value determined at 10^{-10} m/cycle, while Figure 5.17 (a2), (b2), and (c2) shows the S-N prediction using the apparent ΔK_{th} approach.

Both methods of determining ΔK_{th} provide a relatively good fit to the fatigue data with most specimens falling within the bounds set by the minimum and maximum defect sizes. For the as-built CL M2 (CCV-au) specimens tested at 210 MPa fatigue lives were below the predicted bounds. This is attributed to the presence of multiple crack initiation sites. The quantification of initiating defects was performed for each failure site, however the lives were estimated without considering multiple initiation sites. The occurrence of multiple initiation sites in one specimen would serve to reduce the fatigue life of that specimen as the individual fracture surfaces coalesce. This is supported by specimens with more and/or larger secondary fracture surfaces having shorter fatigue lives, as shown in Figure 5.18.

Using the apparent threshold method for the prediction resulted in the S-N prediction in Figure 5.17 (a2), (b2), and (c2). This generally fit better than using ΔK at 10^{-10} m/cycle for the CCV specimens. This fit did not work as well for the PCV-au specimens in Figure 5.17 (c2), which is attributed to the differences between the PCV-au and PPH-ad specimens.

Without the use of the apparent threshold method, the S-N prediction for the as-built CL M2 (CCV-au) and stress-relieved CL M2 (CCV-hu) are quite similar (Figure 5.17 a1 and b1). The reason for this arises from the similar defect sizes in both groups. The method of calculating the crack growth behavior used intrinsically incorporates the residual stress of the specimens being tested as they are not free of residual stresses when tested. However, this means that the effect of residual stresses is not accounted for in the S-N prediction models, leading to a similar prediction for both. Residual stresses effectively change the testing load ratio, leading to mean stress effects not covered in the scope of this work, but by using the apparent threshold method, we can incorporate residual stress effects into the S-N prediction as the fatigue strength is intrinsically influenced by this as well.

5.3.4.3 Predicting S-N response of samples with sub-surface defects

HCF specimens that had either the as-built surface removed (CCV-su) or the AM contour removed (CCV-cu) exhibited sub-surface LOF defects as the initiation site. For these specimens the initial fatigue crack propagation was in vacuum. Prediction of fatigue life behavior for crack growth in vacuum cannot be done using the previously discussed ambient air FCG tests as the crack growth behavior is expected be very different. Using the C and m constants from the S-N prediction shown in Figure 5.17 (a1) and the defect sizes found in Section 5.3.3. on the surface-removed (CCV-su) and contour-removed (CCV-cu) specimens yields the results seen in Figure 5.19 (a1) and (a2). The crack growth data of CCV-ad severely underpredicts the fatigue response of CCV-su and CCV-cu. Although crack growth testing in vacuum was beyond the scope of the current work, previous research in steel has shown that FCG testing in vacuum can reduce the K-values at 10^{-10} m/cycle by 55-70% [52]. Increasing the CCV-au K-value by 70% makes ΔK at 10^{-10} m/cycles 1.70 MPa√m. The S-N prediction using this as the new ΔK_{th} value results in the slightly better fit seen in Figure 5.19 (b1) and (b2). Extending the apparent threshold approach to include best fit values, not only for ΔK_{th} but also for C and m values yielded the predictions shown in Figure 5.19 (c1) and (c2). This fit suggests an apparent Paris law relationship with the constants $C = 2.25 \times 10^{-12}\ \mathrm{m/cycles}$ and $m = 6.5439$ for CCV-su and $C = 2.0 \times 10^{-13}\ \mathrm{m/cycles}$ and $m = 6.9479$ for CCV-cu, with thresholds of $\Delta K_{th} = 1.79$ and $\Delta K_{th} = 2.45$, respectively. This would put crack growth rates for surface-removed at low as $2.25 \times 10^{-12}\ \mathrm{m/cycles}$ and contour-removed as low as $2.0 \times 10^{-13}\ m/cycles$. These are similar in magnitude to the work of Stanzl-Tschegg and Schönbauer which reported crack growth rates in vacuum of ~10^{-12} m/cycle for the FGA and ≤10^{-11} m/cycle for the smooth area. It follows reasonably that the crack growth rate is slower in the CCV-cu than CCV-su due to the presence of a FGA within the fisheye, as discussed in Section 5.3.3.3.

The small crack growth model approach for predicting the HCF (S-N) response of as-built and stress-relieved AM specimens and specimens that have had the as-built surface removed is promising. Using the actual size of the initiating defects and assuming the initiation life is negligible provides a good estimate of the S-N response of specimens fabricated by L-PBF. These findings can be used in conjunction with ICME simulations for predicting the local HCF response of components manufactured using AM processes using predicted defect sizes in place of the measured defect sizes used in the current work.

5.4 Conclusions

The high cycle fatigue behavior of AISI 316L stainless steel manufactured via L-PBF under different processing parameters was characterized using ultrasonic fatigue testing in laboratory air. Specimens built on the Concept Laser M2 and ProX DMP 200 were evaluated for the influence processing parameters and post-processing has on fatigue response, crack initiation, and crack growth behavior. The following conclusions can be drawn:

9) No significant difference in fatigue performance or crack growth behavior was observed between specimens built using the same source powder in the vertical orientation on the CL M2 and ProX 200. Fatigue strength and fatigue crack growth rates do not significantly differ despite differences in processing parameters leading to different sources of fatigue crack initiation and different magnitudes of residual stress.
10) Residual stress relaxation serves to moderately improve the high cycle fatigue behavior but has no significant effect on the observed fatigue crack growth behavior.
11) For the Concept Laser manufactured specimens, removal of the as-built surface changes the source of fatigue crack initiation from surface crevices to sub-surface lack-of-fusion (LOF) pores. Sub-surface LOF pores experience crack growth in vacuum until the crack path reaches the outer surface of the specimen. Crack growth in vacuum grows at significantly slower rates than in ambient air, leading to improved fatigue behavior despite having larger initiating defects.
12) Using a small crack fracture mechanics approach, the high cycle fatigue (S-N) response of as-built and stress relieved specimens can be reasonably well predicted based on the size

of the initiating defect. For application to specimens in which the as-built surfaces have been removed, modifications to this approach are required to account for crack growth in vacuum during the early stages of HCF.

Figures

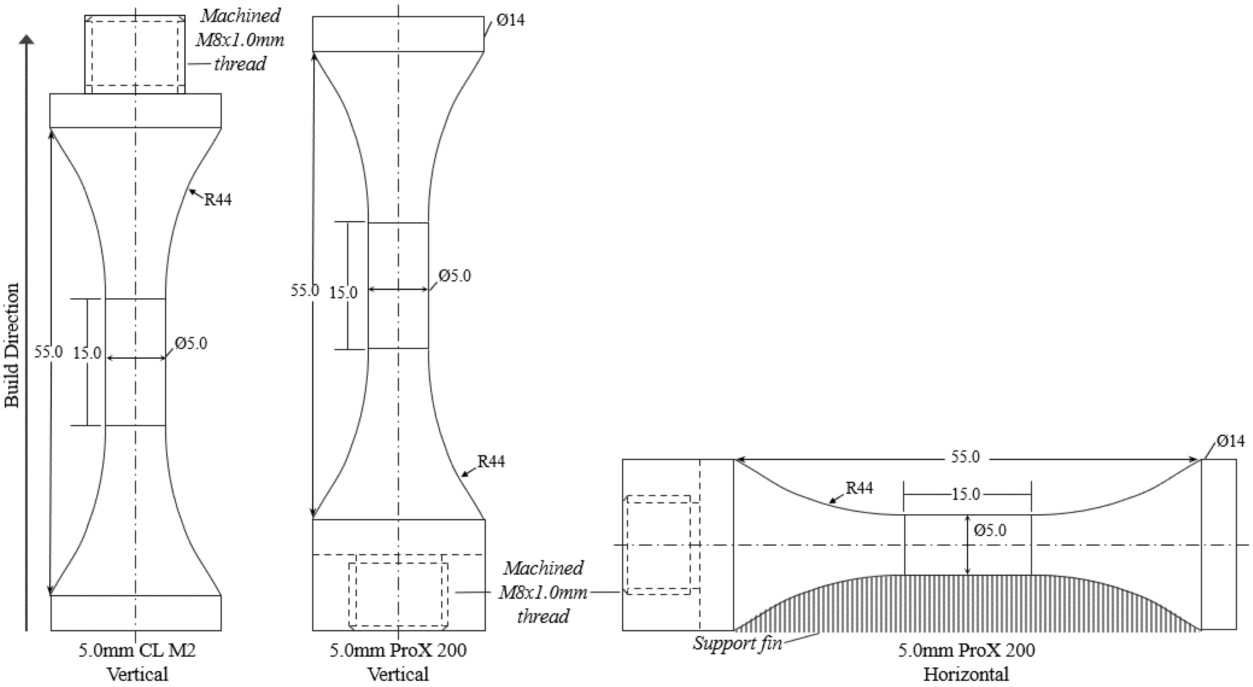

Figure 5.1 As-printed specimen geometry for 5.0 mm diameter dog-bone ultrasonic fatigue tests. Solid lines represent as-printed geometry while dashed lines represent final specimen geometry after machine threading.

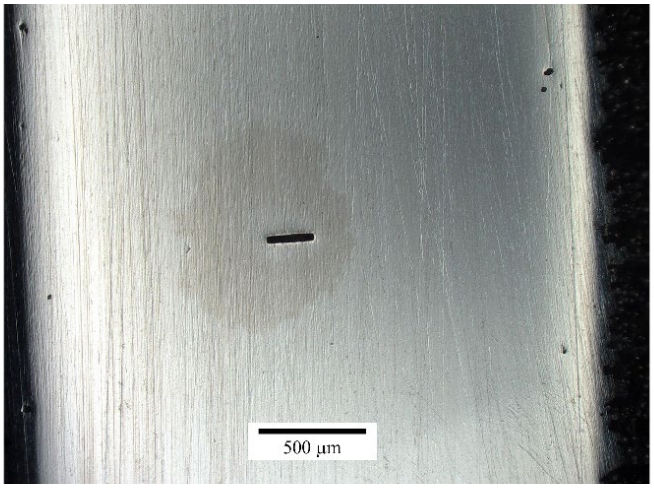

Figure 5.2. Plasma focused ion beam (PFIB) notch cut into the machined flat surface of a fatigue crack growth (FCG) test specimen.

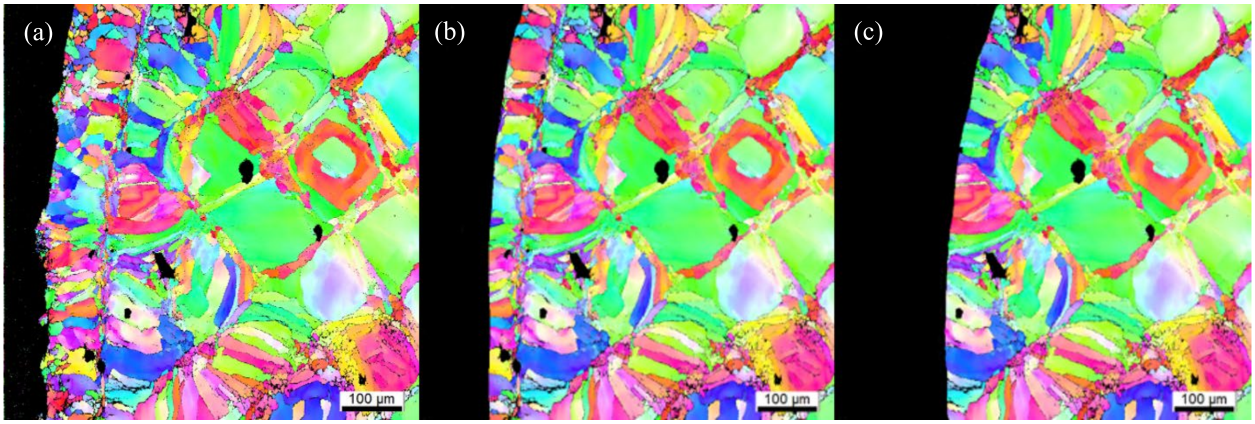

Figure 5.3. Electron Backscatter Diffraction (EBSD) images depicting cross-sections of the CL M2 microstructure in the (a) as-built, (b) surface-removed, and (c) contour-removed states. Note that (b) and (c) are not original EBSD images, rather a depiction of (a) with approximately 75 µm and 150 µm removed, respectively.

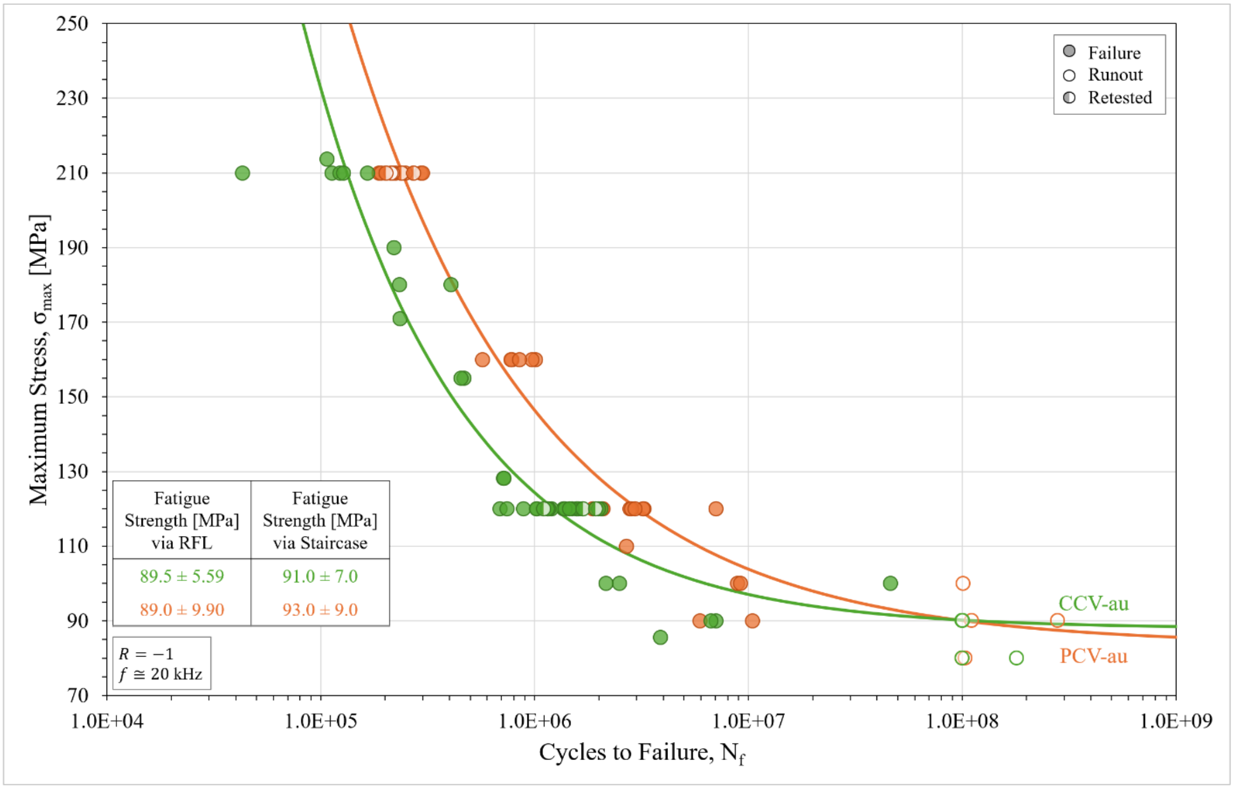

Figure 5.4. Stress-life (S-N) ultrasonic high cycle fatigue curves for as-built CL M2 (CCV-au) and ProX 200 (PCV-au) specimens, Runout samples are indicated by unfilled data icons and are classified as cycling longer than 10^8 cycles without failure. Runout samples were retested at either 120 MPa or 210 MPa and included with the failures dataset. Each dataset is accompanied by a Weibull distribution curve fit determined via random fatigue limit (RFL) analysis.

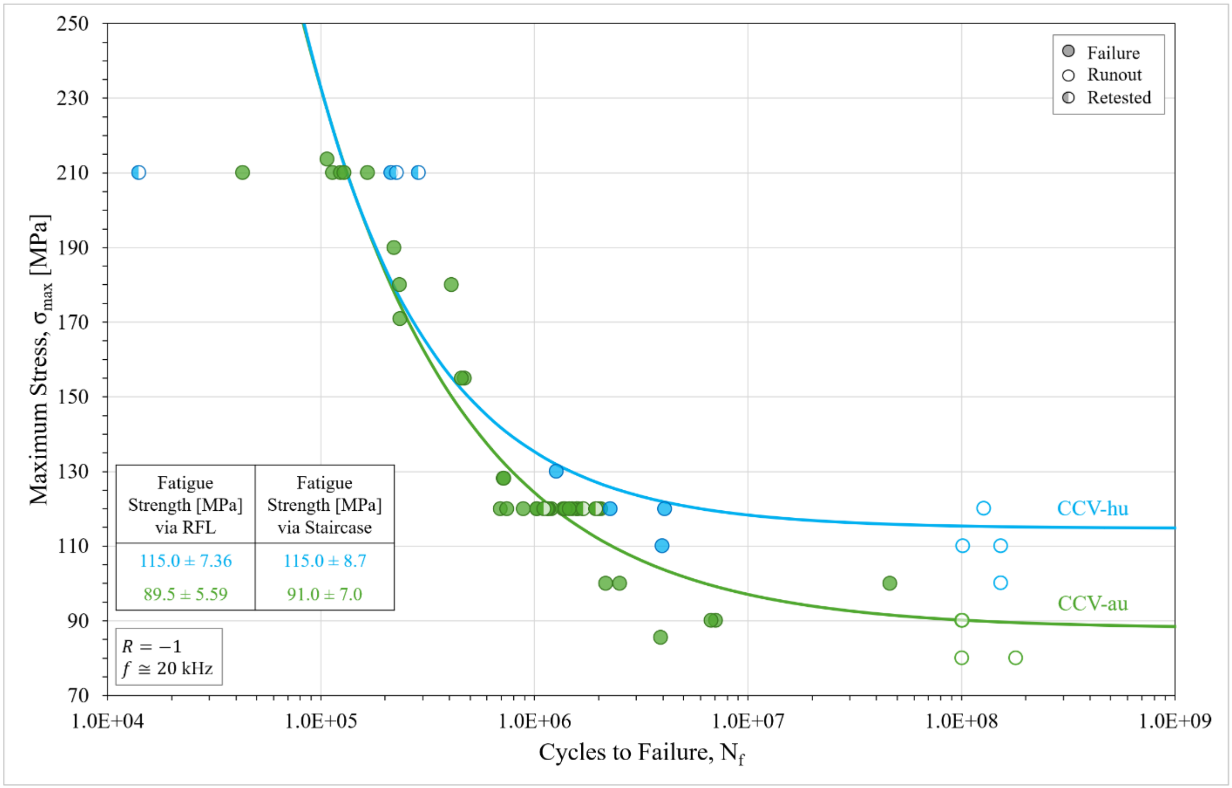

Fatigue Strength [MPa] via RFL	Fatigue Strength [MPa] via Staircase
115.0 ± 7.36	115.0 ± 8.7
89.5 ± 5.59	91.0 ± 7.0

Figure 5.5. Stress-life (S-N) ultrasonic high cycle fatigue curves for stress-relieved CL M2 (CCV-hu) specimens compared to as-built (CCV-au) specimens. Runout samples are indicated by unfilled data icons and are classified as cycling longer than 10^8 cycles without failure. Runout samples were retested at 120 MPa or 210 MPa and included with the failures dataset. Each dataset is accompanied by a Weibull distribution curve fit determined via random fatigue limit (RFL) analysis.

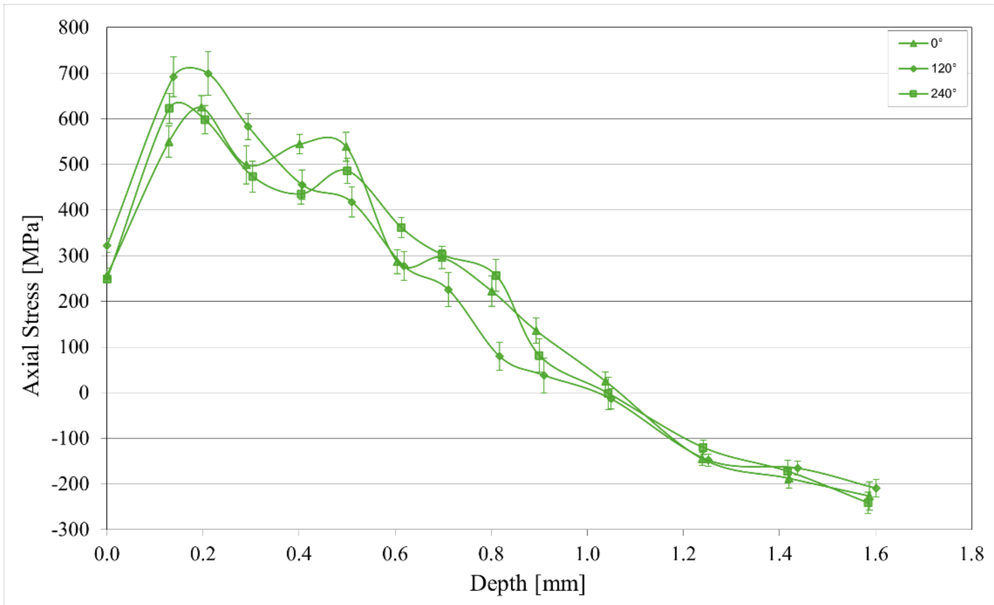

Figure 5.6. Axial residual stress depth profile of an as-built CL M2 (CCV-hu) specimen before stress-relieving. The three lines represent three separate angular positions in which measurements were taken on the same sample.

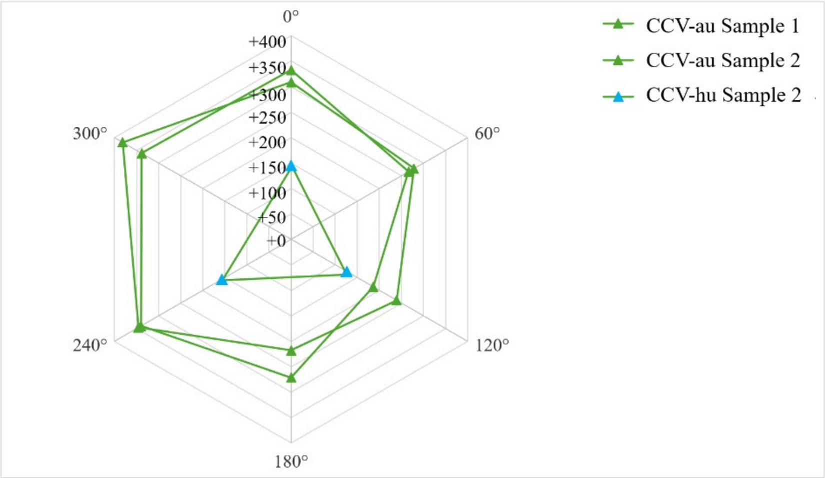

Figure 5.7. Surface axial residual stress profiles of one CCV-au specimen (CCV-au Sample 1) and one CCV-hu specimen before (CCV-au Sample 2) and after (CCV-hu Sample 2) stress-relieving.

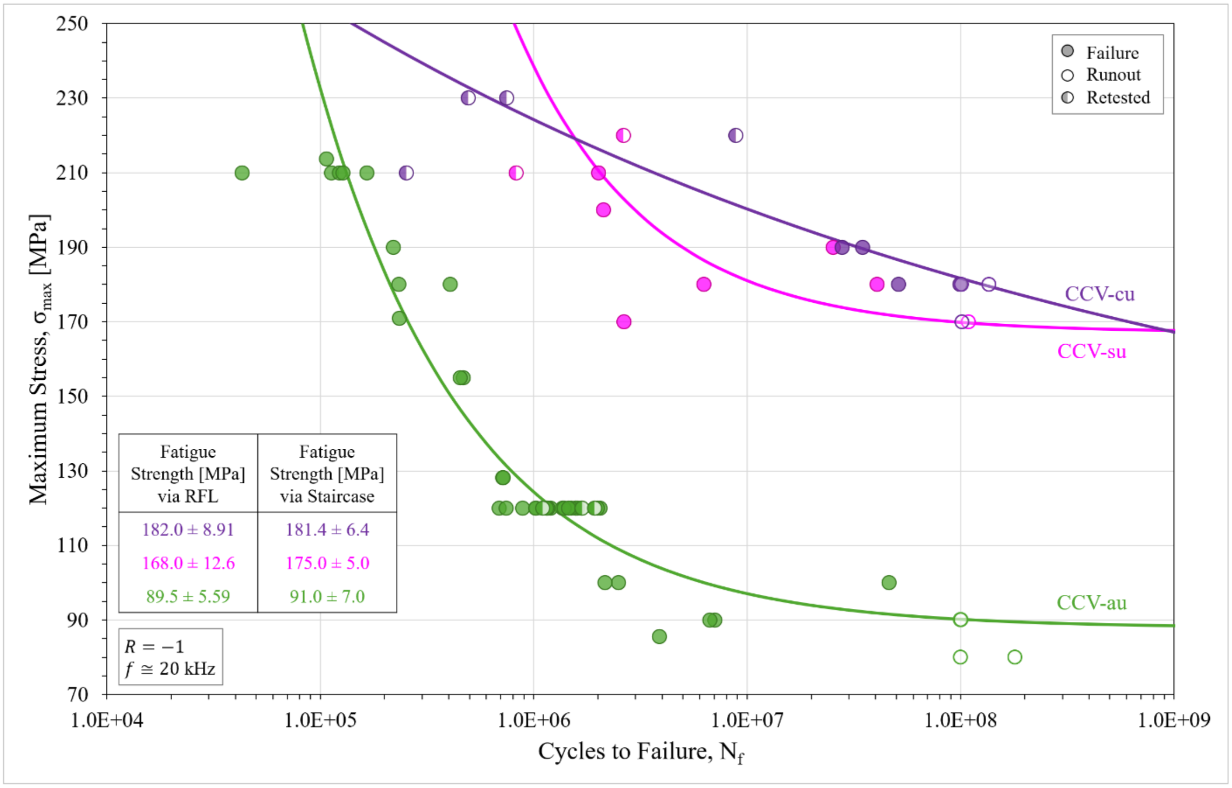

Figure 5.8. Stress-life (S-N) ultrasonic high cycle fatigue curves for surface-removed (CCV-su) and contour-removed (CCV-cu) CL M2 specimens compared to as-built specimens. Runout samples are indicated by unfilled data icons and are classified as cycling longer than 10^8 cycles without failure. Runout samples were retested at 210 MPa or higher and included with the failures dataset. Each dataset is accompanied by a Weibull distribution curve fit determined via random fatigue limit (RFL) analysis.

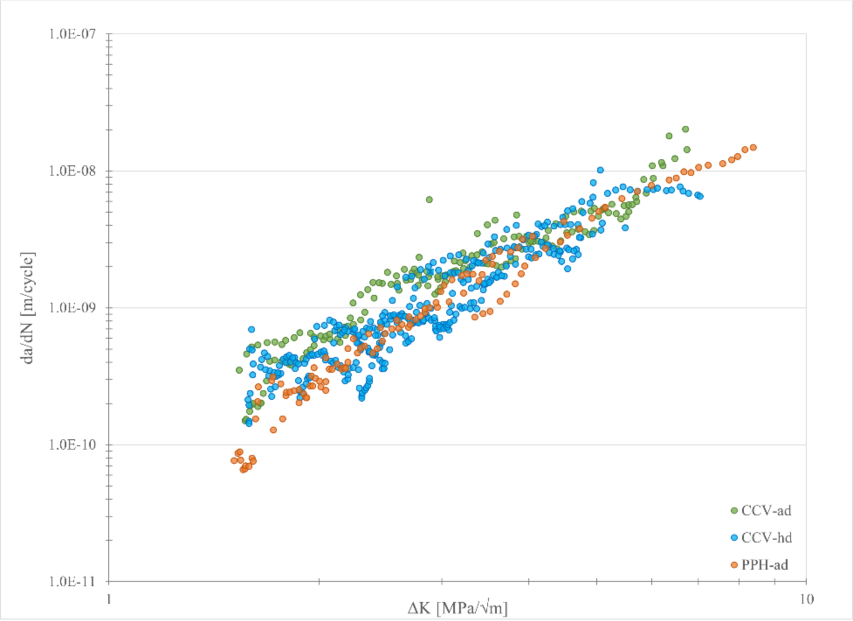

Figure 5.9. Fatigue crack growth rates (da/dN) as a function of ΔK for three groups: as-built vertical CL M2 (CCV-ad), stress-relieved vertical CL M2 (CCV-hd), and as-built horizonal ProX 200 (PPH-ad).

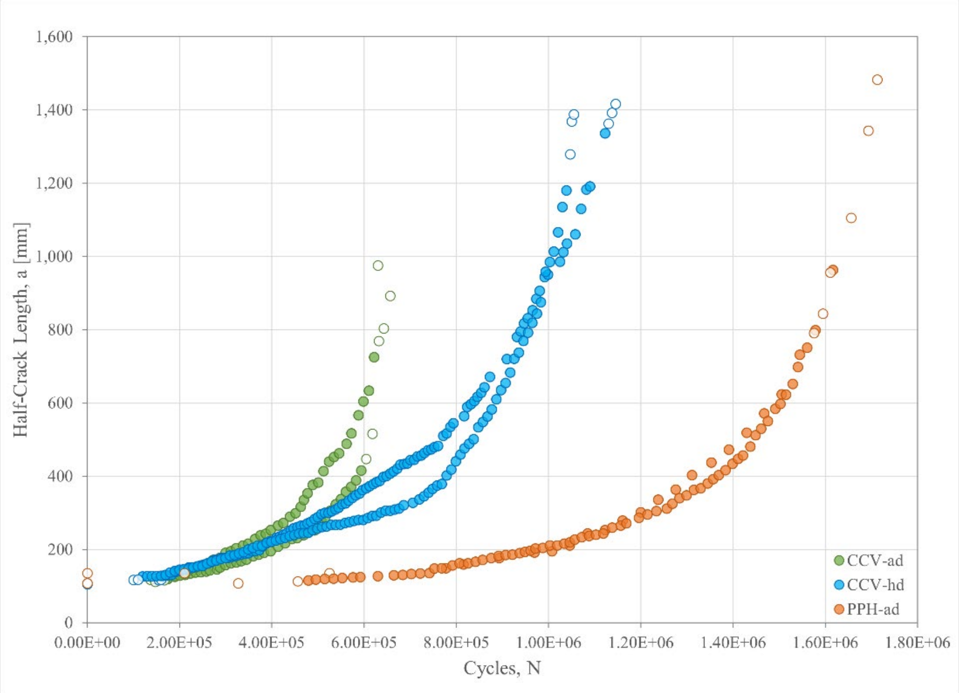

Figure 5.10. Fatigue crack growth rates tested at 120 MPa for the three specimen groups: as-built vertical CL M2 (CCV-ad), stress-relieved vertical CL M2 (CCV-hd), and as-built horizontal ProX 200 (PPH-ad). Unfilled data icons indicate fatigue crack growth rates not included in the da/dN vs. ΔK calculations as a result of using the seven-point sliding polynomial method to calculate da/dN.

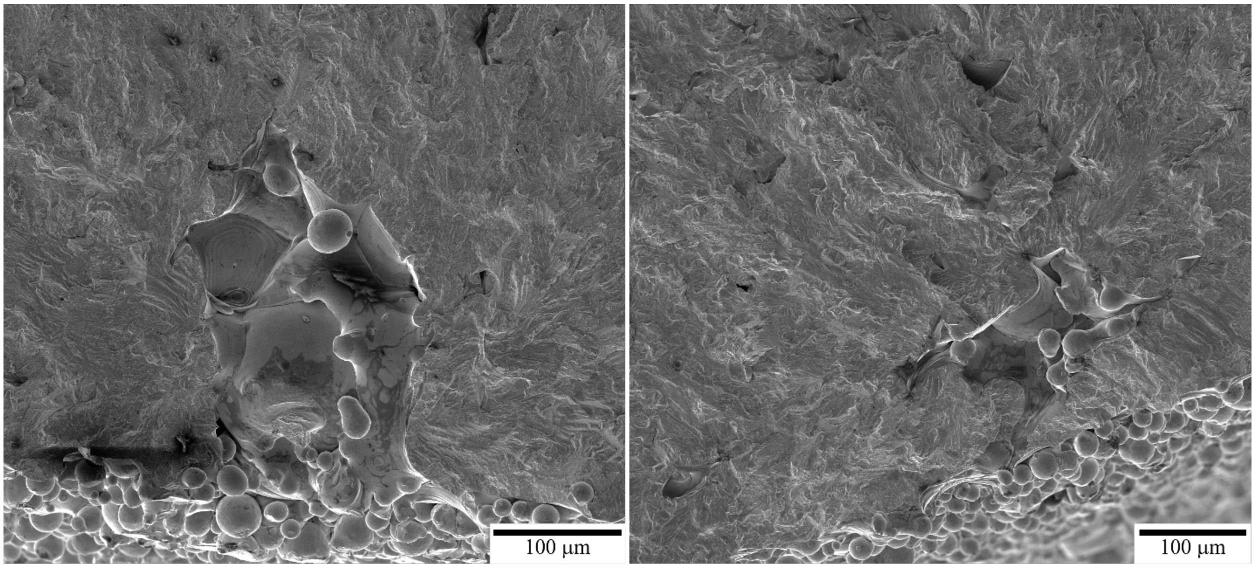

Figure 5.11. Two examples of lack-of-fusion (LOF) initiating defects found on the fracture surface of as-built, vertical ProX 200 specimens (PCU-au).

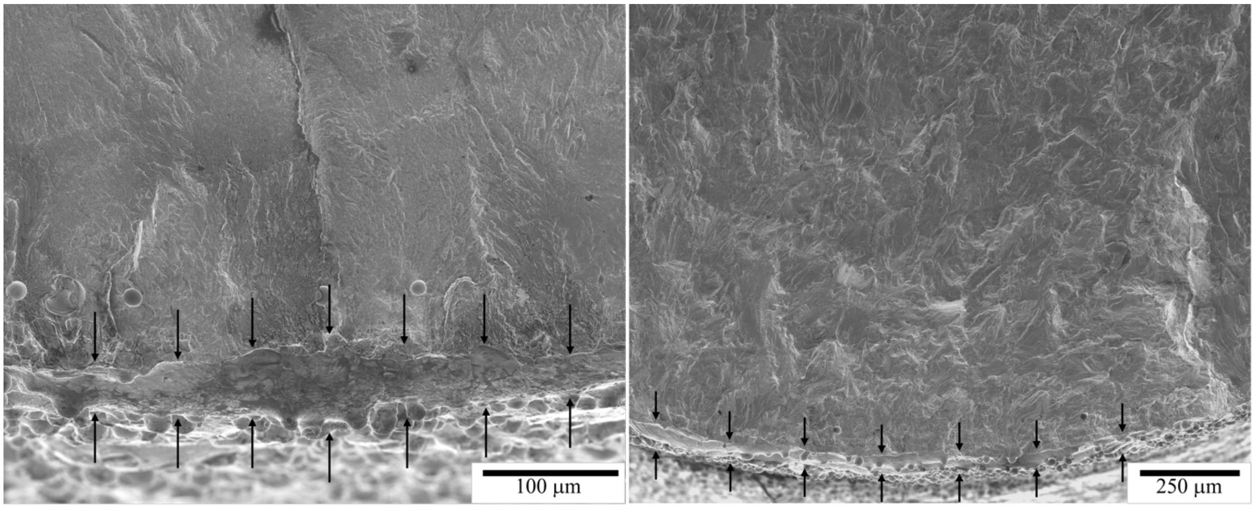

Figure 5.12. The fracture surface of two examples of surface crevice fatigue crack initiation in as-built, vertical CL M2 (CCV-au) specimens.

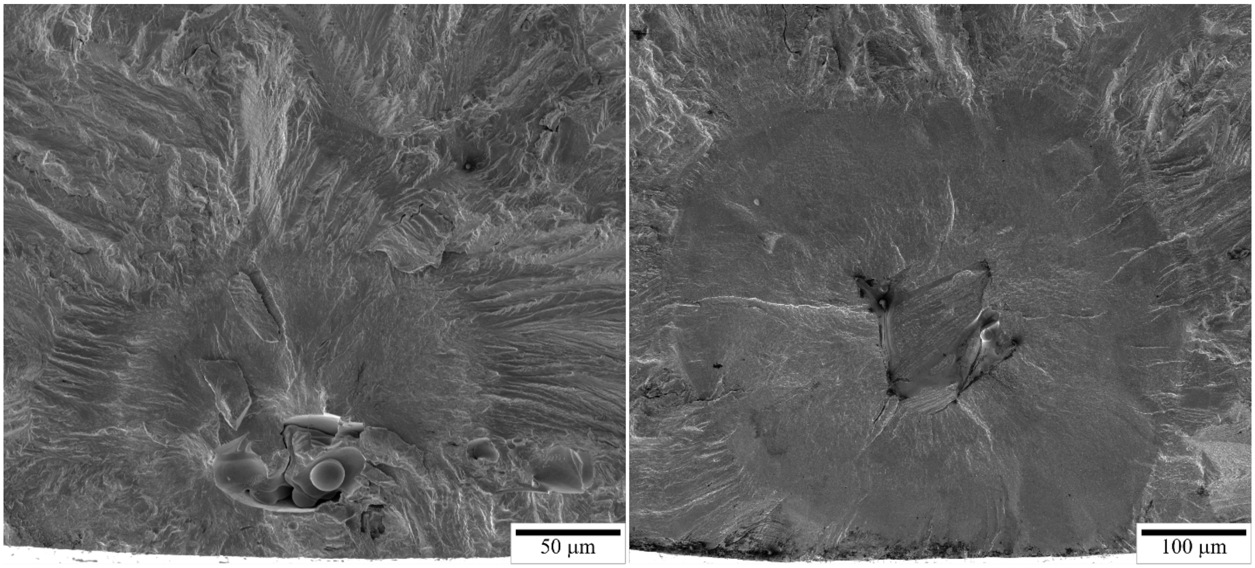

Figure 5.13. Representative initiating defects seen in (left) surface-removed CL M2 (CCV-su) specimens and (right) contour-removed CL M2 (CCV-cu) specimens. Both specimens show the formation of a fisheye on the fracture surface, indicative of crack growth in vacuum.

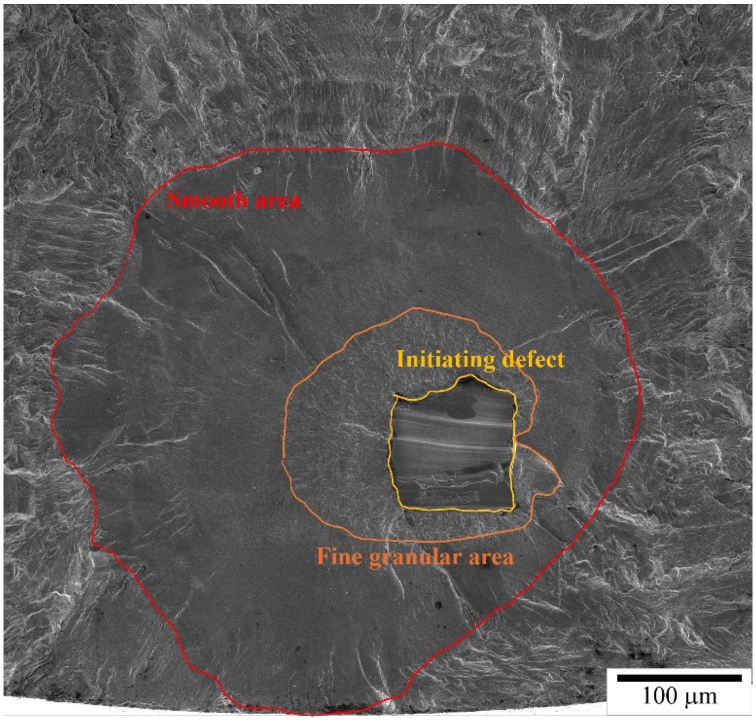

Figure 5.14. Fracture surface of a CCV-cu specimen highlighting the fisheye seen during crack growth in vacuum. The fisheye for these samples is made up of the initiating defect, the fine granular area (FGA), and the surrounding smooth area (SA).

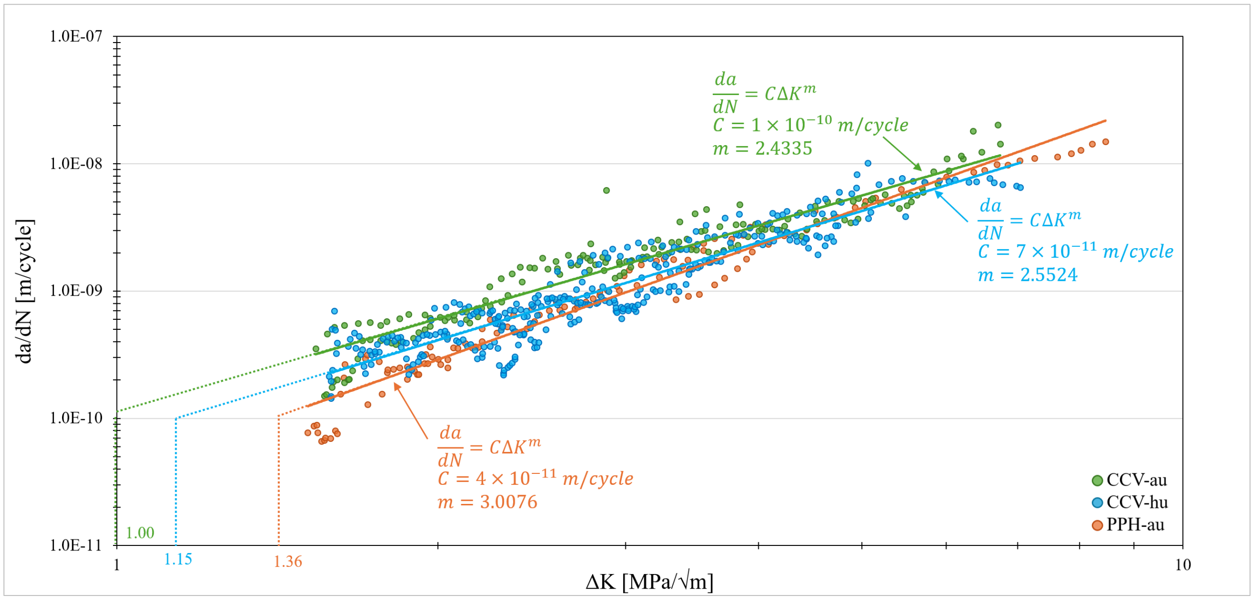

Figure 5.15. Fatigue crack growth (FCG) data for the three specimen groups tested: CCV-ad, CCV-hd, and PPH-ad. The data is fit to the Paris Law and the C and m constants are shown. The ΔK_{th} value as determined by the ΔK value at 10^{-10} m/cycles is shown for each specimen group.

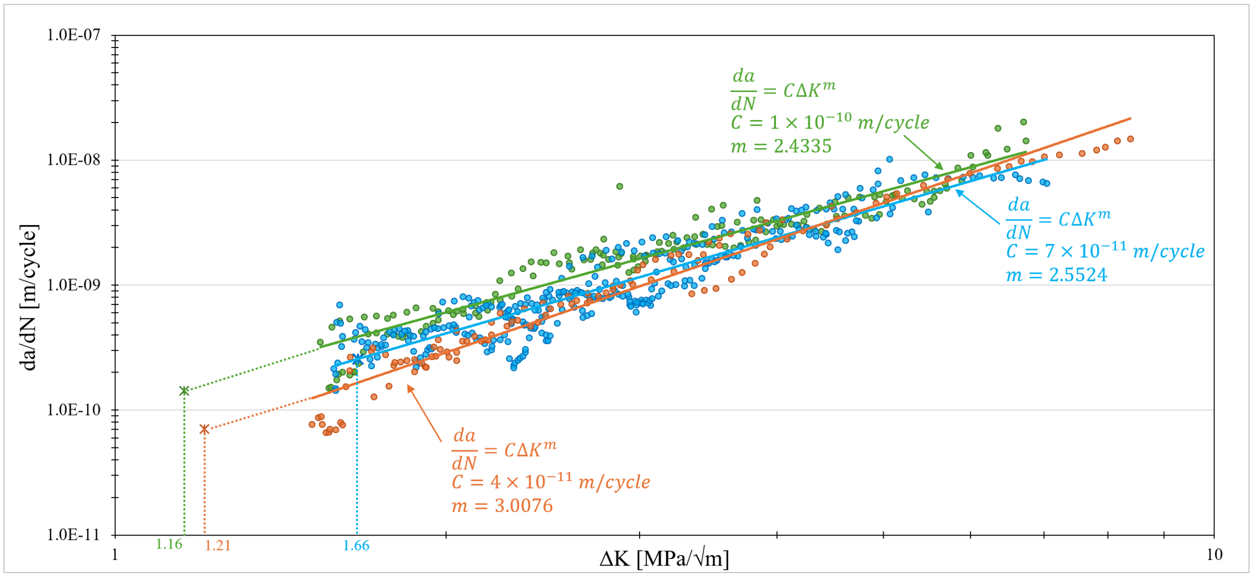

Figure 5.16. Fatigue crack growth (FCG) data for the three specimen groups tested: CCV-ad, CCV-hd, and PPH-ad. The data is fit to the Paris Law and the C and m constants are shown. The apparent ΔK_{th} value as determined by the fatigue strength from the UF test data is shown for each specimen group.

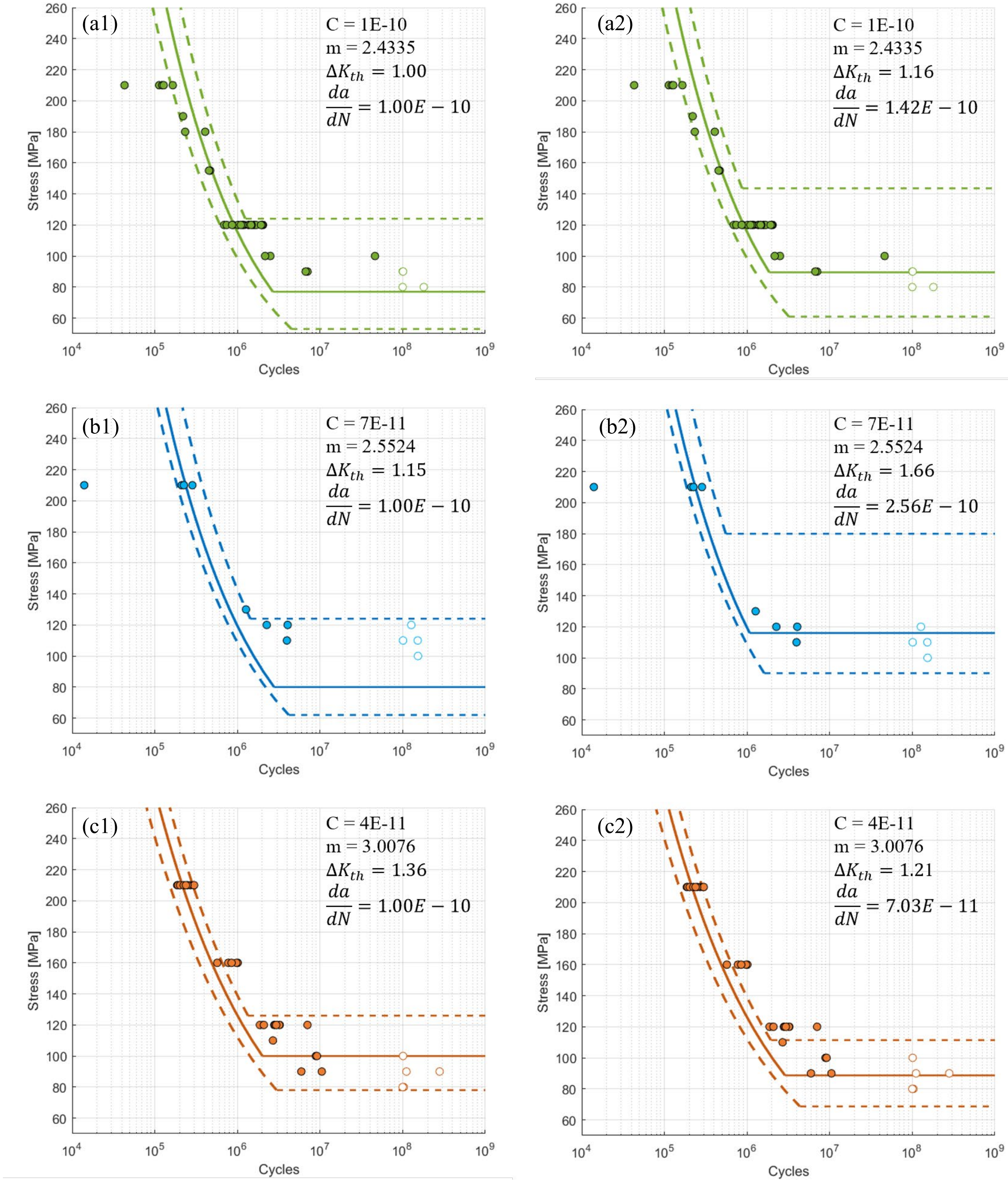

Figure 5.17. S-N prediction informed by crack growth behavior and initiating defect size. (a1) as-built, vertical CL M2 (CCV-au) ultrasonic fatigue data paired with the 10^{-10} m/cycle S-N prediction method. (a2) as-built, vertical CL M2 (CCV-au) ultrasonic fatigue data paired with the apparent threshold S-N prediction method. (b1) stress-relieved, vertical CL M2 (CCV-hu) ultrasonic fatigue data paired with the 10^{-10} m/cycle S-N prediction method. (b2) stress-relieved, vertical CL M2 (CCV-hu) ultrasonic fatigue data paired with the apparent threshold S-N prediction method. (c1) as-built, vertical ProX 200 (PCV-au) ultrasonic fatigue data paired with the 10^{-10} m/cycle S-N prediction method. (c2) as-built, vertical ProX 200 (PCV-au) ultrasonic fatigue data paired with the apparent threshold S-N prediction method.

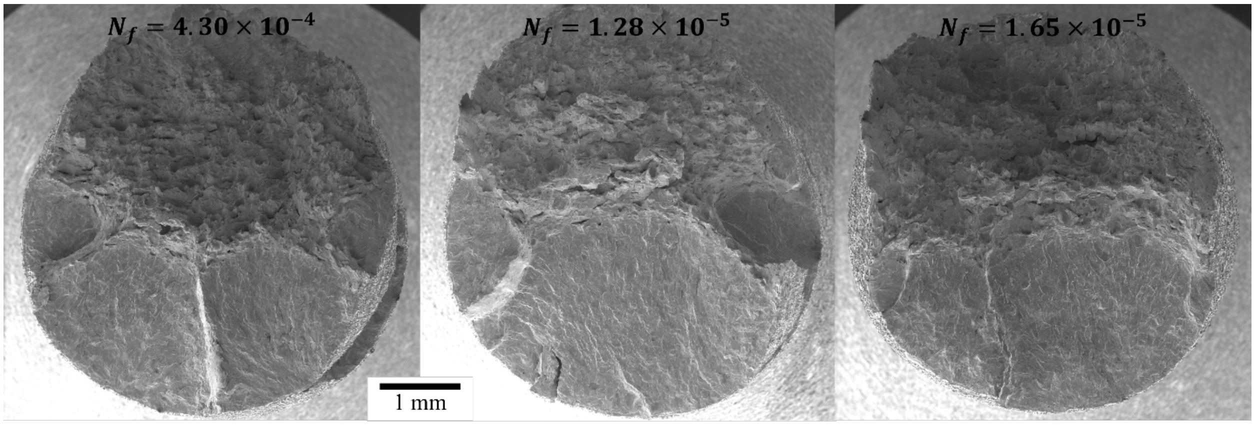

Figure 5.18. Evidence of multiple crack initiation sites occurring in CCV-au specimens UF tested at 210 MPa.

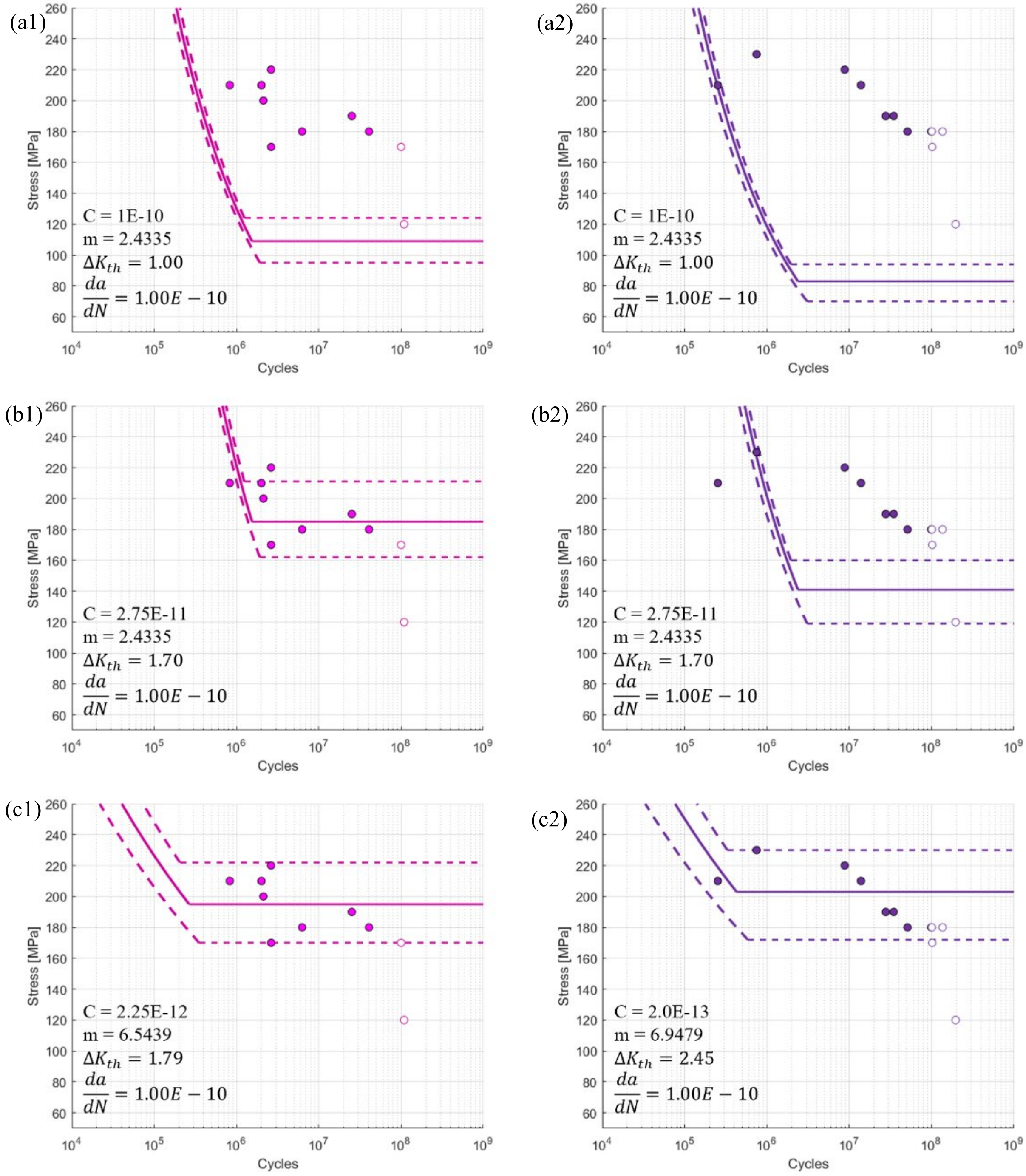

Figure 5.19. S-N prediction informed by crack growth behavior and initiating defect size of (left) surface-removed, vertical CL M2 (CCV-su) and (right) contour-removed, vertical CL M2 (CCV-cu) paired with their respective ultrasonic fatigue data. The S-N prediction is generated via (a1, a2) CCV-ad FCG data, (b1, b2) a 70% increase in the ΔK_{th} value at 10^{-10} m/cycles, and (c1, c2) apparent (best fit) values of ΔK_{th}, C and m.

References

[1] ISO/TC 261, ASTM Committee F42, ISO/ASTM 52900:2017 Additive manufacturing. General principles. Terminology, (2017).

[2] T. DebRoy, H.L. Wei, J.S. Zuback, T. Mukherjee, J.W. Elmer, J.O. Milewski, A.M. Beese, A. Wilson-Heid, A. De, W. Zhang, Additive manufacturing of metallic components – Process, structure and properties, Prog. Mater. Sci. 92 (2018) 112–224. https://doi.org/10.1016/j.pmatsci.2017.10.001.

[3] J. Allison, D. Backman, L. Christodoulou, Integrated computational materials engineering: A new paradigm for the global materials profession, JOM 58 (2006) 25–27.

[4] S.A.H. Motaman, F. Kies, P. Köhnen, M. Létang, M. Lin, A. Molotnikov, C. Haase, Optimal design for metal additive manufacturing: An integrated computational materials engineering (ICME) approach, JOM 72 (2020) 1092–1104. https://doi.org/10.1007/s11837-020-04028-4.

[5] P.-A. Pires, O. Desmaison, M. Megahed, ICME manufacturability assessment in powder bed fusion additive manufacturing, JOM 70 (2018) 1677–1685. https://doi.org/10.1007/s11837-018-3024-8.

[6] Y. Murakami, N.N. Yokoyama, J. Nagata, Mechanism of fatigue failure in ultralong life regime: Fatigue failure in ultralong life regime, Fatigue Fract. Eng. Mater. Struct. 25 (2002) 735–746. https://doi.org/10.1046/j.1460-2695.2002.00576.x.

[7] Y. Murakami, T. Nomoto, T. Ueda, Factors influencing the mechanism of superlong fatigue failure in steels: Superlong fatigue failure in steels, Fatigue Fract. Eng. Mater. Struct. 22 (1999) 581–590. https://doi.org/10.1046/j.1460-2695.1999.00187.x.

[8] D.R. Clymer, J. Cagan, J. Beuth, Power–velocity process design charts for powder bed additive manufacturing, J. Mech. Des. 139 (2017) 100907. https://doi.org/10.1115/1.4037302.

[9] K. Carpenter, A. Tabei, On residual stress development, prevention, and compensation in metal additive manufacturing, Materials 13 (2020) 255. https://doi.org/10.3390/ma13020255.

[10] T. Simson, A. Emmel, A. Dwars, J. Böhm, Residual stress measurements on AISI 316L samples manufactured by selective laser melting, Addit. Manuf. 17 (2017) 183–189. https://doi.org/10.1016/j.addma.2017.07.007.

[11] T. Mukherjee, V. Manvatkar, A. De, T. DebRoy, Mitigation of thermal distortion during additive manufacturing, Scr. Mater. 127 (2017) 79–83. https://doi.org/10.1016/j.scriptamat.2016.09.001.

[12] T. Larimian, M. Kannan, D. Grzesiak, B. AlMangour, T. Borkar, Effect of energy density and scanning strategy on densification, microstructure and mechanical properties of 316L stainless steel processed via selective laser melting, Mater. Sci. Eng. A 770 (2020) 138455. https://doi.org/10.1016/j.msea.2019.138455.

[13] G.R. Buican, G. Oancea, C. Lancea, M.A. Pop, Influence of layer thickness on internal structure of parts manufactured from 316-L steel using SLM technology, Appl. Mech. Mater. 809–810 (2015) 369–374. https://doi.org/10.4028/www.scientific.net/AMM.809-810.369.

[14] O.O. Salman, F. Brenne, T. Niendorf, J. Eckert, K.G. Prashanth, T. He, S. Scudino, Impact of the scanning strategy on the mechanical behavior of 316L steel synthesized by selective

laser melting, J. Manuf. Process. 45 (2019) 255–261. https://doi.org/10.1016/j.jmapro.2019.07.010.

[15] T. Kurzynowski, K. Gruber, W. Stopyra, B. Kuźnicka, E. Chlebus, Correlation between process parameters, microstructure and properties of 316 L stainless steel processed by selective laser melting, Mater. Sci. Eng. A 718 (2018) 64–73. https://doi.org/10.1016/j.msea.2018.01.103.

[16] A.K. Agrawal, G. Meric de Bellefon, D. Thoma, High-throughput experimentation for microstructural design in additively manufactured 316L stainless steel, Mater. Sci. Eng. A 793 (2020) 139841. https://doi.org/10.1016/j.msea.2020.139841.

[17] Y. Deng, Z. Mao, N. Yang, X. Niu, X. Lu, Collaborative optimization of density and surface roughness of 316L stainless steel in selective laser melting, Materials 13 (2020) 1601. https://doi.org/10.3390/ma13071601.

[18] D. Gu, Y. Shen, Balling phenomena in direct laser sintering of stainless steel powder: Metallurgical mechanisms and control methods, Mater. Des. 30 (2009) 2903–2910. https://doi.org/10.1016/j.matdes.2009.01.013.

[19] G.B. Bang, W.R. Kim, H.K. Kim, H.-K. Park, G.H. Kim, S.-K. Hyun, O. Kwon, H.G. Kim, Effect of process parameters for selective laser melting with SUS316L on mechanical and microstructural properties with variation in chemical composition, Mater. Des. 197 (2021) 109221. https://doi.org/10.1016/j.matdes.2020.109221.

[20] A. Röttger, K. Geenen, M. Windmann, F. Binner, W. Theisen, Comparison of microstructure and mechanical properties of 316 L austenitic steel processed by selective laser melting with hot-isostatic pressed and cast material, Mater. Sci. Eng. A 678 (2016) 365–376. https://doi.org/10.1016/j.msea.2016.10.012.

[21] O. Andreau, E. Pessard, I. Koutiri, J.-D. Penot, C. Dupuy, N. Saintier, P. Peyre, A competition between the contour and hatching zones on the high cycle fatigue behaviour of a 316L stainless steel: Analyzed using X-ray computed tomography, Mater. Sci. Eng. A 757 (2019) 146–159. https://doi.org/10.1016/j.msea.2019.04.101.

[22] G. Wang, Q. Liu, H. Rao, H. Liu, C. Qiu, Influence of porosity and microstructure on mechanical and corrosion properties of a selectively laser melted stainless steel, J. Alloys Compd. 831 (2020) 154815. https://doi.org/10.1016/j.jallcom.2020.154815.

[23] W.M. Tucho, V.H. Lysne, H. Austbø, A. Sjolyst-Kverneland, V. Hansen, Investigation of effects of process parameters on microstructure and hardness of SLM manufactured SS316L, J. Alloys Compd. 740 (2018) 910–925. https://doi.org/10.1016/j.jallcom.2018.01.098.

[24] R. Cunningham, S.P. Narra, C. Montgomery, J. Beuth, A.D. Rollett, Synchrotron-based X-ray microtomography characterization of the effect of processing variables on porosity formation in laser power-bed additive manufacturing of Ti-6Al-4V, JOM 69 (2017) 479–484. https://doi.org/10.1007/s11837-016-2234-1.

[25] R. Cunningham, C. Zhao, N. Parab, C. Kantzos, J. Pauza, K. Fezzaa, T. Sun, A.D. Rollett, Keyhole threshold and morphology in laser melting revealed by ultrahigh-speed x-ray imaging, Science 363 (2019) 849–852. https://doi.org/10.1126/science.aav4687.

[26] T. Niendorf, S. Leuders, A. Riemer, H.A. Richard, T. Tröster, D. Schwarze, Highly anisotropic steel processed by selective laser melting, Metall. Mater. Trans. B 44 (2013) 794–796. https://doi.org/10.1007/s11663-013-9875-z.

[27] A. Riemer, S. Leuders, M. Thöne, H.A. Richard, T. Tröster, T. Niendorf, On the fatigue crack growth behavior in 316L stainless steel manufactured by selective laser melting, Eng. Fract. Mech. 120 (2014) 15–25. https://doi.org/10.1016/j.engfracmech.2014.03.008.

[28] O. Fergani, A. Bratli Wold, F. Berto, V. Brotan, M. Bambach, Study of the effect of heat treatment on fatigue crack growth behaviour of 316L stainless steel produced by selective laser melting, Fatigue Fract. Eng. Mater. Struct. 41 (2018) 1102–1119. https://doi.org/10.1111/ffe.12755.

[29] F. Brenne, T. Niendorf, Damage tolerant design by microstructural gradation – Influence of processing parameters and build orientation on crack growth within additively processed 316L, Mater. Sci. Eng. A 764 (2019) 138186. https://doi.org/10.1016/j.msea.2019.138186.

[30] J. Suryawanshi, K.G. Prashanth, U. Ramamurty, Mechanical behavior of selective laser melted 316L stainless steel, Mater. Sci. Eng. A 696 (2017) 113–121. https://doi.org/10.1016/j.msea.2017.04.058.

[31] J. Kluczyński, L. Śnieżek, K. Grzelak, J. Torzewski, I. Szachogłuchowicz, M. Wachowski, J. Łuszczek, Crack growth behavior of additively manufactured 316L steel—Influence of build orientation and heat treatment, Materials 13 (2020) 3259. https://doi.org/10.3390/ma13153259.

[32] ASTM International, F3184-16 Standard specification for additive manufacturing stainless steel alloy (UNS S31603) with powder bed fusion, (2023).

[33] S. Leuders, T. Lieneke, S. Lammers, T. Tröster, T. Niendorf, On the fatigue properties of metals manufactured by selective laser melting – The role of ductility, J. Mater. Res. 29 (2014) 1911–1919. https://doi.org/10.1557/jmr.2014.157.

[34] Q. Chao, S. Thomas, N. Birbilis, P. Cizek, P.D. Hodgson, D. Fabijanic, The effect of post-processing heat treatment on the microstructure, residual stress and mechanical properties of selective laser melted 316L stainless steel, Mater. Sci. Eng. A 821 (2021) 141611. https://doi.org/10.1016/j.msea.2021.141611.

[35] V. Cruz, Q. Chao, N. Birbilis, D. Fabijanic, P.D. Hodgson, S. Thomas, Electrochemical studies on the effect of residual stress on the corrosion of 316L manufactured by selective laser melting, Corros. Sci. 164 (2020) 108314. https://doi.org/10.1016/j.corsci.2019.108314.

[36] B. Blinn, F. Krebs, M. Ley, R. Teutsch, T. Beck, Determination of the influence of a stress-relief heat treatment and additively manufactured surface on the fatigue behavior of selectively laser melted AISI 316L by using efficient short-time procedures, Int. J. Fatigue 131 (2020) 105301. https://doi.org/10.1016/j.ijfatigue.2019.105301.

[37] Institute of Physics and Materials Science, BOKU, Vienna, Ultrasonic Fatigue Testing Equipment, (2009).

[38] M. Fitzka, B.M. Schönbauer, R.K. Rhein, N. Sanaei, S. Zekriardehani, S.A. Tekalur, J.W. Carroll, H. Mayer, Usability of ultrasonic frequency testing for rapid generation of high and very high cycle fatigue data, Materials 14 (2021) 2245. https://doi.org/10.3390/ma14092245.

[39] F.G. Pascual, W.Q. Meeker, Estimating fatigue curves with the random fatigue-limit model, Technometrics 41 (1999) 277–289. https://doi.org/10.1080/00401706.1999.10485925.

[40] C.C. Engler-Pinto Jr, J.V. Lasecki, R.J. Frisch Sr, J.E. Allison, Statistical approaches applied to very high cycle fatigue, in: VHCF4, TMS, 2007: pp. 369–376.

[41] O.H. Basquin, The exponential law of endurance tests, in: ASTM Proc., 1910: pp. 625–630.

[42] C.C. Engler-Pinto Jr, J.V. Lasecki, R.J. Frisch Sr, M.A. Dejack, J.E. Allison, Statistical approaches applied to fatigue test data analysis, in: SAE 2005 World Congr. Exhib., SAE, 2005: pp. 2005-01–0802. https://doi.org/10.4271/2005-01-0802.

[43] J.C. Newman, I.S. Raju, An empirical stress-intensity factor equation for the surface crack, Eng. Fract. Mech. 15 (1981) 185–192. https://doi.org/10.1016/0013-7944(81)90116-8.

[44] M.J. Caton, J.W. Jones, J.M. Boileau, J.E. Allison, The effect of solidification rate on the growth of small fatigue cracks in a cast 319-type aluminum alloy, Metall. Mater. Trans. A 30 (1999) 3055–3068. https://doi.org/10.1007/s11661-999-0216-4.

[45] Q. Shi, S.A. Hsie, J.W. Jones, J.E. Allison, Effects of alloying and processing on ultrasonic fatigue behavior in binary Ti-Al alloys, Mater. Sci. Eng. A 756 (2019) 564–577. https://doi.org/10.1016/j.msea.2019.03.079.

[46] P. Paris, F. Erdogan, A critical analysis of crack propagation laws, J. Basic Eng. 85 (1963) 528–533. https://doi.org/10.1115/1.3656900.

[47] Y. Murakami, Stress concentration, in: Met. Fatigue Eff. Small Defects Nonmet. Incl., Second, Elsevier, 2019.

[48] Y. Murakami, S. Nemat-Nasser, Growth and stability of interacting surface flaws of arbitrary shape, Eng. Fract. Mech. 17 (1983) 193–210. https://doi.org/10.1016/0013-7944(83)90027-9.

[49] R. Evans, J. Gockel, Surface Roughness Variation in Laser Powder Bed Fusion Additive Manufacturing, in: Solid Free. Fabr. 2021 Proc. 32nd Annu. Int. SFF Symp., University of Texas at Austin, 2021. https://doi.org/10.26153/TSW/17566.

[50] Y. Murakami, T. Nomoto, T. Ueda, Y. Murakami, On the mechanism of fatigue failure in the superlong life regime (N>10^7 cycles). Part 1: influence of hydrogen trapped by inclusions, Fatigue Fract. Eng. Mater. Struct. 23 (2000) 893–902. https://doi.org/10.1046/j.1460-2695.2000.00328.x.

[51] Y. Murakami, T. Nomoto, T. Ueda, Y. Murakami, On the mechanism of fatigue failure in the superlong life regime (N>10^7 cycles). Part II: influence of hydrogen trapped by inclusions, Fatigue Fract. Eng. Mater. Struct. 23 (2000) 903–910. https://doi.org/10.1046/j.1460-2695.2000.00343.x.

[52] S. Stanzl-Tschegg, B. Schönbauer, Near-threshold fatigue crack propagation and internal cracks in steel, Procedia Eng. 2 (2010) 1547–1555. https://doi.org/10.1016/j.proeng.2010.03.167.

[53] T. Sakai, Y. Sato, N. Oguma, Characteristic S-N properties of high-carbon-chromium-bearing steel under axial loading in long-life fatigue, Fatigue Fract. Eng. Mater. Struct. (2002) 765–773. https://doi.org/10.1046/j.1460-2695.2002.00574.x.

[54] Y. Murakami, M. Endo, Effects of hardness and crack geometry of ΔKth of small cracks, J Soc Mater Sci Jpn 35 (1986) 911–917.

[55] E.J. Czyryca, ASM Committee on Fatigue Crack Propagation, R.P. Gangloff, eds., Fatigue Testing, in: Met. Handb. Mech. Test., 9th ed., American Society for Metals, Metals Park, Ohio 44073, 1985: pp. 361–436.

[56] Y. Murakami, Mechanism of fatigue in the absence of defects and inclusions, in: Met. Fatigue Eff. Small Defects Nonmet. Incl., Second, Elsevier, 2019.

[57] Y. Murakami, T. Nomoto, T. Ueda, Factors influencing the mechanism of superlong fatigue failure in steels, Fatigue Fract. Eng. Mater. Struct. 22 (1999) 581–590. https://doi.org/10.1046/j.1460-2695.1999.00187.x.

Chapter 6 Conclusions and Proposed Future Work

6.1 Conclusions

In this dissertation, a quantitative investigation into the role gauge section diameter and stress relief heat treatment have on the short crack growth behavior and high cycle fatigue response of L-PBF 316L stainless steel specimens was performed. The final conclusions are summarized as follows:

1. Additive manufacturing (AM) of 316L was observed to exhibit a significant size effect on high cycle fatigue (HCF), whereby a specimen with a smaller (1.5 mm) gauge diameter will have a higher fatigue strength than a specimen with a larger (5.0 mm) gauge diameter. Both the fatigue strength at 10^8 cycles and fatigue life in all stress regimes are increased with decreasing gauge diameter. This effect has been shown to occur regardless of L-PBF machine, processing parameters, surface roughness, microstructure, and initiating defect morphology.
2. In as-built AM specimens, crack initiation most readily occurs at surface-connected defects, due to the higher stress concentration factor at these features compared to sub-surface defects. When the as-built surface is removed, crack initiation can still occur at surface-connected defects, if they exist. If the surface is relatively free from defects, crack initiation will occur at sub-surface defects. In L-PBF, the most common defects seen in this dissertation are lack-of-fusion (LOF) porosity and build layer related surface crevices. LOF pores arise from low energy densities, as dictated by the processing parameters. In

3. specimens with LOF pores, the porosity is seen equally dispersed throughout the gauge section. Surface crevices arise from a combination of print discrepancies leading to incomplete adhesion at build layer edges and mild layer delamination as a result of tensile axial residual stresses. Both surface-connected LOF pores and surface crevices can be treated as surface cracks and time to crack initiation can be largely neglected when discussing crack propagation in HCF testing.
4. When the as-built surface is removed, a significant improvement in fatigue strength at 10^8 cycles and fatigue life in all stress regimes is observed. When crack initiation occurs at surface-connected defects, the fatigue behavior is improved due to a slight reduction in the size of the surface-connected LOF pores. When crack initiation occurs at sub-surface defects, the fatigue behavior is improved because the initial crack growth occurs in vacuum. The time a crack spends growing in vacuum is visually indicated by the fisheye on the fracture surface. Specimens with evidence of a fine granular area (FGA) within the fisheye show longer lives than those without, likely due to reduced crack growth rates in that area.
5. Axial residual stresses play a significant role in producing the diameter effects observed in this investigation. Specimens built with a larger gauge diameter exhibit higher tensile residual stresses at the surface compared with smaller diameter samples. Stress relief heat treatment reduces the overall level of residual stress and this improves the HCF resistance in large diameter specimens. The effect of stress relieving on HCF is less pronounced in small diameter samples due to the generally lower level of residual stress produced during AM.

6. The small crack growth behavior is not significantly different for different L-PBF machines, build orientations, and source of feedstock powder.
7. Using a small crack fracture mechanics modeling approach, the high cycle fatigue (S-N) response can be reasonably well predicted for as-built and stress-relieved specimens when informed by the initiating defect size and crack growth behavior. This understanding lays the foundation for use of ICME models to predict local fatigue behavior in geometrically complex AM specimens.

6.2 Recommendations for future work

Based on the results and conclusions presented in this dissertation, the following recommendations are proposed for future work:

1. This dissertation mentions briefly the concept of the weakest link theory, though a complete study of this was unable to be conducted. The weakest link is a proposed hypothesis for explaining the size effects seen on the high cycle fatigue (HCF) behavior. This theory suggests that specimens of a larger size have a higher probability of containing a crack initiating element, leading to shorter fatigue lives and lower fatigue strengths. This dissertation touched on this idea by comparing gauge diameter but did not take into account gauge length or gauge volume. To resolve this, specimens of modified geometry – a 5.0 mm diameter specimen with identical gauge length to a 2.5 mm specimen and 5.0 mm diameter specimen with identical gauge volume to a 2.5 mm specimen – would be fatigue tested to note any changes to fatigue behavior. This would allow for conclusions to be made whether the size effects seen are more weakest link dependent or residual stress dependent.
2. The short fatigue crack growth (SFCG) behavior was characterized for 5.0 mm specimens in this dissertation. SFCG testing was not conducted on 2.5 mm or 1.5 mm specimens,

though it would be beneficial to do so. It has been concluded that the residual stress state has some level of influence on the high cycle fatigue (HCF) response with regard to size effects. Despite this, there is little to no noticeable effect on the SFCG behavior between the as-built and stress-relieved specimens. Since SFCG testing was conducted on specimens not free from residual stresses, the influence of the residual stress state is inherently included in the crack growth behavior. For this reason, it would be beneficial to conduct SFCG testing on smaller samples as their residual stresses have been shown to be lower than the stress-relieved 5.0 mm specimens.

3. The short fatigue crack growth (SFCG) studies conducted in this dissertation were able to measure the crack growth behavior at crack growth rates (CGR) as low as 10^{-10} m/cycle, though it is possible that the true crack growth threshold values exist below this. For this reason, further SFCG studies should be conducted using the methods described in Chapter 5 but at lower stress values, such that CGRs between 10^{-11} and 10^{-12} m/cycle can be achieved.
4. A total of 33 specimens across both L-PBF machines and various gauge diameters (5.0 mm diameter specimens built on a Concept Laser M2 AM machine and 1.5 mm diameter specimens built on a ProX DMP 200 AM machine) were subjected to some form of surface removal. This dissertation was able to show that surface removal results in an improved fatigue strength at 10^8 cycles and fatigue life in all stress regimes regardless of L-PBF machine or specimen size. Due to lack of availability of sufficient high quality AM specimens of two diameters on both machines, it was not feasible to conduct a systematic study of this effect. A systematic study on this topic would be of value. To achieve this, the studies in Chapter 3 and 4 would need to be duplicated to include surface removal of

both 5.0 mm and 1.5 mm specimens on each L-PBF machine. Chapter 3 would also benefit from having more specimens across a wider range of stresses tested to fill out the rest of the S-N curve.

5. This dissertation has concluded that specimens with sub-surface crack initiation have longer fatigue lives and higher fatigue strengths at 10^8 cycles due to a reduced crack growth rate (CGR) for cracks growing in vacuum. This conclusion is aided by other published research that has shown reduced CGRs in vacuum for other stainless steels, but has not been explicitly shown to occur in L-PBF 316L. It would be beneficial to conduct short fatigue crack growth (SFCG) studies in vacuum to accurately measure the value of CGRs in vacuum for L-PBF 316L. This would allow for more accurate prediction of S-N curves in instances where crack growth begins in vacuum.
6. The entirety of this dissertation focused on initiating defect analysis post-mortem, by means of investigating the fracture surface of failed samples, determining the source of crack initiation, and quantifying the defect. Studies have been conducted previously by others in which x-ray CT scans are done on L-PBF specimens before and after fatigue testing. These methods give a better understanding of the global, 3D defect morphology and distribution for use in ICME models. A 3D view of the initiating defects may be beneficial in terms of stress intensities and stress concentration factors. The use of x-ray CT also provides information about defect morphology before and after fatigue, should there be any defect coalescence or secondary crack initiation. Additionally, x-ray CT would be particularly useful in further studies on the weakest link, as this method could be used to quantify the number of potential crack initiation sites across the different gauge diameters (5.0 mm and 1.5 mm).

7. It has been shown in other work that both the short crack growth behavior (SFCG) and high cycle fatigue (HCF) behavior is influenced by the load ratio, R. This dissertation demonstrates size effects occurring under fully reversed loading, $R = -1$. To obtain a complete understanding the SFCG and HCF behavior, testing should be conducted at various load rations (i.e., $R = 0.1$, $R = 0.5$, etc.). This is important for being able to accurately model and predict fatigue behavior in a range of loading scenarios.
8. This dissertation demonstrates size effects occurring in ultrasonic high cycle fatigue. Traditional servo-hydraulic fatigue testing would allow testing in the lower frequency range (20-150 Hz), to assess the degree to which size effects occur in this regime. Literature has conflicting results whether discrepancies in fatigue behavior exist between servo-hydraulic and ultrasonic fatigue testing, so it would be beneficial to investigate this thoroughly.